Atomistic Simulations of Spin-Dynamics

Maria Stamenova

School of Physics, Department of Science

University of Dublin

A thesis submitted to the University of Dublin in part-fulfilment of the requirements for the degree of

Doctor of Philosophy

February, 2009

Declaration

This thesis is submitted by the undersigned for examination for the degree Doctor of Philosophy at the University of Dublin. It has not been submitted as an exercise for a degree at any other University or other degree-giving institution.

This thesis, apart from the advice, assistance and joint effort mentioned in the acknowledgements and in the text, is entirely my own work.

I agree, that the Library may lend or copy this thesis freely upon request.

Maria Stamenova

Acknowledgements

Apparently, for almost five years of Ph.D. studies one is indebted to many people, who in their own special ways have contributed to one's journey. Now that this is almost done, I would like to give my sincere thanks to everyone, who helped me get to this point. As it is practically impossible to mention each and every person I have learned something from, I ask to be forgiven in advance.

Most of all, I am greatly indebted to my supervisor Prof. Stefano Sanvito. Firstly, for giving me the chance to escape from the nuclear physics, come to Dublin and work in The Computational Spintronics Group of Trinity College, which under Stefano's leadership in the past few years has expanded and diversified with brilliant people from three-four continents. Then, for guiding me in my research, together with being 1000% supportive on the personal side. I highly appreciate all the time which he has dedicated to discussions of my work, helping me make sense of new results or giving me ideas of what to do next. I am also grateful for his careful reading and corrections on my thesis.

The next person I would like to thank most sincerely is Tchavdar Todorov from the Queen's University of Belfast. Indeed my project was established as a collaboration between Stefano and him. Together with the numerous meetings with Tchavdar and Stefano both in Belfast and in Dublin, my own visits to Belfast and telephone conferences, he has always been in email-reach for me, should there be problems to be discussed. I have availed a lot from the discussions with him and his experience. Very accurate and rigorous in his approach to matters, his comments were always spot-on and always helped me find the answers.

Then come my lab-mates and all the people from our group. I should mention Alex Rocha, from whom I inherited a non-spin polarised version of the transport code and who, together with Cormac Toher, who also worked on a tight-binding code, were very helpful in the early days. Also Ivan and Das, who also started nearly the same time as I did and now are my neighbours in desk-space with whom to discuss all sorts of issues. As I started chronologically, from the times we all worked in the "Arches", I should

mention Nicola with his fresh sense of humour and our Post Docs Tom and Miguel, who were also our sys-admins, and again – very helpful.

Now, our group has grown dramatically in the last couple of years. We are even spread over two buildings so I see some of the people (those in CRANN) only at Group Meetings. The newer members are Akin Aakande, Nadjib Baadji (PostDoc), Sankar, Nuala Caffrey, Andrea Droghetti, Mauro Mantega and Anna Pertsova. They have all been very kind and helpful in many ways. Particularly Anna, a very positive and talented young person, who joined only recently, has been so friendly and supportive.

I should also mention Jimmy Tang from TCHPC who is our sys-admin at present and has been very helpful.

Last but not least, I would also like to mention Cristian Sanchez, who I met in Belfast and from whom I learnt a lot about Ehrenfest-dynamics simulations. I am also grateful to Olga and S. Sahoo with whom I was collaborating in Belfast.

On the personal side – here is my first official opportunity to acknowledge my husband Plamen and he is the one who has always been my closest friend and a colleague too, with whom to discuss physics at anytime and anywhere. Actually, we have been through our PhD studies in Trinity College together but it has always been him, helping me with his impeccable physical intuition and knowledge. The past year since our son Stanislav was born was indeed very special and very hectic for us. I have only made it this far because of his encouragement, positive attitude and efforts. Plamen graduated last year and is currently a Post Doctoral Fellow in Trinity.

I would also like to express my deepest gratitude to my parents Katia and Tsonyo and to my granddad Kostadin back in Bulgaria, and to my sister Nadia and her family, who live in Germany, for their sacrifices, encouragement and support through all these years.

Thank you!

Abstract

Current-induced *spin-transfer torque* effects form an exciting branch in the field of spintronics with a huge potential for applications. Magnetization dynamics phenomena like switching or GHz frequency precession in spin valves, enhanced Gilbert damping, etc. are all generated by spin-polarized currents in nano-scale structures. Also in a close proximity to technological applications is the field of molecular spintronics where the quantum properties of molecules trapped in constrictions can be utilized to control spin-currents and even engineer spin logic-elements. In order to investigate theoretically spin-transfer torque effects in atomic-scale conductors in this Thesis we develop a combined microscopic description of the magnetization dynamics together with the open-boundary quantum transport of the itinerant electrons.

Our method is based on the $s-d$ model and the adiabatic spin approximation, in which the localized d electrons are the source of localized spins and are treated as classical variables and the s electrons are itinerant and carry the current. We take two approaches to the spin dynamics. Firstly, we consider the typical Landauer ballistic transport set-up and investigate the effects of the current on the activation barriers for quasi-static rotations of the local spins under current-carrying conditions. We find that current can change the stability of the spin-state in the constriction and favour a state with particular transport properties. In the case when there is an abrupt spin domain wall (DW) inside the junction current may promote both pinning and de-pinning. We further introduce structural degrees of freedom into this model and find that structural readjustments induced by the current can have significant effects on the spin dynamics and be a source of pinning for the DW in the constriction. Conversely, we find that the spin-dynamics has little or no effect on the current-driven structural deformation.

The other approach is a time-dependent scheme for Ehrenfest spin-dynamics. Its development and testing is in fact one of the main objectives of this work. We apply this method to investigate dynamical effects in closed systems, where we address magnon spectra calculations, dynamical indirect exchange coupling and generation of a spin-motive force by a precessing DW. We also extend this method to an empirical open-boundary augmentation in order to treat spin-transfer phenomena in the time-domain and to assess the adiabaticity of the mechanism driving the motion of an atomic-scale DW.

Contents

Chapter 1

Introduction

The discovery of the giant magnetoresistance effect (GMR) [9, 19] in the late eighties has since been driving an unprecedented growth in the magnetic storage densities (particularly in the last decade), surpassing that established by the Moore's law [71] in the semiconductor industry. The technology in the GMR-based hard-drive read-heads, stemming from the experimentally observed very large magnetoresistance in certain magnetic multilayers, has found its way to the commercial-scale production and thus to the every-day lives of people in record times. In recognition Peter Grünberg and Albert Fert, the experimentalists who were first to observe GMR and recognize its potential, were awarded the Nobel prize for Physics in 2007.

Together with its immediate technological applications the GMR, by demonstrating a way of controlling the transport properties of the carriers (electrons) in acting upon their spin, has become the triggering factor to a whole new scientific-research field, commonly known as *spintronics* [1]. This new branch of magnetism, stimulated by the industry and by the rapid progress in the ability to manipulate the magnetization on length-scales smaller than the spin-diffusion length, rapidly spread away from its GMR root with branches like the spin transfer, spintronics with semiconductors, molecular spintronics and single-electron spintronics [38].

The last two categories set a direction for development of spintronics into what is called nanospintronics [92]. At this end there are the studies of electron transport in reduced dimensions. The typical sample is a junction that consists of two electrodes (leads) attached to a nano-scale object. In the case of molecular spintronics this object is a molecule, while in single-electron spintronics it is a quantum dot [2] separated from the leads by two tunnel barriers. The magnetism can be carried either by the object, like in the case of the single-molecule magnets (SMM) [20],

[1] The term comes from spin-transport electronics or spin-based electronics [129].

[2] Quantum dots are nanoscale solid-state systems (e.g. semiconducting islands of 10^2-10^5 atoms) where electrons are spatially confined. They constitute an intermediate step from bulk material to single molecule.

or by the leads. In any case, these systems display a variety of quantum effects (either due to their internal spin-degrees of freedom as in the SSM case, or due to the quantum confinement they create) and are even candidates for quantum-computing [129, 20]. A more immediate possibility in molecular spintronics is, for instance, the utilization of organic molecules and nanotubes for spin-transport devices at the nano-scale. These carbon-based structures preserve the spin-coherence at distances longer than conventional metals and semiconductors and can be used as spin-valves [116, 51]. Recent theoretical studies [83] have clearly demonstrated the importance of the non-equilibrium quantum-transport effects, which determine the spin-valve properties of a range of organic molecules.

Another promising area of spintronics is the so-called *spin-transfer*. In the mid nineties Slonczewski [93] and Berger [16] predicted the possibility of inducing spin-dynamics by means of a spin-polarized current. This effectively was the prediction of the "inverse" GMR effect, i.e. the possibility that a spin-polarized current could change the magnetic state of a device. The essential idea is that a spin-polarized current can transfer angular momentum to the magnetization of a magnetic system, thus generating a torque. In the right conditions this current-induced torque can balance or even surpass the magnetic Gilbert damping [42], thus creating new dynamical solutions to the equations of motion for the magnetization. Magnetic switching, magnetic resonators and enhanced Gilbert damping can all be generated by a spin-polarized current. Importantly the current-induced torque depends on the local current density and not on the total current through the sample. This allows for down-scaling the size and the power consumption and opens new prospects for switching magnetic random access memories (MRAM) [36], which largely motivates the growing interest for this area of research.

Theory and modeling of current-induced magnetic phenomena is largely based on solving the Landau-Lifshitz-Gilbert equations with additional terms describing the current-induced torques. At a more advanced level transport theory for diffusive transport is also introduced in the description, effectively creating a sort of Kirchkoff magneto-ciruitry theory [24]. A much less explored area is that of atomistic simulations of magneto-dynamics. These however are expected to occupy an increasingly important place in theoretical magnetism, since nanoscale and even monoatomic one-dimensional [40] magnetic devices are already available and examples of atomic scale magnetic phenomena, such as transport in magnetic point contacts [125] and ultra-thin domain walls [78], have been already demonstrated.

To date there is a notable and important attempt towards the atomistic calculation of quantities related to spin-dynamics. This is represented by the extension of density functional theory

(DFT) to time-dependent phenomena. Within this framework the theoretical foundation for time-dependent DFT for spin-dynamics was laid several years ago [68, 27] and practical calculations based on the adiabatic approximation have been rather successful in describing dynamical properties of magnetic transition metals, although in absence of an electron current [7, 6]. Currents were introduced only recently and simulations for open systems, carried out by using non-equilibrium transport theory combined with DFT, are now available [45].

Importantly, all the calculations to date, based on the atomistic evaluation of the spin-torque, do not perform real molecular dynamics in the presence of evolving currents. In Ref. [45], for instance, the torques acting on the free layer of a spin-valve are calculated, but the magnetisation itself is not relaxed. Since the conducting state of a device can be seriously affected by its magnetic configuration, particularly at the nanoscale, this is an important limitation for realistic magneto-device simulations. Note that there are no fundamental obstacles to molecular dynamics involving spins. Ultra-fast spin-switching in the pico-second range has been demonstrated, indicating that the fastest time-scale of atomic spin-dynamics is indeed in (or below) the ps range [41]. Since the typical time scale for electronic processes is in the fempto-second range, one needs between 10^3 to 10^5 time steps to evolve the electronic structure to times relevant for the spin-dynamics. This is well in reach of state of the art time integration techniques.

This Thesis aims to present recent advances towards the development of a truly atomistic time-dependent theory for spin-dynamics. The *s-d* tight-binding model including electrostatic corrections at the Hartree level will be our underlining electronic structure theory and whenever available we will make contact with other theoretical approaches. In particular we will be focussing on introducing the main theoretical concepts behind our approach and providing a range of examples where such scheme offers insights well beyond what is achievable by standard static theory. These include the investigation of the spin-wave dispersion in nanoscale magnets, spin-spin correlation in non-magnetic nano-wires, current-induced domain wall motion, and distortion and the generation of an electromotive force obtained by domain wall precession.

The Thesis is organized in the following way. It has five major chapters (apart from the introductory Chapter 1 and the epilogue Chapter 7) and four Appendices. The chapters, as they are ordered, form three logical kernels. Chapter 2 and 3 discuss the quasi-static approach to spin-dynamics in atomic junctions. This is in a sense the preliminary stage of just probing the actual dynamical spin behaviour but the quantum transport is based on a conceptually clear platform. Chapter 5 and 6 introduce the actual time-dependent (TD) spin description. This atomistic spin-dynamics method, suited for closed finite systems, is then further extended by an empirical TD transport method in order to enable us to address spin-torque effects. Chapter 4 is about the

methodological comparison of the static and the time-dependent approach to steady-state transport and it describes the conditions for their equivalence.

Going in more details, in Chapter 2 we introduce the basic concepts of ballistic transport in the spirit of the Landauer scattering theory [63, 64]. We then extend this picture to allow for the fully-quantum description of the conduction by means of the non-equilibrium Green's function (NEGF) formalism. We achieve this by gradually introducing the non-equilibrium concepts into the static quantum description, by firstly analyzing the case of a device coupled to a reservoir with a certain chemical potential [33]. Then we add a second reservoir and follow the same path to finally obtain the corresponding result for the non-equilibrium steady-state conductance. Once, we have introduced all the concepts in an invariant form, we consider a particular implementation, based on a two-spin tight-binding (TB) representation of the electronic structure, and sketch the algorithm for self-consistent calculations of the conductance away from equilibrium.

In Chapter 3 we investigate the spin dynamics inside an atomic-scale magnetic point contact (MPC) in current-carrying conditions, as sketched in Fig. 1.1. The leads are oppositely polarised so that an abrupt DW is formed in the constriction, where we consider a uniform chain of atoms with localised spins, bridging over the two leads.

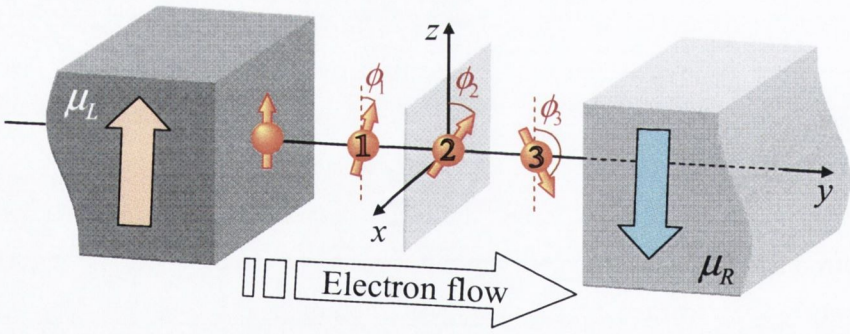

Figure 1.1: Scheme on the MPC described in Chapter 3.

We consider the steady-state non-equilibrium regime and describe the ballistic transport by means of the (previously described) NEGF method. This is implemented in a two-band TB basis. We describe the local spins as classical variables exchange-coupled to the expectation values of the on-site itinerant spin densities and compute the current-induced torques by applying the generalized to open boundaries Hellman-Feynman theorem [111]. We then study the spin-dynamics inside the constriction in terms of quasi-static local-spin rotation and map-out the activation barrier for thermally-activated DW migration. We discuss the symmetries, the stability pattern favoring collinear or non-collinear spin states, as a function of the two exchange parameters, the effects

of the structural disorder and by calculating the work for a closed loop of spin-transitions we address the problem of the conservativeness of current-induced forces in open systems. Finally we, introduce the structural degrees of freedom within the same framework and study the interplay of structural and magnetic properties under bias and its dependence on material parameters. We identify a predominant direction in this magneto-mechanical interplay. Our calculations show that minor structural readjustments have a great effect upon the spin-transfer torque, while the spin-dynamics is practically not affecting the structure.

In Chapter 4 we depart slightly from our main objective of spin-dynamics. We take this opportunity to introduce an empirical time-dependent (TD) approach to the steady-state transport, inspired by the idea of mapping out the Landauer problem onto a finite ("micro-canonical") one [124]. We compare the steady-state conductance results obtained by the TD approach to those obtained by the self-consistent NEGF method (static). Our model-system is that of an atomic dimer weakly-coupled to leads attached to the plates of a capacitor [87]. For certain range of parameters and above certain bias-voltages in this system, the static approach shows the occurrence of multiple (three) different steady states but only one of them is observed in the TD simulation. At the end of this Chapter we demonstrate analytically the conditions under which the empirical TD approach is equivalent to the Landauer steady-state.

In Chapter 5 we introduce the concepts of the time-dependent quantum-classical (Ehrenfest) approach to spin-dynamics. This scheme is then applied to a few test situations, with the aim of reproducing results from static theories in certain limits but also for going beyond the accessible facts. These cases include the calculation of the spin-wave spectra for a monoatomic chain of spins, modelled by an *s-d* model and the temporal correlations of spin-impurities in non-magnetic medium (finite monoatomic wire).

Chapter 6 has two Sections. In the first part we describe the current-induced DW motion by implementing the TD method of steady-state transport from Chapter 4 and the Ehrenfest spin dynamics from Chapter 5, in a common scheme, which is then applied to the 1D spin-chain containing a DW (Fig. 1.2). We investigate the simulated DW motion with respect the well-known adiabatic spin-torque contributions [66]. We compare the dynamics of two walls that differ in width by factor of four and the thinner one of them is just a few lattice spacings thick. Non-adiabatic effects are analyzed and qualitatively compared to the proposed micro-magnetic form of the non-adiabatic torque [135].

In the second part of Chapter 6 we investigate the opposite in certain aspects effect. That is the induction of a spin-motive force (SMF) [1] upon the itinerant electrons by a precessing in an

[1] This, in essence, is the spin-analogue the Faraday's electromotive force.

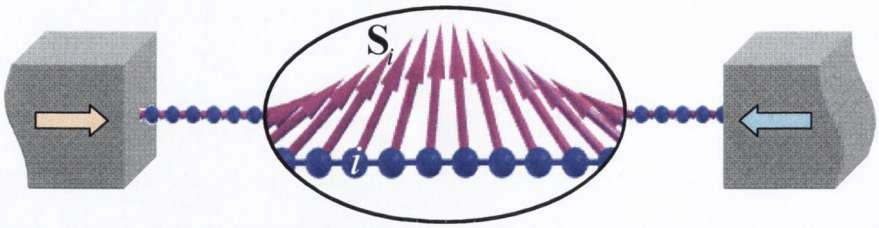

Figure 1.2: Scheme of the atomic-scale DW, investigated in Chapter 6. The blocks at the ends represent current or voltage probes.

external magnetic field wall. Using our quantum-classical spin-dynamics scheme for a closed and finite system, we reproduce numerically the result in Ref. [15] for the magnitude of the pure-SMF (generated by the precessing local-spin texture) and extend it into a separate formulation, valid for the *s-d* model description. We present an analytical argument for the classical origin of the SMF and support it with purely classical simulations.

This thesis has four Appendices where certain concepts or methods are described in greater detail.

In Appendix A we derive the surface Green's function of a semi-infinite cubic lattice with a finite cross-section.

In Appendix B we describe the most common mixing schemes in self-consistent electronic-structure calculations and particularly the Pulay mixing scheme used in NEGF calculations in Chapter 3.

Appendix C is about the concept and the description of current within a TB model of the electronic structure. The expression for bond-current, used in Chapter 4 and Chapter 6 is derived.

In Appendix D we discuss the time-integrators used for solving second order differential equation in Molecular Dynamics. We describe the leap-frog method, used in our spin-dynamics simulations (Chapter 4, 5, 6) and its problems with dissipative forces. We describe the method used in Ref. [22] to fix the divergencies and illustrate its effect with an example from Chapter 6.

Chapter 2

On the steady-state transport theory

2.1 The Landauer formula

In the late 50-ties Landauer [63] studied theoretically the problem of residual resistivity in metals, introducing a novel viewpoint in the transport theory. He considered the transport process as a result of the incident current flowing into the specimen and thus the build-up of electric field as a consequence of the electron flow through a structure of scattering centres. This viewpoint, as opposed to the typical view of the electric field as a cause and the current as a response, basically converted the problem of electrical conductance into a scattering problem, where the conductance was related to the ease with which the carriers transmit through the conductor [52]. Landauer's approach proved to be of great practical importance as it allowed conductance to be calculated in systems of mesoscopic dimensions where the carriers, being quantum objects, propagate coherently within the specimen and where the interfaces with the current /voltage/ probes are key elements of the circuit.

In his work on disordered one-dimensional lattices [64], Landauer derived (based on the diffusion equation) the following expression for the conductance

$$\mathcal{G}_{1D} = \frac{e^2 v}{2} \frac{T}{1-T} \left(\frac{dn}{d\mu} \right) = \frac{2e^2}{h} \frac{T}{1-T}, \tag{2.1.1}$$

where T is the transmission probability for an electron with an initial velocity v to pass through the whole scattering array of length L, n is the electron density, μ the chemical potential and $dn/d\mu = 2/hv$ for a one-dimensional Fermi gas [8]. In Eq. (2.1.1) an incoherent superposition of states originating from two reservoirs at the two ends of the chain is assumed. These reservoirs are the electronic equivalent of a radiative blackbody. They emit electrons (source) according to

their Fermi distribution (which is considered unaffected by the transport) and absorb all incident electrons (drain), completely destroying their phases. The electronic temperature here is considered zero.

Eq. (2.1.1) can readily be generalized to higher dimension structures, having M transverse modes, as $\mathcal{G} = M\mathcal{G}_{1D}$. However, what is referred to as the *Landauer formula* in the literature is

$$\mathcal{G} = \frac{2Me^2}{h}T\,. \tag{2.1.2}$$

The difference between Eq. (2.1.1) and Eq. (2.1.2) comes from the fact that the former [1], which we now denote by $\mathcal{G}_S$, is the conductance of the scattering sample itself subjected to a current flow, while the latter is the conductance of the sample coupled to the reservoirs. That difference in terms of resistance is exactly the resistance of the interfaces (or contacts), which are considered in series to the sample resistance. Thus for a perfect (or ballistic) conductor $T = 1$ the conductance Eq. (2.1.1) goes to infinity, or the resistance tends to zero, while Eq. (2.1.2) tends to the *contact resistance* [32]

$$\mathcal{R}_C \equiv \mathcal{G}_C^{-1} = \mathcal{G}^{-1} - \mathcal{G}_S^{-1} = \frac{h}{2e^2M}\,. \tag{2.1.3}$$

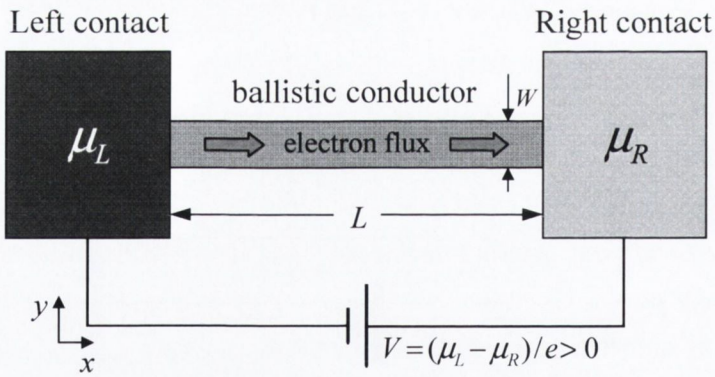

Figure 2.1: Scheme of the circuit used for derivation of the contact resistance (2.1.3).

For the derivation of the contact resistance (2.1.3), we consider a *ballistic* conductor as in Ref. [32], connected to two reservoirs with chemical potentials μ_L and μ_R [$L(R)$ designate the left(right)-hand side of the specimen, see Fig. 2.1] and calculate the current through it for a given

[1] Eq. (2.1.1) is also known as the *four-probe conductance* [99], illustrating the actual physical conditions leading to it as brought out in Ref. [37]. In four-probe conductance measurements fixed current can be fed through one pair of leads, while the resulting voltage drop across the regions of the sample is measured by attaching a second pair of leads to it once steady state is established. Ref. [37] has demonstrated that Eq. (2.1.1) represents the conductance in this case under the assumption of a week coupling between the current-probes and the measuring reservoirs.

applied bias $V = (\mu_L - \mu_R)/e$. [1] The length L or the conductor is assumed such that $L << l_0$ in order for it to be ballistic (l_0 is the mean free path). [2] The contacts depicted in Fig. 2.1 (which are in fact the Landauer reservoirs) are considered to be *reflectionless*, meaning that all incident electrons from the conductor are fully absorbed and none are reflected back into the conductor. This assumption allows to discriminate the right-going $+k$ electrons in the conductor from the left-going $-k$ ones as they originate from different reservoirs, i.e. the left or the right reservoir respectively. Thus each of these two sub-ensembles has the statistical properties of the reservoir, from which it originates, so that there are two quasi-Fermi levels in the conductor (μ_L for $+k$-states and μ_R for $-k$-states) and the current is only carried by the right-going $+k$-states with energies in the range from μ_R to μ_L.

A single transverse mode of the $+k$-states at energies E is occupied according to the Fermi function $f_L(E) = f_0(E - \mu_L)$ [3] of the left reservoir and carries a current $(ev/L)f_L$ per longitudinal $+k$-state, thus it carries through the conductor a current of

$$I^+ = \frac{e}{L}\sum_k v f_L(E) = \frac{e}{\hbar L}\sum_k \frac{\partial E}{\partial k} f_L(E) \longrightarrow \frac{2e}{h}\int_{\mu_R}^{\mu_L} f_L(E)\mathrm{d}E\,, \tag{2.1.4}$$

where periodic boundary conditions are assumed in the transverse direction, so that $\sum_k \longrightarrow 2(\text{for spin}) \times (L/2\pi)\int \mathrm{d}k$. Finally, for $M(E) = \sum_i \theta(E - E_i)$ (E_i being the cut-off energy of the i-th mode) transverse modes of the conductor open at energy E, the total current is

$$I = \frac{2e}{h}\int_{\mu_R}^{\mu_L} M(E) f_L(E)\mathrm{d}E \longrightarrow \frac{2eM}{h}(\mu_L - \mu_R) \text{ for } M(E) = const \text{ in } [\mu_R, \mu_L] \tag{2.1.5}$$

and thus the contact resistance (as the conductor is assumed ballistic) is

$$\mathcal{G}_c^{-1} = \frac{V}{I} = \frac{(\mu_L - \mu_R)}{eI} = \frac{h}{2e^2 M} \approx \frac{12.9\mathrm{k}\Omega}{M}\,, \tag{2.1.6}$$

which is a result identical to Eq. (2.1.3). Apparently the contact resistance is related to the mismatch of the conductivity of the contacts and the conductor, which is considered having a very small transverse dimension $W \ll W_C$ compared to the contacts dimension W_C. In the limit $W \approx W_C$ the Ohmic resistance is restored. The power associated with the contact resistance is dissipated in the contacts [32].

If the conductor were not ballistic, but had a finite transmission probability, a circuit as the one in Fig. 2.2(a) would have measured a conductance according to the Landauer formula (2.1.2),

[1] Here and throughout this work we define the bias $V := (\mu_L - \mu_R)/e$, which is a positive quantity when it is driving the electrons from left to right, i.e. along the x-axis as depicted in Fig. 2.1.

[2] For the following semiclassical arguments it is also assumed that the phase relaxation length λ_{ph} is small in order to neglect quantum interference effects.

[3] Here and throughout $f_0(E - \mu) \equiv 1/\left(1 + \exp\left[(E - \mu)/k_B T\right]\right)$ is the Fermi distribution function.

where M would have been the number of open modes in the leads [32]. Omitting the leads, the conductance is still given by Eq. (2.1.2) only this time M refers to the number of modes in the scatterer (see Fig. 2.2(b)).

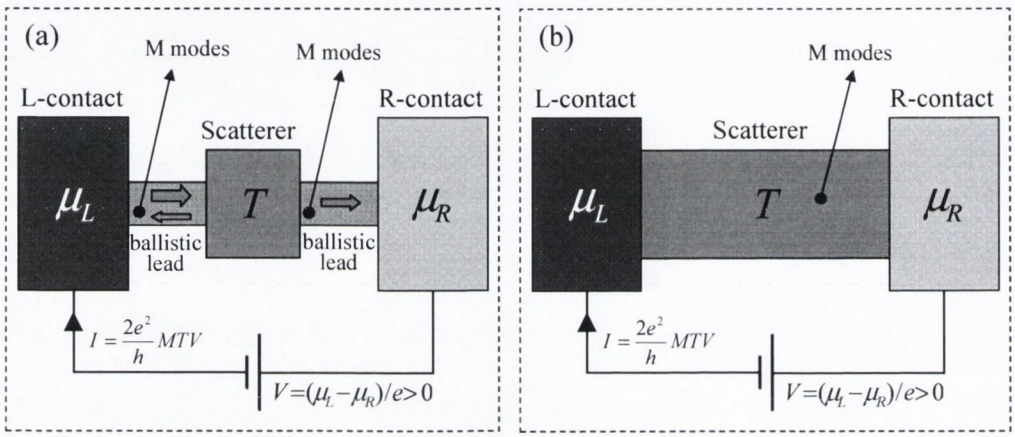

Figure 2.2: Typical circuits for which the Landauer formula [Eq. (2.1.2)] applies: (a) scatterer with average transmission probability T coupled to reflectionless reservoirs via ballistic leads with M transverse modes; (b) scatterer with M open modes, coupled directly to reservoirs. Note that, unlike the typical convention, we denote by I the electron flow and it is opposite to the conventional direction of the current in these circuits.

The Landauer formula [Eq. (2.1.2)] can be generalized for the case of a finite temperature, when the reservoirs are occupied according to a Fermi distribution function. The transport in this case is no longer restricted to the bias window $\mu_L - \mu_R$ but it also exists at a few k_BT's [1] around this energy range. The current is not only carried by states originating from the left reservoir but inside the ballistic leads there are current-carrying states from both sources [see Fig. 2.3]. The net balance of electron fluxes per unit energy in this case is [32]

$$i(E) = i_L^+ - i_L^- = Ti_R^+ - T'i_R^- = \frac{2e}{h}\left[M(E)T(E)f_L(E) - M'(E)T'(E)f_R(E)\right] \tag{2.1.7}$$

because the influxes from the reservoirs are simply $i_L^+(E) = (2e/h)Mf_L(E)$ and $i_R^-(E) = (2e/h)M'f_R(E)$. Finally, the total current can be written as

$$I = \frac{2e}{h}\int \overline{T}(E)\left[f_L(E) - f_R(E)\right], \tag{2.1.8}$$

where the definition $\overline{T}(E) := M(E)T(E)$ is used and it is assumed that $T(E) = T'(E)$, which if away from equilibrium implies the absence of inelastic scattering inside the two-terminal device

[1] Here T is for temperature and in this work it is always used together with the Boltzmann constant k_B so there is no context ambiguity with the transmission probability used in this section.

[32]. Eq. (2.1.8) gives the current through the mesoscopic device, depicted in Fig. 2.3, as a function of the local transmission properties of the scattering region and the Fermi function of the contacts. The corresponding conductance I/V coincides with the Landauer formula (2.1.2) in the limit of low temperatures and low biases V (linear response regime), where $\overline{T}(E)$ is nearly a constant inside the bias window.

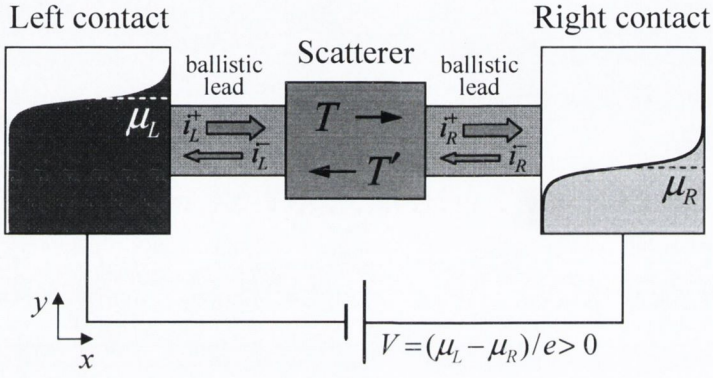

Figure 2.3: Representative circuit at finite temperature.

In summary, the Landauer formula gives a prescription for calculating the current through mesoscopic conductors and it all boils down to calculating the transmission probability for the current-carrying states. The results, obtained in this section, apply to the transport of ballistic but non-interacting carriers (the latter two are not mutually exclusive as the electron-electron interactions are elastic they do not affect the momentum-relaxation path). In this approximation the Pauli exclusion principle does not need to be accounted for, quantum interference effects are neglected (by assuming that either $L \gg \lambda_{\rm ph}$ or simply that the reservoirs are incoherent sources) and the description is semiclassical. For quantum treatment of the mesoscopic transport problem we consider in the next section the Non-Equilibrium Green's Function (NEGF) method.

2.2 The NEGF method

2.2.1 Green's functions in quantum mechanics

The Green's functions are a conceptual tool for solving linear differential equations of the form $\mathrm{D}(x)\Psi(x) = S(x)$, where x is a generalized coordinate in real space, $\mathrm{D}(x)$ is a linear differential operator and $S(x)$ is an excitation. The solution can be expressed as a convolution of a Green's

function G(x,x') and the excitation function

$$\Psi(x) = \int G(x,x')S(x')\mathrm{d}x' \,, \tag{2.2.1}$$

where the two-point function $G(x,x')$ satisfies the equation

$$D(x)G(x,x') = \delta(x-x') \tag{2.2.2}$$

and $\delta(x-x')$ is a Dirac δ-function. Thus the Green's function represents the response of the system at x to a point-like excitation at x' and when convoluted with the actual excitation it produces the actual response of the system $\Psi(x)$. In the operator version of the equation above, G would be inverse of the differential operator D, i.e. $G = D^{-1}$ and $\Psi = GS$.

Green's functions appear often in physics and engineering where linear differential equations are involved. They are particularly popular in quantum scattering theory for solving the Schrödinger equation (see for example Ref. [90]). The time-independent Schrödinger equation

$$(E\hat{I} - \hat{H})\Psi = 0, \quad \text{where in general the Hamiltonian is} \quad \hat{H} = \frac{i\hbar\nabla + e\mathbf{A}}{2m} + U(r) \tag{2.2.3}$$

and $\hat{I}$ is an identity operator, has a Green's function

$$\hat{G}(E) = \left(E\hat{I} - \hat{H}\right)^{-1} . \tag{2.2.4}$$

In the N-dimensional eigenspace $\{\phi_i\}_{i=1}^{N}$ of the Hamiltonian $G(E)$ is a diagonal matrix $[G(E)] = \mathrm{diag}\,[1/(E-\varepsilon_n)]_{n=1}^{N}$, where ε_n is an eigenenergy. Fourier transformed to the time domain this Green's function reads

$$[G(t)] = \frac{1}{2\pi\hbar}\int_{-\infty}^{+\infty} e^{-iEt/\hbar}\,[G(E)]\,\mathrm{d}E = \frac{1}{2\pi\hbar}\,\mathrm{diag}\left[\int_{-\infty}^{+\infty}\frac{e^{-iEt/\hbar}}{E-\varepsilon_n}\mathrm{d}E\right]_{n=1}^{N} . \tag{2.2.5}$$

The above integral is indefinite for real ϵ_n. As $\hat{H}$ is Hermitian and ϵ_n are indeed real, a small infinitesimal imaginary component $-i\eta$ is added to the eigenenergies. The result for $\eta > 0$ is called the retarded Green's function. For $\eta < 0$ we obtain the advanced Green's function but the latter violates the causality principle and we abandon it as unphysical. The *retarded* Green's function, expressed in time or energy domain, is [33]

$$[G^{\mathrm{r}}(t)] = \frac{-i}{\hbar}\theta(t)e^{-\eta t}\mathrm{diag}\left[e^{-i\varepsilon_n t/\hbar}\right]_{n=1}^{N} \quad \longleftrightarrow \quad [G^{\mathrm{r}}(E)] = \mathrm{diag}\,[1/(E-\varepsilon_n+i\eta)]_{n=1}^{N} . \tag{2.2.6}$$

Further in this work we shall drop the "r" index of $G^{\mathrm{r}} \equiv G$ and refer to it simply as "the Green's function". In time domain $[G(t)]$ satisfies the time-dependent Schrödinger equation with an impulse source at $t = 0$

$$\left(i\hbar\frac{\partial}{\partial t} - [H]\right)[G(t)] = [I]\delta(t) . \tag{2.2.7}$$

In energy domain the (retarded) Green's function in operator form is expressed as

$$\hat{G}(E) = \lim_{\eta \to 0^+} \left((E + i\eta)\hat{I} - \hat{H} \right)^{-1} . \tag{2.2.8}$$

Finding $\hat{G}(E)$ is equivalent to solving the time-independent Schrödinger equation (2.2.3) and fully describing the closed conservative system it refers to. For example, the *spectral function* of the system, which is defined as $A(\mathbf{r}, \mathbf{r}'; E) \equiv 2\pi \sum_i \phi_i(\mathbf{r}) \delta(E - \varepsilon_i) \phi_i^*(\mathbf{r}')$ and its diagonal elements represent the local density of states (LDOS) in the system

$$D(\mathbf{r}, E) = \sum_i |\phi_i(\mathbf{r})|^2 \delta(E - \varepsilon_i) = \frac{1}{2\pi} \mathrm{Tr}\left[A(E)\right] , \tag{2.2.9}$$

can be expressed in an invariant (operator) form in terms of the Green's function [33]

$$\hat{A}(E) = 2\pi\delta(E\hat{I} - \hat{H}) = i\left[\hat{G}(E) - \hat{G}^\dagger(E)\right] . \tag{2.2.10}$$

Other important quantities can be related to the spectral function. The density matrix of the system in the eigenspace of $\hat{H}$ is $\rho(\mathbf{r}, \mathbf{r}') = \sum_i |\phi_i(\mathbf{r})\rangle\langle\phi_i(\mathbf{r}')| f(\varepsilon_i)$, where $f(\varepsilon_i) = f_0(\varepsilon_i - \mu)$ is the Fermi function for a given chemical potential μ. The invariant expression for the density operator is [33]

$$\hat{\rho} = f_0\left(\hat{H} - \mu\hat{I}\right) . \tag{2.2.11}$$

If the isolated system, we describe here, is very big and the eigenstates of its Hamiltonian are nearly a continuum, the density operator can be related to the spectral function as

$$\rho(\mathbf{r}, \mathbf{r}') = \frac{1}{2\pi} \int_{-\infty}^{+\infty} A(\mathbf{r}, \mathbf{r}'; E) f_0(E - \mu) \mathrm{d}E . \tag{2.2.12}$$

The integrant in Eq. (2.2.12) describes the actual number of electrons per unit energy and is called *correlation function* $G^{\mathrm{n}}(E)$ [33]. For a system in equilibrium (with a Fermi energy distribution) the correlation function operator is defined as

$$\hat{G}^{\mathrm{n}}(E) = \hat{A}(E) f_0(E - \mu) . \tag{2.2.13}$$

Note that the latter is not necessarily the true expression for the correlation function if the system is not in equilibrium.

The quantum transport problems often involve open heterogeneous systems or something more like the Landauer setup (see e.g. Fig. 2.3), where a device (or scatterer, or channel) of mesoscopic dimensions is coupled to two contacts (or leads, or reservoirs) of, say, microscopic dimensions, connected to a battery, which maintains the latter at different chemical potentials. Once the circuit is closed this system is no longer in equilibrium and cannot be broken into parts, each described

separately by Eq. (2.2.3), as the particle number may vary locally. Often we are interested only in the properties of the device and certain assumptions can be made about the contacts. In the next section we shall demonstrate that a "separate" treatment of the device is indeed possible in certain systems and in these cases a modification of Eq. (2.2.3) is needed to account for the open boundary conditions.

2.2.2 Device attached to a contact

We consider a device that is somehow depleted of all the conduction electrons and then brought in contact with a reservoir [33], the idea being to focus on the states that "spill-over" from the contact. In principle the electrons in the contact (see Fig. 2.4(a)), if the latter is isolated, should be described by Eq. (2.2.3) but we shall consider it as an open system where electron can hop in and out. Phenomenologically, such an open system can be described by [33]

$$\left[(E+i\eta)\hat{I}_R - \hat{H}_R\right]|\Phi_R\rangle = |S_R\rangle \ , \tag{2.2.14}$$

where index R is used to denote that operators belong to the reservoir, η is an infinitesimal quantity, related to the energy level broadening in the contact (or the rate of particle loss, due to the finite life-time) and $|S_R\rangle$ is another phenomenological quantity describing the inflow or gain of particles in the contact from external sources.

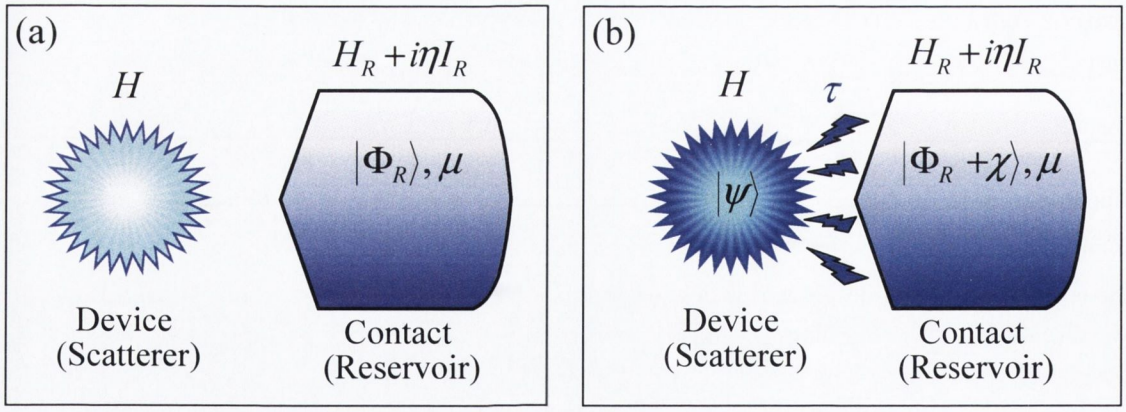

Figure 2.4: (a) Mesoscopic device, fully depleted of electrons and a well separated reservoir of electrons; (b) The device and the reservoir are brought in contact - electrons spill into the device, developing a $|\psi\rangle$ state.

If the device is then brought together with the contact, electrons will hop from the contact to the device. Once a *steady state* is established, i.e. the electron density ceases to change locally

inside the device, a state $|\psi\rangle$ develops in the device (see Fig. 2.4) and also the state of the contact changes from $|\Phi_R\rangle$ to $|\Phi_R\rangle + |\chi\rangle$. If the strength of the contact interaction is described by τ, then the whole system is described by

$$\begin{pmatrix} (E+i\eta)I_R - H_R & -\tau^\dagger \\ -\tau & EI - H \end{pmatrix} \begin{pmatrix} |\Phi_R\rangle + |\chi\rangle \\ |\psi\rangle \end{pmatrix} = \begin{pmatrix} |S_R\rangle \\ 0 \end{pmatrix} \tag{2.2.15}$$

where H is the device Hamiltonian. The key assumption here is that the source and drain terms (i.e. $|S_R\rangle$ and η) from Eq. (2.2.14), describing the isolated contact, have not changed when it has been attached to the device. We recognise the Green's function of the isolated contact

$$G_R(E) \equiv [(E+i\eta)I_R - H_R]^{-1} \tag{2.2.16}$$

and express from (2.2.14) $|S_R\rangle = G_R^{-1}|\Phi_R\rangle$. We can also eliminate $|\chi\rangle = G_R\tau^\dagger|\psi\rangle$ from (2.2.15) and we are left with one equation for the device

$$[EI - H - \Sigma(E)]\,|\psi\rangle = |S\rangle\ , \tag{2.2.17}$$

where we have defined a new source term $|S\rangle \equiv \tau|\Phi_R\rangle$ (this time for the device connected to the contact) and $\Sigma(E) \equiv \tau\, G_R(E)\,\tau^\dagger$ is the so-called *self-energy* . The Green's function of the device is then

$$G(E) = [(E+i\eta)I - H - \Sigma(E)]^{-1} \tag{2.2.18}$$

and thus wavefunction of the device is $|\psi\rangle = G\,|S\rangle$. The spectral function can be calculated from Eq. (2.2.10).

Let us for a moment consider working in a localized in the real space representation, say, a tight-binding representation [8]. Though $G_R(E)$ in Eq. (2.2.19) is the Green's function of the whole contact, when contracted with τ the only part of the G_R-matrix actually contributing to the product would be the part that describes the surface area where the device is attached. In this sense, practically even if the contact is enormous in size, the only relevant information about it for the device is its *surface* Green's function $g_R(E)$ (see Appendix A), which enters in the self-energy (2.2.19), which can instead be written as

$$\Sigma(E) = \tau\, g_R(E)\,\tau^\dagger\,. \tag{2.2.19}$$

This makes the result in Eq. 2.2.18 practically usable as it only contains finite-dimensional matrices. The only assumption it lays upon is that the contact (or reservoir) is big enough for its inflow-outflow to not be affected by the device.

The self-energy, we defined here, is more than just a quantity that appears in the derivation. It is a simplifying concept that allows us to mask the effect of various degrees of freedom in the

composite system, such as the dimension of the contact, into a single term in the Schrödinger equation of the device. Other abstract degrees of freedom can be the electron-electron or electron-phonon interactions [32].

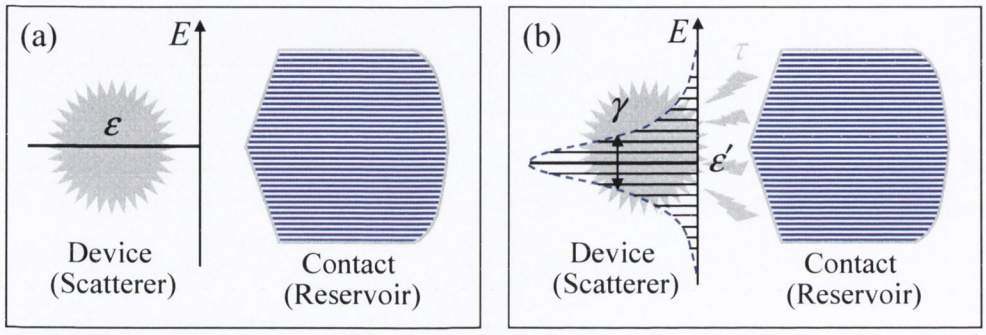

Figure 2.5: Level diagram of a one-level device which is (a) isolated or (b) coupled to a contact with nearly continuous density of states.

To get some understanding of the effect of Σ on the device we consider the simple case when Σ does not depend on the energy. Then, its spectral function [see Eq. (2.2.10)] is

$$\frac{A(E)}{2\pi} \equiv D(E) = i\left(\frac{1}{E-\varepsilon'+i\gamma/2} - \frac{1}{E-\varepsilon'-i\gamma/2}\right) = \frac{\gamma}{(E-\varepsilon')^2+(\gamma/2)^2}\,, \tag{2.2.20}$$

where we have redefined the eigenenergies of the device $\varepsilon' = \varepsilon + \mathrm{Re}(\Sigma)$ and $\gamma \equiv 2\mathrm{Im}(\Sigma)$. Thus the effect of Σ in Eq. (2.2.18) is that the local density of states on the device is shifted by $\mathrm{Re}(\Sigma)$ and broadened into a Lorentzian of width $2\mathrm{Im}(\Sigma)$ (see e.g. Fig. 2.5). In general the quantity used to represent the broadening due to the self-energy is by definition

$$\Gamma(E) \equiv i\left[\Sigma(E) - \Sigma^\dagger(E)\right] \quad \Longrightarrow \quad \Gamma(E) = \tau A_R(E)\tau^\dagger\,, \tag{2.2.21}$$

where we have used the definition of Σ in Eq. (2.2.19) and $A_R(E)$ is the *surface* spectral function of the reservoir

$$A_R(E) \equiv i\left[g_R - g_R^\dagger\right]\,. \tag{2.2.22}$$

In matrix form Γ, the broadening matrix, is the anti-Hermitian part of the self-energy Σ. Using Eq. (2.2.18) and (2.2.21) we arrive at new expressions for the spectral function of the device

$$A \equiv i\left[G - G^\dagger\right] = G\Gamma G^\dagger = G^\dagger\Gamma G\,. \tag{2.2.23}$$

To evaluate the current through the device's interface, defined as $I \equiv 2e\,\mathrm{d}(\langle\psi|\psi\rangle)/\mathrm{d}t$ (the factor of 2 is for two degenerate spins), we look at the time-dependent version of Eq. (2.2.15)

$$i\hbar\frac{\mathrm{d}}{\mathrm{d}t}\begin{pmatrix} |\Phi_R+\chi\rangle \\ |\psi\rangle \end{pmatrix} = \begin{pmatrix} H_R - i\eta I_R & -\tau^\dagger \\ -\tau & H \end{pmatrix}\begin{pmatrix} |\Phi_R+\chi\rangle \\ |\psi\rangle \end{pmatrix}\,. \tag{2.2.24}$$

Since the Hamiltonian $H = H^\dagger$ is Hermitian we obtain for the current

$$I = \frac{2e}{i\hbar}\left[\langle\psi|\,\tau\,|\Phi_R\rangle + \langle\Phi_R|\,\tau^\dagger\,|\psi\rangle\right] - \frac{2e}{i\hbar}\left[\langle\psi|\,\tau\,|\chi\rangle + \langle\chi|\,\tau^\dagger\,|\psi\rangle\right] \equiv I_{\text{in}} - I_{\text{out}}\,, \tag{2.2.25}$$

where we have identified the two terms in square brackets as an inflow I_{in} and outflow I_{out} current, respectively. The latter can be rewritten

$$I_{\text{in}} = \tfrac{2e}{i\hbar}\left(\langle S|\,G^\dagger\,|S\rangle - \langle S|\,G\,|S\rangle\right) = \tfrac{2e}{\hbar}\text{Tr}\left[|S\rangle\langle S|\,A\right] = \tfrac{2e}{\hbar}\int \text{Tr}\left[\tau A_R \tau^\dagger A\right] f_0(E-\mu)\text{d}E \tag{2.2.26}$$

$$I_{\text{out}} = \tfrac{2e}{i\hbar}\left\langle\psi\left|\tau\left(G_R^\dagger - G_R\right)\tau^\dagger\right|\psi\right\rangle = \tfrac{2e}{\hbar}\text{Tr}\left[|\psi\rangle\langle\psi|\,\Gamma\right] = \tfrac{2e}{\hbar}\int \text{Tr}\left[\Gamma G^{\text{n}}\right]\text{d}E\,, \tag{2.2.27}$$

where we have used a few of the relations in this section and the fact that $\langle a|\,M\,|b\rangle = \text{Tr}\left[|b\rangle\langle a|\,M\right]$ for arbitrary vectors $|a\rangle$, $|b\rangle$ and matrix M. We can then write for the net interface current [33]

$$I = \frac{2e}{h}\int \text{Tr}\left[\Gamma A f_0(E-\mu) - \Gamma G^{\text{n}}\right]\text{d}E\,. \tag{2.2.28}$$

Apparently in equilibrium there is no net current through the device-contact interface ($I_{\text{in}} = I_{\text{out}}$) because the correlation function is $G^{\text{n}} = A f_0$ [see Eq. (2.2.13)]. As we shall see in the next section in order for the current to flow non-equilibrium conditions need to be introduced. The simplest non-equilibrium situation will be a device coupled to two contacts (or reservoirs) at different chemical potentials.

2.2.3 Device in a two-contact circuit

In this section we consider a device sandwiched between two contacts as described in Ref. [33]. The contacts will be of the type described in the previous section and will have fixed chemical potentials μ_L and μ_R respectively for the left and the right-hand side contact (see Fig. 2.6). When isolated, the contacts obey the modified Schrödinger equation with source and dissipation terms [see Eq. (2.2.14)]. The composite system of contacts + device is described by

$$\begin{pmatrix} (E+i\eta)I_L - H_L & -\tau_L^\dagger & 0 \\ -\tau_L & EI - H & -\tau_R \\ 0 & -\tau_R^\dagger & (E+i\eta)I_R - H_R \end{pmatrix}\begin{pmatrix} |\Phi_L + \chi\rangle \\ |\psi\rangle \\ |\Phi_R + \chi\rangle \end{pmatrix} = \begin{pmatrix} |S_L\rangle \\ 0 \\ |S_R\rangle \end{pmatrix}, \tag{2.2.29}$$

which under the assumption of the source terms $|S_{L;R}\rangle$ being unaffected by the coupling to the device, results in an analogous equation to (2.2.17) describing solely the device

$$\left[EI - H - \Sigma(E)\right]|\psi\rangle = |S\rangle\,, \tag{2.2.30}$$

where $|S\rangle \equiv \tau_L\,|\Phi_L\rangle + \tau_R\,|\Phi_R\rangle$. The new self-energy Σ is defined as the sum of the two self-energies coming from the contacts

$$\Sigma \equiv \Sigma_L + \Sigma_R\,, \tag{2.2.31}$$

where the one-contact self-energies and Green's functions are defined as in the previous section, i.e.

$$\Sigma_{L(R)}(E) \equiv \tau_{L(R)} G_{L(R)} \tau_{L(R)}^{\dagger}, \quad G_{L(R)} = \left[(E + i\eta) I_{L(R)} - H_{L(R)}\right]^{-1}. \tag{2.2.32}$$

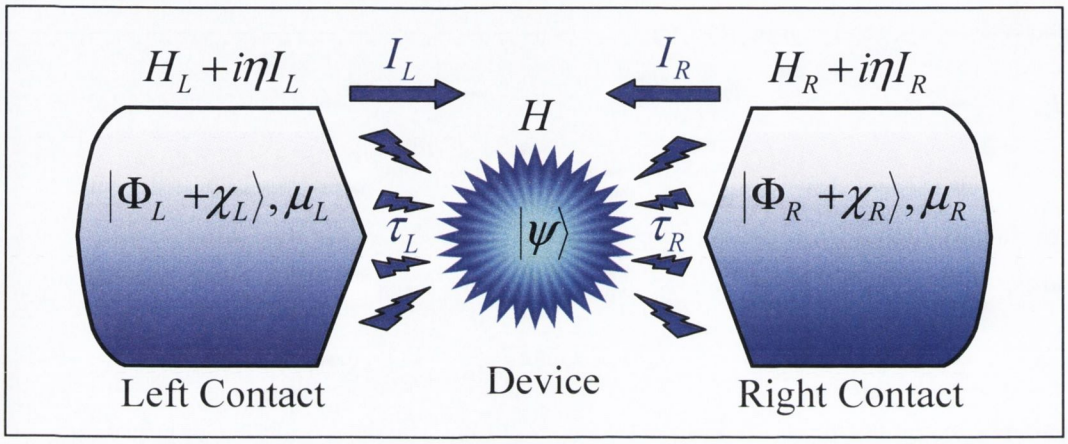

Figure 2.6: Scheme of a device, sandwiched between two reservoirs with different chemical potentials μ_L and μ_R.

The Green's function G of the device is supposed to generate a solution $|\psi\rangle = G\,|S\rangle$, thus from Eq. (2.2.30)

$$G(E) \equiv \left[EI - H - \Sigma_L(E) - \Sigma_R(E)\right]^{-1}. \tag{2.2.33}$$

Expressed through G, the density matrix of the device is

$$\rho \equiv 2\,|\psi\rangle\langle\psi| = 2G\,|S\rangle\langle S|\,G^{\dagger} = 2G\left(\tau_L\,|\Phi_L\rangle + \tau_R\,|\Phi_R\rangle\right)\left(\tau_L^{\dagger}\,\langle\Phi_L| + \tau_R^{\dagger}\,\langle\Phi_R|\right)G^{\dagger}, \tag{2.2.34}$$

where the factor 2 stands for two degenerate spin populations and since the wavefunctions of the isolated contacts ($|\Phi_L\rangle$ and $|\Phi_R\rangle$) span separate spaces with no overlap, the inter-contact terms disappear. By applying Eq. (2.2.11) for the density matrices $|\Phi_X\rangle\langle\Phi_X|$ of the isolated contacts, we obtain [33]

$$\rho = \frac{1}{\pi}\int \left(\left[G\Gamma_L G^{\dagger}\right] f_L + \left[G\Gamma_R G^{\dagger}\right] f_R\right) \mathrm{d}E, \tag{2.2.35}$$

where we have substituted the left(right) broadening matrix $\Gamma_{L(R)} = \tau_{L(R)} A_{L(R)} \tau_{L(R)}^{\dagger}$ as defined in Eq. (2.2.21) and all E arguments are omitted for simplicity. The above expression (2.2.35) is equivalent to the following equation for the correlation function [see Eq. (2.2.13) for the definition of G^{n}]

$$G^{\mathrm{n}} = G\Sigma^{\mathrm{in}}G^{\dagger}, \tag{2.2.36}$$

where $\Sigma^{\text{in}} \equiv \Gamma_L f_L + \Gamma_R f_R$ is the so called *in-scattering function*. Eq. (2.2.36) is known as the *kinetic equation* and is the central equation in the NEGF theory [33]. It needs to be solved self-consistently together with Eq. (2.2.33) in order to determine the steady-state properties of the device out of equilibrium (i.e. for $\mu_L \neq \mu_R$). Actually, Eq. (2.2.36) can be rewritten in the form

$$G^{\text{n}} = A_L f_L + A_R f_R \tag{2.2.37}$$

where by definition here $A_{L(R)} \equiv G\Gamma_{L(R)}G^\dagger$ are similar to the spectral function from the single contact in the previous section [see Eq. (2.2.22)], but not identical as here G is the Green's function of the device and includes the full self-energy $\Sigma = \Sigma_L + \Sigma_R$ [see Eq. (2.2.33)]. It is thus natural to define total spectral function

$$A \equiv G\left[\Gamma_L + \Gamma_R\right] G^\dagger = A_L + A_R\,. \tag{2.2.38}$$

If we are interested in the current through the interfaces and not in details of its spatial variation inside the device, the expression Eq. (2.2.25) from the previous section is still valid, the only difference being the notation for τ is becoming here $\tau_{L(R)}$ for the left(right) interface. It can be shown straightforwardly [33] that the interface inflows and outflows still have literally the same form as Eq. (2.2.28) with the difference that Γ is replaced by $\Gamma_{L(R)}$, if we are talking about the left (right) interface. Thus the net current through the system, which is identical in magnitude to either interface current for the case of two contacts, and which we define as positive when it coincides with the direction of I_L, i.e. $I = I_L = -I_R$ (see Fig. 2.6), is

$$I = \frac{2e}{h}\int \left(\text{Tr}\left[\Gamma_L A\right] f_L - \text{Tr}\left[\Gamma_L G^{\text{n}}\right]\right) \text{d}E = -\frac{2e}{h}\int \left(\text{Tr}\left[\Gamma_R A\right] f_R - \text{Tr}\left[\Gamma_R G^{\text{n}}\right]\right) \text{d}E\,. \tag{2.2.39}$$

With the help of Eq. (2.2.37) and (2.2.38) the above expression for the current can be rewritten in the form

$$I = \frac{2e}{h}\int \overline{T}(E)\left[f_L(E) - f_R(E)\right] \text{d}E\,, \tag{2.2.40}$$

which is identical to the one we discussed for the Landauer formalism at finite temperature [see Eq. (2.1.8)]. Here we have obtained an expression for the *transmission function* $\overline{T}(E)$ in terms of the Green's function of the device and the broadening matrices

$$\overline{T} \equiv \text{Tr}\left[\Gamma_L A_R\right] = \text{Tr}\left[\Gamma_R A_L\right] = \text{Tr}\left[\Gamma_L G \Gamma_R G^\dagger\right] = \text{Tr}\left[\Gamma_R G \Gamma_L G^\dagger\right]\,. \tag{2.2.41}$$

The above expression for the transmission function is a rather general result in the NEGF theory. It can accommodate arbitrary static potentials (as addition to the Hamiltonian) and even account for phase-breaking electron-electron or electron-phonon interactions (incorporated into the self-energies) [33]. In this work phase-breaking processes will be neglected inside the device, which

will be much shorter than the mean free path for inelastic scattering of the conduction electrons in bulk. Nevertheless, mean-field electrostatic interactions will be taken into account. In this case the device Hamiltonian is an explicit function of the electronic density and the non-equilibrium steady-state transport problem needs to be solved self-consistently. A basis-invariant scheme of the algorithm is sketched in Fig. 2.7.

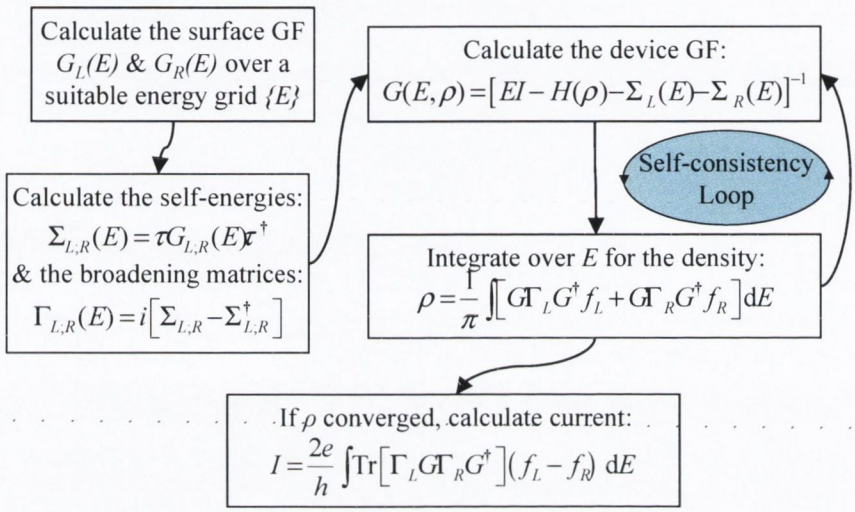

Figure 2.7: Scheme of a self-consistent NEGF algorithm.

The actual integration over the energy is not trivial as the Green's function has poles on the real axis and the integral is in principle unbound. The integration method used in our simulations is discussed in Appendix A. Density mixing methods to accelerate convergence of the iterative self-consistent field (SCF) procedure are discussed in Appendix B. Typically, the non-interacting electron density ρ_0 is used as an initial input.

2.3 Tight-binding implementation of the NEGF method

The built-in real-space partitioning in the NEGF method naturally suits best a localized basis representation of the electronic structure. In this work we adopt an empirical two-spin-band tight-binding (TB) model where the twos pin channels are treated quasi-independently [1] [96]. It is a good starting approximation for describing low-dimensional systems, which typically exhibit high level of localization. The TB model also keeps the computational efforts to a minimum.

Our main objective is the interaction between the spin carried by the conduction electrons and the localized ionic spins under non-equilibrium but steady-state conditions. Before we introduce

[1] They only "feel" each other through the mean-field electrostatic term $U(\rho)$, where $\rho = \rho_\uparrow + \rho_\downarrow$ [see Eq. (2.3.1)].

any concrete spin-polarized atomistic structure, we look at the single band (spin-degenerate) tight-binding implementation of the NEGF method, described in an invariant form in the previous sections.

The systems we study have the typical layout depicted in Fig. 2.8. There is a central (elastic) scattering region "C", which breaks the periodicity of otherwise perfectly homogeneous infinite conductor into two semi-infinite electrodes (leads) – one on the left and one on the right of the centre, marked by "L" and "R". Each semi-infinite lead is coupled smoothly at "infinity" to a reservoir maintained at a constant electrochemical potential $\mu_L \neq \mu_R$ by a battery.

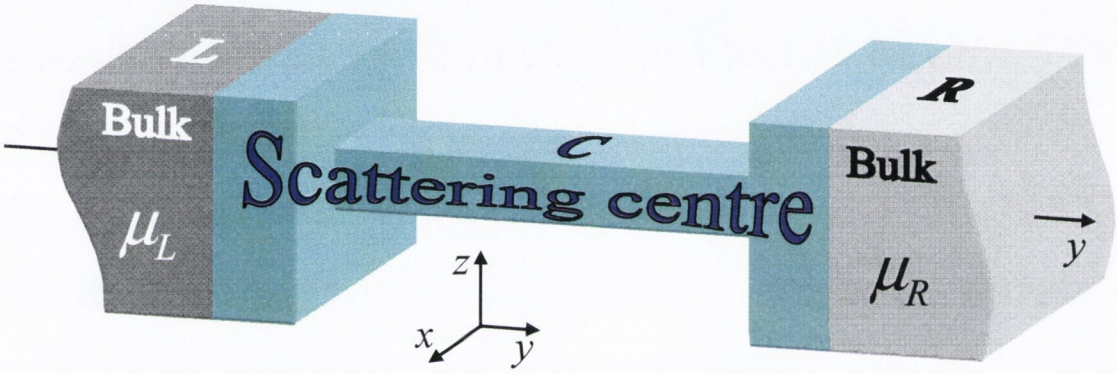

Figure 2.8: Scheme of the mesoscopic device investigated in this thesis.

Though the division of L-C-R is rather arbitrary, typically pieces of the leads thicker than the electron screening length [1] are included in C to ensure smooth transition to bulk at its boundaries. With this partitioning it is assumed that there are no direct L-R terms in the Hamiltonian, L and R are connected only through C and the overlap of orbitals from the two leads is zero. We adopt a nearest-neighbour TB Hamiltonian, which projected onto a mesh of single-level atomic sites in C reads

$$(H_C)^{\sigma}_{ij}(\rho) = [\mathcal{E}^{\sigma}_0 + U(\rho_i - \rho_0)]\,\delta_{ij} + \chi\delta_{i,j\pm1}\,, \tag{2.3.1}$$

where $\sigma = 1, 2$ represents the two collinear spin bands, $\mathcal{E}^{\sigma}_0$ is the density-independent (but possibly spin-dependent) part of the onsite energy, $\rho_i = \sum_\sigma \rho^\sigma$ is the onsite charge density and χ is the hopping integral. Included in H_C is a meanfield potential U, depending on the excess onsite electron density $\Delta\rho_i \equiv \rho_i - \rho_0$, where ρ_0 is the free atom occupancy.

[1] The appropriate thickness of the leads' slabs in the C region can be established numerically for a particular nonequilibrium property of interest – the thickness can be gradually increased until that property (say the net current at a given voltage) does not change any further.

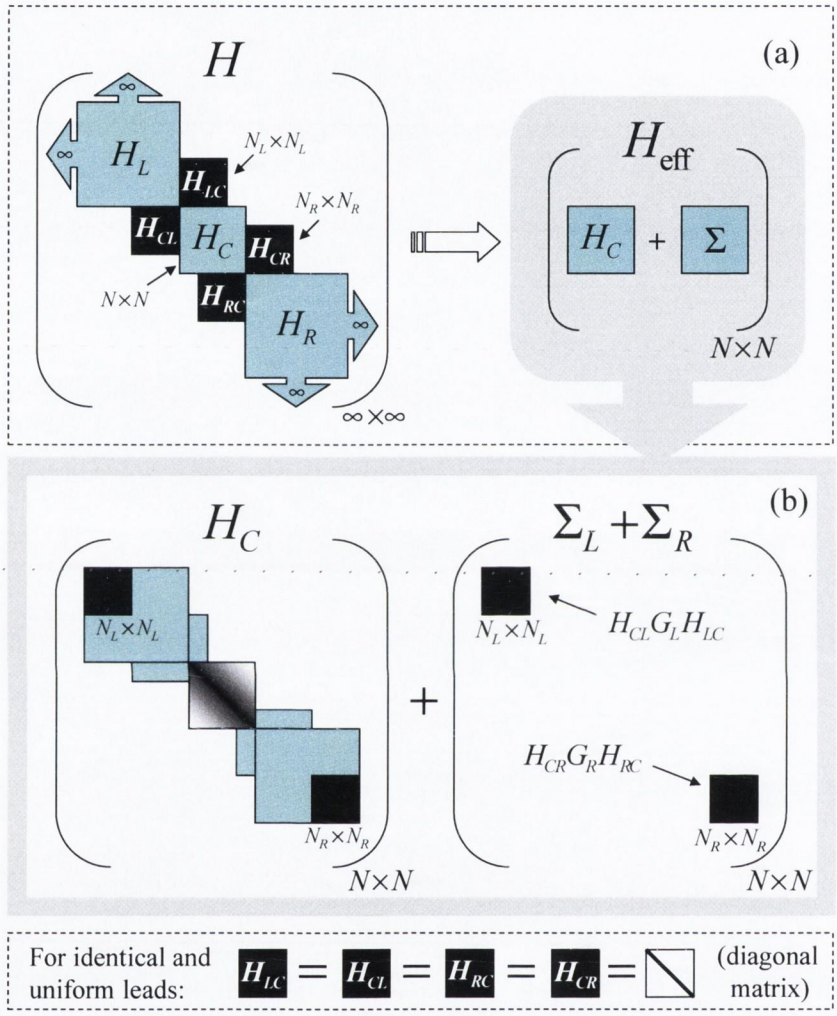

Figure 2.9: Scheme of the projection of the full infinite Hamiltonian matrix H onto an effective one H_{eff}, which is composed of the Hamiltonian of the central scattering region H_C and the self-energy $\Sigma = \Sigma_L + \Sigma_R$, sketched in panel (b). All nonzero elements are located in the shaded areas. The central block of H_C represents the quasi-one-dimensional sample and the outer blocks – the pieces of the leads included in the selfconsistent calculation. The black boxes with dimension $N_L \times N_L$ (or $N_R \times N_R$) in H_C correspond to the interfaces with the bulk leads, while in H they represent the interaction between the lead and the central region. N_L (N_R) is the number of sites in the cross-sectional area of the left (right) lead, while N is the total number of sites in the selfconsistent region.

In view of Eq. (2.2.33) we define an effective Hamiltonian

$$H_{\text{eff}}(E,\rho) \equiv H_C(\rho) + \Sigma_L(E) + \Sigma_R(E) = H_C + H_{CL}G_L(E)H_{LC} + H_{CR}G_R(E)H_{RC}\,, \tag{2.3.2}$$

where $G_L(E) = [EI_L - H_L]^{-1}$ ($G_R(E) = [EI_R - H_R]^{-1}$) is the surface Green's functions of the left (right) lead and $H_CL \equiv H_{LC}^\dagger$ ($H_CR \equiv H_{RC}^\dagger$) is the interaction between the central scattering region and the left (right) lead. Note that, though the Hamiltonians of the semi-infinite leads are infinite matrices, their surface Green's functions have dimension $N_{L(R)} \times N_{L(R)}$, where $N_{L(R)}$ designates the number of sites in the leads cross-section (see Appendix A for the derivation of surface GF of a cubic lattice lead).

The external bias, applied to the L-C-R system, acts as a rigid shift to the onsite energies of the leads

$$H_L \to H_L + V/2, \qquad H_R \to H_R - V/2\,, \tag{2.3.3}$$

where $V \equiv \mu_L - \mu_R$ is the external bias voltage. This is effectively a boundary condition for the C region, brought in by the surface GF's of the leads which enter the self-energies. The GF of the central region, G_C, is then (see Eq. (2.2.33))

$$G_C(E,\rho) = [EI_C - H_{\text{eff}}(E,\rho)]^{-1}\,, \tag{2.3.4}$$

where I_C is the identity matrix and the electron density matrix is given by the recursive expression

$$\rho = \frac{1}{2\pi}\sum_\sigma \int \left[G_C(E,\rho)\Gamma_L(E)G_C^\dagger(E,\rho)f_L(E) + G_C(E,\rho)\Gamma_R(E)G_C^\dagger(E,\rho)f_R(E)\right]^\sigma \mathrm{d}E\,, \tag{2.3.5}$$

which is solved iteratively (see Fig. 2.7) starting with an initial guess for the density $\rho^{(0)}$ and cycling until self-consistency is reached, i.e. on the n-th iteration $\left|\left|\rho^{(n)} - \rho^{(n-1)}\right|\right| < \delta\rho$, where $\delta\rho$ is a preset tolerance for convergence. $\Gamma_X \equiv i\left[\Sigma_X - \Sigma_X^\dagger\right]$ ($X = L, R$) are the broadening matrices [see Eq. (2.2.21)].

Practically, the density matrix from Eq. (2.3.5) is calculated separately in equilibrium ($\mu_L = \mu_R = \mu_0$) and out of equilibrium contribution is added to it [23]. In equilibrium, the system is invariant to time reversal and $G^\dagger = G^*$. In this case the spectral function is simply $A = -\mathrm{Im}[G]$ [see Eq. (2.2.20)] and the density matrix is real and expressed as

$$\{\rho_{\text{eq}}\}^\sigma(\mu_0) = -\frac{1}{2\pi}\mathrm{Im}\int \{G_C(E)\}^\sigma f_0(E-\mu_0)\mathrm{d}E\,. \tag{2.3.6}$$

The non-equilibrium contribution is due to the states in the "bias window" $[\mu_R, \mu_L]$ (we consider the case $\mu_L > \mu_R$). We can take $\rho_{\text{eq}}(\mu_0 = \mu_R)$ and then

$$\{\Delta\rho_L\}^\sigma = \frac{1}{2\pi}\int \left\{G_C\Gamma_L G_C^\dagger\right\}^\sigma [f_L - f_R]\,\mathrm{d}E \tag{2.3.7}$$

is the contribution of the states originating from the left lead. The full non-equilibrium density is finally

$$\rho = \sum_{\sigma} \{\rho_{\text{eq}}(\mu_R)\}^{\sigma} + \{\Delta\rho_L\}^{\sigma} \ . \tag{2.3.8}$$

The integration in Eq. (2.3.6) is not trivial and has to be done in the complex plane as $G_C(E)$ has got poles on the real axis. On the other hand, at finite temperature the Fermi distribution has poles on the imaginary axis through μ_0 (see Fig. 2.10). The so called Matsubara frequencies are located at $z_n = \mu_0 + i(2n+1)\pi k_B T$ and the complex contour is chosen such that it encloses a certain number N_p of these poles.

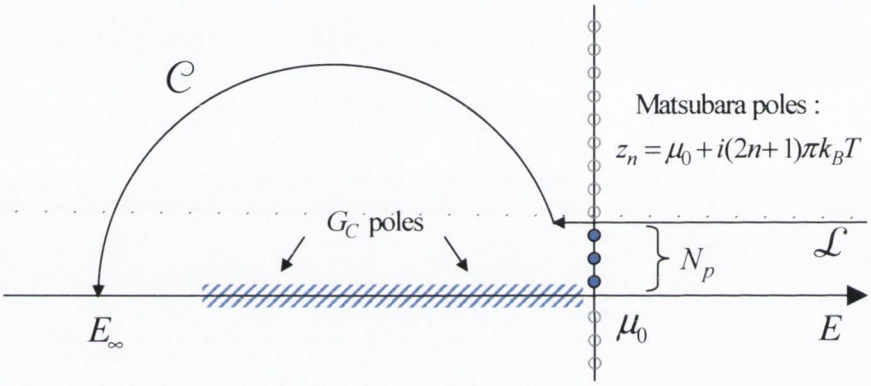

Figure 2.10: fGF7 The complex contour used for integrating the equilibrium density in Eq. (2.3.6).

The Green's function $G_C(E)$ is, however, analytic away from the real axis. A computationally-friendly choice of the contour [23], which keeps away from the real axis, consists of a somewhat incomplete half circle $\mathcal{C}$ connected to a straight segment $\mathcal{L}$, parallel to the real axis. The circle drops to the real axis on the left at an energy E_∞ far bellow the poles of $G_C(E)$ and is closed by a line $[E_\infty + i\eta, \infty + i\eta]$ that is infinitesimally close and parallel to the real axis. The equilibrium density matrix (2.3.6) can be obtained through the residue theorem and the result is

$$\begin{aligned} \{\rho_{\text{eq}}\}^{\sigma} &= -\frac{1}{2\pi}\text{Im}\int_{E_\infty}^{\infty} \{G_C(E)\}^{\sigma} f_0(E-\mu_0) \\ &= \frac{1}{2\pi}\text{Im}\left[\int_{\mathcal{C}+\mathcal{L}} G_C(z) f_0(z-\mu_0) + 2\pi i k_B T \sum_{n=1}^{N_p} G_C(z_n)\right]^{\sigma} , \end{aligned} \tag{2.3.9}$$

where the integral over $\mathcal{C}+\mathcal{L}$ done numerically with a Gaussian quadrature.

Once self-consistency is established the net current through the system is calculated from Eq.

(2.2.40), i.e.

$$I = \frac{e}{h} \sum_{\sigma} \int_{\mu_R}^{\mu_L} \mathrm{Tr} \left[\Gamma_L G \Gamma_R G^{\dagger} \right]^{\sigma} (f_L - f_R) \, \mathrm{d}E \, . \tag{2.3.10}$$

In the following Chapter we shall elaborate further on the NEGF method and use it to study the current-induced torques on a magnetic domain wall, trapped in an atomistic-scale point contact.

Chapter 3

Magnetic point contacts

3.1 Introduction

The intriguing properties of nano-scale magnetic structures arise from the close interplay between their magnetic texture and the spin-coherent electronic transport. Particularly exciting in this respect are the low-dimensional constrictions, consisting of a tiny number of magnetic (transition-metal) atoms, which have now become experimentally achievable [91]. These *magnetic point-contacts* (MPC) show quantized conductance and significant magneto-resistance effects [30, 125], acting as some sort of *quantum spin valves*. This behaviour is determined by the spin-dependent transmission, which is ballistic, due to the truly atomistic dimensions. Nevertheless the elastic spin-scattering, in a similar fashion like the "electron-wind force" due to elastic momentum transfer from the electrons to the scattering centres (impurities) in the mesoscopic electromigration problems [95], gives rise to "spin-transfer torque" (STT) as semi-classically derived by Slonczewski [93] for spin-valve trilayers. The STT effects have been found to introduce macroscopic magnetization dynamics in point-contact-like pillar structures [82, 118] or induced by a nonmagnetic (Cu) tip switching of adjacent magnetic layers in STM-like geometry [29]. Though in these STT experiments the point-contacts in question are still rather "bulky" ($\sim 40\,\mathrm{nm}$), in a genuine atomic-scale point-contact the STT could introduce microscopic spin-rearrangements and in turn manipulate its quantum spin-valve properties.

In this Chapter we investigate the ballistic STT-induced microscopic spin-rearrangements inside a magnetic point contact. Here we adopt a quasi-static approach to analyze the spin-dynamics under steady-state current-carrying conditions. Using the NEGF method, which we described in the previous Chapter, as a self-consistent transport core in our scheme, we map-out and examine the energy landscape for quasi-static thermally-activated transitions between stationary spin

configurations. Our model MPC consists of a monoatomic spin chain, sandwiched between two oppositely polarized magnetic leads, creating an atomically abrupt DW in the constriction (as theoretically justified in Ref. [26]).

In the second part of this Chapter we develop further our model by adding to it parametrically (within the Born-Oppenheimer approximation) the mechanical degrees of freedom of the atoms in the junction. This allows us to investigate microscopically the non-equilibrium (steady-state) magneto-structural interplay in MPCs and the combined effect these degrees of freedom have on the transport. Such information could, in principle, be relevant for understanding the dispersion in the conductance histograms [91, 117] obtained in transport measurements of magnetic break-junctions.

3.2 Spin dynamics in point contacts

It is clear that the modeling of the ballistic atomic-scale ferromagnetic devices requires the combined description of electronic transport and that of the spin dynamics at the atomic level. For this purpose we have developed a general scheme for evaluating spin-polarized currents and associated current-induced torques, which allows us to investigate the magnetization (spin) dynamics and the transport in magnetic point contacts under bias within a common framework. Our problem and our method mimic closely, in philosophy, the electromigration problem (thermally-activated current-driven structural rearrangement), where now the direction of the local spin (or magnetic moment) takes the place of the atomic positions as "the reaction coordinate".

Although our scheme is general and is conceptually transferable to first-principles Hamiltonians (for instance, density functional theory), here we apply the method to a simple self-consistent tight-binding (TB) model. This has the benefit of being reasonably realistic in capturing the atomistic level quantum effects, while keeping the computational overheads to a minimum.

3.2.1 Current-induced generalized forces

Before we describe our approach to the spin dynamics in magnetic point contacts under current-carrying conditions, we need to introduce the current-induced forces, which are not trivial quantities in a non-equilibrium quantum system. Let us start from the Hellman-Feynman theorem (HFT) [39] which gives a very useful expression for computing the mechanical forces acting on the atomic nuclei (or the ionic cores) in molecular or solid state systems. It is based on the Bohn-Oppenheimer approximation (in which the nuclei are treated as classical particles) and it is valid (in its original formulation) only when the electronic subsystem is in one of its eigenstates. If U is the energy

corresponding to a many-body (electrons) eigenstate $|\Psi\rangle$, i.e. $\hat{H}|\Psi\rangle = U|\Psi\rangle$, and λ is a collective variable, which specifies the nuclear positions, then the force in the direction of λ is

$$F_\lambda \equiv -\frac{\partial U}{\partial \lambda} = -\left\langle \Psi \left| \frac{\partial \hat{H}}{\partial \lambda} \right| \Psi \right\rangle / \langle \Psi | \Psi \rangle \,. \tag{3.2.1}$$

The right-hand-side of Eq. (3.2.1) represents the conventional HFT. It is easily proven for square-integrable eigenstates $\langle \Psi | \Psi \rangle = |\Psi|^2$ of the Hermitian Hamiltonian $\hat{H}$ of the system. Then $U = \left\langle \Psi \left| \hat{H} \right| \Psi \right\rangle / |\Psi|^2$ and by definition

$$F_\lambda = -\frac{1}{|\Psi|^2}\frac{\partial}{\partial \lambda}\left\langle \Psi \left| \hat{H} \right| \Psi \right\rangle = -\frac{1}{|\Psi|^2}\left\langle \Psi \left| \frac{\partial \hat{H}}{\partial \lambda} \right| \Psi \right\rangle + \frac{1}{|\Psi|^2}\underbrace{\left(\left\langle \frac{\partial \Psi}{\partial \lambda} \left| \hat{H} \right| \Psi \right\rangle + \left\langle \Psi \left| \hat{H} \right| \frac{\partial \Psi}{\partial \lambda} \right\rangle \right)}_{= U \frac{\partial}{\partial \lambda}\langle \Psi | \Psi \rangle = 0 \text{ in HFT}} , \tag{3.2.2}$$

where the underlined term in the parentheses vanishes under the above conditions and Eq. (3.2.1) is recovered. However, Eq. (3.2.2) is used as a definition of the force in more general situations. It is often called the *generalized* Hellman-Feynman theorem and the underlined term, which may not vanish, is the so called *Pulay force* (originally called by Pulay *wavefunction force*, as it is related to the gradient of the wavefunction) [79]. In fact, the Pulay force can be viewed as a correction to the Hellman-Feynman force when incomplete basis sets are used and the wavefunction is to some extent inaccurate (as always in practical calculations). It has been recognized that the error of the wavefunction enters the energy derivative [right-hand side of Eq. (3.2.1)] at the second order in λ, while it enters the Hellman-Feynman force at the first order and thus it is often numerically more advantageous to work with a medium quality wavefunction and Pulay forces than with a highly-accurate wavefunction and the HF force alone [79].

In the general time-dependent (TD) description of a closed quantum system [1] the force can be defined [123] through the expectation value of the momentum operator by the Ehrenfest theorem

$$F_\lambda \equiv -\frac{i}{|\Psi|^2}\frac{\mathrm{d}}{\mathrm{d}t}\left\langle \Psi \left| \frac{\partial}{\partial \lambda} \right| \Psi \right\rangle = \left\langle \Psi \left| \frac{\partial \hat{H}}{\partial \lambda} \right| \Psi \right\rangle + \text{TD Pulay forces}\,, \tag{3.2.3}$$

where Ψ in this case is the square-integrable time-dependent wave function of the system. In practical implementations where the exact eigenstate Ψ can not be exactly reproduced in an incomplete basis, again Pulay forces should be taken into account. This is not the case for the tight-binding description where the full eigen-space of the TB Hamiltonian is used. In the steady-state Landauer-type transport problem the square-integrability can be provided by a renormalization in

[1] This refers to the number of particles. The Hamiltonian can, in principle, have a parametric dependence on external degrees of freedom like the atomic positions in the BO approximation.

terms of one-electron-energy-centred wave packages [123, 121] and there are no other obstructions for applying the expression for the force in Eq. (3.2.3).

In fact the Landauer steady-state transport [1] has been found closer to the static picture than to the time-dependent one in Ref. [111, 100]. In this regime the charge density in the junction is static and it is the sum of the left and right-lead originating electrons so that their partial occupancies and total energy E are constants of motion, if the structure remains stationery. This invariant total energy E of the current-carrying system excludes the kinetic energy of any atomic motion and the energy dissipation in the reservoirs. Todorov *et al* [111] showed explicitly that infinitesimal changes in E, the total particle numbers N_L and N_R of the left and right-lead originating electrons, and the position $\mathbf{R}_n$ of the n-th atomic core in the structure are related by

$$\mathrm{d}E = T\mathrm{d}S + \mu_L \mathrm{d}N_L + \mu_R \mathrm{d}N_R - \mathbf{F}_n \cdot \mathrm{d}\mathbf{R}_n \,, \tag{3.2.4}$$

where $S = -k_B \sum_{i\in\{\text{“}L\text{”},\text{“}R\text{”}\}} [f_i \ln f_i + (1-f_i)\ln(1-f_i)]$ is the entropy of the junction, T is the ambient temperature. Thus the full force $\mathbf{F}_n$ acting on the n-th atom and which includes both the force at equilibrium and the current-induced contribution is given by

$$\mathbf{F}_n = -(\nabla_n E)_{S,N_L,N_R} \,, \tag{3.2.5}$$

where ∇_n denotes the gradient with respect to the coordinates of the n-th atom while the remaining atoms are still. Though Eq. (3.2.5) looks very much like the HFT [see Eq. (3.2.1)], it is actually more general as it applies to a thermodynamically open system, carrying a steady state current as opposed to the thermodynamically closed system from the HFT. In fact, the same expression for the force can also be derived for a non-steady-state TD transport from a Lagrangian formulation of semi-classical electron-nuclear dynamics in Ref. [108]. There the whole derivation is axiomatic and the force is not introduced as an energy gradient.

In one of the following sections we shall introduce current-induced mechanical forces to our model of spin-polarized junctions. What has been rigorously demonstrated in the literature (cited above) is that a Hellman-Feynman-like theorem does apply for the Landauer-type transport problems, but it should be implemented cautiously in view of the non-negligible Pulay forces in certain situations. Our primary aim in the next section is to model the spin-dynamics in point contacts

[1] Here we also refer to our hypothetic system cartooned in Fig. 2.6, which consists of an atomistic structure sandwiched between two semi-infinite leads. The leads, because of their dimension can play the role of Landauer reservoirs, maintaining stable electrochemical potentials (μ_L and μ_R) irrespective of what they are attached to. Then in an out-of-equilibrium situation, $\mu_L \neq \mu_R$, there are two statistically separable ensembles of electrons in the junction - originating from each of the two leads and populated according to the Fermi function of that lead (f_L, f_R).

under bias. There we take advantage of the analogy between the inert atomic cores and the localized core-spins (in the spirit of the *spin* adiabatic approximation [7, 6]) and apply the generalized to the steady-state transport HFT from Eq. (3.2.3) to calculate the current-induced torques.

3.2.2 Scheme for mapping out spin activation barriers

Our scheme for studying current-induced dynamical effects of the spin (or magnetization) in atomic-sized metallic nanostructures is indeed a generalization of the combined quantum-classical dynamical methods used in electromigration problems [112]. Here we treat the structural magnetic degrees of freedom as classical variables and the conduction electrons as a quantum system. The former are identified with the localized total angular momenta of the atomic cores which we hereafter refer to as *local spins* or simply spins. Note that our spin picture is absolutely transferable to the language of magnetic moments or magnetization as will become clear when we introduce the Hamiltonian. For this reason we sometimes refer to the set of local spins, represented by a set of classical vectors $\mathbf{S} \equiv \{\mathbf{S}_i\}$, as *spin state* [1].

Such classical description of the spins is appropriate when they are localized, i.e. arise from some deep orbital levels, such as in the case of rare earth ferromagnets, but it may appear questionable for magnetic transition metals (Fe, Co and Ni), where the d-electrons responsible for the moment also take part in the conduction [69]. However, since the Coulomb energy is orders of magnitude larger than any energies connected with the electron flow, it is safe to assume that only the direction of the local spin is affected by the current but not its magnitude. This effectively is an adiabatic approximation, in the spirit of the Born-Oppenheimer approximation for the nuclear dynamics, where now the orientation of the local spins is a slow variable compared with the internal electron-electron interactions that determine their magnitude [7, 6]. The Hamiltonian for the combined conduction-electron + local spins system can be then written in general as

$$H(\mathbf{S}) = H_{\mathrm{e}} + V_{\mathrm{spin}}(\mathbf{S}), \tag{3.2.6}$$

where we have isolated the "free" electron Hamiltonian H_{e} from the term $V_{\mathrm{spin}}(\mathbf{S})$, describing all the spin interactions.

We may now write down the generalized forces (in this case, torques) conjugate to the classical variables $\mathbf{S}$:

$$\mathbf{T} = -\left\langle \Psi \left| \frac{\partial H(\mathbf{S})}{\partial \mathbf{S}} \right| \Psi \right\rangle, \tag{3.2.7}$$

[1] We sometimes refer to $\mathbf{S}$ as the *magnetic configuration* of the system, if we envisage the adjoint to the spins local magnetic moments.

where $|\Psi\rangle$ is the normalized state vector of the electronic system. Equation (3.2.7) has the appearance of the usual Hellmann-Feynman theorem for stationary states [see Eq. (3.2.1)] but it is also valid in general dynamical situations, for systems driven arbitrarily far from equilibrium [123, 108]. Note that Pulay forces do not arise in our model as we are always working in the full eigenspace of the Hamiltonian.

The set of equations (3.2.6) and (3.2.7), combined with an appropriate method for calculating the non-equilibrium electron state vector $|\Psi\rangle$, and therefore the current, is the basis for our method for describing the interplay between transport and magnetic properties. In this work, we seek to map out the activation energy barriers for magnetic rearrangements, in order to determine the preferential magnetic configurations of the system and to study transitions between them. We achieve that as follows. First, we seek the stable configurations. We evaluate the non-equilibrium state vector $|\Psi\rangle$, in a one-electron picture, for a given initial local spin configuration $\boldsymbol{\mathcal{S}}^{(0)}$ by solving the scattering problem associated with the Hamiltonian $H\left(\boldsymbol{\mathcal{S}}^{(0)}\right)$. Then, by using Eq. (3.2.7) the torques for that configuration are calculated. Static iterative relaxation of the torques, which involves recalculating the self-consistent current-carrying electronic structure and the torques, is carried out as follows

$$\boldsymbol{\mathcal{S}}^{(\mathrm{n})} = \boldsymbol{\mathcal{S}}^{(\mathrm{n}-1)} + \alpha \mathbf{T}^{(\mathrm{n}-1)}\,, \tag{3.2.8}$$

where $\boldsymbol{\mathcal{S}}^{(\mathrm{n})}$ and $\mathbf{T}^{(\mathrm{n}-1)}$ are respectively the spin configuration and the torques on the n-th iteration. A positive value of α guarantees that the $\mathbf{T} = 0$ solution corresponds to a stable magnetic configuration $\tilde{\boldsymbol{\mathcal{S}}}$.

Once the stable magnetic configurations are found, we can calculate the activation energy barriers for thermally activated transitions between two different configurations $\tilde{\boldsymbol{\mathcal{S}}}_{\mathrm{initial}}$ and $\tilde{\boldsymbol{\mathcal{S}}}_{\mathrm{final}}$. We then choose one of the classical dynamical variables $\mathbf{S}_j$ as the reaction coordinate and rotate it from its initial value $\mathbf{S}_j^{\mathrm{initial}}$ to its final value $\mathbf{S}_j^{\mathrm{final}}$. At every step on the way the torques acting on all other spins are kept relaxed to zero. The work done by the classical degrees of freedom during this quasi-static transition is then obtained by integrating the torque on the reaction coordinate $\mathbf{S}_j$ over the migration path. The work done over the full transition is

$$W = -\frac{1}{|\mathbf{S}_j|} \int_{\tilde{\boldsymbol{\mathcal{S}}}_{\mathrm{initial}}}^{\tilde{\boldsymbol{\mathcal{S}}}_{\mathrm{final}}} \mathbf{T}_j \cdot \mathrm{d}\mathbf{S}_j\,. \tag{3.2.9}$$

The energy barrier profile, on the other hand, is given by

$$W\left(\boldsymbol{\mathcal{S}}_j\right) = -\frac{1}{|\mathbf{S}_j|} \int_{\boldsymbol{\mathcal{S}}_{\mathrm{initial}}}^{\boldsymbol{\mathcal{S}}_j} \mathbf{T}_j \cdot \mathrm{d}\mathbf{S}_j\,, \tag{3.2.10}$$

where $\mathbb{S}_j = \{\mathbf{S}_1(\mathbf{S}_j), \mathbf{S}_2(\mathbf{S}_j), \ldots, \mathbf{S}_j, \ldots, \mathbf{S}_N(\mathbf{S}_j)\}$ is the magnetic configuration, for a given spin $\mathbf{S}_j$ (reaction coordinate), defined by the condition $\mathbf{T}_i = 0$ for every $i \neq j$.

3.2.3 Tight-binding implementation

The techniques described in the previous sections are general and can be applied to a large class of Hamiltonians. In this work we focus our attention on a simplified model, which contains the fundamental ingredients for describing a current-carrying magnetic point contact, but at the same time does not present massive computational overheads. The structure we investigate is schematically represented in Fig. 3.1.

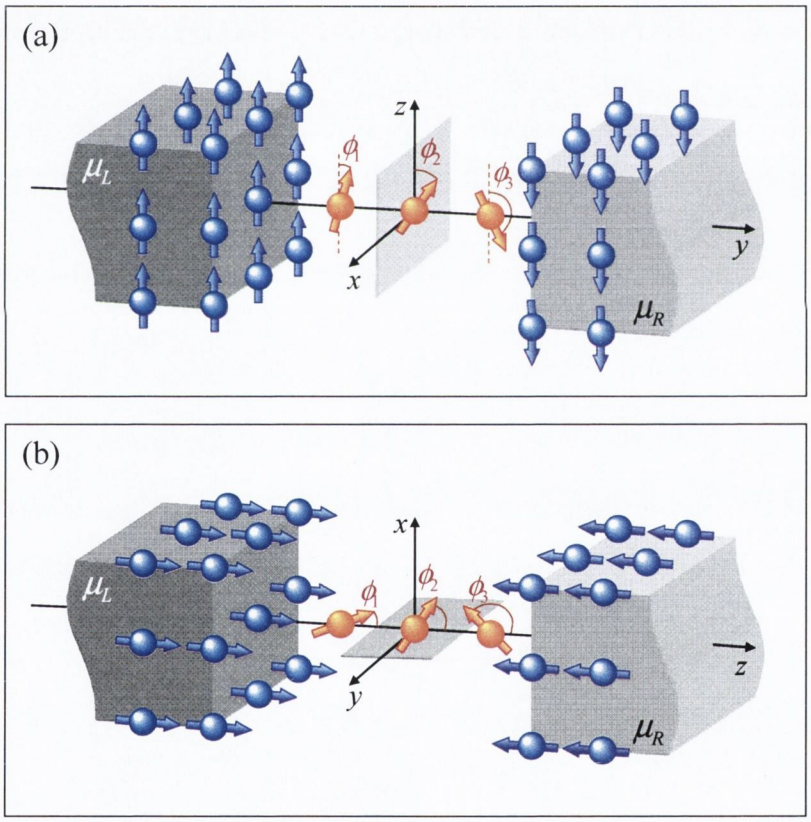

Figure 3.1: Schemes of the MPC with two different choices of the polarization axis z: (a) transverse and (b) parallel to the longitudinal direction. These choices determine whether the DW in the constriction is a Bloch (a) or a Nèel (b) type, which are, nonetheless, equivalent in our model.

It consists of two semi-infinite leads with a simple cubic lattice structure and a 3×3-atom cross section connected through a linear chain of three atoms. Each atom carries a local spin, arising from the deeply localized d-electrons and described with a classical vector $\mathbf{S}_i$. The two

leads are fully but oppositely polarized with all spins in each lead pointing in the same direction and antiparallel to the other lead. In contrast the three spins of the atoms in the chain are allowed to rotate.

The current is carried by electrons belonging to an s-band, which is described by means of a single-orbital (plus spin) TB model. We neglect spin non-collinearity of the current-carrying electrons, assuming that the time needed to cross the constriction is considerably shorter than their spin-relaxation time.

In our collinear-spin model a given magnetic configuration of the chain $\boldsymbol{S}$ is thus described by the vector $\boldsymbol{\phi} \equiv (\phi_1, \phi_2, \phi_3)$ of the three angles ϕ_i $(i = 1, 2, 3)$, which the three spins form with respect to the z-axis. This axis is also the quantization axis for the conduction electrons and in our simulations is chosen to be parallel to the spin-polarization of the left lead. With this choice of the z-axis $\phi_i = 0$ ($\phi_i = \pi$) for a local spin $\mathbf{S}_i$ of the chain aligned parallel (antiparallel) to the spin of the left lead. However, as far as we neglect the magneto-crystalline anisotropy in our model, there is no relation of the z-axis to a particular spatial direction. Hence the two situations presented in Fig. 3.1 (a) and (b) where the z-axis is either transverse or longitudinal to the leads, are equivalent in our spin-collinear model. This means that our model does not distinguish between Bloch and Nèel walls.

For the sake of definiteness, we hereafter refer to the case depicted in Fig. 3.1 (a). The local spins of the chain are restricted to rotations only in the x-z plane and longitudinal components are neglected (as in a Bloch wall).

With the above assumptions the electron Hamiltonian from Eq. (3.2.6) now reads

$$H(\boldsymbol{\phi}) = \sum_{i,j,\sigma} \left[(H_\mathrm{e})_{ij} + (V_\mathrm{eS})^\sigma_{ij}(\boldsymbol{\phi}) \right] c^\dagger_{i\sigma} c_{j\sigma} + V_\mathrm{SS}(\boldsymbol{\phi}) \,, \tag{3.2.11}$$

where $c^\dagger_{i\sigma}$ and $c_{j\sigma}$ are creation and annihilation operators for electrons with spin $\sigma \equiv \sigma_z = \pm 1$ at the atomic sites i and j respectively. The matrix elements of the "free" electron part are those of a nearest-neighbour TB model

$$(H_\mathrm{e})_{ij} = \left[\mathcal{E}_0 + U_0 (\rho_i - \rho_0) \right] \delta_{ij} + \chi \delta_{i,j\pm1} \,, \tag{3.2.12}$$

where $\mathcal{E}_0$ is the on-site energy, χ is the hopping parameter, U_0 is the on-site Coulomb repulsion, ρ_0 is the reference on-site particle number corresponding to the neutral free atom and $\rho_i \equiv \rho_0^\uparrow + \rho_0^\downarrow$ is the full self-consistent number of electrons on the i-th site. The spin interaction potential V_spin from Eq. (3.2.6) is here separated in two parts: V_eS and V_SS. The former contains the interaction between conduction electrons and local spins

$$(V_\mathrm{eS})^\sigma_{ij} = -\frac{J}{2} \boldsymbol{\sigma} \cdot \mathbf{S}_i \delta_{ij} = -\sigma \frac{J}{2} \cos\phi_i \, \delta_{ij} \,, \tag{3.2.13}$$

where $J > 0$ is a ferromagnetic exchange energy parameter and $\boldsymbol{\sigma} = (0, 0, \sigma) = (0, 0, \pm 1)$ is the normalized projection of the electron spin on the quantization axis z. As it stands, Eq. (3.2.13) describes a local Heisenberg-type interaction between the local classical spins and the spin-polarized current carrying s-electrons.

Finally, the term V_{SS} parameterizes the interaction between the classical local spins. Here we assume again a Heisenberg nearest-neighbour spin-spin interaction

$$V_{\mathrm{SS}} = -\frac{J_S}{2} \sum_{i,j} \mathbf{S}_i \cdot \mathbf{S}_j = -\frac{J_S}{2} \sum_{i,j} \cos\left(\phi_i - \phi_j\right), \tag{3.2.14}$$

where $J_S > 0$ is the intersite exchange integral. We are working with the notion of dimensionless and normalized classical spins $|\mathbf{S}_i| = 1$, i.e. their actual magnitude $|\mathbf{S}_i|$ is incorporated in the definitions of J and J_S, which both have a dimension of energy. In summary our model is that of conduction electrons exchange-coupled to local spins, in turn described by a Heisenberg-type energy. This is usually known as the s-d model [133].

The torque experienced by the i-th local spin in the chain is then obtained from equation (3.2.7) and reads

$$T_i = -\frac{J}{2} \sigma_i \sin\phi_i - \frac{J_S}{2} \left[\sin\left(\phi_i - \phi_{i-1}\right) + \sin\left(\phi_{i+1} - \phi_i\right)\right], \tag{3.2.15}$$

where $\sigma_i \equiv \rho_i^{\uparrow} - \rho_i^{\downarrow}$ for $i = 1, 2, 3$ are expectation values the local itinerant-spin densities (polarizations), and we have defined $\phi_0 \equiv 0$, $\phi_4 \equiv \pi$ since the magnetization of the two leads is considered pinned in an antiparallel alignment.

In our simple-cubic lattice model the surface Green's function (at a general complex energy E) of the leads have an analytical form (see Appendix A). In reciprocal space, the surface GF of the left (right) lead reads

$$G_{L;R}(E, \mathbf{q}) = \frac{E - \mathcal{E}_0^{L;R} - \mathcal{E}(\mathbf{q}) - \sqrt{\left(E - \mathcal{E}_0^{L;R} - \mathcal{E}(\mathbf{q})\right)^2 - 4\chi^2}}{2\chi^2}, \quad \mathrm{Im(E)} > 0\,, \tag{3.2.16}$$

where $\mathcal{E}_0^{L;R}$ is the onsite energy in the left (right) lead and

$$\mathcal{E}(\mathbf{q}) = -2\,|\chi| \cos\left(\frac{q_x \pi}{N_x + 1}\right) - 2\,|\chi| \cos\left(\frac{q_z \pi}{N_z + 1}\right) \tag{3.2.17}$$

is the energy shift, as a function of the transverse wavevector (in appropriate units) $\mathbf{q} = (q_x, q_y)$ with $q_x = 1, \ldots, N_x$, $q_z = 1, \ldots, N_z$ for an $(N_x \times N_z)$-atom simple-square lattice monoatomic slab in a nearest-neighbor orthogonal $1s$ TB model and the definition of the complex square-root is given in Ref. [107]. The expression of equation (3.2.16) is then expanded over the real-space basis (see Appendix A) and used in the matrix equation for the self-energies as defined in Section 2.3.

The leads are considered as typical Landauer-type contacts/reservoirs, i.e. their electronic properties are not affected by the coupling to the chain. The bias voltage, applied to the leads, is assumed only to shift rigidly their energy levels. Thus their chemical potentials starting from equilibrium $\mu_L = \mu_R = \mu_0$ with the applied voltage $V > 0$ become $\mu_L = \mu_0 + eV/2$ and $\mu_R = \mu_0 - eV/2$. That is implemented as a rigid shift in the onsite energies of the L (R) part of the Hamiltonian, away from the junction (see Fig. 2.8; in our simulations, typically, we take 2-3 slabs from the leads in the C region)

$$\mathcal{E}_0^L \longrightarrow \mathcal{E}_0^L + eV/2 \quad \text{and} \quad \mathcal{E}_0^R \longrightarrow \mathcal{E}_0^R - eV/2 \tag{3.2.18}$$

and is felt in the selfconsistent region through the lead self-energies

$$\Sigma_L(E) = H_{CL} G_L(E) H_{LC}\,, \qquad \Sigma_R(E) = H_{CR} G_R(E) H_{RC}\,, \tag{3.2.19}$$

where in case of nearest-neighbour TB and uniform in cross section identical left and right lead $H_{LC} = H_{CL} = H_{RC} = H_{CR} = \chi I_L$, where I_L is an $N_L \times N_L$ identity matrix, N_L being the number of atoms in the cross-sectional area of each lead (see Fig. 2.9).

The numerical algorithm we apply for investigating the activation barrier for a quasi-static spin flip in the constriction is sketched in Fig. 3.2. Details on the NEGF core are described in Fig. 2.7 and technicalities on the energy integration and the SCF mixing scheme are described in Appendix A and B, respectively. We are using a Pulay's mixing scheme with $m = 4$ (see Appendix B).

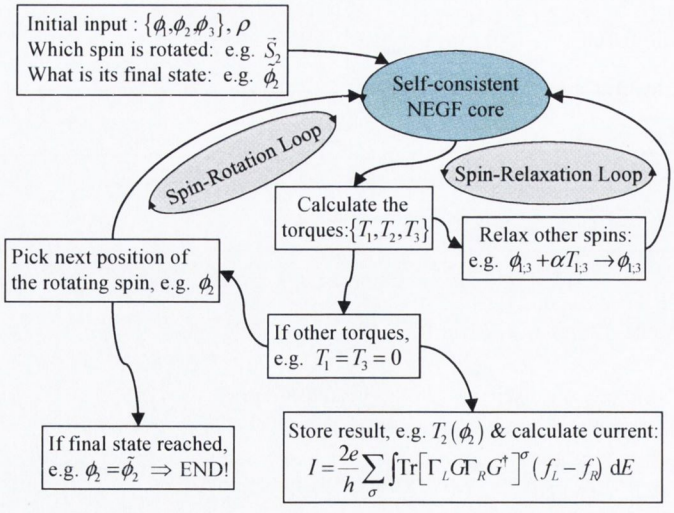

Figure 3.2: Algorithm for simulating quasi-static spin transitions in steady-state current-carrying conditions.

3.2.4 Simulating domain wall migration

Here we investigate the spin-dynamics of the three-atom chain, spanned inside the atomic MPC as depicted in Fig. 3.1(a). For the anti-parallelly aligned leads a Bloch type DW is nucleated in the chain. Having the external spins initially pinned to the polarization of their adjacent leads, we investigate the DW translation achieved by quasi-statically rotating the middle spin.

The TB parameters, used in the calculations, are $\mathcal{E}_0 = -3\,\mathrm{eV}$, $\chi = -1\,\mathrm{eV}$, $\rho_0 = 1$, $U_0 = 12\,\mathrm{eV}$, which provides for a metallic-like local charge neutrality. We consider the values $J = 1\,\mathrm{eV}$ and $J_S = 50\,\mathrm{meV}$ as a realistic choice for simulating bulk properties of magnetic transition metals [85, 47, 72]. As we describe quasi-one dimensional systems, where the exchange integrals can be quite different from bulk [78], we also investigate the whole ranges $0 \leq J \leq 3$ eV and $0 \leq J_S \leq 5$ eV and identify three regions in the $J - J_S$ parameter space where spin-dynamics is qualitatively different.

We also consider departures from other symmetry imposing conditions and parameters. For example, we simulate spatially inhomogeneous chain (sites that are not uni-distant, giving rise to non-uniform hopping parameters) and also partially filled band ($\rho_0 = \rho_0^{\uparrow} + \rho_0^{\downarrow} \neq 1$). Finally, we revisit the problem of whether or not generalized forces away from equilibrium are conservative, and demonstrate numerically that the torques in the present system under a current flow are not conservative.

3.2.4.1 Activation barriers

By performing numerical minimization of all the torques, exerted on the spins in the constriction, with various initial conditions, we have determined that all eight collinear arrangements, such as $(0,0,0)$, $(0,0,\pi)$, $(0,\pi,\pi)$, $(\pi,\pi,0)$, etc, are stable (zero-torque) spin configurations (for the choice of model parameters specified above). Thus we usually start the simulations from one of these states. The states $(0,0,\pi)$ and $(0,\pi,\pi)$, which we designate by $\mathcal{S}_1$ and $\mathcal{S}_2$ respectively, are of particular interest to us as they correspond to two positions of an abrupt DW inside the constriction shifted (with respect to each other) by one atomic site. We investigate the energy activations barrier for a transition $\mathcal{S}_1 \longrightarrow \mathcal{S}_2$, achieved by rotating $\mathbf{S}_2$ from 0 to π in the x-z plane. This process, which we refer throughout this Chapter as *DW migration*, is modelled as a quasi-static process. The rotation of $\mathbf{S}_2$ is discretized and on each step its neighbouring spins $\mathbf{S}_1$ and $\mathbf{S}_3$ are readjusted so that they experience no net torques.

Some of the dynamical characteristics of this process of actual DW migration for unbiased junction as a function of the reaction coordinate ϕ_2 are presented in Fig.3.3. We see that during the rotation of $\mathbf{S}_2$ its adjacent spins $\mathbf{S}_{1,3}$ experience small tilts from the collinear alignment and

after a turning point fall back onto their initial directions [see Fig.3.3(a)]. The intersite exchange coupling is not strong enough to induce spin flips on the sites neighboring the site where the spin is rotated and even hypothetical values of J_S up to 0.4 eV do not affect this picture [see later Fig.3.8]. This observation suggests that (within our parameter space) all complex dynamical processes of the spins in the constriction can be decomposed into series of single-spin rotations. Because of the inherent centrosymmetric properties the spin-polarized contact (these are discussed in the next subsection) the relaxed directions of the two adjacent spins $\mathbf{S}_1$ and $\mathbf{S}_3$ are related

$$\phi_3(\phi_2) = \pi - \phi_1(\pi - \phi_2) \tag{3.2.20}$$

and unless this inherent symmetry is deliberately broken in our discussion we only look at ϕ_1.

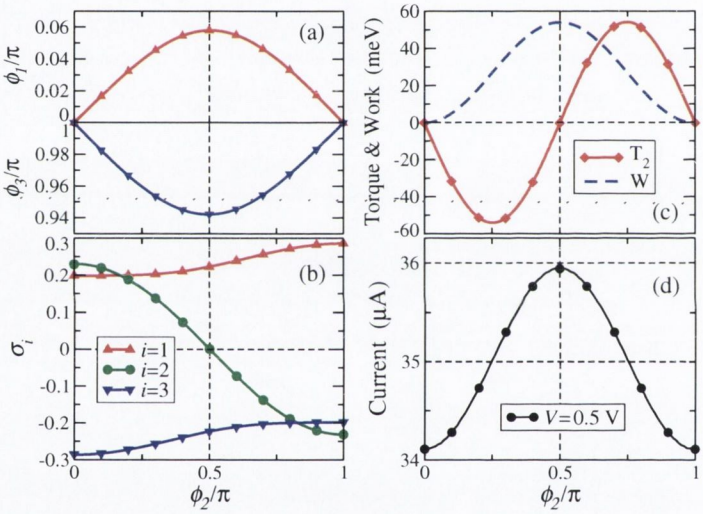

Figure 3.3: Characteristic quantities in a typical calculation on the one-site DW migration in the contact as function of the reaction coordinate ϕ_2: (a) The stable angular variables ϕ_1 and ϕ_3; (b) The three on-site spin polarizations $\sigma_i = \rho_i^{\uparrow} - \rho_i^{\downarrow}$; (c) Torque experienced and work performed by the rotating spin; (d) Net current at $V = 0.5$ V. The voltage in panels (a)-(c) is zero. $J = 1$eV, $J_S = 50$meV.

The only non-zero torque in the system during the quasi-static DW migration process is T_2, the torque acting upon the rotating spin [Fig.3.3 (c)]. This torque is computed as a function of ϕ_2 at every point on the way, then interpolated and integrated according to Eq. (3.2.9) to determine the effective energy barrier for the DW migration

$$W(\phi_2) = -\int_0^{\phi_2} T_2 \, \mathrm{d}\phi_2' \,. \tag{3.2.21}$$

Because of the inherent symmetries of our model system (see next subsection), the two states $(0, 0, \pi)$ and $(0, \pi, \pi)$ are indistinguishable from the transport perspective at any bias. Thus the

calculated energy barrier between them is symmetric about $\phi_2 = \pi/2$ and the total work $W(\pi)$ for the quasi-static process is zero [Fig. 3.3 (c)]. The activation energy for this process in our TB parameterization is 54 meV.

The conductance depends on the alignment of the spins and varies during the DW migration process. At a finite bias voltage V the net current I shows a symmetric bell-shaped dependence on ϕ_2 [see Fig.3.3(d)]. This resulting curve is very similar in shape to the conductance of a three-terminal non-collinearly spin-polarized device, described in Ref. [25] from a semi-classical perspective in the framework of the so-called magneto-circuitry theory [24]. In our case for $V = 0.5\,\mathrm{V}$, the conductance varies from $1.76e^2/h$ at the collinear states $\phi_2 = 0, \pi$ to a maximum of $1.86e^2/h$, reached at $\phi_2 = \pi/2$. That gives a relative variation of 5%, which is also in the order of magnitude of the result in Ref. [25]. This interesting similarity suggests a "topological" proximity between our model system and multi-nodal magnetic systems modelled by the "macrospin" [1] approximation, i.e. each of the localized (atomic) spins in our model can instead represent the spin of one component (described as a macrospin) in the multi-terminal device (circuit).

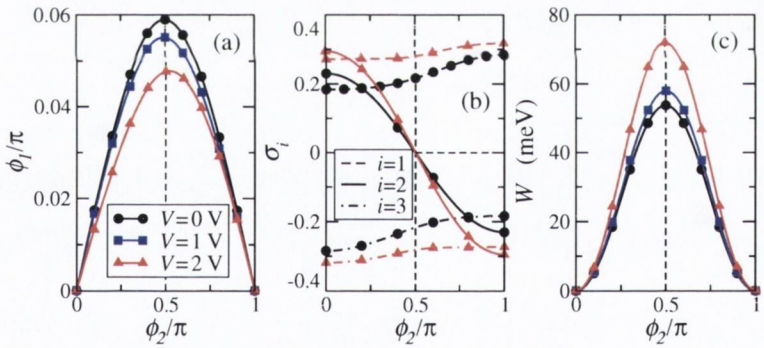

Figure 3.4: Effect of the external bias on some microscopic properties of the contact as function of the reaction coordinate ϕ_2: (a) the zero-torque positions of ϕ_1 (ϕ_3 can be deduced from Eq. (3.2.20)); (b) the on-site spin polarizations $\sigma_i = \rho_i^{\uparrow} - \rho_i^{\downarrow}$, $i = 1, 2, 3$; (c) the activation energy barrier.

Further, we look at the effect the external bias voltage V (driving a spin-polarized current) has on the microscopic dynamic observables as a function of the reaction coordinate. We observe a current-induced suppression of the response of $\mathbf{S}_{1,3}$ to the rotation of $\mathbf{S}_2$ [Fig.3.4(a)] and an increase in the absolute values of the onsite spin-polarizations (non-equilibrium spin-density accumulation)

[1] The *macrospin model* is based on the fact that in most of its volume the magnetic moments in a magnetic domain [50] are aligned in parallel to each other because of the exchange interaction. With this approximation the magnetization in complex heterogenous magnetic system is often mapped onto series of macrospins, representing the individual mono-domains.

[Fig.3.3(b)]. As a result of the increased misalignments and onsite polarizations, the energy barrier height also increases with V [Fig.3.4(c)] and the pace is non-linear at high biases. Increase of barrier height corresponds to enhanced spatial pinning of the wall. At any finite temperature, this phenomenon would manifest itself as suppression, with increasing bias, of the frequency of DW transitions back and forth between the two stable magnetic configurations.

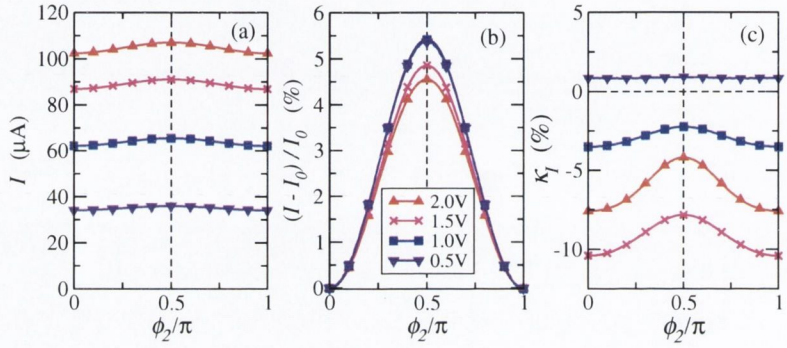

Figure 3.5: (a) The net current I, (b) its relative variation with respect to $I_0 \equiv I(\phi_2 = 0)$ and (c) its polarization $\kappa_I \equiv (I_\uparrow - I_\downarrow)/(I_\uparrow + I_\downarrow)$ as functions of ϕ_2 at different voltages V.

The profile of the net current over the reaction coordinate is similarly bell-shaped as the energy barrier. However, unlike the barrier, the relative height of the current bell drops with the bias [see Fig.3.5(b)]. This correlates with the suppressed response of the two adjacent spins [Fig. 3.4(a)]. A common tendency we find in our calculations is that the smoother the angular spin distribution in the junction the higher the conductance, hence the bell shape and the peak of the current at $\phi_2 = \pi/2$. The net current also becomes more spin-polarized [Fig.3.5(c)], though that tendency is not monotonous with the bias (clearly, in the limit of zero-bias the Fermi level spin-polarization is 0 for $\rho_0 = 1$, at finite bias κ_I is an integral quantity, that depends on the band-alignments of the two leads).

3.2.4.2 Inherent symmetries

This subsection is dedicated to the geometrical and electronic symmetries inherent to our model system (see Fig. 3.1). Starting with geometry, we introduce a rotation operation by an angle π about one of the coordinate axes, say x, as $\mathcal{R}_x$. There are three such rotations that map the system onto itself, i.e. $\mathcal{R}_x$, $\mathcal{R}_y$, $\mathcal{R}_z$ as sketched in Fig. 3.6(a), and the resulting configurations are all equivalent to the initial one.

Note that the direction of the external bias changes after two of these operations ($\mathcal{R}_x$ and $\mathcal{R}_z$). For example, from $\mathcal{R}_x$ we obtain the following identity relation between two spin-states in the

constriction

$$\{V;\, 00\pi\} \equiv \{-V;\, 0\pi\pi\}\ . \tag{3.2.22}$$

In this case the leads map perfectly on to each other and the only difference is the change of the voltage direction. Eq. (3.2.22) is valid for purely geometrical reasons and irrespective of the electronic structure, as long as the leads are identical and oppositely polarized. In particular, this means that at equilibrium the (00π) and $(0\pi\pi)$ states are identical from transport viewpoint for any choice of electronic-structure model.

As far as the electronic structure is concerned, the half-filled band ($\rho_0 = 1$) of our simple cubic lattice in the orthogonal TB model brings in additional symmetry. That is the perfect match of the electron and hole subbands in the leads upon spin inversion [see Fig. 3.6(b)]. Because of the two oppositely polarized leads (which set identical boundary conditions for electrons and holes) and the identity of the electron and hole descriptions of the transport problem [8], we recognize a set of relations between spin states, cartooned in Fig. 3.6(c). At half band-filling we have that instead of Eq. (3.2.22) a more extended one holds

$$\{V;\, 00\pi\}_{\rho_0=1} \equiv \{-V;\, 0\pi\pi\}_{\rho_0=1} \equiv \{V;\, 0\pi\pi\}_{\rho_0=1} \equiv \{-V;\, 00\pi\}_{\rho_0=1}\ . \tag{3.2.23}$$

This inherent symmetry of our spin system is the reason for which the energy barrier for transitions between these two spin states is symmetric at any finite bias [see Fig. 3.4(c)]. The above argument can be generalized to longer spin-chains in the constriction [Fig. 3.6(c)].

Similar relations can be written for other couples of collinear states of the three spins in the chain. There are in total $2^3 = 8$ such states, which can be divided in four pairs

$$(00\pi) \longleftrightarrow (0\pi\pi), \quad (000) \longleftrightarrow (\pi\pi\pi), \quad (\pi 0\pi) \longleftrightarrow (0\pi 0), \quad (\pi\pi 0) \longleftrightarrow (\pi 00) \tag{3.2.24}$$

of equivalent (with respect to transport observables) states at any bias, obeying Eq. (3.2.23). These stronger relations are due to the electronic structure symmetry, induced by the simple cubic lattice and the (effectively) half-filled band (we actually have two nearly half-filled spin-split bands). We acknowledge their existence and in Section 3.2.6 we investigate how the results become different if the above symmetries are broken.

3.2.4.3 Spin-state stability and DW migration under bias

The torques, defined in Eq. (3.2.15), depend explicitly on the exchange parameters J, J_S and the balance of these two coupling mechanisms is what determines the spin dynamics in the constriction. In this section we describe the effect of the intersite exchange coupling strength on the equilibrium (zero-bias) magnetic properties of the $(0, 0, \pi) \rightarrow (0, \pi, \pi)$ transition.

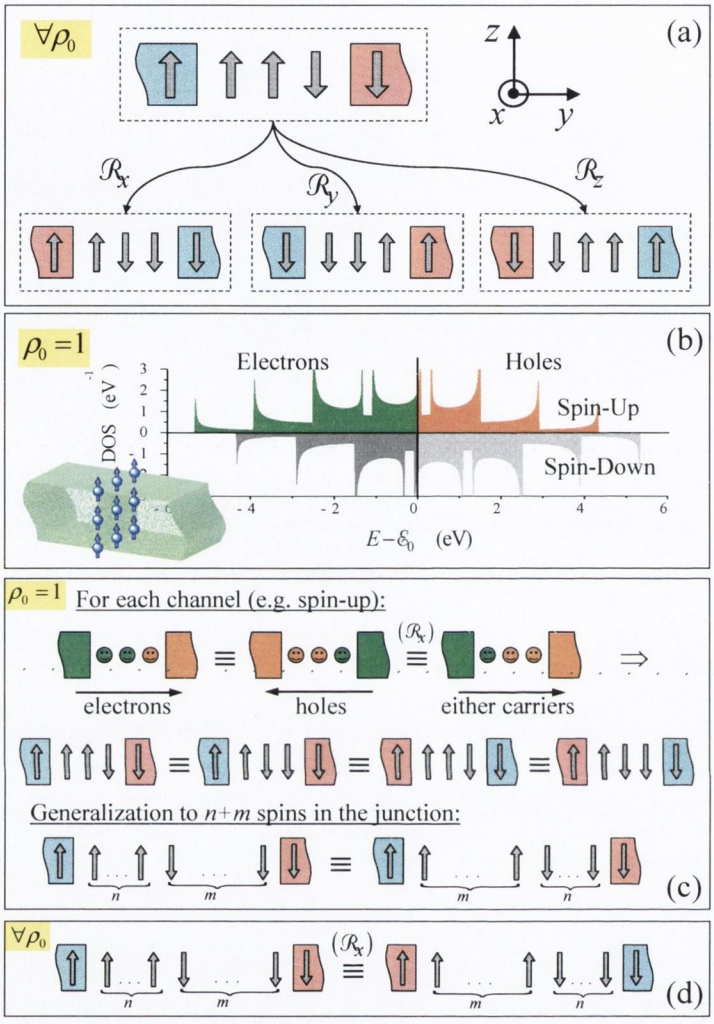

Figure 3.6: (a) Equivalent configurations produced by rotations to π about the coordinate axes, originating in chain site #2. The leads are sketched in different colour to indicate the bias applied to the system (blue for lead attached to the negative pole of the battery, red – for the positive). (b) Density of states of an infinite uniformly magnetized lead with 3×3 atoms in cross section. Tight-binding parameters are the ones already specified, i.e. $\chi = J = -1\,\mathrm{eV}$. The Fermi level corresponding to half-filled band ($\rho_0 = 1$) is marked and the spin-up electron (hole) subband DOS is highlighted in green (orange). For this particular ρ_0, if the magnetization of the lead is reversed, the DOS of electrons and holes interchange. (c) A cartoon demonstrating the validity of Eq. (3.2.23) for $\rho_0 = 1$. The shades of the leads match those of the subbands for the majority electrons or holes depicted in panel (b), while the shades of the sites correspond to that of the lead their spin is parallel to. The identity signs refer to the transport properties. The first identity is because of the duality of the electron and hole description of the one-band transport problem, while the second is obtained by a rotation. Based on this Eq. (3.2.23) can be generalized to $n+m$ local spins in the point contact. Panel (d) represents a generalization of Eq. (3.2.22).

As J_S is increased the adjacent spins $\mathbf{S}_1$ and $\mathbf{S}_3$ understandably tend to respond stronger to the rotation of $\mathbf{S}_2$. Starting at $(0, 0, \pi)$, ϕ_1 initially increases [1] rather linearly with ϕ_2 and $\mathbf{S}_1$ tilts away from the z-axis [Fig. 3.7(a)]. This suggests that for small misalignments the J_S (linear in ϕ_1) is the leading term in Eq. (3.2.15) as the J-term, depending on the self-consistent onsite spin-density $\mathbf{s}_1$, is potentially higher order in ϕ_1. Indeed, during the early stages of the $\mathbf{S}_2$-rotation, s_1 is nearly constant before the turning point [Fig. 3.7(c)]. As ϕ_2 increases further, a turning point is reached and $\mathbf{S}_1$ falls back on to the axis. From the turning point on the spin-density drifts continuously towards its final stable value at $(0, \pi, \pi)$ (the spin-densities for the end collinear states clearly do not depend on J_S).

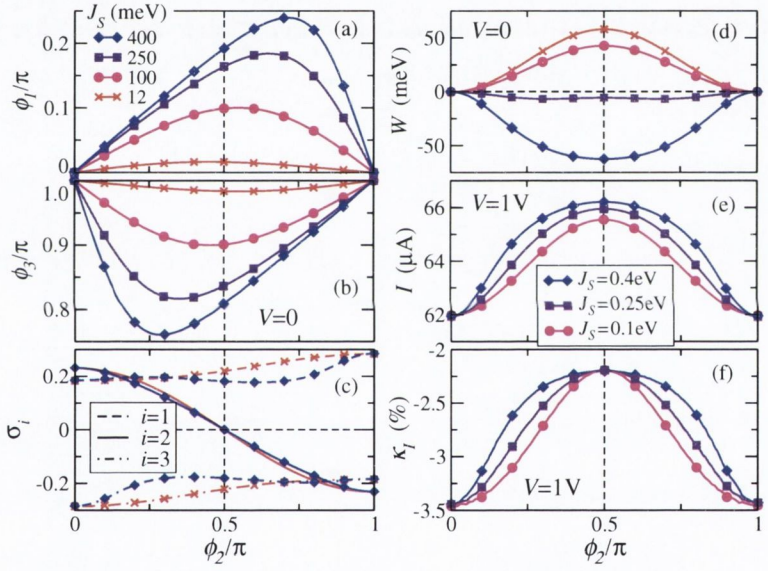

Figure 3.7: Effect of the strength of the intersite coupling J_S on the equilibrium variables (a,b,c,d) and on the net current and its polarization at $V = 1\,\mathrm{V}$ (e,f).

The typical bell-shape of the current vs. ϕ_2 is broadened as J_S increases [Fig.3.7(d)] due to the fact that stronger intersite exchange coupling tends to make the three spins in the constriction more continuously distributed in angle, which in turn increases the overall conductivity of the system for any ϕ_2. Also the current is somewhat less spin-polarized in the case of stronger J_S [Fig.3.7(e)].

Together with this rather minor effect on the macroscopic observables (e.g. the current) there is an interesting microscopic implication of the variation of J_S for the spin-dynamics. That is the fact that the energy barrier for the migration of the abrupt DW in the junction changes its profile

[1] From Eq. (3.2.20) it is sufficient to follow the response of $\mathbf{S}_1$.

qualitatively or fully disappears. With increasing J_S, this transforms from a barrier to a well [see Fig.3.7(c)] thus making the collinear states unstable and the more symmetric and homogeneous one with $\phi_2 = \pi/2$ stable.

By studying the activation energy for DW migration, we deduce a pattern of local-spin stability in the exchange-parameter space J-J_S (see Fig.3.8). Three distinct regimes are recognized depending on the values of the exchange parameters: (1) *"magnetostatic regime"* associated with the presence of 2 stable magnetic states, for which $\phi_2 = \pm\pi/2$; (2) *"mixed regime"*: 4 stable configurations, 2 in each half-plane for which $0 < \phi_2 < \pi/2$ and $\pi/2 < \phi_2 < \pi$; (3) *'current-driven regime"*: 8 stable configurations, namely all the collinear spin alignments $(0,0,0)$, (π,π,π), $(0,0,\pi)$, $(0,\pi,\pi)$, $(\pi,0,0)$, $(\pi,\pi,0)$, $(0,\pi,0)$, $(\pi,0,\pi)$ [1]. Interestingly, the three regions of stability in the J-J_S space are separated by parabolic borders. This correlates to the Feynman-path notion that the indirect intersite exchange coupling is in its leading contribution a second-order process with respect to the onsite exchange and the J^2 factor in the expression for the RKKY interaction (see for instance Ref. [67]).

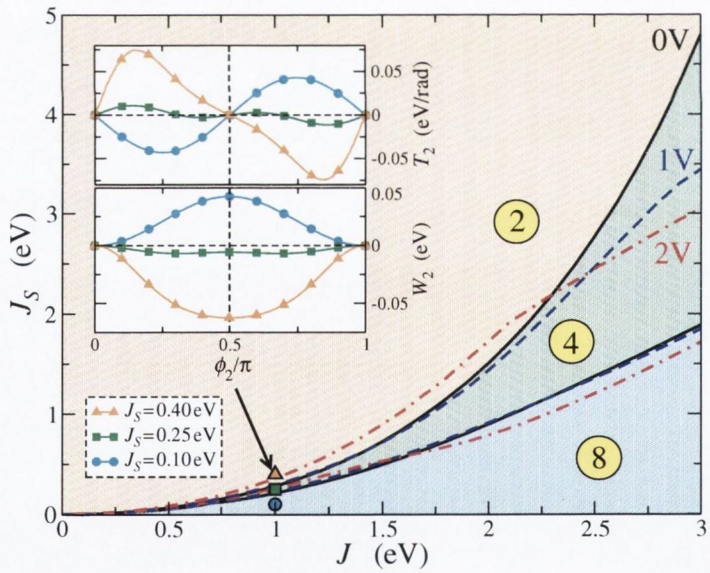

Figure 3.8: Diagram showing the three regions, with 2, 4 and 8 stable magnetic configurations respectively (see text), in a J-J_S cut of the parameter space. The border lines between the three regimes are calculated from the energetics of the $(0,0,\pi) \rightarrow (0,\pi,\pi)$ transition (see inset and text). The blue dashed lines correspond to voltages of 1 and the red dash-dotted ones – to 2 V.

The exchange-parameter values that we previously considered as realistic ($J = 1\,\text{eV}$ and $J_S = 50\,\text{meV}$) are well within the *current-driven* region (marked with "8" in Fig.3.8). Obviously, the

[1] The last case is also confirmed by full torque relaxations at various initial conditions.

correct values of these parameters in reduced dimensions are very system-dependent. Experimental results for J_S, for instance, in quasi-1D Fe magnetic strips show a significant reduction by almost an order of magnitude compared to bulk values [78]. This goes further in favour of the collinear stability or the presence of a barrier for the DW migration (see Fig.3.8). We continue using the foregoing values, noting that the DW energetics qualitatively remain the same for a range of values of J_S in the region of tens of meV and $J \gtrsim 0.5\,\text{eV}$.

The application of a bias, driving spin-polarized current, distorts the border lines between the three regions in Fig. 3.8 significantly. The border lines for different biases even cross each other. As moving up in Fig. 3.8 corresponds to lowering of the barrier, this means that the increase of the current flow (with increasing bias) can either increase or decrease the barrier. Indeed, in Fig.3.9 we demonstrate the effect of the bias on the DW migration energetics along two verticals of the $J - J_S$ parameter space separated by a crossing of the border lines, i.e. $J = 1$ eV and $J = 2.5$ eV. Three values of J_S are considered, one in each of the above regimes. As expected in one case the increase of bias increases the barrier (effectively pinning the wall), while in the other the bias suppresses the barrier (effectively depinning the wall). Our calculations show that the spin-transfer torque effect within our transport model can either increase of decrease the barrier for a DW migration, depending on the balance of exchange parameters which in practice are very system-dependent characteristics.

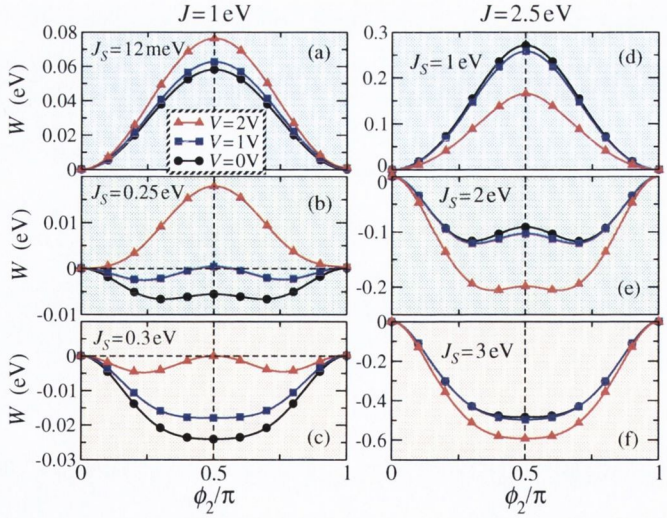

Figure 3.9: The biased energy barriers for the transition $(0, 0, \pi) \rightarrow (0, \pi, \pi)$ at different voltages $V = 0, 1, 2\,\text{V}$, $J = 1.0\,\text{eV}$ (left) and $J = 2.5\,\text{eV}$ (right) and for three values of J_S (one in each of the ranges, discussed in the text): (a) $J_S = 12\,\text{meV}$; (b) $J_S = 0.25\,\text{eV}$; (c) $J_S = 0.3\,\text{eV}$; (d) $J_S = 1\,\text{eV}$; (e) $J_S = 2\,\text{eV}$; (f) $J_S = 3\,\text{eV}$.

3.2.4.4 Current-voltage characteristics

The current-voltage characteristics of the system for all the different stable (collinear) alignments of the spins in the chain are presented in Fig. 3.10. All the I-V curves are symmetric about the origin and form four separate branches as the eight possible stable magnetic states are 4×2 degenerate. This is due, as mentioned earlier, to the spatial reflection and time-reversal symmetry of the atomic point contact.

The slopes of the $I - V$ curves (differential conductances) at low bias are not directly proportional to the number of abrupt DWs in the junction (including the leads interfaces), e.g. three DWs for $(0, \pi, 0)$ and $(\pi, 0, 0)$, one for $(0, 0, 0)$ and $(0, 0, \pi)$ states. Clearly, the interfacial DWs have a different contribution to the overall conductance. For instance $dI/dV(0, 0, \pi) > dI/dV(0, 0, 0)$ at biases below 1 V. Interestingly, the $(0, 0, \pi)$ and the $(\pi, 0, 0)$ states have the same low-bias slopes, regardless of the fact that the latter has two more interfacial walls (it could be that opposite interfacial walls cancel their contribution as a result of the quantum interferences). The least steep curve indeed corresponds to the $(0, \pi, 0)$ state, having highest number of two walls in the chain and just one at the interface. What is more important, however, is that there is a very significant dependence of the current on the magnetic state of the constriction, i.e. a magneto-resistance effect. The microscopic single-spin reversals, which distinguish the four I-V curves in Fig. (3.10), can result in massive current variations (of up to 50%) at a given bias. At a given finite temperature this could result in a random telegraph noise in conductance measurements and such effects have been observed experimentally [118, 125].

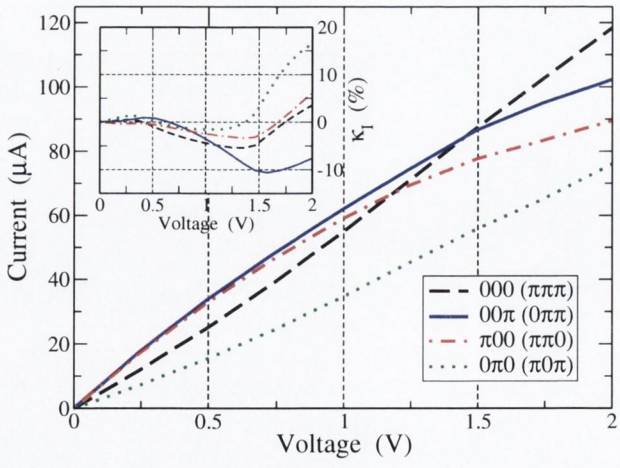

Figure 3.10: The current-voltage characteristics at all stable collinear alignments for the local spins in the chain. The inset represents the correspondent spin-polarization of the net current $\kappa_I \equiv (I_\uparrow - I_\downarrow)/(I_\uparrow + I_\downarrow)$. It is a non-monotonic function of the bias.

3.2.4.5 Summary on DW migration

In summary, we have proposed a microscopic quantum-classical scheme for computing the current-induced torques on the local magnetization in MPCs under bias. This scheme, based on the adiabatic spin approximation [7, 6] and the $s-d$ model, has been applied to study the STT effect in an atomistic MPC, which consists of a monoatomic chain of three atoms, bridging over two semi-infinite leads with opposite magnetizations, so that at least one magnetic DW is formed within the junction. We have investigated the stability under current-carrying conditions of various magnetic configurations and the effect the flowing spin-polarized current has on the energy-barrier for the migration of the abrupt DW. For an extensive range of echange parameters about the realistic bulk values only the collinear spin-states are stable. These, however, carry different (by up to 50 %) net currents and the average activation barrier for transitions is about 65–70 meV. This in turn could be a source of a random telegraph noise in current with significant amplitude as a result of the thermally-activated spin rearrangements inside the constriction. Regarding the DW migration, we have found that the increase of the bias can both enhance and suppress the barrier (effectively pinning or de-pinning the wall) depending on the balance of the $s-d$ and $d-d$ exchange parameters.

3.2.5 Cyclic processes and conservativeness

3.2.5.1 A special cyclic example

Figure 3.11 represents the work for series of one-spin rotations. The sequence of transitions is chosen such that it goes through each of the 8 stable magnetic configurations once, and then returns to the initial state. In equilibrium (zero-bias) the depths of the wells in this graph correspond to the relative energies of our system in various stable magnetic states with respect to the initial one. Based on this, we can recognize rather unexpectedly the "anti-ferromagnetic" $(0,\pi,0)$ and $(\pi,0,\pi)$ alignments, which can be thought of as featuring three abrupt DWs [1] and are the least conducting states [see Fig. (3.10)], as the most stable among the collinear alignments at equilibrium. [2]

The external bias has a non-trivial effect on the effective energy barriers for these single-spin transitions. The total work for the closed loop (starting and ending at the same state) cancels out for any bias. This, however, is not an indication of conservativeness of the current-induced torques (3.2.7), but is rather an artefact of the specific properties of this particular closed path, which includes all the states and can be decomposed into two sub-loops going through identical

[1] Here domain wall (DW) is used in a very wide sense, allowing for notions like single-atom domain.

[2] This effect is a direct manifestation of the quantum nature of the transport involved. It resembles the effect of indirect (electron-mediated) RKKY exchange interaction (see for instance Ref. [8]) and in this case is further complicated by the geometry of the system which moulds the quantum interference pattern.

(by symmetry, see section 3.2.4.2) states in opposite direction and thus their contributions to the total work cancel out.

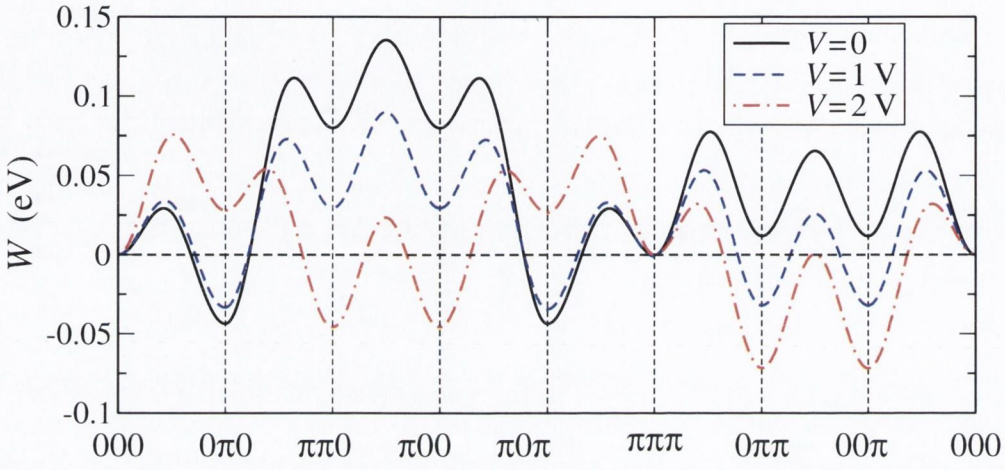

Figure 3.11: Work for consecutive transitions between the 8 stable magnetic configurations at different bias $V = 0, 1, 2\,\mathrm{V}$.

There are in total $12 = (5 \times 2 + 2)$ transitions between non-identical pairs of stable collinear alignments based on single-spin rotation, out of which $5+2 = 7$ are indeed different transitions from the point of view of the electron transport. The average activation barrier for these 7 transitions at equilibrium is 71 meV with a variance of 36 meV and it depends slightly on the bias: 65.6 meV at 1 V and 68 meV at 2 V. These values for the activation barriers suggest switching frequencies, and hence random telegraph noise in the current, in the microwave range at room temperature.

3.2.5.2 Are spin torques conservative?

The question if, and under what conditions, forces under steady-state current are conservative remains an open fundamental problem in the theory of transport [122]. A thermodynamic formulation of forces under non-equilibrium steady-state conditions, proposed in reference [111], leads to the explicit identification of a thermodynamic potential for electromigration [100]. However, as a consequence of the infinite nature of open-boundary systems, this potential involves a conditionally convergent real-space summation. If the sequence of terms in this summation remains invariant along a given path in the configuration space of the system, then along that path, current-induced generalized forces are rigorously expressible as gradients of a scalar potential and are therefore conservative. The possibility remains open, however, that the order of terms in the conditionally convergent sum may change, as specific points, or manifolds, in configuration space are traversed

[100]. This constitutes an effective breakdown of the Born-Oppenheimer approximation, with the consequence that paths spanning such points are non-conservative [100].

We now carry out a numerical test to see whether or not the generalized forces (torques) in Eq. (3.2.15) are conservative in the present current-carrying system. We chose suitable closed processes composed of single-spin rotations and calculate the total work as a sum of the works on the sub-processes, each calculated analogously to Eq. (3.2.21). Since the intersite exchange field is conservative, a non-zero total work for the cycle is suggestive of the non-conservativeness of the current-induced torques. As a sign of consistency with the former observation, we expect the total work to be a numerical zero at zero bias.

The work for a set of four consecutive one-spin rotations between collinear spin configurations, which form a closed-loop, is calculated at different voltages. The full work for three different loops as a function of the applied voltage is presented in Fig. 3.12. As expected the closed-loop work is zero at equilibrium. However it shows a significant variation with the bias for all three cyclic processes.

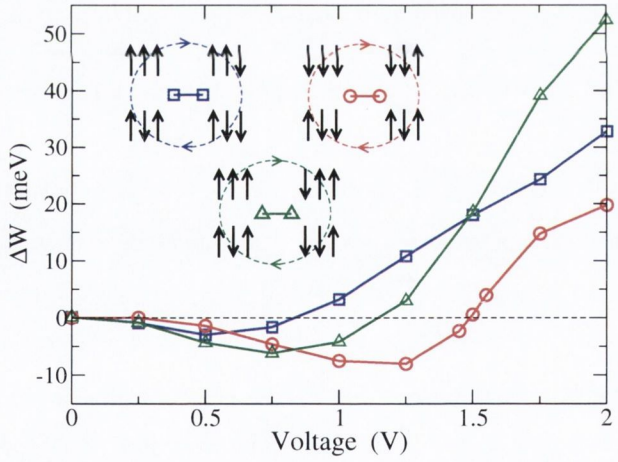

Figure 3.12: Dependence of closed-loop work on the voltage for four different closed loops of one-spin rotations between collinear states, which are shown on the insets.

In order to resolve the numerical error we have performed a series of tests with different levels of accuracy. We recognise a few sources of numerical error: (1) The level of convergence of the density matrix $\delta\rho$. (2) The fineness of the energy mesh for the contour integration in the complex plane δE. (3) The level of torque relaxation δT. (4) The angular mesh for the torque integration which results into the work. As the torque in the current-driven regime is a very smooth function of the reaction coordinate [see Fig.3.3(c)], we have found (4) insignificant for the value of the integral

in Eq. (3.2.10). The effect of the rest of the accuracy parameters on the full-loop work for the loop $\{\pi\pi\pi - \pi\pi 0 - 0\pi 0 - 0\pi\pi - \pi\pi\pi\}$ [see Fig. 3.12] is summarized in Table 3.1. There we have presented the resulting closed-loop work for reduced accuracy levels with respect to the calculation shown in Fig. 3.12.

$(\delta\rho,\delta E,\delta T)$, %	$W_{0\,\mathrm{V}}$	$W_{0.5\,\mathrm{V}}$	$W_{1\,\mathrm{V}}$	$W_{1.5\,\mathrm{V}}$	$W_{2\,\mathrm{V}}$
(100,100,100)	0.0001	-1.407	-7.454	0.601	19.81
(100,20,100)	0.0001	-1.290	-7.361	-0.036	19.79
(1,100,2)	0.0406	-1.300	-7.356	0.662	19.88

Table 3.1: The work (in meV) for the loop $\{\pi\pi\pi - \pi\pi 0 - 0\pi 0 - 0\pi\pi - \pi\pi\pi\}$ as function of the accuracy parameters (in relative units). The value of the bias V is given as subscript. Here the values of the three tolerance parameters are relative to our most accurate calculation (top line), presented in Fig. 3.12.

The results in Table 3.1 demonstrate that the observation of a nonzero work for a closed-loop sequence of transitions is not an error-accumulation effect as it is not substantially affected by variations of 1–2 orders of magnitude about the chosen level of accuracy. Thus we see that in the present case, along all the three selected closed paths, we have an explicit example of non-conservative generalized non-equilibrium forces, emerging here as spin torques. In other words, the result shown above provides a numerical evidence that the current-induced torques are non-conservative, at least in the section of the configuration space spanned by the present calculations.

It should be noted that, for our model system, there is nothing special about the regime where we study the closed loop transitions under bias. We are only facilitated by the fact that the collinear configurations are the stable ones and that one-spin transitions are indeed possible, so that closed loops are easy to construct and calculate the work as a sum of individual one-spin quasi-static rotations. Thus the result for the non-conservativeness of the spin torques, established numerically here, may in principle be transferable to other open systems.

3.2.6 Breaking the symmetries (electronic and structural)

Current-induced relaxation of the atomic positions can break the inherent structural symmetry in point contacts similar to ours [112] and substantially weaken its overall stability. In order to investigate the effect of small inhomogeneities in the interatomic spacings of the chain over the DW migration barrier, we empirically map the displacement of the middle atom (#2) from its centrosymmetric position onto a small variation of the hopping integrals between the atomic site #2 and its neighboring sites in the chain. To mimic a small displacement to the left we rescale the

hoppings from site #2 by $0 < \delta \ll 1$ such that

$$\chi_{12} \equiv \chi(1+\delta), \quad \chi_{23} \equiv \chi(1-\delta)\,. \tag{3.2.25}$$

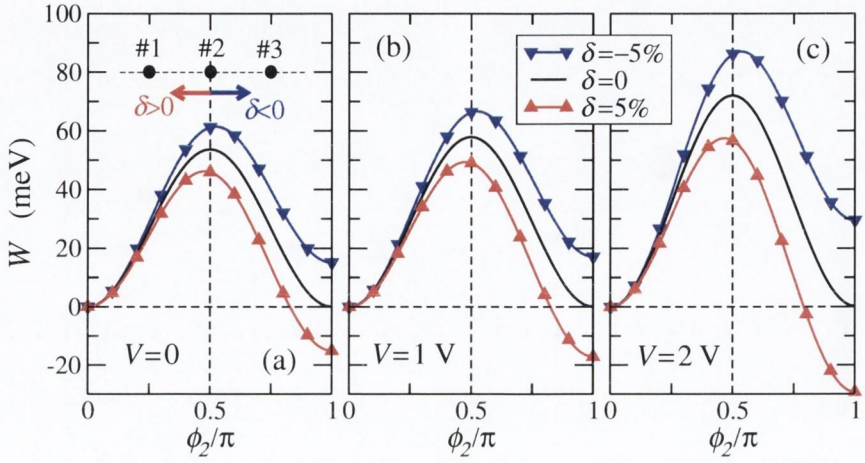

Figure 3.13: Effect of a variation in the hopping parameters of the three-atom chain with $\delta = \pm 0.05$ (see Eq. (3.2.25)) on the barriers for DW migration by one site at different bias voltages: (a) $V = 0$; (b) $V = 1\,\mathrm{V}$; (c) $V = 2\,\mathrm{V}$.

As a result from this action, a tilt in the effective energy barrier profile occurs (compare Fig.3.13 with the uniform-structure results in Fig. 3.4). The total work for the $(0, 0, \pi) \rightarrow (0, \pi, \pi)$ transition is negative thus the internal energy of the classical spins is increased. In this case the degeneracy of the $(0, 0, \pi)$ and $(0, \pi, \pi)$ state is lifted, as the central reflection symmetry, is no longer present. In fact, for $\delta = 5\%$, representing a shift of the middle atom to the left, the $(0, \pi, \pi)$ configuration becomes energetically preferable. Alternatively, $\delta = -5\%$ favours the $(0, 0, \pi)$ state. The dynamical variables of the new inhomogeneous system are now invariant upon the transformation $\{\delta, \phi_2\} \rightarrow \{-\delta, (\pi - \phi_2)\}$ (see Fig.3.13).

The atomistic properties and the net current as a function of the reaction coordinate ϕ_2 are presented in Fig. 3.14. The effective ferromagnetic coupling between the local spins is strengthened by the enhanced electronic hopping and the onsite spin-densities of all the atoms shift almost rigidly as the middle atom is brought towards one or the other of the leads. The net current shows a significant asymmetry when compared to the previously observed symmetric bell-shaped dependence on ϕ_2 and the more stable configuration is always found to be the less conducting one [Fig.3.14(d)]. At a given bias of 1 V we observe a 4-5 % variation of the net current between the initial and the final spin state. Accordingly, the I-V characteristics of the previously degenerate $(0, 0, \pi)$ and $(0, \pi, \pi)$ states is split into two branches [Fig.3.15(a)], whose difference increases rather

linearly with voltage [Fig.3.15(b)] and reaches about 10% for $V = 2\,\mathrm{V}$. Thus we expect DW migrations within the constriction, in the case of small deviations from a uniform geometry, to be accompanied by variations in the net current with the signature of a random-telegraph noise.

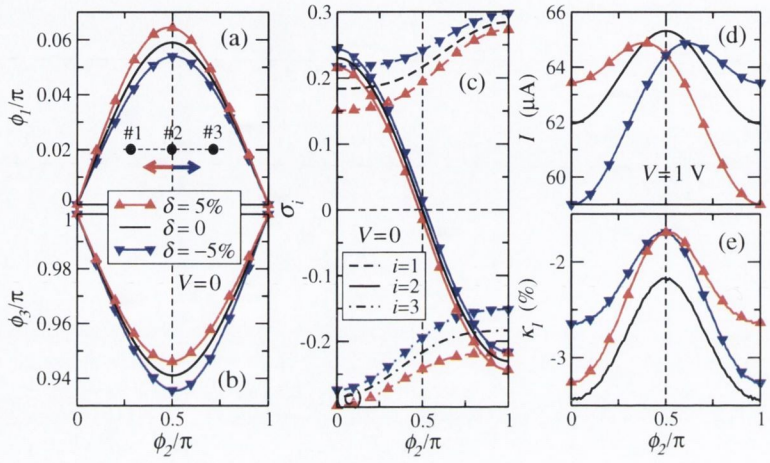

Figure 3.14: Effect of a $\delta = \pm 5\%$ asymmetry in the hopping integrals asymmetry on the atomistic variables during the DW shift – (a,b) $\phi_{1,3}$ (note that the symmetry relation in this case becomes $\phi_3(\phi_2, \delta) = \pi - \phi_1(\pi - \phi_2, -\delta)$), (c) the on-site spin-polarization, and (d,e) the net current and its spin-polarization at $V = 1\,\mathrm{V}$. The bias on (a,b,c) is $V = 0\,\mathrm{V}$.

The interplay between the current-induced relaxation of the magnetic and mechanical degrees of freedom is studied in a mutually-consistent manner later in this thesis. The simple test above is the motivation for further analysis as it clearly shows that geometrical asymmetries in the atomic structures (which could be induced by the current [112]) affect qualitatively and quantitatively the activation barrier for DW migration. The generated tilt creates energetically preferential spatial traps for the DW in which the system is less conducting. Thermally activated random hops of the DW in the constriction could give rise to a random telegraph noise (with a linearly varying amplitude with bias voltage) in the conductance measurements.

Yet another way to break the inherent symmetry of our model system is to consider a band-filling (ρ_0) which is different from the special case of half-filled band with $\rho_0 = 1$ considered in all previous calculations. This can be interpreted as mimicking the effect of some *spd*-hybridization [101]. To clarify that idea, we have calculated the partial density of spin-up and spin-down states in an "up"-spin-polarized (about an arbitrary polarization axis) infinite lead with the same structure as the leads in our system (see Fig. 3.16) and marked the position of the Fermi level for band fillings ρ_0 from 0.7 to 1.3. With this noninteger filling and the geometrical properties of the system

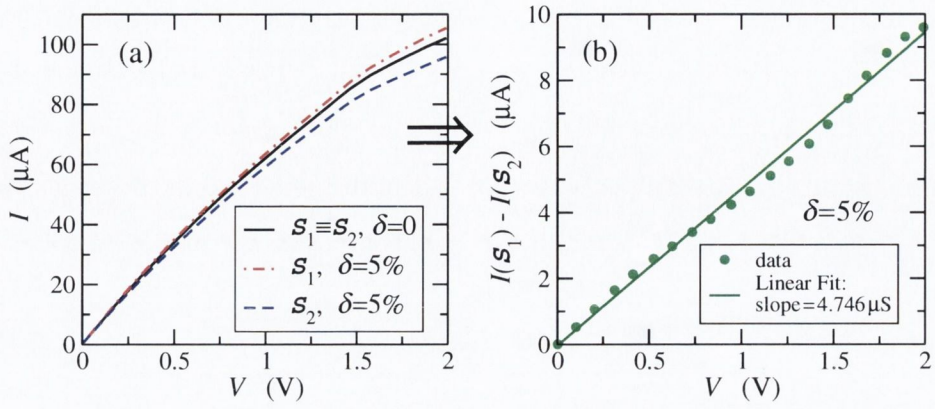

Figure 3.15: (a) The I-V characteristics for the $\mathbb{S}_1 = \{0, 0, \pi\}$ and $\mathbb{S}_2\{0, \pi, \pi\}$ states with $\delta = 0$ and $\delta = 5\%$. The two split $I - V$ curves swap places upon changing the sign of δ. (b) The split of the $I - V$ curves for the two spin states grows linearly with the bias.

(with uniform chain), discussed in Section 3.2.4.2 the new invariance transformation is

$$(\rho_0 + \Delta\rho, V, 00\pi) \equiv (\rho_0 - \Delta\rho, V, 0\pi\pi)\,, \tag{3.2.26}$$

where $\Delta\rho$ is the variation of the band filling from 1.

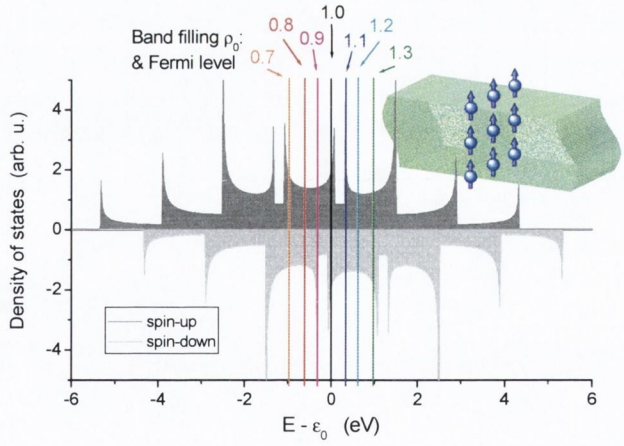

Figure 3.16: Density of states of an infinite uniform lead with 3×3 atoms in the cross section. The tight-binding parameters are the same as those used in all previous calculations ($\chi = -1\,\mathrm{V}$ and $J = -1\,\mathrm{eV}$).

We again look at the energy barrier for a DW shift inside the junction. At equilibrium the non-integer filling does not affect much the barrier profile [Fig. 3.17(a)], there is no tilt [that is a property of the structure at $V = 0$, see Eq. (3.2.22)] and the height is almost unaffected. However

as voltage is introduced the barrier acquires a tilt and the above relation (3.2.26) holds [Fig. 3.17(b)]. The tilt appears to increase with the band-filling deviation from 1. Already at $\rho_0 = 0.7$ the second stable spin state tends to disappear (that indeed happens for further deviations, say at around $\rho_0 = 0.5$, not presented on the graph). Again the initial and the final spin state carry different currents [Fig. 3.17(c)] and thermally activated transitions could be detected through random telegraph noise.

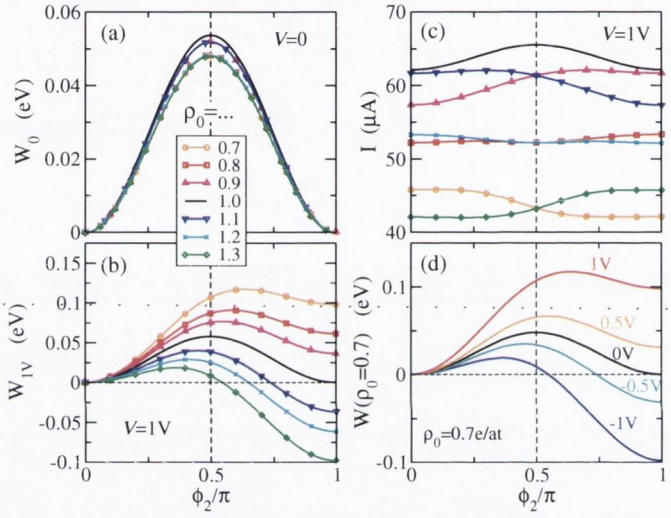

Figure 3.17: Effect of the non-integer band filling ρ_0 on DW-migration barriers (a) at equilibrium, (b) at $V = 1\,\mathrm{V}$ and (c) on the current variation with the DW migration at $V = 1\,\mathrm{V}$. Panel (d) shows the effect on the bias on the barrier for $\rho_0 = 0.7$.

Similar effect is also found with increasing the bias at a fixed band-filling [Fig. 3.17(d)]. The other position of the DW in the constriction becomes energetically instable at high biases and the DW is effectively pinned. The DW could then be manipulated by changing the direction of the bias.

The two means of symmetry braking considered in this section have a common consequence and that is the tilt in the energy barrier for DW migration. In the structural asymmetry case the tilt occurs even and 0 V, while in both cases it increases monotonously with the bias. This opens the possibility for a bias controlled DW migration. In both cases the conductance of the system is found to vary with the DW position.

3.3 Spin and structure interplay under bias

As we pointed out near the end of the previous Section, there have been studies [111] on current-induced embrittlement in similar but non-spin-polarized metallic point contacts, showing a substantial effect. We also demonstrated that, by empirically adjusting the hopping integrals in our model of MPC, a qualitative variation in the DW migration barriers under the current-flow can be obtained. In this Section we have unified the two aspects of the spin-polarized current flowing through an MPC in one common self-consistent framework. That has resulted in a scheme for a combined description of the two current-induced effects in the ballistic transport – the "electron-wind" force due to the elastic momentum exchange and the STT effect due to the exchange of angular momentum.

Here we have extended our foregoing scheme of investigating spin-dynamics under steady-state current to include current-induced mechanical forces, which would allow us to study the interplay of the structural and the spin-rearrangements. With such an extended model we are able to examine the energetics of spin-related dynamical processes, such as the abrupt-DW migration, as a function of the current-induced atomic displacements. Moreover, we can extract the effect of the spin-texture itself on the structural relaxation under the flowing current. Our main finding is that this interplay is strong only in one direction. While the atomic rearrangements can modify drastically the spin-dynamics of the MPC, the magnetic configuration has little effect on the atomic configuration.

The new aspect with respect to our earlier computational scheme is the introduction of the structural degrees of freedom. Similarly to the local spins, they are described as classical variables. The structural state $\mathcal{R}$ of the system is defined by a set of Cartesian coordinates $\mathcal{R} \equiv \{\mathbf{R}_i\}$, where i enumerates the subset of atoms, considered as mechanically active (i.e. contributing to the dynamics). Again the spin state is defined as $\mathcal{S} \equiv \{\mathbf{S}_j\}$ in the subset of spin-active atoms. The interplay between $\mathcal{S}$ and $\mathcal{R}$ is investigated by keeping one frozen and evolving the other.

We apply this method to the previously described MPC (see Fig. 3.1). For example, we address the question of how the particular spin-state in the constriction affects the structural relaxation at the steady state (Fig. 3.18(a)). Conversely, we study what the effect of the current-induced atomic displacements on the DW migration is (Fig. 3.18(b)). We also perform simultaneous structural relaxation with the quasi-static DW migration and evaluate the variation of the current in this process.

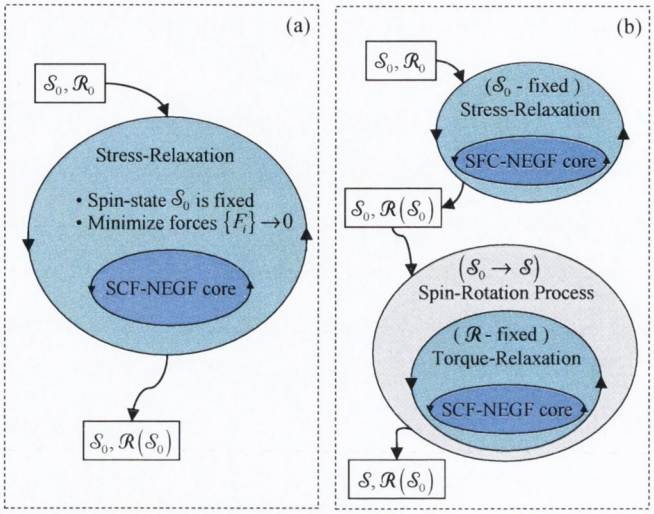

Figure 3.18: Algorithms for investigating the spin-structural interplay: (a) The effect of the spin-state on the structure is studied by relaxing the structure at different fixed states $\mathbf{S}_0$; (b) The reverse effect is studied by mapping out the activation barriers for spin rotation at a fixed structural state, which can be relaxed at different conditions (e.g. different $\mathbf{S}_0$ or bias voltage V) in the initialising stress-relaxation module.

3.3.1 Current-induced mechanical forces

We discussed previously that the mechanical forces acting on the atomic nuclei (or the ionic cores) in steady-state current-carrying conditions can be calculated from the generalized Hellman-Feynman theorem (HFT) [see Eq. (3.2.1)]. Both the thermodynamical approach [111] to the steady-state transport and the axiomatic description [108] of a closed time-dependent (TD) system of quantum electrons and classical nuclei lead to the same expression for the forces on the nuclei [1] as the expectation value of the gradient of the Hamiltonian with respect to the nuclear positions. We extend our previous Hamiltonian (see Eq. (3.2.6)) to account for the dynamics of the cores

$$H\left(\mathbf{S},\mathbf{R}\right) = H_{\mathrm{e}}(\mathbf{R}) + V_{\mathrm{spin}}(\mathbf{S}) + V_{\mathrm{nucl}}(\mathbf{R})\,, \tag{3.3.1}$$

where V_{spin} contains all the spin interactions in the system and V_{nucl} is the inter-site repulsion. The purely electron part now bares an explicit dependence on the positions $\mathbf{R}$ of the atomic cores. We rewrite the above Hamiltonian in a tight binding representation

$$H(\mathbf{S},\mathbf{R}) = \sum_{i,j,\sigma}\left[\left(H_{\mathrm{e}}\right)_{ij}(\mathbf{R}) + \left(V_{\mathrm{eS}}\right)^{\sigma}_{ij}(\mathbf{S})\right] c^{\dagger}_{i\sigma}c_{j\sigma} + V_{\mathrm{SS}}(\mathbf{S}) + V_{\mathrm{nucl}}(\mathbf{R})\,, \tag{3.3.2}$$

[1] We often use different terms to refer to the atomic sites in the system, e.g. nuclei, cores, atoms, ions, sites, etc. to emphasize a particular property of theirs. Here we use "nuclei" as it is closer to the idea of a classical dimensionless mass point.

where the $\mathbb{S}$-dependent terms are the same as the ones used before [see Eq. (3.2.13) and (3.2.14)].

$$(V_{\mathrm{eS}})_{ij}^{\sigma}(\mathbb{S}) = -\frac{J}{2}\boldsymbol{\sigma}\cdot\mathbf{S}_i\delta_{ij} = -\frac{J}{2}\sigma\cos\phi_i\delta_{ij} \tag{3.3.3}$$

$$V_{\mathrm{SS}}(\mathbb{S}) = -\frac{J_S}{2}\sum_{i,j\neq i}\mathbf{S}_i\cdot\mathbf{S}_j = -\frac{J_S}{2}\sum_{i,j\neq i}\cos\left(\phi_i-\phi_j\right), \tag{3.3.4}$$

Here the conduction electrons are again assumed spin-polarized about the z-axis ($\sigma=\pm1$), $J, J_S > 0$ are the onsite and inter-site exchange couplings, $|\mathbf{S}_i|=1$ and ϕ_i is the angle which the i-th local spin in the junction forms with the quantization axis.

The purely electronic part of the Hamiltonian reads

$$\left(H_{\mathrm{e}}\right)_{ij}(\mathfrak{R}) = \left[\mathcal{E}_0+\mathcal{U}_i(\mathfrak{R})\right]\delta_{ij} - \chi(R_{ij}) \tag{3.3.5}$$

where $\chi(R_{ij})$ is the inter-site hopping integral, which now depends on the inter-site distance $R_{ij} = |\mathbf{R}_i-\mathbf{R}_j|$ and U_i is the residual on-site mean-field Coulomb potential created by the excess charge at all other sites

$$\mathcal{U}_i(\mathfrak{R}) = \sum_k U_{ik}(R_{ik})\Delta\rho_k = \sum_k \frac{\kappa\Delta\rho_k}{\sqrt{R_{ik}^2+\kappa^2/U_0^2}} \tag{3.3.6}$$

where the distance dependent factors are denoted by U_{ik} (they decay Coulombically at large distances and have an onsite strength of U_0), $\kappa = e^2/4\pi\varepsilon_0 = 14.4\,\mathrm{eV\AA}$. The residual onsite charges are defined as $\Delta\rho_i \equiv \sum_\sigma \rho_{ii}^{\sigma} - (\rho_0)_i$, where ρ_{ii}^{σ} is the i-th diagonal element of the electron density matrix, corresponding to spin σ and $(\rho_0)_i$ is the charge-neutral number of itinerant electrons on the i-th site.

The inter-site distance dependences of the hopping integral χ and the direct nucleus-nucleus pair repulsion V_{nucl} are material dependent. We assume inverse power laws fitted to elastic properties of bulk noble metals in Ref. [101]

$$\chi(R_{ij}) = \frac{\epsilon c}{2}\left(\frac{a_f}{R_{ij}}\right)^q \quad \text{for } j\neq i \tag{3.3.7}$$

$$V_{\mathrm{nucl}}(\mathfrak{R}) = \frac{1}{2}\sum_{i,j\neq i}(V_{\mathrm{nucl}})_{ij} = \frac{\epsilon}{2}\sum_{i,j\neq i}\left(\frac{a_f}{R_{ij}}\right)^p. \tag{3.3.8}$$

In our calculations we have taken the material parameters of gold: $\epsilon = 7.8680\,\mathrm{meV}$, $c = 139.07$, $a_f = 4.08\,\mathrm{\AA}$, $q=4$, $p=11$.

The mechanical forces acting upon the atomic cores, which according to the generalized Hellman-Feynman theorem are the expectation value of the gradients of the Hamiltonian with respect to the nuclear positions, are as in Ref. [108] given by

$$\mathbf{F}_i = -\sum_{j\neq i}\left[2\left(\nabla_i(H_{\mathrm{e}})_{ij}\right)\mathrm{Re}\left[\sum_\sigma \rho_{ij}^{\sigma}\right] + \Delta\rho_i\Delta\rho_j\nabla_i U_{ij} + \nabla_i(V_{\mathrm{nucl}})_{ij}\right], \tag{3.3.9}$$

where $\nabla_i \equiv \nabla_{\mathbf{R}_i}$ is the gradient with respect to the position of the i-th site.

3.3.2 How spin dynamics is affecting the structure

We consider as mechanically active the five atoms in the constriction, i.e. the three included in the suspended chain plus one adjacent atom from each lead, as depicted in Fig. 3.1. These are relaxed at a given finite bias voltage V for a fixed $\mathcal{S}$. For symmetry reasons the atomic relaxation always results in displacements only along the longitudinal direction (y-axis) and we use y to denote the set of coordinates of the active sites. The conditions, in which the structure has undergone relaxation are specified as subscripts, i.e. $y_{V,\mathcal{S}}$ designates a structure relaxed at a bias voltage V and spin state $\mathcal{S}$.

The initial geometry, denoted by y_{uni}, is that of equidistant atoms with a nearest-neighbor distance of $a = 2.5\,\text{Å}$. This is near to the equilibrium bond length of a periodic 1D chain within our model [112]. However, such a bond length produces a compressive stress in the bulk leads, as a result of which the leftmost and rightmost atoms are pushed slightly out of the leads and the five-atom chain as a whole shrinks by about 2% at zero bias [see Fig. 3.20(a)].

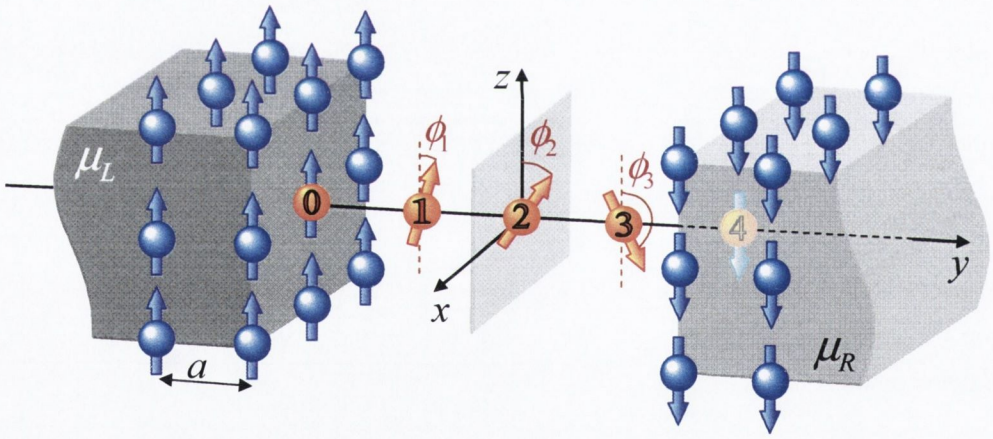

Figure 3.19: Scheme of the magnetic point contact. The mechanically active atoms are depicted in red.

Firstly, we investigate how the spin state of the constriction affects its structural relaxation. We relax the active atomic sites in different spin configurations, e.g. $\mathcal{S}_1 \equiv (0, 0, \pi)$ and $\mathcal{S}_2 \equiv (0, \pi, \pi)$, representing two possible spatial positions of the abrupt DW inside the constriction, but also in some intermediate states with $\phi_2 \in [0, \pi]$ and $\phi_{1,3}$ such that $T_{1,3} = 0$, denoted commonly by $\mathcal{S}(\phi_2)$.

The atomic displacements $y_{V,\mathcal{S}(\phi_2)} - y_{V,\mathcal{S}_1}$, produced during the DW migration, are monotonic functions of ϕ_2 [see Fig. 3.20(b), where $V = 1V$]. They represent nearly rigid translations of the whole atomic chain in the direction of the electron flow. However, the overall DW-shift-induced

displacements $\Delta y_{\mathbf{S}} \equiv y_{V,\mathbf{S}_2} - y_{V,\mathbf{S}_1}$ are very small and constitute about 3% of the displacements from the uniform structure $\Delta y_{\text{uni}} \equiv y_{0,\mathbf{S}_{1,2}} - y_{\text{uni}}$, where $y_{0,\mathbf{S}_{1,2}}$ represents the structure relaxed at equilibrium ($V = 0$) [Fig. 3.20(a)]. The dependence of $\Delta y_{\mathbf{S}}$ on the bias (which is driving a spin-polarized current through the junction) is shown in Fig. 3.20(d). Apparently, independent of the bias, the rotating spin site (#2) is always displaced by the same quantity during the transition. Looking at the external sites, the bias tends to contribute to a small relative shrinkage of the chain during the DW migration. This is indeed a very small effect, amounting to about 0.1% of the intersite distance $a = 2.5$ Å.

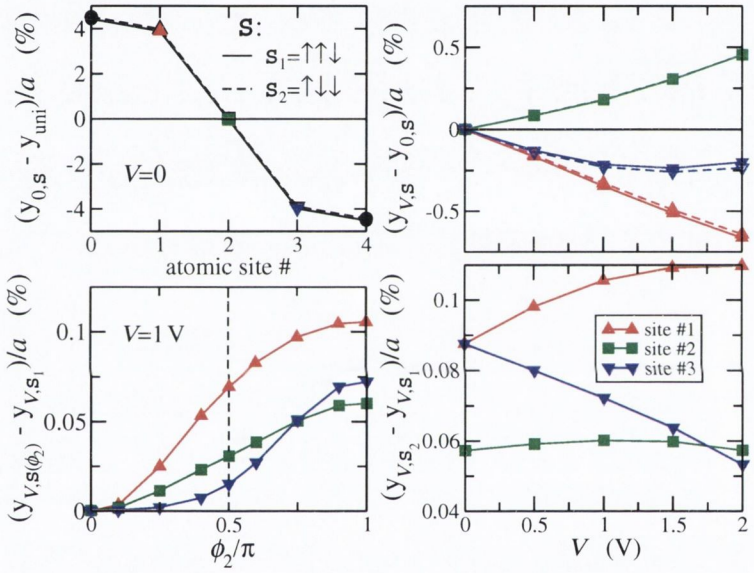

Figure 3.20: Longitudinal displacements (in picometers) of the atoms in the chain: (a) from the uniform geometry at $V = 0$; (b) as function of the DW migration reaction-coordinate ϕ_2 at $V = 1$ V; (c,d) as function of the bias voltage V. See text for details. Here $J = 1$ eV, $J_S = 50$ meV.

The effect of the bias voltage on the structural relaxation at a fixed spin state, imprinted in the quantity $\Delta y_V \equiv y_{V,\mathbf{S}} - y_{0,\mathbf{S}}$ for the two stable collinear configurations $\mathbf{S} = \mathbf{S}_{1,2}$, is presented in Fig. 3.20(c). The purely current-induced displacements are rather linear functions of V (for $V < 1$ V) and promote a tendency toward dimerization. Below 0.5 V the magnitude of the maximal atomic displacement $|\Delta y_V|/a < 0.2\%$ is comparable to the displacements $\Delta y_{\mathbf{S}}$. Interestingly, the Δy_V are almost insensitive to the spin state $\mathbf{S}_{1,2}$, which is a result of the weak bias-dependence of $\Delta y_{\mathbf{S}}$ [see Fig. 3.20(d)]. Indeed, if we define $\Delta y_V(\mathbf{S}_X) \equiv y_{V,\mathbf{S}_X} - y_{0,\mathbf{S}_X}$ for $X = 1, 2$ and impose that $\Delta y_{\mathbf{S}}(V) \equiv y_{V,\mathbf{S}_2} - y_{V,\mathbf{S}_1} \approx \text{const}(V)$ then

$$\Delta y_V(\mathbf{S}_2) - \Delta y_V(\mathbf{S}_1) = y_{V,\mathbf{S}_2} - y_{0,\mathbf{S}_2} - y_{V,\mathbf{S}_1} + y_{0,\mathbf{S}_1} = y_{\mathbf{S}}(V) - y_{\mathbf{S}}(0) \approx 0\,. \tag{3.3.10}$$

This implies that different spin states bear almost indistinguishable structural variations induced by the current. Also transitions between spin states (representing a DW shift by one site) under bias have very little impact on the structure (atomic displacements less that 0.1% of the interatomic distance $a = 2.5\,\text{Å}$). Apart from $\mathcal{S}_{1,2}$ and $\mathcal{S}(\phi_2)$ other spin states, having multiple abrupt DWs [e.g. $(\pi, 0, \pi)$ state], are found to produce an effect very similar in magnitude ($\Delta y_{\mathcal{S}}(1\text{V})/a < 0.3\%$) on the structural relaxation. This establishes that the structural properties of a magnetic nano-device under bias are to a large extent independent of the magnetic state.

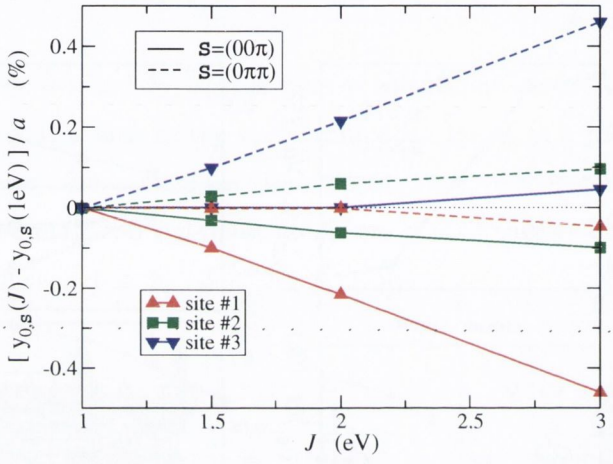

Figure 3.21: J-induced variation in the longitudinal displacements of the chain atoms in the constriction.

For the sake of comprehensiveness, we include the computed J-dependence of the equilibrium ($V = 0$) structural relaxation of the chain at $\mathcal{S}_{1,2}$ (see Fig. 3.21). The observed left-to-right mirror symmetry upon swapping $\mathcal{S}_1 \longleftrightarrow \mathcal{S}_2$ reflects the spatial symmetry of the system. The overall effect of the exchange coupling J on the atomic relaxation is linear up to very large J's. The linear slopes, though, are rather small. Doubling J brings at most a 0.25 % variation in the atomic displacement. Once again this finding supports the observation of the weak effect of the spin of the mechanical properties of the structure.

3.3.3 How structural readjustments are affecting the spin dynamics

Here we address the other aspect of the interplay by looking at how the structural relaxation affects the energy barrier for DW migration over one spin site, i.e. the transition between two stable collinear spin states $\mathcal{S}_1 \longrightarrow \mathcal{S}_2$. This is again calculated by integrating the torque T_2 over the reaction coordinate ϕ_2 as $\mathbf{S}_2$ is quasi-statically rotated while the other two active spins $\mathbf{S}_{1,3}$ are constantly relaxed so that their associated torques are kept at zero [see Eq. 3.2.21].

We investigate these barriers in different structural states. Three such groups of structures are considered (i) the uniform structure y_{uni} which is not relaxed and all atomic sites are equispaced, (ii) $y_{0,\mathbf{S}}$, relaxed at equilibrium and $\mathbf{S}$ and (iii) $y_{V,\mathbf{S}}$, relaxed at a bias V and $\mathbf{S}$, where typically $\mathbf{S} = \mathbf{S}_{1,2}$. We introduce subscript indices to indicate the structural state, thus $W_{V,\mathbf{S}}(V, \phi_2)$ is the work as defined in Eq. (3.2.21) a function of the reaction coordinate ϕ_2 and describes the profile of the non-equilibrium DW migration barrier at a bias V for structure relaxed at V and $\mathbf{S}$. For brevity in Fig. 3.22 (top panels) the latter quantity is designated simply by $W \equiv W_{V,\mathbf{S}}(V, \phi_2)$, where $\mathbf{S} = \mathbf{S}_{1,2}$. A key feature of all the profiles W is the tilt of the barrier at any finite bias even for a uniform atomic arrangement. This tilt is attributed to the non-integer electron occupancy per site, used in these simulations ($\rho_0 = 0.7$) as opposed to 1 e/atom used previously (see Section 3.2.4). In the latter case of a half-filled band the density of states of the simple cubic leads has the special property of being invariant with respect to reflection about the Fermi level and then the leading contributions to current-induced forces and torques are linear in the bias. This asymmetry manifests itself as a preferential spatial localization of the DW at a given bias V: under the present bias $V > 0$ the $\mathbf{S}_1 = (0, 0, \pi)$ configuration is stable, while the $\mathbf{S}_2 = (0, \pi, \pi)$ is at most metastable. Hence, the DW can be driven back and forth in the constriction by an alternating current. This is an explicit example of a current-driven DW motion.

We now focus on the contribution of the atomic relaxation to the DW migration barrier profile. The bottom panels of Fig. 3.22 depict the differences $\Delta W_0 \equiv W - W_0$ and $\Delta W_{\text{uni}} \equiv W - W_{\text{uni}}$ as functions of ϕ_2 at different bias voltages V, where $W_{0,\mathbf{S}}(V, \phi_2)$ and $W_{\text{uni}}(V, \phi_2)$ are the barriers at the given voltage V and atomic structure relaxed at $V = 0$ and at a uniform (homogeneous and unrelaxed) structure respectively.

Thus we can isolate the effect of the current-induced atomic displacements [see Fig. 3.20(c)] on the DW migration barriers by looking at ΔW_0 and those resulting on the full atomic relaxation, starting with the uniform structure and going to a steady state at voltage V [see Fig. 3.20(a)], by looking at ΔW_{uni}. One observation is that $\Delta W_0 > 0$ for any choice or parameters or bias, which means that the current induced rearrangement systematically increases the barrier height. Quantitatively, this is a rather small effect – the barrier height increase $\max(\Delta W_0)/\max(W)$ is up to 2% for $J \geq 1.5\,\text{eV}$. The actual atomic displacements though, which invoke it are also very small – $\Delta y_V/a \leq 0.4\,\%$ [see Fig. 3.20(c), we have found that there is no significant J-induced effect to it].

However, the relaxation from the uniform arrangement, which shortens the interatomic distance in the chain by upto 4% [Fig. 3.20(a)], has an opposite effect and reduces the barrier height approximately by $\max(\Delta W_{\text{uni}})/\max(W) \approx 25 - 30\,\%$ (see Fig. 3.20) for $J \geq 1.5\,\text{eV}$. This is a

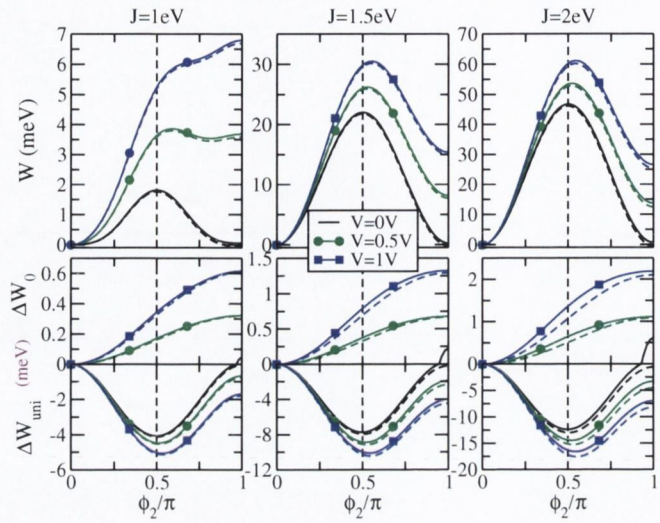

Figure 3.22: DW-migration energy barriers at different biases V for $J_S = 50$ meV and $J = 1, 1.5, 2$ eV (panels from left to right). The solid (dashed) lines are for structure relaxed at $\mathcal{S}_1$ [$\mathcal{S}_2$]. In the top panels $W \equiv W_{V,\mathcal{S}}(V, \phi_2)$ is the work at the given bias V and geometry relaxed also at V. The middle panels depict $\Delta W_0 \equiv W - W_0$, where $W_0 = W_{0,\mathcal{S}}(V, \phi_2)$ is the barrier at the given bias for structure relaxed at 0 V. In the bottom panels is $\Delta W_{\text{uni}} \equiv W - W_{\text{uni}}$, where $W_{\text{uni}} = W_{\text{uni}}(V, \phi_2)$ is the barrier at bias V and uniform geometry.

rather sizeable effect for the spin dynamics and it is induced by such a little adjustment of the structure. In fact, this effect can further increase to about 200 % for exchange parameters close to a separating curve in the spin-state stability diagram in Fig. 3.8. [1] Hence the spin dynamics in the contact is indeed strongly affected by the atomic configuration, especially in the region of parameters where the J coupling mechanism starts competing with the direct exchange mechanism.

Finally, the effect of the structural relaxation upon the conductance of the system is found to be small (Fig. 3.23). The current is clearly insensitive to the DW migration within the constriction. The overall variation of the net current for the rotation of $\mathcal{S}_2$ for fixed geometry, which is in itself a small quantity, is further substantially compensated by the structural rearrangement induced variation, i.e. the structure is found to respond to the spin flip by structural adjustment, which minimizes the conductance variation (see inset of Fig. 3.23). We have also found a decrease in conductance due to relaxation of the structure from the uniform geometry. This agrees qualitatively with the findings in Ref. [94], although the effect we observe is much smaller in magnitude.

[1] This occurs for instance when J and J_S are such that the zero-bias DW migration work as function of the "reaction coordinate" (e.g. ϕ_2) changes from having two stable states with colinear local spins to only one stable state with $\phi_2 = \pi/2$. For $J_S = 50$ meV and this parameterization this occurs for J between 0.8 eV and 0.9 eV (see Fig. 3.8).

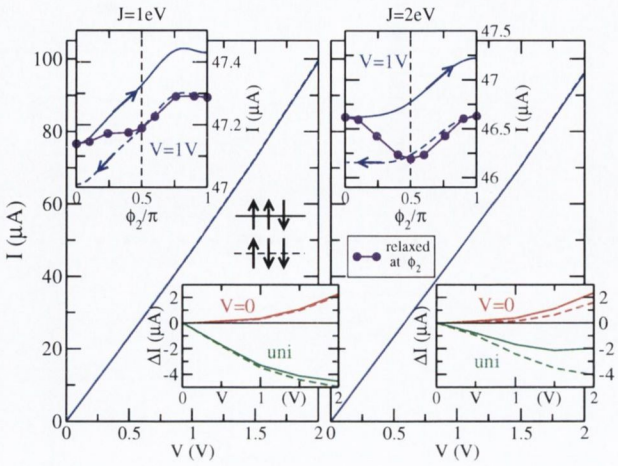

Figure 3.23: I-V curves for a geometry relaxed at V. Solid (dashed) lines represent $(0, 0, \pi)$ $[(0, \pi, \pi)]$ state. Top inset: dependence of net current for $V = 1$ V on the DW-migration reaction coordinate ϕ_2, circles represent structure, relaxed at ϕ_2 [see Fig. 3.20(b)]. Bottom inset: $\Delta I = I - I_{0/\mathrm{uni}}$, where I_0 (I_{uni}) refer to relaxed at $V = 0$ (uniform) structure.

3.3.4 Dependence on material parameters

Here we extend the study of the magneto-mechanical interplay, which is based on material-dependent parameters fitted to cohesive properties of bulk Au, by considering other readily available [101] sets of empirical parameters suited for an orthogonal TB electronic structure model. These represent the bulk cohesion of other transition metals, namely Cu and Ag.

	ε (meV)	a_{f} (Å)	p	q	c	ρ_0	a, Å
Cu	12.61	3.61	9	3	112.4	0.5	2.3
Ag	2.550	4.09	12	3	401.2	0.7	2.6
Au	7.868	4.08	11	4	139.1	0.7	2.5

Table 3.2: The empirical TB parameters for noble metals from Ref. [101]

The atomic displacements $\Delta y_0 = y_{0,\mathbf{s}_{1,2}} - y_{\mathrm{uni}}$ at equilibrium ($V = 0$) are depicted in the left-hand side panels of Fig. 3.24 for the three different parameterizations. They amount to a few percent of the bond lengths a (see Table 3.2). However, Δy_0 are at least an order of magnitude greater than the displacements $\Delta y_{\mathbf{S}} = y_{V,\mathbf{s}_2} - y_{V,\mathbf{s}_1}$, induced by the DW migration for V up to 2V and any set of material parameters (see right-hand side panels of Fig. 3.24). This confirms that the structural properties of a magnetic nano-device under bias are to a large extent independent of the magnetic state and the particular choice of structure-related TB parameters.

The reverse interplay, i.e. the effect of the structural state on the DW migration barriers for all

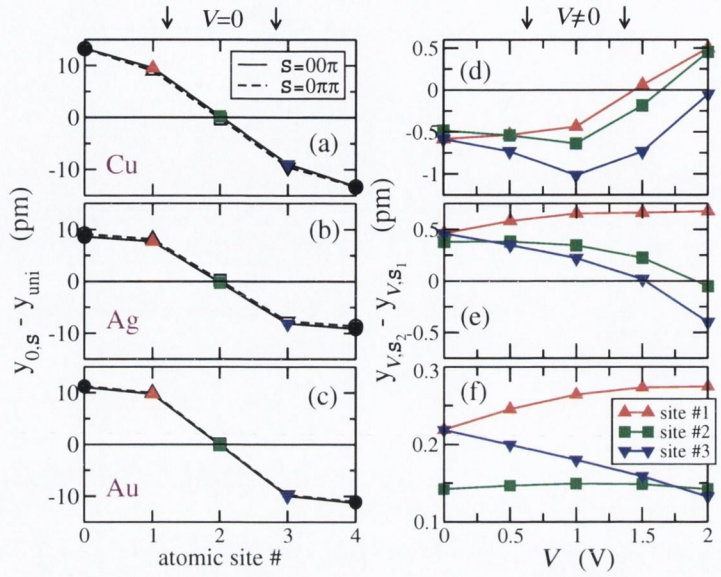

Figure 3.24: Displacements of the atoms in the chain from the uniform geometry at $V = 0$ (panels a, b, c) and as function of the bias voltage V (panels d, e, f) for the three different parameterizations: Cu (top), Ag (middle), Au (bottom panels). See text for details.

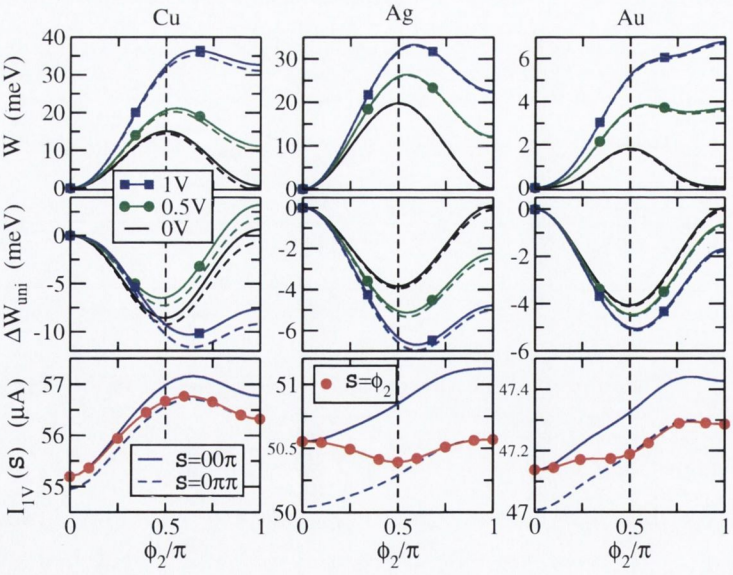

Figure 3.25: Top panels: $W \equiv W_{V,\mathbf{S}}$ at bias $V = 0, 0.5, 1$ V and $\mathbf{S} = \mathbf{S}_1$ ($\mathbf{S} = \mathbf{S}_2$) represented by solid (dashed) lines and TB parameters for Cu, Ag, Au from left to right panels. Middle panels: $\Delta W_{\text{uni}} \equiv W_{V,\mathbf{S}} - W_{\text{uni}}$. Bottom panels: the net current $I_{V,\mathbf{S}}$ for $V = 1$ V. Red dotted line corresponds to $\mathbf{S}(\phi_2) = \{\phi_1, \phi_2, \phi_3\}$, where $\phi_{1,3}$ are such that $T_{1,3} = 0$.

three mechanical parameterizations is demonstrated in Fig. 3.25. The top panels show the barrier profiles for $W \equiv W_{V,\mathcal{S}_{1,2}}(V, \phi_2)$, while the middle ones represent $\Delta W_{\text{uni}} = W - W_{\text{uni}}$, where all quantities are defined as in the previous section. We consider the relative variation of the barrier height, defined by $\max(\Delta W_{\text{uni}})/\max(W_V)$, as a quantitative measure of the effect. The latter is about 30-50% for Cu and Ag and can reach 200% for Au, where the chosen values for the exchange parameters appear close to the critical for the stability of a collinear spin-state (see Fig. 3.22 and the footnote on that page). Thus the effect of a structural relaxation on the DW migration barrier is significant for all the parameterizations, while that of the spin-state $\mathcal{S}$ is practically negligible (see Fig. 3.24).

Finally, the effect of the DW-shift-induced structural variation on the net current $I_V(\mathcal{S})$, described by the ratio $\left(I_{V,\mathcal{S}_2} - I_{V,\mathcal{S}_1}\right)/I_{V,\mathcal{S}_1}$, is found to be very small (less than 1% for a bias of 1V) for any choice of TB parameters (see bottom panels of Fig. 3.25).

Essentially, we have found no critical dependence of the interplay between the magnetic and mechanical relaxation on the choice of structural parameters describing the transition metal. The interplay between the structural relaxation and the mobility of the DW inside a magnetic point contact is only strong in one direction and the DW motion does not affect the structural dynamics nor the conductivity of the system.

3.3.5 Summary on the magneto-mechanical interplay in MPCs

In conclusion we have developed a scheme to investigate the interplay between the magnetic and structural degrees of freedom of atomistic MPCs under current-carrying conditions. We have used it to calculate the effects of the structural relaxation (both in equilibrium and in the presence of current) on the migration barrier for an abrupt DW and, reversely, the effect of the magnetic configuration on the structural relaxation of the junction. Our main finding is that the interplay is predominantly in one direction, that is the structural relaxation strongly modifies the DW migration barrier, while spin state has little effect on the mechanical forces.

Other finding from our calculations is that the barrier typically shows a substantial asymmetry, which increases with the external bias even for a spatially symmetric system. That opens the possibility of voltage-controlled DW motion in such systems. Further, the current-induced displacements from the relaxed at $V = 0$ structure and are of the order of $\Delta y_V/a < 0.7\%$, produce an additional tilt in the DW migration barrier and an increase in height by about 3%. This is small compared to the effect of the relaxation from the initial uniform atomic configuration at the given bias. The latter corresponds to structural distortion by $\Delta y_{\text{uni}}/a < 4\%$ but results in a dramatic effect on the barrier profile, reducing the barrier height by up to 2/3 or even making the alternative

spin-state in the junction unstable, i.e. blocking fully the DW migration, for some exchange parameters. That is a manifestation of the strong non-linear dependence of spin-polarized transport properties on structural rearrangements. However, structure is practically not affected by the DW migration under bias. This is understandable in view of the fact that the mechanical forces depend on the total charge density of the current-carrying electrons, not on their spin polarization. In other words, as long as the conductance is not greatly affected by the spin state, so would be the underlying structure. An interesting observation has been the variation in the conductance as a result of the spin rotation is to a great extent compensated by the structural deformation (see Fig. 3.23 and Fig. 3.25). This can be a possible mechanism for the experimentally observed in Ref. [117] independence of the conductance on the magnetic configuration in MPCs.

Chapter 4

Time-dependent quantum transport

4.1 Introduction

The Landauer approach to electron transport, described and applied to spin-polarized atomic point contacts in the previous chapters, has been widely and successfully used to model the steady-state conduction properties of mesoscopic devices. This static scattering description has also contributed to the understanding of otherwise dynamic phenomena like local heating and electromigration. If the adiabatic [Born-Oppenheimer (BO)] approximation is subsumed, the combined dynamics of the heavy nuclei (or ionic cores) and itinerant electron gas can be course-grained in time as a sequence of quasi-static shifts of the inert cores, with each snapshot of the cores defining parametrically a steady-state electron conduction. In this way the static approach to conduction gives an approximation to the dynamical evolution on the time-scale of the inert degrees of freedom. Because of the open boundary conditions in a typical transport problem, departing from the BO approximation and the static approach is a rather challenging task. There exist true dynamical methods, where open boundary conditions are introduced and the electrons and ions are evolved simultaneously (Ehrenfest dynamics) and even beyond Ehrenfest, quantum corrections to ions are introduced in what is called correlated electron-ion dynamics (see for instance Ref. [70]). Actually, this level of sophistication appears essential for modelling effects like local heating.

For our purposes here we do not need to depart from the BO approximation, i.e. we shall be looking at a snapshot of all inert degrees of freedom. Even when these are eliminated the static approach does not recover all information about the non-equilibrium system. Instead it does produce a self-consistent steady-state, given some initial "guess"-state of the system. Such a

procedure does not provide information about the rest of the phase-space portrait of the system apart from the self-consistently determined steady state. It does not immediately provide an answer to whether or not the state is unique. In fact, for non-linear systems of interacting electrons under constant control parameters there may as well be multiple steady states available [124]. [1] It can be expected that when a battery (pair of reservoirs with different chemical potentials) is connected to the device, the interacting electrons originating from one reservoir, scattered and collected in the other reservoir may establish different steady-states for different initial electron distributions in the device. Without the notion of free-energy by which these states can be discriminated, only the real-time evolution of the system can provide an indication of which state will be realized under the given circumstances.

In what follows we describe one model example where multiple steady-states can be identified by the static approach. We also introduce a semi-empirical open-boundary approach to the time-dependent transport and compare the $I-V$ characteristics calculated statically and dynamically.

4.2 Transport model for a dimer in a chain

We consider an infinite monoatomic wire, described by orthogonal single-band tight-binding model [Fig. 4.1(a)]. The chain has uniform nearest neighbour hopping integrals β except for a pair of atoms (which we refer to as the dimer), coupled to the chain with some different hopping parameter γ and between themselves with δ which in general can have different values. We consider a half-filled spinless band ($0.5\,e$/atom) with all onsite energies set to zero. Hence at equilibrium the Fermi level is at zero too ($E_F = 0$). A bias voltage V is then applied to this system by shifting the onsite energies of the left-hand side semi-infinite wire E_L by $eV/2$ and the right-hand side ones E_R by $-eV/2$ [Fig. 4.1(b)]. In order to determine the non-equilibrium properties of this system we shall employ some results from the NEGF theory described in Chapter 1. Because of the extreme simplicity of this system we can carry out a big portion of the NEGF algorithm analytically.

Since our device consists of only two atoms, we work in 2×2 matrix representation. Firstly, let us introduce the retarded surface GF in the energy domain of the two ("L","R") homogeneous

[1] Slightly departing from the main objective here we point to the fact that steady-state transport is a non-equilibrium mode, though indeed a very special one for which a set of macroscopic parameters does not change in time. As this makes steady-states in some sense closer to the equilibrium states than the general non-equilibrium states, a thermodynamics theory of steady states is actually being developed at present [61]. For the analogous to the Landauer problem where a device is coupled to two reservoirs with different temperatures a steady-state free energy thermodynamic potential has been recognized in the linear non-equilibrium regime of small heat flows. However, we cannot extend the results of that analysis to a general quantum-transport problem away from the linear response regime.

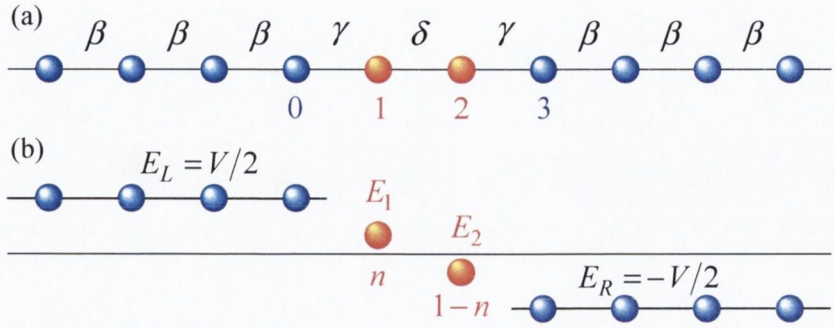

Figure 4.1: A schematic representation of the monoatomic chain with the dimer. Panel (a) illustrates the assignment of hopping parameters, (b) is a cartoon of the model electrostatic arrangement after the application of a bias voltage V to the two semi-infinite sides of the chain.

semi-infinite chains

$$g^0_{L(R)} \equiv g^0_{00(33)} = \frac{E - E_{L(R)} \pm \sqrt{(E - E_{L(R)})^2 - 4\beta^2}}{2\beta^2} \tag{4.2.1}$$

where the convention for the sign is described in Appendix A. As a matter of convenience we also introduce $g_{L(R)}$, the retarded surface GF of the leads, each extended to include one dimer atom at its end. In other words we connect the dimer atoms "1" and "2" to the "0" and "3" sites, respectively (see Fig. 4.1(a)) with hopping integrals γ. The new surface GF $g_L \equiv g_{11}$ and $g_R \equiv g_{22}$ can be determined from the Dyson's equation (see Appendix A). We use the result from Eq. (A.0.3), rewritten as

$$g_L = g^0_{11} + \gamma^2 g^0_{11} g^0_L g_L, \qquad g_R = g^0_{22} + \gamma^2 g^0_{22} g^0_R g_R \tag{4.2.2}$$

where $g^0_{11(22)} = 1/(E - E_{1(2)})$ are the "free"-atom Green's functions of the dimer atoms. Hence we obtain

$$g_{L(R)} = \frac{1}{E - E_{1(2)} - \gamma^2 g^0_{L(R)}}. \tag{4.2.3}$$

We then write the effective Hamiltonian of the "scattering region" (the dimer) as [see Eq. (2.3.2)]

$$H_{\text{eff}} = \begin{pmatrix} E_1 + \gamma^2 g^0_L & \delta \\ \delta & E_2 + \gamma^2 g^0_R \end{pmatrix} \tag{4.2.4}$$

where $\gamma^2 g^0_{L(R)}$ represent the self-energies. From H_{eff} the Green's function [see Eq. (2.3.4)] can be

determined [1]

$$G = [EI - H_{\text{eff}}]^{-1} = \frac{1}{(E - E_1 - \gamma^2 g_L^0)(E - E_2 - \gamma^2 g_R^0) - \delta^2} \begin{pmatrix} E - E_2 - \gamma^2 g_R^0 & \delta \\ \delta & E - E_1 - \gamma^2 g_L^0 \end{pmatrix} \tag{4.2.6}$$

Here we notice that switching to $g_{L(R)}$ [defined in Eq. (4.2.3)] simplifies the expression and we obtain instead

$$G = \frac{1}{1 - \delta^2 g_L g_R} \begin{pmatrix} g_L & \delta g_L g_R \\ \delta g_L g_R & g_R \end{pmatrix}. \tag{4.2.7}$$

Hence the density of states $D_{L(R)} = \frac{1}{\pi} G \Gamma_{L(R)} G^\dagger$ [see Eq. (2.2.35)] of the electrons originating from the left (right) lead (which also play a role of the reservoirs), become

$$D_L = \frac{-\text{Im}\,[g_L]}{\pi \left|1 - \delta^2 g_L g_R\right|^2} \begin{pmatrix} 1 & \delta g_R^* \\ \delta g_R & \delta^2 \left|g_R\right|^2 \end{pmatrix} \tag{4.2.8}$$

$$D_R = \frac{-\text{Im}\,[g_R]}{\pi \left|1 - \delta^2 g_L g_R\right|^2} \begin{pmatrix} 1 & \delta g_L^* \\ \delta g_L & \delta^2 \left|g_L\right|^2 \end{pmatrix} \tag{4.2.9}$$

where the star (*) indicates complex conjugation. Considering zero electronic temperature of the reservoirs, i.e. a step-function for the occupancy $f_{L(R)}(E) = \theta(\mu_{L(R)} - E)$, the steady-state density matrix of the system from Eq. (2.2.35) can be rewritten as

$$\rho = \int_{-\infty}^{0} D(E)\mathrm{d}E - \int_{-eV/2}^{0} D_R(E)\mathrm{d}E + \int_{0}^{eV/2} D_L(E)\mathrm{d}E \tag{4.2.10}$$

where $D(E) = D_L(E) + D_R(E) = -\frac{1}{\pi}\text{Im}\,[G(E)]$ is the steady-state density of states [2]. For the steady-state current [see Eq. 2.3.10] we obtain

$$I = \frac{2e}{h} \int_{-V/2}^{V/2} \text{Tr}\left[\Gamma_L G \Gamma_R G^\dagger\right] \mathrm{d}E = \frac{2e}{h}\, 4\delta^2 \int_{-V/2}^{V/2} \frac{\text{Im}[g_L]\text{Im}[g_R]}{\left|1 - \delta^2 g_L g_R\right|^2} \mathrm{d}E\,, \tag{4.2.12}$$

where we have used the fact that the broadening matrices $\Gamma_{L(R)} = i(\Sigma_{L(R)} - \Sigma_{L(R)}^\dagger) = -2\text{Im}\left[\Sigma_{L(R)}\right]$ for the dimer read

$$\Gamma_L = \begin{pmatrix} 2\text{Im}[g_L]/\left|g_L\right| & 0 \\ 0 & 0 \end{pmatrix}, \qquad \Gamma_R = \begin{pmatrix} 0 & 0 \\ 0 & 2\text{Im}[g_R]/\left|g_R\right| \end{pmatrix}. \tag{4.2.13}$$

Here we have also used the relation $\text{Im}[g_L^0] = \text{Im}[g_L]/\gamma^2\left|g_L\right|$.

[1] We use the fact that the inverse of a 2×2 matrix

$$A = \begin{pmatrix} a & b \\ c & d \end{pmatrix} \quad \text{is} \quad A^{-1} = \frac{1}{\det[A]} \begin{pmatrix} d & -b \\ -c & a \end{pmatrix}. \tag{4.2.5}$$

[2] Equivalent forms of expressing ρ are

$$\rho = \int_{-\infty}^{-eV/2} D(E)\mathrm{d}E + \int_{-eV/2}^{eV/2} D_L(E)\mathrm{d}E = \int_{-\infty}^{eV/2} D(E)\mathrm{d}E - \int_{-eV/2}^{eV/2} D_R(E)\mathrm{d}E\,. \tag{4.2.11}$$

Now that we have derived the Landauer machinery for the dimer in a chain, we introduce the mean-field electron-electron interactions in the form of an onsite repulsive potential U so that

$$E_1 = 2U(\rho_{11} - \rho_0) \qquad \text{and} \qquad E_2 = 2U(\rho_{22} - \rho_0)\,. \tag{4.2.14}$$

Because of the perfect electron-hole symmetry of the system we have $\rho_{11} = 1 - \rho_{22}$. Given $\rho_0 = 0.5$ we introduce n as the charge at dimer atom 1 and $\mathcal{E}$ as its energy

$$\rho_{11} = n, \quad \rho_{22} = 1 - n \qquad \Rightarrow \qquad \mathcal{E}(n) \equiv E_1(n) = -E_2(n) = 2U(n - 1/2)\,. \tag{4.2.15}$$

This dependence of $E_{1,2}$ on n makes Eq. (4.2.10) recursive in n

$$n = \mathrm{F}(n) = -\frac{1}{\pi}\int_{-\infty}^{eV/2} \frac{\mathrm{Im}\left[g_L(E,n)\right]\,\mathrm{d}E}{\left|1 - \delta^2 g_L(E,n) g_R(E,n)\right|^2} - \frac{1}{\pi}\int_{-\infty}^{-eV/2} \frac{\mathrm{Im}\left[g_R(E,n)\right]\,\mathrm{d}E}{\left|1 - \delta^2 g_L(E,n) g_R(E,n)\right|^2}\,, \tag{4.2.16}$$

where

$$g_{L(R)}(E,n) = \frac{1}{E \mp \mathcal{E}(n) - \gamma^2 g^0(E)}\,. \tag{4.2.17}$$

Here $g^0_{L(R)}(E)$ are defined in Eq. (4.2.1) and we assume [1]

$$E_L = eV/2 \qquad \text{and} \qquad E_R = -eV/2\,. \tag{4.2.18}$$

We then look for a self-consistent solution of Eq. (4.2.16) and this corresponds to the Landauer steady-state. Interestingly, for this system the root of $\mathrm{F}(n) - n$ is not unique for high enough V and U. In the following we investigate numerically the properties of $\mathrm{F}(n)$ against the variation of model parameters.

Our reference set of parameters for the dimer in the chain is

$$\beta = -3.88\,\mathrm{eV}, \quad \gamma = \delta = -1\,\mathrm{eV} \quad \text{and} \quad U = 7\,\mathrm{eV}\,. \tag{4.2.19}$$

Figure 4.2(a) illustrates the effect of the variation of the applied bias voltage on $\mathrm{F}(n)$. Above $V = 3\,\mathrm{V}$ we see the appearance of two new solutions of $n = \mathrm{F}(n)$. Similarly, at a given bias the multiple solutions appear only above certain value of U [Fig. 4.2(b)]. In this case $\mathrm{F}(n)$ starts bending upward above $n = 0.5$, the point $\{0.5, \mathrm{F}(0.5)\}$ being common for all graphs as $\mathrm{F}(0.5)$ cannot be distinguished from the non-interacting case with $U = 0$. Hence, one of the roots is always below 0.5, corresponding to a depletion of the first dimer atom, and the other two are

[1] Note that in our simplified model only the dimer atoms can be charged and the lead onsite energies are considered constant as implied in Eq. 4.2.18. There is some arbitrariness in the choice of $E_{L(R)}$ as $E_L = E_R = 0$ corresponds to the infinite metallic chain with perfect transmission, while $E_L = -E_R = eV/2$ corresponds to perfectly isolated leads with no transmission between them. However, we have established in calculations that for the regime of parameters we investigate the two extreme values of $E_{L(R)}$ produce very little difference int the result for the current. The difference is negligibly small at low bias and grows to at most 1-2% at $V = 3\,\mathrm{V}$.

above, corresponding to an excess of charge. These latter states both correspond to an electrical dipole with a negative pole facing the electron flow. Before we look at the I-V characteristics for the multiple steady-state solutions we examine the special "structural" setup that predetermines this behaviour.

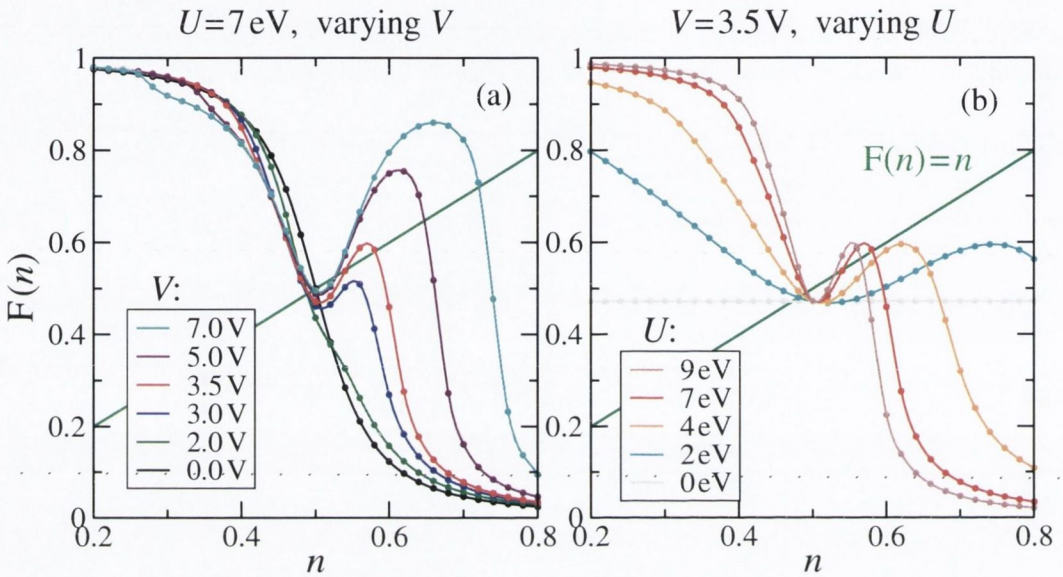

Figure 4.2: F(n) from Eq. (4.2.16) for (a) different voltages and $U = 7\,\mathrm{eV}$ and (b) different U and $V = 3.5\,\mathrm{V}$. Green lines correspond to F(n) = n.

We find the multiple steady-states for the dimer in an arrangement where the dimer atoms are weakly coupled between themselves and to the chain compared to the couplings in the rest of the chain, i.e. $\delta = \gamma \approx \frac{1}{4}\beta$ [see Fig. 4.1(a)]. Depending on the ratio of the couplings $\mathcal{R}_{\mathrm{in/out}} \equiv |\delta| \,/\, |\gamma|$ (the subscript indicates that the ratio is between the hopping integral δ inside the dimer and the outside hopping γ to the chain) we can distinguish two extremes, namely, $\mathcal{R}_{\mathrm{in/out}} \ll 1$ and $\mathcal{R}_{\mathrm{in/out}} \gg 1$. In the first case the dimer atoms would behave like adsorbates to the two semi-infinite leads. When the bias is increased, each of the dimer atoms would charge so that its onsite energy is close to the quasi-Fermi level of its corresponding lead, i.e. $E_1 \sim eV/2 \sim -E_2$. Hence, an electrical dipole would form with a negative pole (excess of electrons) facing left lead (where the electron stream originates). This assembly would conduct by a mechanism akin to the scanning tunnelling microscope (STM), i.e. by adsorbate-adsorbate tunnelling, modulated by the convolution of the two surface density of states (LDOS). In the ideal case of small U and $\gamma = \beta$, at voltages exceeding the width of the two LDOSs, we expect the charge[1] on the first dimer atom to increase and the

[1]Here and throughout the text what we name charge is actually the electron number excess.

current to drop and decrease to 0. Our calculated $n(V)$ and $I(V)$ for the case of $\gamma = 10\delta = 1\,\text{eV}$ and for $U = 7$, presented in Fig. 4.3, indeed show this behaviour qualitatively. The fact that the calculated current drops before reaching the total bandwidth ($\sim 15\,\text{eV}$) is due to the high value of U for which the charging of the dimer is suppressed and the fact that γ, nonetheless being much bigger than δ, is also quite smaller than β. Because of this the STM-like transmission is modulated by the broadened by γ double resonance (merged bonding and antibonding states because of the small δ) around the Fermi level.

We have also studied the other regime $\mathcal{R}_{\text{in/out}} \gg 1$, by swapping the values of δ and γ (see Fig. 4.3). In this case we anticipate that the dimer will behave as a molecule, weakly coupled to the leads. Because of the bigger split ($2\delta = 2\,\text{eV}$) between the bonding and antibonding states we expect a gap in the transmission at low biases. Once the bias window is wide enough to contain the two resonances we see an increase in current. Indeed that is what we see in the calculated I-V and the dimer remains nearly perfectly neutral (Fig. 4.3).

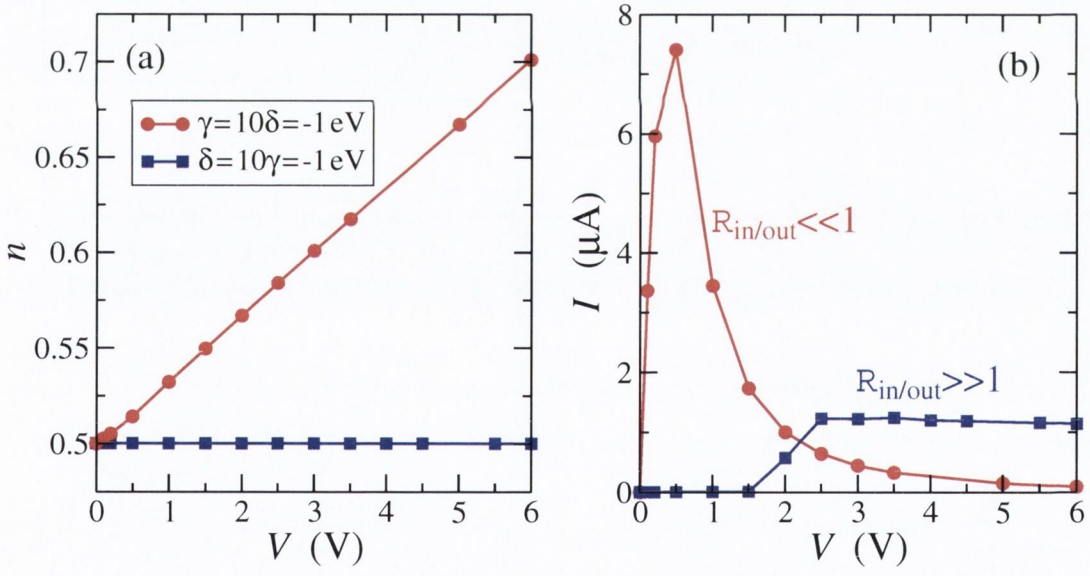

Figure 4.3: (a) Electron number at the first dimer atom as a function of bias voltage and (b) net current through the system for two extreme regimes of coupling of the dimer to the chain. Here $U = 7\,\text{eV}$.

In the intermediate regime of hoppings $\mathcal{R}_{\text{in/out}} \approx 1$ the system cannot be identified with either of the two extremes described above. This is the case in which at high biases we find multiple steady-states (see Fig. 4.2), solutions to $\text{F}(n) = n$. As a function of the bias, the three branches of solutions $n(V)$ are presented in Fig. 4.4(a) and the corresponding current [see Eq. (4.2.12)] $I(V)$

at these states is in panel (b). What we find is that the two of the solutions match qualitatively the two extreme-coupling cases described above. The solution with high current and low (and nearly constant) n is the resonant-transmission solution, similar to the case $\mathcal{R}_{\mathrm{in/out}} \gg 1$. The lower-current and higher-n solution of the two that bifurcate around 3.26 V looks similar to the STM-like solution ($\mathcal{R}_{\mathrm{in/out}} \ll 1$), with a potential at the first dimer site almost pinned to $eV/2$.

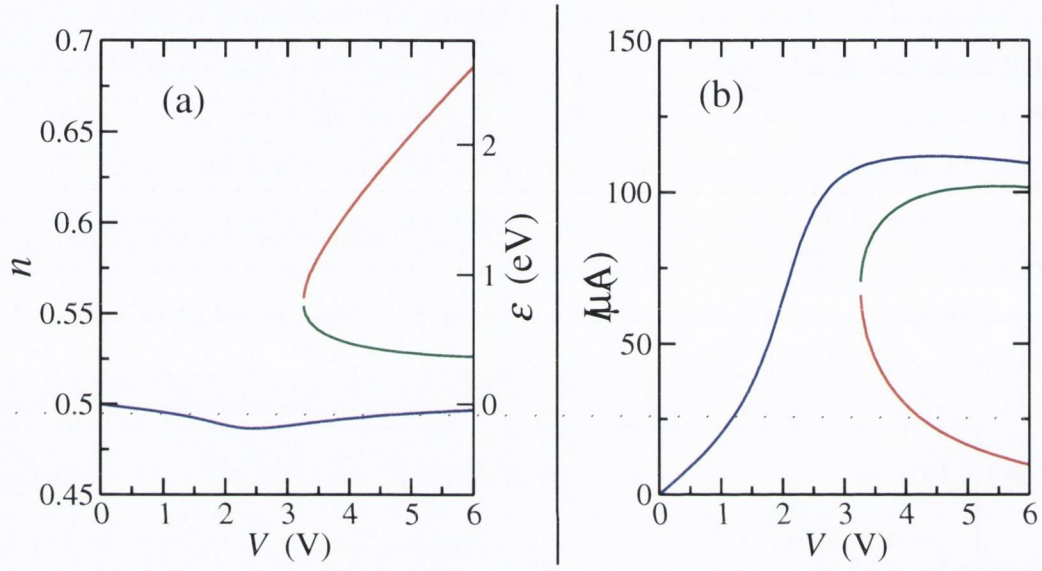

Figure 4.4: (a) Electron number at the first dimer atom as a function of bias voltage and (b) net current through the system for two extreme regimes of coupling of the dimer to the chain. Here $U = 7\,\mathrm{eV}$. Colour code is chosen so as to demonstrate qualitative similarities with Fig. 4.3.

In the following section we shall introduce a time-dependent (TD) approach to such a transport problem and test it for this particular situation where the static approach suggests multiple steady-state solutions.

4.3 Time-dependent open-boundary method

The idea of this approach originates from Ref. [124], where the terms of mapping the conventional Landauer-type steady-state transport problem onto a finite microcanonical one are rigorously analyzed. The latter is described as the long-lived (quasi-steady state) discharge of a macroscopic capacitor through the much smaller device, together forming an isolated system. It has been demonstrated [124] that the total current in the true interacting many-electron system is identical to the one-electron current, obtained from time-dependent density-functional theory (TDDFT) [84] as long as the system is finite. Thus the reduction of the conventional transport problem to

a time-dependent one for a finite system looks like a promising way to go when concerned about time-dependent quantum transport.

Here we follow Ref. [87] and consider the *finite* system cartooned in Fig. 4.5. It consists of a capacitor (C), connected to a device (D) by a pair of leads. Initially (at $t = 0$) the capacitor is statically polarized, i.e. there is a static charge imbalance between its plates. Such can be achieved by the application of an electric field (voltage source) across the capacitor. At $t > 0$ this external source is removed over a short time interval and the system, which is no longer in a stationary state, is allowed to evolve according to the Liouville equation of motion

$$\frac{\partial \hat{\rho}}{\partial t} = \frac{1}{i\hbar}\left[\hat{H}[\hat{\rho}], \hat{\rho}\right] . \tag{4.3.1}$$

Here, $\hat{\rho} = \hat{\rho}(t)$ is the reduced spinless one-particle electronic density matrix (DM) and $\hat{H}[\hat{\rho}]$ is a generic effective one-electron Hamiltonian, such as that produced by TDDFT [84].

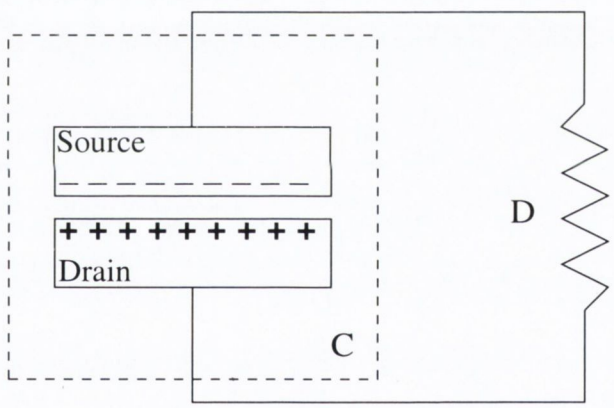

Figure 4.5: Sketch of the partitioning of the system into a device (D) and a capacitor (C).

As we said earlier, if the discharge of such a capacitor in the circuit is long-enough, it could be described by the above Eq. (4.3.1) and provide a finite steady-state analogue to the Landauer transport. However the capacitor sizes needed to provide discharge times significantly exceeding the femptosecond range are unfeasible for atomistic simulations [1]. A solution is to continually feed electrons that have flown across back into the starting electrode. As this cannot be done in our quantum DM description of the electron gas, we choose to maintain the charge imbalance in the capacitor, and hence the current, through a driving source/drain like term in the equation of motion of the DM

$$\frac{\partial \hat{\rho}}{\partial t} = \frac{1}{i\hbar}\left[\hat{H}[\hat{\rho}], \hat{\rho}\right] - \Gamma\left(\hat{\rho} - \hat{\rho}_0\right) , \tag{4.3.2}$$

[1] For instance, wrap-gate transistors of $\sim 100\,\text{nm}$ length have a gate time delay of $\sim 100\,\text{fs}$ [58].

where Γ is a real parameter and $\hat{\rho}_0$ is a specially prepared DM, which in real-space positional basis reads

$$\{\hat{\rho}_0\}_{ij}(t) = \begin{cases} \rho_{ij}(t=0) & \text{for } i,j \in \mathrm{C} \\ \rho_{ij}(t) & \text{otherwise} \end{cases}, \tag{4.3.3}$$

Here $\hat{\rho}(t=0)$ is the initial statically polarized DM. Hence, the role of this new Γ-term is to damp the DM of the capacitor plates (only) back toward that initially charged state. Physically, this achieves two objectives. First, it describes the effect of connecting the capacitor to an external voltage source, which maintains the charge-imbalance in the system. Second, as $\hat{\rho}(0)$ is purely real, it damps the imaginary parts of $\hat{\rho}$ in the capacitor region and thus incorporates into the description of electrons a generic phase-breaking scattering mechanism inside the electrodes. For both Γ too small and too large the current is suppressed. In the first case this is because of the inability to maintain the instantaneous charge imbalance, while in the in second case – because of "over-scattering" causing localization. For the following simulations of a specific atomistic system a value of $\Gamma = 4\,\mathrm{eV}$ has been used and found to be able to establish a steady-state electron flow.

This scheme has been implemented within an orthogonal tight-binding model with mean-field interactions

$$\hat{H} = \sum_{i \neq j} |i\rangle H_{ij}^{\mathrm{TB}} \langle j| + \sum_i |i\rangle \left(U\Delta q_i + \sum_{j \neq i} f_{ij} \Delta q_j \right) \langle i| , \tag{4.3.4}$$

where $\Delta q_i = 2(\rho_{ii} - \rho_0)$ is the total particle imbalance on site i with $\rho_0 = 0.5$. The function of interatomic separation $f_{ij} = \kappa / \sqrt{R_{ij}^2 + \kappa^2/U^2}$, with $\kappa = e^2/4\pi\epsilon_0$, interpolates smoothly between onsite interactions with strength U and the bare Coulomb interaction at large separation. This model may be viewed as the simplest form of TDDFT in the adiabatic local density approximation (ALDA) [134]. In the simulations below $U = 7\,\mathrm{eV}$ [1].

As described in Eq. (4.3.3) the source/drain term is applied only to the "source" and "drain" plates of the capacitor, i.e. $\rho_{ij}(t=0)$ is set in such a way that the source and the drain carry an electron imbalance by an applied (as a rigid shift to the onsite energies) external potential V_{ini}

$$\hat{H}_{ij}^{\mathrm{TB}}(t) = -\chi_{ij} \sum_{k \in \mathrm{n.n.}} \delta_{i,j+k} + f_V(t)\delta_{ij} \begin{cases} -eV_{\mathrm{ini}}/2\,, & \text{for } i,j \in \text{Source} \\ eV_{\mathrm{ini}}/2\,, & \text{for } i,j \in \text{Drain} \end{cases}, \tag{4.3.5}$$

where χ_{ij} is the nearest-neighbour hopping integral between sites i and j, $f_V(t)$ is a smoothly decaying to 0 polynomial ramp over a few femptoseconds, included in order to damp the charge oscillations which could be triggered from the abrupt removal of the initial bias.

The model system simulated is the following. It consists of a two-dimensional (2D) capacitor with 15×20-atom simple-cubic lattice plates and two leads represented by two 15-atom long one-dimensional (1D) atomic chains. The device is a dimer, coupled to the leads through a mismatching

[1] This value of U corresponds to the difference between the ionization energy and electron affinity of the gold atom.

hopping integrals as described in the previous section. The hopping integrals are just as the one used there

$$\chi_{ij} = \begin{cases} \beta &= -3.88\,\text{eV}, & \text{for } i,j \in \text{C + leads} \\ \gamma &= -1\,\text{eV}, & \text{for } i \in \text{leads},\ j \in \text{dimer} \\ \delta &= -1\,\text{eV}, & \text{for } i,j \in \text{dimer} \end{cases} . \tag{4.3.6}$$

After the removing of the external potential ΔV (over a finite time interval), Eq. (4.3.2) is integrated numerically using the method described in Ref. [22]. The current flowing through the dimer as a function of time is shown in Fig. 4.6(a). This is in fact the bond current at the dimer, defined as the electron particle current [110, 109] between the two dimer sites

$$I = \frac{2e}{\hbar} \text{Im}\left[\rho_{12}\right] H_{21} . \tag{4.3.7}$$

We observe that after some transient period the current finally settles at a steady state. The actual bias at this state ΔV is calculated from the average onsite energy in each plate at the end of the simulation and is typically smaller than the initially applied bias V_{ini} [see Eq. (4.3.5)] due to the finite size of the capacitor. For small bias, the steady state is reached after a short rising transient of about 10 fs. For biases larger than about 4 V, the current first rises up to about 120 μA and then gradually decreases to reach a much lower value of about 25 μA in the steady state.

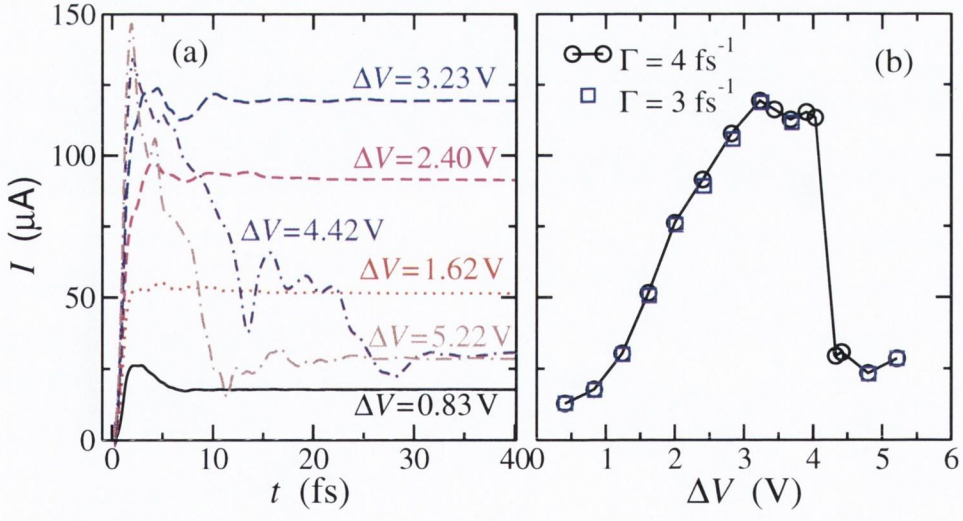

Figure 4.6: (a) Current as function of time from the integration of Eq. (4.3.2). The bias ΔV shown corresponds to the final steady state (see text for details). (b) Current-voltage curve obtained from the final values of the current and potential difference after a steady state has been reached, for two different values of the parameter Γ.

The I-V characteristic obtained from the steady-state current and potential difference ΔV is shown in Fig. 4.6(b). Up to about 4 V the curve matches what could be expected for a resonant

transmission [see Fig. 4.4(b)]. However, we then see a sudden drop in the current and a heavily suppressed conduction at biases above 4.2 V. With the parameters used, the bandwidth of the 2D plates is ~31 eV and in the 1D leads it is ~16 eV. Therefore, the reason for the drop in the conductance cannot be that the bias is so high that the source and drain bands are completely mismatched. Also a variation in the value of Γ from 4 to 3 fs^{-1} has no significant effect on the I-V.

4.4 Fully selfconsistent NEGF results and comparison

Together with the semi-analytic static calculation we have also performed two full selfconsistent NEGF calculations in the spirit of the previous chapter - one with 1D and another with 2D leads/reservoirs (see top panels in Fig. 4.7). The former case is closer to the semi-analytic treatment as serves as a test, while in the latter case we have used two 2D 15-atom across (same as the width of the capacitor plates) semi-infinite cubic-lattice structures as leads/reservoirs and the tight-binding Hamiltonian is the one from Eq. (4.3.4), i.e. with the additional mean-field interactions considered in the TD approach. In order to seek for all the steady state solution we have developed an automated quasi-random initial DM feeding procedure. The "quasi" property stands for the fact that these matrices are true ground-state DMs for systems with randomized onsite potentials (between 0 and 5 V) but same number of electrons. Thus for a given initial DM condition, the selfconsistent steady-state at a given bias is determined iteratively by the algorithm, cartooned in Fig. 2.7, over a region which includes layers from the leads. The results are then classified based on their value of the current. Interestingly, the results from both self-consistent calculations agree quantitatively with the semi-analytic method and pieces of all three branches are recovered.

Results from all three static calculations (including the semi-analytic one) are compared to the TD results (from the previous section, Fig. 4.6) in Fig. 4.7. We see that the different static solutions are in agreement about the existence of multiple steady states, while the dynamical method reproduces parts of two different static branches after a discontinuous jump at around 3.2 V. The difference in n between the TD calculation and the semi-analytical static one at high bias are due to the screening provided by the intersite Coulomb terms in the TD case. This difference is clearly reduced when such interaction is introduced too in the self-consistent NEGF calculation in Fig. 4.7(c).

Our main observation is that the TD calculation naturally selects the low-current solution above a certain bias. The reason for this preference is the increasing instability, with increasing bias, of the high-current solution against spontaneous charge fluctuations in the dimer. If a small fluctuation in n pushes $\mathcal{E}$ away from the spacial value needed for resonant transmission, this kills

the resonance, the current drops and the system switches to an insulating (STM-like) mode, with no recovery mechanism. This instability is also evidential from the corresponding self-consistent NEGF calculation where this high-voltage parts of the resonant solution have not been recovered despite the numerous attempt with randomized DMs.

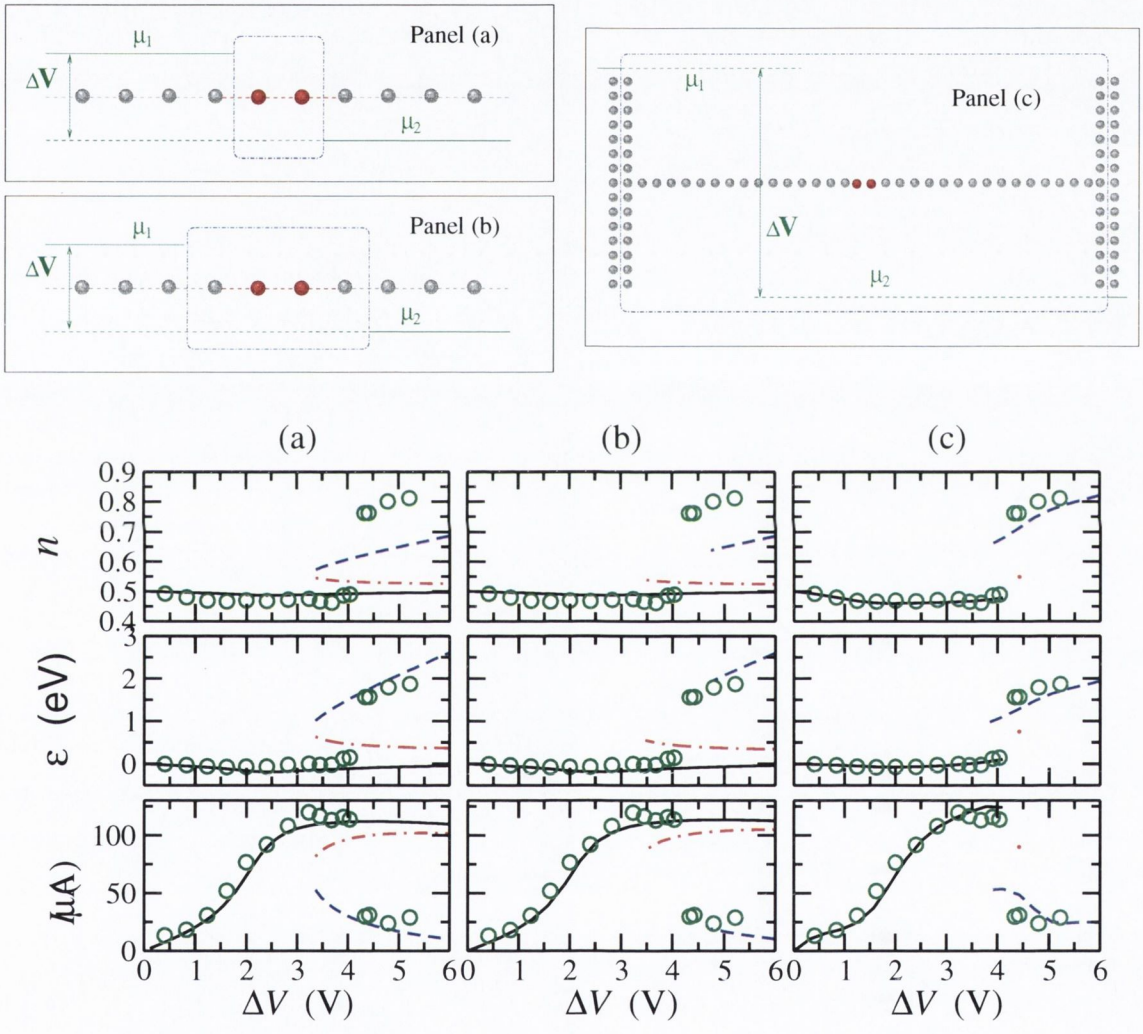

Figure 4.7: Top three panels: Cartoons of the systems considered in the other panels. In all panels the framed region is calculated self-consistently. The bottom triplets of graphs are organized as follows: spinless onsite occupancy (top panel) and onsite energy (middle panel) on dimer atom 1 (facing the electron current), together with the total current (bottom panel), as a function of bias. Lines are the different Landauer steady state solutions: (a) Semi-analytical solution, (b) self-consistent 1D solution with the parameters of the semi-analytical model, (c) full self-consistent solution with 2D electrodes and with the parameters of the time-dependent simulation (including intersite screening). Circles are solutions of the time-dependent calculation.

4.5 Understanding the source/drain equation of motion

We have seen that the extra Γ-term used in Eq. (4.3.2) helps to establish in real time a steady-state in the discharging capacitor. This effective damping term in the equation of motion for the one-electron density matrix, which we identify as a flux-driving source/drain term, is meant to provide an approximate description of the influence of the environment on the piece of the system being the focus of the investigation (the device, or in our case the dimer in the chain). In the following we discuss the physical interpretation of the Γ-term and the conditions upon which the approximation it represents is based on.

4.5.1 A heuristic derivation

We partition the system into a device (D) and an environmental (E) component. In this representation all matrices have the block form

$$\begin{pmatrix} \mathrm{DD} & \mathrm{DE} \\ \mathrm{ED} & \mathrm{EE} \end{pmatrix} . \tag{4.5.1}$$

Hence, starting from the Liouville equation for the propagation of the one-particle density matrix by a one-particle Hamiltonian,

$$\frac{\partial \hat{\rho}}{\partial t} - \frac{1}{i\hbar}\left[\hat{H}, \hat{\rho}\right] = 0 \tag{4.5.2}$$

we obtain an equation of motion for the density matrix ρ_{DD} of the device region

$$\frac{\partial \hat{\rho}_{DD}}{\partial t} - \frac{1}{i\hbar}\left[\hat{H}_{DD}, \hat{\rho}_{DD}\right] = \frac{1}{i\hbar}\left(\hat{H}_{DE}\hat{\rho}_{ED} - \hat{\rho}_{DE}\hat{H}_{ED}\right) , \tag{4.5.3}$$

where $\hat{\rho}_{DE} = \hat{\rho}^{\dagger}_{ED}$ ($\hat{H}_{DE} = \hat{H}^{\dagger}_{ED}$) is the part of the density matrix (Hamiltonian) which links the device to the environment. We see that the environment operates as a driving force on the device. Proceeding further, we choose a convention in which the matrix index α corresponds to the device region and β corresponds to the environment. Thus we obtain for the diagonal ($\alpha\alpha$) element (density at the site α of the device) of the right-hand side (RHS) of Eq. (4.5.3)

$$\{\mathrm{RHS}\}_{\alpha\alpha} = \frac{1}{i\hbar}\sum_{\beta}\left(H_{\alpha\beta}\rho_{\beta\alpha} - \rho_{\alpha\beta}H_{\beta\alpha}\right) = \frac{2}{\hbar}\sum_{\beta} H_{\alpha\beta}\mathrm{Im}\left[\rho_{\beta\alpha}\right] , \tag{4.5.4}$$

where we have assumed that the Hamiltonian is real. This equation gives the rate of charge injection into site α of the device from the environment. We consider a short-ranged Hamiltonian which can be factorized by an energy parameter $\hbar\Gamma$ as $H_{\alpha\beta} = \hbar\Gamma V_{\alpha\beta}$ for all α, β and $V_{\alpha\beta}$ is a dimensionless quantity carrying the angular dependencies of the hopping integrals. With this approximation Eq. (4.5.4) becomes

$$\{\mathrm{RHS}\}_{\alpha\alpha} = 2\Gamma\sum_{\beta} V_{\alpha\beta}\mathrm{Im}\left[\rho_{\beta\alpha}\right] . \tag{4.5.5}$$

When the system is in its initial state, $\hat{\rho}^0_{DD}$, i.e. at the moment when the statically-charged environment is brought in contact with the device, the left-hand side of Eq. (4.5.3) is zero by construction in the regions close to the interface. Since in this initial state there is no net current from the environment into the device (any such current needs time to develop), the RHS must also be zero. Therefore, any net flow of charge from the environment into the device must be a consequence of deviations of the device density matrix from its initial value. We can combine these observations into a single ansatz, namely,

$$\{\text{RHS}\} = \begin{cases} -\Gamma(\hat{\rho}_{DD} - \hat{\rho}^0_{DD}) & \text{near the interface} \\ 0 & \text{away from the interface} \end{cases} . \tag{4.5.6}$$

4.5.2 Relation to the Landauer formalism

In the following we seek a relation between the damped equation of motion (4.3.2) and the static Landauer picture, described in Chapter 2. We find that indeed the steady-state of Eq. (4.3.2) could coincide with the Landauer steady-state, if the latter is subject to certain conditions which we identify and acknowledge.

We start from the Landauer picture of a lead-device-lead system, carrying a steady state current. As this has been described in detail in Chapter 1, we assume known all the concepts introduced there and repeat here only the results, needed for the derivation. Let $\hat{H}$ be the Hamiltonian of the scattering region, composed of the device plus some finite section of each lead (longer than the electron screening length), then the Green's function (GF) [see Eq. (2.2.33)] for that region is

$$\hat{G}(E) \equiv \left[E\hat{I} - \hat{H} - \hat{\Sigma}(E)\right]^{-1} = \left[E\hat{I} - \hat{H}_{\text{eff}}(E)\right]^{-1} . \tag{4.5.7}$$

where $\hat{H}_{\text{eff}}(E) = \hat{H} + \hat{\Sigma}(E)$,

$$\hat{\Sigma}(E) = \hat{\Sigma}_L(E) + \hat{\Sigma}_R(E) = \hat{V}\hat{g}_L(E)\hat{V} + \hat{V}\hat{g}_R(E)\hat{V} . \tag{4.5.8}$$

Here $\hat{V}$ is the (real) Hamiltonian that couples the scattering region to the rest of the semi-infinite leads, and $\hat{g}_{L(R)}(E)$ is the surface GF of the left (right) lead, interfacing the scattering region.

The density matrix for the current-carrying system in the scattering region is [see Eq. (2.2.35)]

$$\hat{\rho} = \bar{\rho} + \Delta\hat{\rho} \tag{4.5.9}$$

where

$$\bar{\rho} = \int_{-\infty}^{0} \hat{D}(E)\,\mathrm{d}E = \frac{1}{2\pi}\int_{-\infty}^{0} \left[\hat{G}(E)\hat{\Gamma}_L(E)\hat{G}^\dagger(E) + \hat{G}(E)\hat{\Gamma}_R(E)\hat{G}^\dagger(E)\right]\mathrm{d}E \tag{4.5.10}$$

and

$$\Delta\hat{\rho} = \tfrac{1}{2\pi}\int_0^{eV/2} \underbrace{\hat{G}(E)\hat{\Gamma}_L(E)\hat{G}^\dagger(E)}_{D_L(E)}\,\mathrm{d}E - \tfrac{1}{2\pi}\int_{-eV/2}^{0} \underbrace{\hat{G}(E)\hat{\Gamma}_R(E)\hat{G}^\dagger(E)}_{D_R(E)}\,\mathrm{d}E\,. \tag{4.5.11}$$

Here, $\hat{\Gamma}_{L(R)} = i\left[\hat{\Sigma}_{L(R)} - \hat{\Sigma}^\dagger_{L(R)}\right] = -2\mathrm{Im}\left\{\hat{\Sigma}\right\}$ are the broadening matrices [see Eq. (2.2.21)],

$$\hat{D} = \frac{i}{2\pi}\left[\hat{G} - \hat{G}^\dagger\right] = \frac{1}{2\pi}\left(\hat{G}\hat{\Gamma}_L\hat{G}^\dagger + \hat{G}\hat{\Gamma}_R\hat{G}^\dagger\right) = \hat{D}_L + \hat{D}_R \tag{4.5.12}$$

is the local density of states [see Eqs. (2.2.9,2.2.10)] and we have assumed that $E_F = 0$ and $T = 0$.

We now consider

$$\begin{aligned} 2\pi\left[\hat{H}, \hat{D}_L\right] &= -\left[\hat{H}_{\mathrm{eff}} + \hat{\Sigma}, \hat{G}\hat{\Gamma}_L\hat{G}^\dagger\right] \\ &= -\hat{H}_{\mathrm{eff}}\hat{G}\hat{\Gamma}_L\hat{G}^\dagger + \hat{G}\hat{\Gamma}_L\hat{G}^\dagger\left(\hat{H}^\dagger_{\mathrm{eff}} - \hat{\Sigma} + \hat{\Sigma}^\dagger\right) - \hat{\Sigma}\hat{G}\hat{\Gamma}_L\hat{G}^\dagger + \hat{G}\hat{\Gamma}_L\hat{G}^\dagger\hat{\Sigma} \\ &= -\hat{\Gamma}_L\hat{G}^\dagger + \hat{G}\hat{\Gamma}_L - 2\pi\hat{\Sigma}\hat{D}_L + 2\pi\hat{D}_L\hat{\Sigma}^\dagger \end{aligned} \tag{4.5.13}$$

At this point we make our principal approximation. We approximate the action of the self-energy on GFs or density of state operators with a multiplication to a scalar and a projection. In other words if $\hat{q}$ is a GF or a density of states operator, we assume

$$\hat{\Sigma}_X\hat{q} = \gamma^*_X\hat{q}^{(X)}\,, \qquad \hat{\Sigma}^\dagger_X\hat{q} = \gamma_X\hat{q}^{(X)} \qquad \text{for} \qquad X = L, R\,, \tag{4.5.14}$$

which translates in terms of the broadening operator as

$$\hat{\Gamma}_L\hat{q} = 2\mathrm{Im}\left[\gamma_L\right]\hat{q}^{(L)}\,, \quad \hat{\Gamma}_R\hat{q} = 2\mathrm{Im}\left[\gamma_R\right]\hat{q}^{(R)} \tag{4.5.15}$$

where γ_X (for $X = L, R$) is an energy-independent scalar and $\hat{q}^{(X)}$ is the projection of $\hat{q}$ to the area where the lead "X" couples to the scattering region. This approximation physically describes a smearing of the atomistic structure and it neglects the energy dependence of the coupling to the reservoirs. Also assumed is a locality of the GF [1]. With the above approximation Eq. 4.5.13 becomes

$$\begin{aligned} \left[\hat{H}, \hat{D}_L\right] &= -\frac{1}{2\pi}\left(\hat{\Gamma}_L\hat{G}^\dagger - \hat{G}\hat{\Gamma}_L\right) - \hat{\Sigma}\hat{D}_L + \hat{D}_L\hat{\Sigma}^\dagger \\ &= -\frac{1}{\pi}\mathrm{Im}\left[\gamma_L\right]\left(\hat{G}^\dagger - \hat{G}\right)^{(L)} - (\gamma^*_L - \gamma_L)\hat{D}^{(L)}_L + (\gamma^*_R - \gamma_R)\hat{D}^{(R)}_L \\ &= -2i\,\mathrm{Im}\left[\gamma_L\right]\hat{D}^{(L)} + 2i\,\mathrm{Im}\left[\gamma_L\right]\hat{D}^{(L)}_L + 2i\,\mathrm{Im}\left[\gamma_R\right]\hat{D}^{(R)}_L \\ &= 2i\,\mathrm{Im}\left[\gamma_R\right]\hat{D}^{(R)}_L - 2i\,\mathrm{Im}\left[\gamma_L\right]\hat{D}^{(L)}_R\,, \end{aligned} \tag{4.5.16}$$

[1] This is not an extra restriction for the Landauer picture, in which all phase information is lost in the reservoirs. As long as there is a scattering mechanism in the semi-infinite leads with a small enough scattering time τ, it would translate itself into a self-energy $-i\hbar/2\tau$, shifting the poles of the GF away from the real axis by that amount. As a result the GF would be spatially localized on the scale $\sim v_F\tau$, where v_F is the Fermi velocity.

where we have used that $D^{(L)} = D_L^{(L)} + D_R^{(L)}$. We thus obtain

$$\frac{1}{i\hbar}\left[\hat{H}, \hat{D}_L\right] = \Gamma_R \hat{D}_L^{(R)} - \Gamma_L \hat{D}_R^{(L)} \tag{4.5.17}$$

$$\frac{1}{i\hbar}\left[\hat{H}, \hat{D}_R\right] = \Gamma_L \hat{D}_R^{(L)} - \Gamma_R \hat{D}_L^{(R)} \tag{4.5.18}$$

in which we have introduced two scalars Γ_L, Γ_R (without the hats, not to be confused with the broadening operators)

$$\Gamma_L \equiv \frac{2}{\hbar}\mathrm{Im}\left[\gamma_L\right] \qquad \text{and} \qquad \Gamma_R \equiv \frac{2}{\hbar}\mathrm{Im}\left[\gamma_R\right]. \tag{4.5.19}$$

Hence, in this approximation, from Eqs. (4.5.17, 4.5.18) it follows that

$$\frac{1}{i\hbar}\left[\hat{H}, \hat{D}\right] = \frac{1}{i\hbar}\left[\hat{H}, \hat{D}_L\right] + \frac{1}{i\hbar}\left[\hat{H}, \hat{D}_R\right] = 0 \qquad \Rightarrow \qquad \frac{1}{i\hbar}\left[\hat{H}, \bar{\rho}\right] = 0\,. \tag{4.5.20}$$

However, the commutator $\left[\hat{H}, \Delta\hat{\rho}\right]$ is non-zero

$$\begin{aligned}\frac{1}{i\hbar}\left[\hat{H}, \Delta\bar{\rho}\right] &= \int_0^{eV/2} \left[\hat{H}, \hat{D}_L(E)\right] \mathrm{d}E - \int_{-eV/2}^{0} \left[\hat{H}, \hat{D}_R(E)\right] \mathrm{d}E \\ &= -\Gamma_L \int_{-eV/2}^{eV/2} \hat{D}_R^{(L)}(E)\,\mathrm{d}E + \Gamma_R \int_{-eV/2}^{eV/2} \hat{D}_L^{(R)}(E)\,\mathrm{d}E \end{aligned} \tag{4.5.21}$$

At this point we make our final approximation. The integrals in Eq. (4.5.21) represent the non-equilibrium charge density on each of the interfaces to the leads, imposed by the presence of the other lead. We approximate

$$\int_{-eV/2}^{eV/2} \hat{D}_R^{(L)}(E)\,\mathrm{d}E \approx \hat{\rho}^{0(L)} - \bar{\rho}^{(L)} \tag{4.5.22}$$

$$\int_{-eV/2}^{eV/2} \hat{D}_L^{(R)}(E)\,\mathrm{d}E \approx -\left(\hat{\rho}^{0(R)} - \bar{\rho}^{(R)}\right), \tag{4.5.23}$$

where $\hat{\rho}^0$ is the initial, statically polarized, non-current-carrying density matrix in Eq. (4.3.2). In other words, we have found a Landauer steady-state which satisfies

$$0 = \frac{1}{i\hbar}\left[\hat{H}, \hat{\rho}\right] - \Gamma_L\left(\hat{\rho}^{0(L)} - \bar{\rho}^{(L)}\right) - \Gamma_R\left(\hat{\rho}^{0(R)} - \bar{\rho}^{(R)}\right), \tag{4.5.24}$$

which is also the steady-state solution of Eq. (4.3.2) with $\Gamma = \Gamma_L = \Gamma_R$. This is what we aimed to show. Thus in our finite time-dependent driven transport the Γ-terms are applied at the "open"-boundaries of the system. A sensible value for Γ, in accordance with the above Landauer picture interpretation [see Eq. (4.5.19)], would be

$$\Gamma \sim 2\pi\beta^2 d/\hbar\,, \tag{4.5.25}$$

where β is the system-environment hopping integral and d is a surface LDOS per atom. This estimation produces the same order of magnitude Γ as the ones used in Section 4.3.

4.6 Summary and discussion

In this Chapter we have looked at a time-dependent treatment of the quantum transport problem in a finite system at the atomistic level. Instead of taking a huge capacitor to discharge as suggested in Ref. [124] as a prescription for swapping the Landauer system for a finite one, we have introduced a source/drain damping terms to maintain the charge imbalance of the capacitor and been able to achieve a steady state. We have demonstrated analytically that such approach could in fact lead to the correct steady-state of a slightly modified Landauer problem in which the connection to the reservoirs has no atomistic properties and no energy dependence. For the particular system of a loosely coupled dimer in a monoatomic chain with enforced local-charge neutrality, where the static approach results in a multiple steady-states, the TD calculation is able to self-select the most stable solution. This goes beyond the capabilities of the static methods, which in the absence of a total energy criterion, say little about the relative stability of multiple solutions.

We underline that the aim of this Chapter has not been to find a rigorous TD description of the open-boundary system. One such description must unavoidably go beyond the ALDA platform and we mention two such methods, namely, the TDDFT-NEGF and the Master-equation approach [59]. We have also not aimed at correctly describing the weakly coupled dimer which is a particularly treacherous system for LDA-based potentials (lacking of the derivative discontinuity of the density functional) [113]. All we wanted to show is that for the same conditions (the same base electronic structure model), the time-dependent method is the one to recognise the physically feasible solution.

Chapter 5

Atomistic spin dynamics - theory and tests

5.1 Introduction

With the progress of nanomagnetism, constantly fuelled by the industrial demand for increasing magnetic storage density, nanoscale and even monoatomic one-dimensional [40] magnetic devices have become experimentally accessible and examples of atomic scale magnetic phenomena, such as transport in magnetic point contacts [125] and ultra-thin domain walls [78], have been already demonstrated. Theory and modeling of current-induced magnetic phenomena is still, however, largely based on solving the classical Landau-Lifshitz-Gilbert (LLG) equation [42] with additional terms describing the current-induced torques. At a more advanced level transport theory for diffusive transport has been introduced into the description, effectively creating a sort of Kirchkoff magneto-circuitry theory [24]. A much less explored area is that of atomistic simulations of magneto-dynamics. These however are expected to occupy an increasingly important place in theoretical magnetism with the advance in the ability to manipulate devices at the atomic length and time-scales.

This chapter is devoted to presenting a truly atomistic time-dependent theory for spin-dynamics. The *s-d* tight-binding model including electrostatic corrections at the Hartree level will be our underlining electronic structure theory and we shall be focussing on introducing the main theoretical concepts behind our approach. As an illustration, we shall provide a range of examples where such scheme offers insights beyond what is achievable by standard static theory. These include the investigation of the spin-wave dispersion in nanoscale magnets and spin-spin correlation in non-magnetic nano-wires. The next chapter will address the application of the approach, presented

here, to investigate current-induced domain wall motion and distortion, and the generation of an electromotive force obtained by domain wall precession.

5.2 Model Hamiltonian

Throughout this chapter we shall always consider one-dimensional (1D) magnetic atomic wires and we will describe their electronic structure by means of the *s-d* model [133], where conduction electrons (s) are exchange-coupled to a number of classical spin $\mathbf{S}_i$ (d). When written in a tight-binding form, the electronic Hamiltonian reads

$$\hat{H}_e(t) = \sum_{i,j,\alpha} H_{ij}^{\mathrm{TB}} c_i^{\alpha\dagger} c_j^{\alpha} - \sum_{i,\alpha,\beta} c_i^{\alpha\dagger} \hat{\boldsymbol{\sigma}}_{\alpha\beta} c_i^{\beta} \cdot \boldsymbol{\Phi}_i(t)\,, \tag{5.2.1}$$

where $c_i^{\alpha\dagger}$ (c_i^{α}) is the creation (annihilation) operator for an electron with spin $\pm 1/2$ ($\alpha = 1, 2$) at the atomic site i and $\hat{\boldsymbol{\sigma}} = 1/2(\tilde{\sigma}^x, \tilde{\sigma}^y, \tilde{\sigma}^z)$ is the electron spin operator, $\{\tilde{\sigma}^n\}$ being the set of Pauli matrices [1].

The first term in Eq. (5.2.1) is the spin- and time-independent tight-binding (TB) part, while the second describes the spin interaction with a time-dependent effective local field $\boldsymbol{\Phi}_i(t)$,

$$H_{ij}^{\mathrm{TB}} = \left(\mathcal{E}_0 + \sum_n \frac{\kappa \Delta q_n}{\sqrt{R_{in}^2 + (\kappa/U)^2}} \right) \delta_{ij} + \chi \delta_{i,j\pm 1} \tag{5.2.2}$$

$$\boldsymbol{\Phi}_i(t) = J\mathbf{S}_i(t) + g_e \mu_B \mathbf{B}(t)\,. \tag{5.2.3}$$

Here $\mathcal{E}_0$ is the onsite energy (identical for all sites), $\kappa = e^2/4\pi\varepsilon_0 = 14.4\,\mathrm{eV\,\AA}$ (or $\kappa = 0$ for describing non-interacting electrons), χ is the hopping parameter, g_e is the electron g-factor and $\mathbf{B}(t)$ is the external magnetic field (in general time-dependent). The second term in brackets in Eq. (5.2.2) is a mean-field repulsive electrostatic potential with onsite strength U and a Coulombic decay at large intersite distances R_{ij}. Finally $\Delta q_i = q_i - q_i^{(0)}$ is the excess number of electrons on site i, $q_i^{(0)}$ being the ground state electron density distribution. The total number of electrons N_e in the system is a model parameter

$$N_e = \sum_i q_i^{(0)} = N\rho_0 \tag{5.2.4}$$

where N is the total number of sites and ρ_0 the band-filling, i.e. the average number of electrons per site.

[1] For a right-handed coordinate system (for which $\mathbf{e}^x \times \mathbf{e}^y = \mathbf{e}^z$ is fulfilled for the basis vectors), the basis of the Pauli matrix representation reads

$$\tilde{\sigma}^x = \begin{pmatrix} 0 & 1 \\ 1 & 0 \end{pmatrix}, \qquad \tilde{\sigma}^y = \begin{pmatrix} 0 & -i \\ i & 0 \end{pmatrix}, \qquad \tilde{\sigma}^z = \begin{pmatrix} 1 & 0 \\ 0 & -1 \end{pmatrix}.$$

In Eq. (5.2.3) $\mathbf{S}_i(t)$ is the unit vector in the direction of the local spin at site i at time t. $\{\mathbf{S}_i\}$ are treated as classical variables, nonetheless exchange-coupled with strength $J > 0$ to the conduction electrons according to a classical Hamiltonian

$$H_S(t) = -\sum_i \mathbf{S}_i(t) \cdot \mathbf{\Theta}_i(t) - \frac{1}{2} J_S \sum_{i,j \in \mathrm{nn}[i]} \mathbf{S}_i(t) \cdot \mathbf{S}_j(t) - J_z \sum_i \left(\mathbf{S}_i(t) \cdot \hat{\mathbf{z}}\right)^2 , \tag{5.2.5}$$

where

$$\mathbf{\Theta}_i(t) \equiv J \left\langle \hat{\boldsymbol{\sigma}} \right\rangle_i (t) + \frac{g_S \mu_B}{\hbar} S \mathbf{B}(t) \tag{5.2.6}$$

is the effective field for the classical spins, analogous to $\mathbf{\Phi}_i$. In Eq. (5.2.5) g_S is the g-factor of $\mathbf{S}_i$ which could be of mixed spin and orbital origin, J_S is the direct intersite exchange coupling parameter (only first nearest neighbours, nn$[i]$, are considered), $\hat{\mathbf{z}}$ ($|\hat{\mathbf{z}}| = 1$) is the unit vector and J_z the anisotropy constant along the easy z-axis. Note that the actual norm S of the classical spins is incorporated in the definition of the exchange parameters. Unless stated otherwise, we consider $S = \hbar$. Appearing in Eq. (5.2.6) is also the expectation value of the electron spin at site i, $\left\langle \hat{\boldsymbol{\sigma}} \right\rangle_i (t) = \mathrm{Tr}\left[\rho_{ii}(t)\boldsymbol{\sigma}\right]$, where $\rho_{ii} = \langle i | \hat{\rho} | i \rangle$ is the i-th diagonal element of the density matrix $\hat{\rho}$ in the real-space orthonormal basis $\{|i\rangle\}$ (in a tight-binding fashion, $|i\rangle$ represents one electron s-orbital at site i) and the trace is over the spin coordinates. At $t = 0$ the density matrix is constructed as

$$\hat{\rho}(0) = \sum_n f_F(\epsilon_n - E_F) \, |n\rangle \langle n| \tag{5.2.7}$$

where $\{\epsilon_n, |n\rangle\}$ is the set of eigenvalues and eigenvectors of $\hat{H}_e(t = 0)$, f_F is the Fermi distribution and the Fermi level E_F is determined, so that $\sum_i \rho_{ii} = \sum_i \langle i | \hat{\rho} | i \rangle = N_e$. In the case of interacting electrons [$\kappa \neq 0$ in Eq. (5.2.3)] $\hat{H}_e(t = 0, \hat{\rho})$ is determined self-consistently.

The corresponding quantum and classical Liouville equations of motion for the two subsystems are

$$\frac{\mathrm{d}\hat{\rho}}{\mathrm{d}t} = \frac{i}{\hbar} \left[\hat{\rho}, \hat{H}_e\right] , \qquad \frac{\mathrm{d}\mathbf{S}_i}{\mathrm{d}t} = \{\mathbf{S}_i, H_S\} , \tag{5.2.8}$$

where $\{\ ,\ \}$ represents the classical Poisson bracket and $[\ ,\ ]$ the quantum mechanical commutator. In order to calculate the right-hand side of the classical Liouville equation we need the expression for the Poisson bracket of the classical spins. As the classical spins are essentially angular momenta they obey the same relation [1] as do the classical angular momenta [132], i.e.

$$\{S_i^n, S_i^m\} = \frac{1}{S} \varepsilon^{nmk} S_i^k , \tag{5.2.9}$$

[1] The Poisson bracket of two components of an angular momentum is $\left\{L^i, L^j\right\} = \left\{\varepsilon^{iab} x^a p^b, \varepsilon^{jcd} x^c p^d\right\} = \varepsilon^{iab}\varepsilon^{jca}\left(x^c p^b - x^b p^c\right) = x^i p^j - x^j p^i = \varepsilon^{ijk} L^k$, where we have used the Einstein notation for repeated indices, the Levi-Civita tensor contraction identity $\varepsilon^{iab}\varepsilon^{icd} = \delta^{ac}\delta^{bd} - \delta^{ad}\delta^{bc}$ and the canonical variables Poisson brackets $\left\{x^i, p^j\right\} = \delta^{ij}$. Note that upper indices for Cartesian components (here and throughout this chapter) are only used for aesthetic reasons as lower indices have already been used for designating site positions.

where $S_i^n = \mathbf{S}_i \cdot \hat{\mathbf{e}}^n$ is the n-th Cartesian projection ($\{\hat{\mathbf{e}}^n\}_{n=1}^3 \equiv \{\hat{\mathbf{x}}, \hat{\mathbf{y}}, \hat{\mathbf{z}}\}$) of the spin on site i, ε^{nmk} is the Levi-Civita tensor and we assume summation over repeated indices (Einstein notation). Note that in Eq. (5.2.9) we have factorized the spin magnitude S in order to obtain an expression involving only components of the dimensionless spin unit-vector $\mathbf{S}_i$. We thus obtain the following terms in the classical equation of motion

$$\{\mathbf{S}_i, \mathbf{S}_j \cdot \boldsymbol{\Theta}_j\}^n = \{S_i^n, S_i^m\}\,\Theta_i^m = \frac{1}{S}\varepsilon^{nmk} S_i^k \Theta_i^m = -\frac{1}{S}\left(\mathbf{S}_i \times \boldsymbol{\Theta}_i\right)^n \tag{5.2.10}$$

$$\sum_j \left\{ \mathbf{S}_i, \mathbf{S}_j \cdot \sum_{k \in \mathrm{nn}[j]} \mathbf{S}_k \right\}^n = \frac{2}{S} \sum_{k \in \mathrm{nn}[i]} \{S_i^n, S_i^m\}\, S_k^m = -\frac{2}{S} \sum_{k \in \mathrm{nn}[i]} \left(\mathbf{S}_i \times \mathbf{S}_k\right)^n \tag{5.2.11}$$

$$\sum_j \left\{ \mathbf{S}_i, \left(\mathbf{S}_j \cdot \hat{\mathbf{z}}\right)^2 \right\}^n = \frac{2}{S} S_i^m z^m z^k \left\{S_i^n, S_i^k\right\} = \frac{2}{S} S_i^m z^m z^k \varepsilon^{nkl} S_i^l = -\frac{2}{S}\left(\mathbf{S}_i \cdot \hat{\mathbf{z}}\right)\left(\mathbf{S}_i \times \hat{\mathbf{z}}\right)^n . \tag{5.2.12}$$

Hence we finally obtain the following equation of motion for the classical spin at site i

$$\frac{\mathrm{d}\mathbf{S}_i}{\mathrm{d}t} = \frac{1}{S}\left(\mathbf{S}_i \times \boldsymbol{\Theta}_i + J_S \sum_{j \in \mathrm{nn}[i]} \mathbf{S}_i \times \mathbf{S}_j + 2J_z \left(\mathbf{S}_i \cdot \hat{\mathbf{z}}\right)\left(\mathbf{S}_i \times \hat{\mathbf{z}}\right) \right) . \tag{5.2.13}$$

The above equations for all classical spins in the system are integrated together with the quantum Liouville equation (5.2.8) for the conduction electrons to give the combined quantum-classical time evolution of the s-d system.

5.3 Test simulations

5.3.1 Spin-wave dispersion in a s-d monoatomic chain

Molecular dynamics (MD) simulations, based on empirical tight binding model and realistic interatomic potentials, provide a valuable tool for accessing the vibrational properties of condensed matter systems, especially in situations where temperature and pressure related effects are investigated [127, 55]. Phonon dispersion and density of states are calculated from the Fourier transform of the velocity-velocity correlation function, resulting from MD simulation [28]. The phonon spectral intensity [127] is simply

$$\mathcal{I}(\mathbf{k}, \omega) \sim \int \mathrm{d}t e^{i\omega t} \sum_n e^{-i\mathbf{k}\cdot\mathbf{R}_n(t)} \left| \frac{\mathbf{v}_n(t) \cdot \mathbf{v}_0(0)}{\mathbf{v}_n(0) \cdot \mathbf{v}_0(0)} \right| , \tag{5.3.1}$$

where $\mathbf{k}$ and ω are the wave vector and the frequency of the phonon, $\mathbf{R}_n(t)$ and $\mathbf{v}_n(t)$ are the position and velocity of the n-th atom at time t. Similar schemes are often used in the framework of time-dependent density functional theory [28] for calculating optical excitation of molecules.

We extend this idea to calculating the spin wave (*magnon*[1]) spectra in our *s-d* spin systems, which, within the nearest-neighbour direct exchange approximation, are the spin analogue to the discrete harmonic chain. Similarly, our approach is based on the time evolution of the local spins as described in the previous section. Let us briefly introduce the spin wave approximation in a Heisenberg exchange-coupled ferromagnet by following Ashcroft and Mermin [8]. If $|0\rangle$ is the ground state of the spin system, where all spins are aligned along the same direction [say z, Fig. 5.1], then the most elementary spin excitation corresponds to the state $|n\rangle \equiv |S_n^z - 1\rangle = \frac{1}{\sqrt{2S}}\mathbf{S}_n^- |0\rangle$ (normalized to unity, i.e. $\langle n|n\rangle = 1$). Here $\mathbf{S}_n^- \equiv \mathbf{S}_n^x - i\mathbf{S}_n^y$ is the lowering of the spin ladder operators acting on the n-th site [8]

$$\mathbf{S}_n^{\pm} |S_n^z\rangle = (\mathbf{S}_n^x \pm i\mathbf{S}_n^y) |S_n^z\rangle = \sqrt{(S \mp S_n^z)(S + 1 \pm S_n^z)}\, |S_n^z \pm 1\rangle \tag{5.3.2}$$

which reduces the S^z spin component at n from S to $S-1$. This state is, however, not an eigenstate of the Heisenberg Hamiltonian

$$\mathcal{H}_H = \sum_{n,m} J_S(\mathbf{R}_n - \mathbf{R}_m)\mathbf{S}_n \cdot \mathbf{S}_m \,. \tag{5.3.3}$$

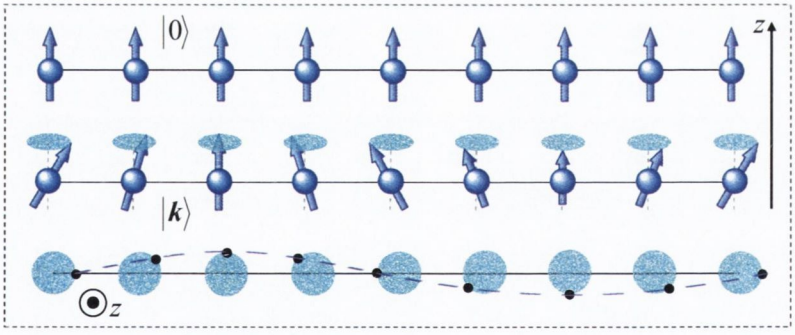

Figure 5.1: Schematic representation of the ground state, $|0\rangle$, and an excited spin-wave state, $|\mathbf{k}\rangle$, of a Heisenberg exchange-coupled monoatomic spin chain.

With the help of the following relation for the spin operators acting on the elementary excitation $|n\rangle$

$$\mathbf{S}_m^- \mathbf{S}_n^+ |n\rangle = 2S\,|m\rangle \qquad \text{and} \qquad \mathbf{S}_m^z |n\rangle = \begin{cases} S\,|n\rangle \,, & n \neq m \\ (S-1)\,|n\rangle \,, & n = m \end{cases} \tag{5.3.4}$$

and the fact that $\mathbf{S}_n \cdot \mathbf{S}_m = \frac{1}{2}(\mathbf{S}_n^+ \mathbf{S}_m^- + \mathbf{S}_n^- \mathbf{S}_m^+) + \mathbf{S}_n^z \mathbf{S}_m^z$ we can express the action of the Heisenberg Hamiltonian (5.3.3) on the $|n\rangle$ state as

$$\mathcal{H}_H |n\rangle = E_0 |n\rangle + 2S \sum_m J_S(\mathbf{R}_n - \mathbf{R}_m)\,[|n\rangle - |m\rangle] \,, \tag{5.3.5}$$

[1] Magnons are the bosonic quasi-particles corresponding to the spin waves.

where $E_0 = -\sum_{n,m} J_S(\mathbf{R}_n - \mathbf{R}_m)S^2$ is the ground state energy (no spin-excitations) and the terms of the order of S^0 are neglected as the spin wave approximation assumes $S \gg 1$ (in the classical analogue that would correspond to small misalignments). Thus $\mathcal{H}_H |n\rangle$ is a linear combination of states $|n\rangle$. Because of the translational invariance of J a Bloch wave

$$|\mathbf{k}\rangle = \frac{1}{\sqrt{N}} \sum_n e^{i\mathbf{k}\cdot\mathbf{R}_n} |n\rangle \ , \tag{5.3.6}$$

where N is the number of sites in the system, is an eigenstate of $\mathcal{H}_H$ with an eigenvalue $E_k = \langle \mathbf{k} | \mathcal{H}_H | \mathbf{k} \rangle$ corresponding to an excitation energy

$$\mathcal{E}(\mathbf{k}) = E_k - E_0 = 4S \sum_n J_S(R_n) \sin^2 \left(\frac{1}{2} \mathbf{k} \cdot \mathbf{R}_n \right) . \tag{5.3.7}$$

This represents the magnon dispersion relation for a finite Heisenberg spin chain. If only nearest-neighbour exchange interaction is considered, i.e. $J_S(\mathbf{R}) = J_S \neq 0$ only for $|\mathbf{R}| = a$, then Eq. (5.3.7) reduces to the familiar expression

$$\mathcal{E}(k) = 4SJ_S \sin^2 \left(\frac{ka}{2} \right) , \tag{5.3.8}$$

where $k = |\mathbf{k}|$. As a test of our time-dependent scheme we will reproduce this result with time-dependent dynamics by using the *s-d* model and setting the exchange coupling $J = 0$.

We consider a uniformly polarized (ferromagnetic) mono-atomic chain with N sites, in which at $t = 0$ the spin at site i_0 is tilted to a finite angle (e.g. $\phi_0 = \pi/6$) with respect to the rest of the spins, i.e. at $t = 0$ the ferromagnetic chain is subjected to a spin excitation. We then integrate numerically the time-evolution of this system, described by Eq. (5.2.8), to obtain a two-dimensional array of values for each local spin Cartesian component as a function of position and time (see Fig. 5.2) for a sequence of N_T discrete timesteps $\{t_j\}_{j=1}^{N_T} : \mathbf{S}_i(t_j) \rightarrow \mathbf{S}_{ij}$. These arrays undergo a two-dimensional discrete Fourier transformation (dFT), resulting in an approximation of the system response spectrum in the (k, E)-domain. Out of the three orthogonal local spin components, S^x and/or S^y are more useful when transformed, since in the common limit of small excitations [small angles like in the conventional ferro-magnetic resonance (FMR)] the major spin component $S^z \approx const$ and the variation is strictly transverse. Only one of the transverse components is normally sufficient, as the dominant precessional motion of the local spins implies a definite phase relation between the two, while the major one is insensitive to the precession phase. As an example, the dFT (as implemented in the mathematical software environment *Maple*^{TM} *10* [1]) of S^y_{ij} yields the reciprocal image

$$\mathrm{dFT}\left[S^y\right]_{l,m} = \frac{1}{\sqrt{NN_T}} \sum_{i=1}^{N} \sum_{j=1}^{N_T} S^y_{ij} e^{-\frac{2\pi i}{N}(i-1)(l-1)} e^{-\frac{2\pi i}{N_T}(j-1)(m-1)} S^y_{ij}, \tag{5.3.9}$$

where $l \in [1, N]$ and $m \in [1, N_T]$. This array is then mapped into the (k, E)-space by the change of variables $l \to k = \frac{(l-1)\pi}{(N_{\frac{1}{2}}-1)a}$ for $1 \leq l \leq N_{\frac{1}{2}}$ and $l \to k = -\frac{(l-N_{\frac{1}{2}}+1)\pi}{(N_{\frac{1}{2}}-1)a}$ for $l > N_{\frac{1}{2}}$ where $N_{\frac{1}{2}} \equiv \lceil N/2 \rceil$ is the nearest integer greater than $N/2$, and similarly $m \to E = \frac{(m-1)\pi\hbar}{T_{\max}}$ for $E > 0$, where $T_{\max} = t_{N_T}$ is the total time of the simulation and $N_T \sim 10^5 \gg N$ (so that we have neglected corrections of the order of 1 in the denominator of the right-hand side). Thus obtained, the (k, E)-space portrait of $S_i^y(t)$ (Fig. 5.2) exhibits a preferential and almost uniform population of modes obeying the correct dispersion relation, given by Eq. (5.3.8).

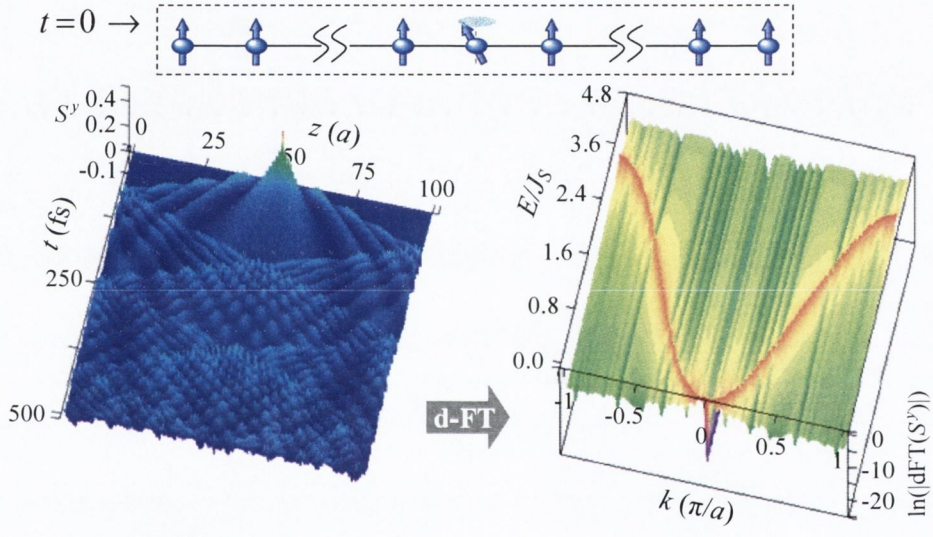

Figure 5.2: Example of how to extract the spin-wave dispersion from a time-dependent spin dynamics simulation: $J = 0$, $J_z = 0$, $N = 101$. On the left-hand side we present the time and space evolution of S_i^y along the chain ($i \equiv z/a$), with the grey-scale shade representing the magnitude of the $S_i^y(t)$. Note that the spin-excitation is emitted from one initially tilted spin at $i_0 = 51$ and then propagates from it and is reflected from the boundaries, forming a complex interference pattern. On the right-hand side panel we present the natural logarithm (for better contrast) of the absolute value of $\mathrm{dFT}\,[S^y]\,(k, E)$ as described by Eq. (5.3.9) and mapped into the (k, E)-space. The brighter the region, the higher is the intensity.

This calculation of a Heisenberg spin-chain serves as an example of the applicability of the time-dependent spin-dynamics simulation, defined by Eqs. (5.2.8) and (5.2.13), in extracting the magnon spectrum for atomistic structures. We note that the form of the initial spin excitation is of crucial importance for this method to work and to produce a full portrait of the magnon dispersions in the reciprocal space. The excitation should contain enough energy to populate all the available spin-modes and should not bear restricting spatial symmetries. We now demonstrate

how an initial excitation with a certain spatial symmetry produces incomplete reciprocal-space portraits, i.e. it is unable to populate same regions of the spin-wave spectrum. For the following spin-dynamics simulations we use parameter values $J_S = 0.2\,\mathrm{eV}$, $J_z = 0$, $0 \leq J \leq 3\,\mathrm{eV}$. The hopping parameter is $\chi = 1\,\mathrm{eV}$ and the band-filling is $\rho_0 = 1.75$. [1]

Similarly to vibrational modes, the natural spin-wave modes of a one-dimensional system can be visualized as standing waves in a suspended wire. For a N-atom wire of length $L = (N-1)a$ the natural modes have wavelengths λ_n with an integer n such that $n\lambda_n/2 = L$. Hence their wave vectors are

$$k_n = \frac{2\pi}{\lambda_n} = \frac{n\pi}{L} = \frac{n\pi}{(N-1)a} \quad \text{for} \quad n = 0, 1, \ldots, N-1\,. \tag{5.3.10}$$

This accounts for $N-2$ nontrivial modes as the $n = 0$ mode represents the fully aligned chain (not necessarily along z) and $n = N-1$ is the trivial spin-wave with one node at each site. Note that this mode labeling is valid for both fixed-fixed and loose-loose boundary conditions for the wire (corresponding to nodes or anti-nodes at both ends), the latter being the case of our spin-chain simulations.

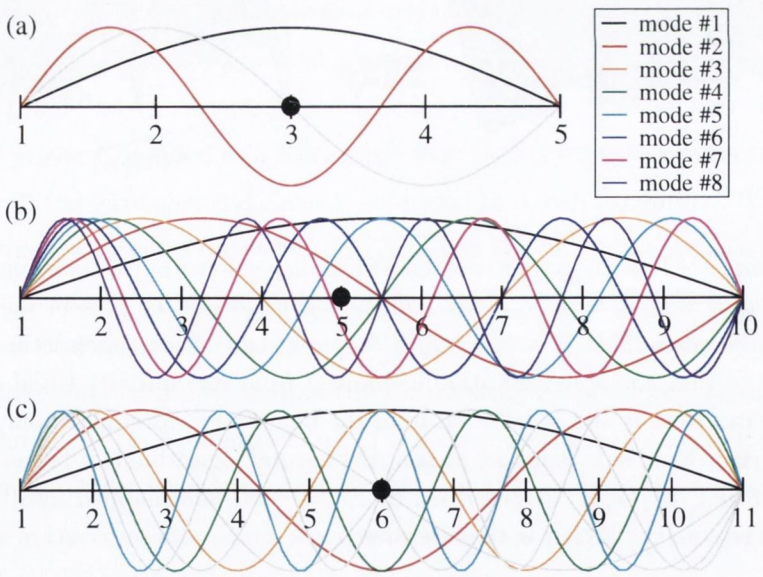

Figure 5.3: Standing wave modes in chains of 5, 10 and 11 sites. The black circle represents the site where the excitation is applied. The modes plotted in grey (solid lines) cannot be excited because they have a node at the exciting site.

[1] These values mimic a half-metallic electronic structure (for the chains with more than 20 atoms and $J \gtrsim 1\,\mathrm{eV}$) with a Fermi level $\gtrsim 0.5\,\mathrm{eV}$ above the fully occupied spin-up band and a spin polarization $|P(E_F)| = 1$. This promotes the highest attainable spin signal and it has been particularly chosen for simulations of current-driven DW motion (see section 6.1.2) where the pressure produced by the current scales linearly with P.

If the initial excitation is in the form of a spin tilt at one or more atomic sites, there are two reasons for which certain modes cannot be excited. Firstly they may have nodes at those particular sites, where the excitation is applied. Secondly they may not comply with the spatial symmetry inherent to the excitation. Particularly, if the $t = 0$ spin excitation is applied only to the middle site of a chain with an odd number of sites then nearly half the spin modes cannot be excited as they have a node at that site. In this situation only $N_M = \lfloor N/2 \rfloor$ modes are excited [see Fig. 5.3, where $N_M = 2$ for $N = 5$ in (a) and $N_M = 5$ for $N = 11$ in (c)]. If there are no nodes at the site of the excitation, all $N_M = N - 2$ modes can in principle be excited [Fig. 5.3(b)].

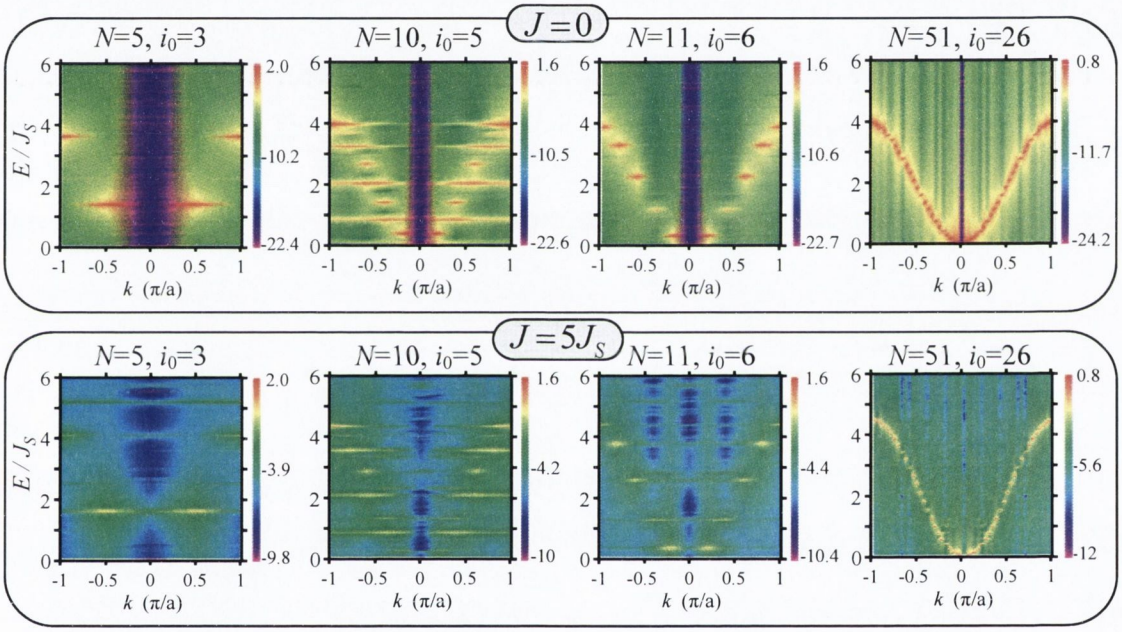

Figure 5.4: Calculated magnon spectra for several short Heisenberg spin-hains either decoupled ($J = 0$, upper panels) or exchange-coupled to the electron gas ($J = 1\,\mathrm{eV}$, lower panels). The grey scale bar to the right of each contour plot corresponds to the value of $\ln|\mathrm{dFT}[S_i^y(t)]|$. From left to right panels $N = 5, 10, 11, 51$ and the location of the $t = 0$ excitation is $i_0 = 3, 5, 6, 26$, respectively.

These considerations are verified by the calculations presented in Fig. 5.4. Here the number of excited spin modes (bright spots) for $k > 0$ (and identically for $k < 0$ due to the time-reversal symmetry), subsequent to the applied excitation, agrees with the scheme pictured in Fig. 5.3. The top panels of Fig. 5.4 represent classical Heisenberg chains non-interacting with the conducting electrons ($J = 0$), while in the bottom panels the exchange interaction with the conduction electrons is switched on ($J = 1\,\mathrm{eV}$) to yield our full *s-d* model. As a result of the *s-d* interaction, the energy and the intensity of the excited magnons are somewhat altered. We observe a shift in the

energies and some level-splitting but the overall spectral pattern remains the same (especially for the longer chains). One eye-catching difference is the less pronounced dark stripe at $k = 0$, corresponding to zero signal in the logarithmic scale. Despite the appearance, the offset that electrons produce at $k = 0$ is actually very small ($\approx 10^{-5}$ of the bright spots intensity).

The most significant effect of the *s-d* exchange, which is independent of the particular type of excitation, is an energy blue shift by as much as 10% in the short-wavelength range. From simulations for 51-atom chain, where the dispersion is close to continuous, we can clearly extract a magnon dispersion relation $\propto \sin^2(ka/2)$. This maps onto a standard Heisenberg chain with an effective interatomic exchange coupling which is about 10% greater than the actual J_S. Hence, for this particular choice of parameters, the interaction with the conduction electrons effectively adds an extra positive contribution to the ferromagnetic spin-spin interaction, making it stronger.

In order to further investigate the interplay of the coupled dynamics of the electronic and local-spin subsystems we look at the time evolution of a longer spin chain ($N = 101$) after a transverse spin excitation at the $i_0 = 51$ site for different values *s-d* exchange constant J. The gray-scale plots of the $\ln|\mathrm{dFT}[\,]|$ of both $S_i^y(t)$ and $\sigma_i^y(t)$, the latter defined as

$$\sigma_i^y(t) \equiv \langle \hat{\sigma}^y \rangle_i (t) = \sum_{\alpha,\beta} \frac{1}{2} \{\tilde{\sigma}^y\}^{\alpha\beta} \rho_{ii}^{\beta\alpha}(t) \tag{5.3.11}$$

(with $\tilde{\sigma}^y$ designating the second Pauli matrix), for 500 fs simulations are presented on Fig. 5.5 for three particular values of J. For the given band-filling $\rho_0 = 1.75$, these correspond to Fermi levels lying (a) inside both y-spin polarized bands (for $J = 0.05\,\mathrm{eV}$); (b) at the edge of the y-spin-up band and inside the y-spin-down (for $J = 0.5\,\mathrm{eV}$) and (c) inside the y-spin-down band, while the up band is fully filled (for $J = 10\,\mathrm{eV}$).

For all three regimes the Fourier transforms of the local spins are relatively featureless – they all show the typical $4J_S^{\mathrm{eff}} \sin^2(ka/2)$ band with an effective direct exchange J_S^{eff} which increases when J gets bigger (Fig. 5.5, second row of panels). Interestingly, only the (b)-case (where the Fermi level is very close to the spin-up band-edge) shows some deviations from the classical dispersion [see Fig. 5.6 (a,b)], while the case of very big J is again very close to the classical. The latter is attributed to the increased spin-up localization for large J, where the electrons from the fully-filled band are so deeply bound that they behave as a classical complement to the local spin.

It is also interesting to look at the evolution of the electron (s) spins. The three spectra of the electronic transverse-spin density $\sigma_i^y(t)$ ($\equiv \sigma^y(z_i, t)$) also show the very same magnon band from their corresponding local-spin spectra. Here, however, this band shows an increasing intensity with J. The presence of the classical spin-wave band in the electronic spectra is interpreted as a parametric excitation – as the electrons tend to align to the local spins, they reproduce the local

transverse-spin spacial distribution at any instant of time. In the adiabatic limit (large J) the electrons are nearly in their ground state for each local spin arrangement and indeed for these cases we observe an increase of the intensity of the local-spin band.

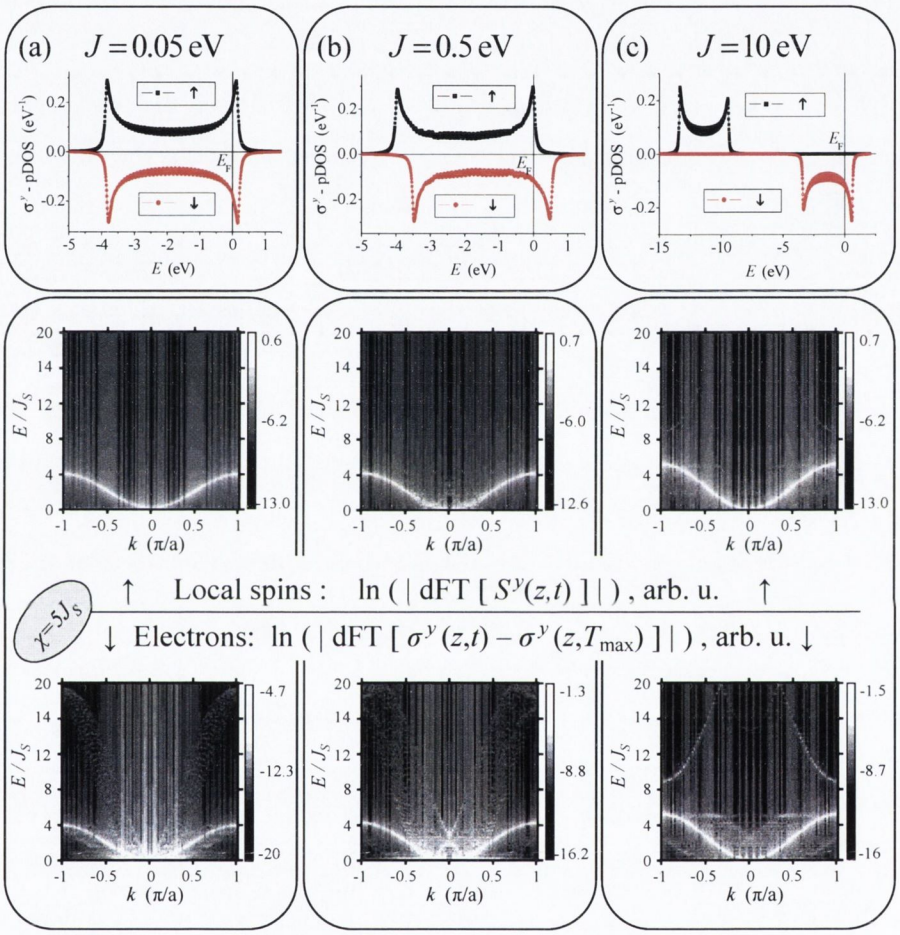

Figure 5.5: Spin-wave spectra in a 101-atom spin-chain for three values of the s-d exchange strength $J = 0.05, 0.5, 10\,\mathrm{eV}$ (columns from left to right). Top panels illustrate the y spin-polarized DOS at $t = 0$ when the spin on site $i_0 = 51$ is tilted to $\pi/6$ in the $y - z$ plane. Middle panels represent the classical spin waves spectra and the bottom ones are for the electrons. Here $J_S = 0.2\,\mathrm{eV}$.

Another recognizable (though with very low intensity) feature in the electronic spectra is the shade of a 4χ ($= 20J_S$ in our parameterization) wide band in the two lower J cases. This is apparently the signature of the nearest-neighbor tight binding dispersion $\mathcal{E}(k) \propto 2\chi\cos(ka)$, with $\chi = 1\,\mathrm{eV}$ being the hopping parameter. This structure in the electron spin-density spectrum is very diffuse and it looks like a superposition of bands for the different local spin configurations. This is supported by the fact that its actual spread increases as J becomes larger. However, for

J in the half-metallic regime (fully filled up-band) the purely electronic excitations are suppressed due to the enhanced localization of the spin-up electrons. The actual magnon spectrum is still very similar in shape to the Heisenberg one ($J = 0$) and fits rather well to the expression given in Eq. (5.3.7) with an enhanced effective direct exchange [1]. In this regime we also observe a second band [2] similar to the optical phonon bands [3].

It is worth noting here that whatever signal is seen in the electron reciprocal-space portrait, this is due to excitations originating from the local spin subsystem as it is the only one excited at $t = 0$. This means that the local spins can exchange energy with the electron bath. In the next section we will prove that the energy can also be exchanged in the other direction, i.e. that our classical-quantum mixed Ehrenfest spin-dynamics is also able of describing energy transfer from the quantum electrons to the classical local spins. We remark that this aspect may appear to be in contrast with the well-established fact that the Ehrenfest approximation suppresses thermal equilibration [104, 49]. However, although microscopic thermal noise cannot be transferred from quantum to classical degrees of freedom in the Ehrenfest dynamics, because of the mean-field description of the interaction between the two, temporal and spatial excitations at the level of the mean electron density can be captured and transferred between the two subsystems. This is indeed the case here where the energy exchange is driven by the short wavelength spin-excitations.

Finally, by fitting our calculated local-spin dispersions for different values of J (J_S=const) to Eq. (5.3.7), we are able to determine the dependence of the effective intersite exchange J_S^{eff} on the s-d exchange [Fig. 5.6(c)]. We observe a monotonic increase of J_S^{eff} with J. For small J (when neither of the two spin bands is fully occupied) the dependence is nonlinear (seemingly parabolic). As the system passes into the half-metallic regime, the dependence $J_S^{\text{eff}}(J)$ slows down for large J and tends to saturation (not shown on this graph, for instance $J_S^{\text{eff}}/J_S - 1 \approx 32\,\%$ for $J = 10\,\text{eV}$). In simple terms we could interpret the increase and tendency to saturation of $J_S^{\text{eff}}(J)$ with electron localization for large J. That is, the local spins "dressed" with the localized spin-polarized electron cloud are effectively larger in magnitude, hence their direct coupling becomes stronger. The precise

[1] The modification of the direct inter-site exchange, which we find in the presence of the conduction electrons, actually has an oscillatory signature similar to that of the conventional Ruderman-Kittel-Kasuya-Yosida (RKKY) interaction (see Ref. [67] for the 1D result). We have observed that a different value of the band-filling (defining a different Fermi wave-vector) could result instead in an anti-ferromagnetic indirect exchange, reducing J_S^{eff}. For instance at half-filling ($1e$/atom) we obtain a much lower $J_S^{\text{eff}} \approx \frac{1}{4} J_S$.

[2] Note that the middle region of this band appears folded down because of the sampling rate we are using (our sampling period $\Delta t = 0.5\,\text{fs}$ corresponds to a maximum energy of about $\pi\hbar/\Delta t = 4.1\,\text{eV} \approx 20 J_S$).

[3] The population of the optical modes is suggestive of a spontaneous "dimerization" of the spin system. This additional band can be seen in our magnon spectra only for large $J > 2\,\text{eV}$ for which our system is half-metallic. Similar effects have been found to result from the RKKY interaction in Kondo spin chains [130].

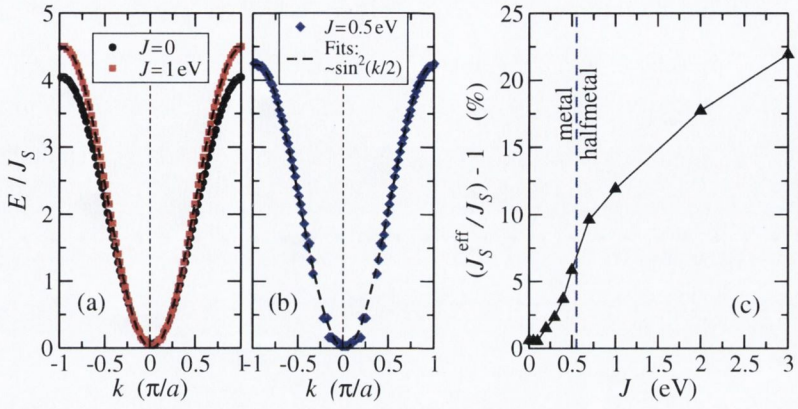

Figure 5.6: Calculated magnon dispersion curves in a 101-atom chain with $J_S = 0.2\,\text{eV}$ (a-b) in each of the three different regimes of exchange parameters considered in the text. These are fitted to the analytic expression of Eq. (5.3.7) to extract an effective Heisenberg exchange J_S^{eff}. In panel (c) is the dependence of J_S^{eff} on J and the dashed line marks the transition between metallic and half-metallic system.

interpretation of this effect has to be along the lines of the 1D RKKY interaction. Evidently presence of itinerant electrons is important for the dynamics of the localized spins.

5.3.2 Spin impurities in a non-magnetic chain

Understanding the magnetization dynamics in hybrid ferromagnetic/normal metal structures is important for applications and challenging for the theory. Two complementary non-local effects are now well-recognized [114] – one is the so called *spin pumping* and the other is the spin transfer torque effect, which we have already mentioned. The idea of the spin-pump is that the time-dependent magnetization emits (or pumps) a non-equilibrium spin-angular momentum into the adjacent non-magnetic materials. If for instance there is another ferromagnetic layer and the normal metal spacer is thinner than the spin-diffusion length, the pumped spin can excite magnetization dynamics in the second layer and effectively couple the two layer. This dynamic coupling has been observed in FMR experiments [46] and recognized as a novel form of collective behavior in magnetic heterostructures generated through the spin pumping.

As an illustration of another spin-dynamics aspect that can be addressed by time-dependent simulations, in this section we consider the spin-pump effect at the atomic level. Here we investigate the indirect (electron-mediated) dynamical coupling of two well-separated localized spin impurities $\mathbf{S}_{j_1}$ and $\mathbf{S}_{j_2}$ in a finite metallic wire by analyzing their temporal correlations. In fact, understanding the indirect exchange coupling of magnetic impurities implanted in low-dimensional

metallic structures could be important for engineering their response to applied magnetic fields. For instance, a sizable change in the conductance of a nanotube with the applied magnetic field is a strongly desired effect [51]. In a recent theoretical work [56] the static indirect exchange of magnetic moments sitting on metallic nanotubes has been found to strongly depend on their actual positions and be affected by quantum interference. Dynamical coupling in the presence of a charge and a spin current has been investigated in Ref. [76]. There a tendency for a steady-state, periodic motion of the spins has been found in the low-spin-current regime and a chaotic motion for high currents.

Here we consider the following dynamical situation for a closed quantum-classical spin system with no net currents. An excitation is produced at $t = 0$ only upon one of the two spins in the wire, say $\mathbf{S}_{j_1}$, but it is then mediated by the itinerant electrons and detected in the dynamical response of second spin $\mathbf{S}_{j_2}$. We anticipate that the latter response bears the signature of the electronic structure and depends on the size of the system, the location of the two spins and the local exchange coupling parameter J. Without aiming for thoroughness we describe a few cases which capture some of the specifics of this problem. The calculation is fully in the spirit of the quantum-classical spin dynamics described in Section 5.2. The electron Hamiltonian is simplified by removing the electrostatic term from Eq. (5.2.2) ($\kappa = 0$) and the external magnetic field from Eq. (5.2.3). The actual system of equations now reads (in a matrix form)

$$\frac{\mathrm{d}\rho_{ij}^{\alpha\beta}}{\mathrm{d}t} = \frac{i}{\hbar}\left[\hat{\rho}, \hat{H}_e\right]_{ij}^{\alpha\beta}, \tag{5.3.12}$$

$$\frac{\mathrm{d}\mathbf{S}_i}{\mathrm{d}t} = \frac{1}{\hbar}\left\{\mathbf{S}_i, -J\mathbf{S}_i \cdot \langle\hat{\boldsymbol{\sigma}}\rangle_i - g_S\mu_B B_i\hat{\mathbf{z}}\right\}, \qquad \text{for } i = j_1, j_2, \tag{5.3.13}$$

where $\langle\hat{\boldsymbol{\sigma}}\rangle_i$ is the expectation value of the spin density on the i-th site [see Eq. (5.3.11)], $g_S = 2$, B_i is a magnetic field applied locally only to $\mathbf{S}_i$ and

$$\left\{\hat{H}_e\right\}_{ij}^{\alpha\beta} = -|\chi|\,\delta_{\alpha\beta}\left(\delta_{i,j+1} + \delta_{i,j-1}\right) - J\left\{\mathbf{S}_i \cdot \hat{\boldsymbol{\sigma}}\right\}^{\alpha\beta}\left(\delta_{ij_1} + \delta_{ij_2}\right) \tag{5.3.14}$$

is the electronic Hamiltonian matrix, coupling the conduction electron spin to the local one only at the two spin-impurity sites, j_1 and j_2.

As an example, we consider a monoatomic chain with $N = 31$, intersite hopping $\chi = 1\,\mathrm{eV}$ and a band-filling of $\rho_0 = 1$ (i.e. 1 e/atom). The system is initialized with the spin at j_1 tilted to a small angle in the x-z plane ($\angle(\mathbf{S}_{j_1}, \hat{\mathbf{z}})_{t=0} = \pi/30$). A magnetic field is then applied $B_{j_1} \neq 0$ in order to achieve a steady precession of $\mathbf{S}_{j_1}$, while $B_{j_2} = 0$. We thus call $\mathbf{S}_{j_1}$ the "driven" spin, as opposed to the "free" spin $\mathbf{S}_{j_2}$, which is not coupled to the magnetic field. The exchange interaction to the conduction electrons is tuned through the $J > 0$ parameter. In our first set of simulations, we set

$J = \chi = 1\,\text{eV}$ and place the two spins at the end sites of the chain, i.e. $j_1 = 1$ and $j_2 = N = 31$, as we are interested mainly in the transportation of the spin excitation between the two spins.

Typical time evolutions of various spin quantities are shown in Fig. 5.7. We start our analysis by comparing the field-driven dynamics of $\mathbf{S}_1$ in the presence of the electron gas only (orange curves) to that obtained when also the second spin is present. When the driven spin is decoupled from the electrons ($J = 0$) it simply performs a uniform steady precession at the Larmor frequency $\omega_\text{L} = (2\mu_B/\hbar)B_1$. We use $B_1 = 1000\,\text{T}$, which corresponds to $\omega_\text{L} = 0.028\,\text{fs}^{-1}$, in order to obtain a large enough number of oscillations for the time of the simulation to provide a reasonable resolution for our spectral analysis. In this regime the local spin precession period ($\approx 35\,\text{fs}$) is compatible with the times for the electron passage along the chain.

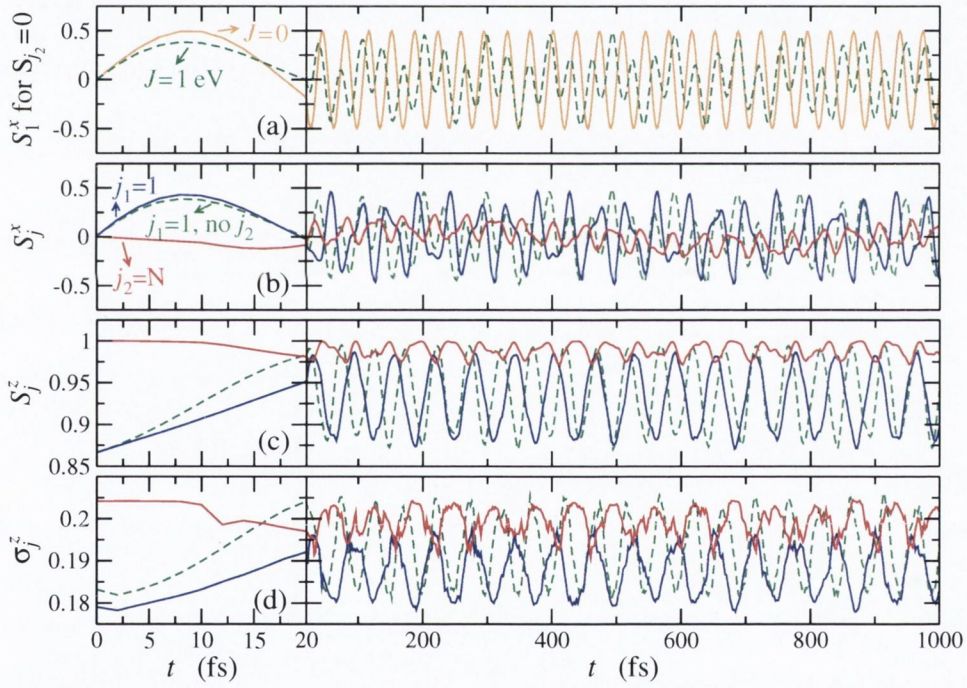

Figure 5.7: Time evolution of spin components: (a) x-component of the driven spin with (green curve) and without (orange curve) interaction to the electron gas when the free spin is absent (no spin at site j_2); (b,c) x- and z-components of the two spins for $J = 1\,\text{eV}$; (d) the electron spin polarization (with respect to the quantization axis z, i.e. $\sigma_i^z \equiv (\rho_{ii}^{11} - \rho_{ii}^{22})/2$) at the spin sites. Blue and red solid curves represent site 1 and site $N = 31$, respectively, while the grey underlying curves represent the $j_1 = 1$ site when there is no spin at j_2.

When $J \neq 0$ and the free spin $\mathbf{S}_N$ is present in the system, the latter starts to oscillate after a small time-delay. The small drift in S_N^x since the start of the simulation is due to the evolution of the small transverse electron density present on the site since the moment $t = 0$ when $\mathbf{S}_1$ is tilted.

At around $t = 10\,\text{fs}$ we find a step in σ_N^z [see Fig. 5.7(d)] and that is when the excited by $\mathbf{S}_1$ arrives at the N-th site. Because of the finite group velocity of the conduction electrons, the spin-polarized wave-packet takes a time $T \sim L/v_F$ (v_F is the Fermi velocity) to propagate from $\mathbf{S}_1$ to $\mathbf{S}_N$. The free spin also starts precessing about the z-axis but with a smaller transverse amplitude S_N^x (dashed curves). Neither of the two spins performs a pure precession. The z-components S_1^z and S_N^z oscillate too, with similar rates and opposite phases. Such a pattern is present also in the evolution of the electron spin densities on the two magnetic sites. This is a manifestation of two restrictions acting on the system: (i) the conservation of the z-component (along the external field) of the total spin and (ii) the spin-adiabaticity, i.e. the tendency of the electron spin to follow the direction of the local spins. The latter property is ensured by the strength of the s-d exchange, which in these simulation is $J = 1\,\text{eV}$. [1]

We investigate how the electron gas mediates the interaction between the two spins by varying the s-d exchange J. In order to quantify the temporal correlations between the two spins, we use the following normalized spin-spin correlation function

$$\mathrm{C}\left(S_1^x, S_N^x, \Delta t\right) = \frac{1}{\int (S_1^x(t))^2 \mathrm{d}t \int (S_N^x(t))^2 \mathrm{d}t} \int S_1^x(t) S_N^x(t + \Delta t) \mathrm{d}t\,. \tag{5.3.15}$$

The right-hand side panels of Fig. 5.8 represent the square of the above quantity as a function of the time delay Δt for a wide range of values of J. All results show a similar high-rate oscillatory decay pattern as Δt increases. Apparently the maximum of $C^2(S_1^x, S_N^x, \Delta t)$ is in the very early stages, compared to the whole length of the simulation. This demonstrates the very quick ($\sim 10\,\text{fs}$ for 30 atoms) transfer of angular momentum carried by the itinerant electrons. As the electron ticking rates (the inverse of the time to propagate forth and back between the two spins) are comparable to the precession rate of the driven spin and both are rather high, we find a very rapidly oscillating correlation function. In order to roughly estimate the maximum correlation amplitude (which is very close to the origin) we fit these results to a decaying exponent $C_0 \exp(-\Delta t/\tau)$ and the results for $C_0(J)$ are presented in Fig. 5.9. The constant $C_0 \sim C^2(t \approx 0)$ is a measure of the level of correlation and reaches its highest value for J in the range between 1.5 eV and 4 eV. For smaller J there is little energy transfer between the local spin and the electron gas and for very large J the majority (minority) electrons are too localized (delocalized) [2] to convey the spin information, hence the correlation is suppressed in both cases.

[1] This value of J is typically large enough to provide for good spin-transport adiabaticity in such systems, as will become evident in the next Chapter on current-induced domain wall motion.

[2] In connection with this last point one should note that the larger J, the deeper (shallower) the potential associated with the on-site spin-interaction for majority (minority) conduction electrons [see equation (5.2.3)].

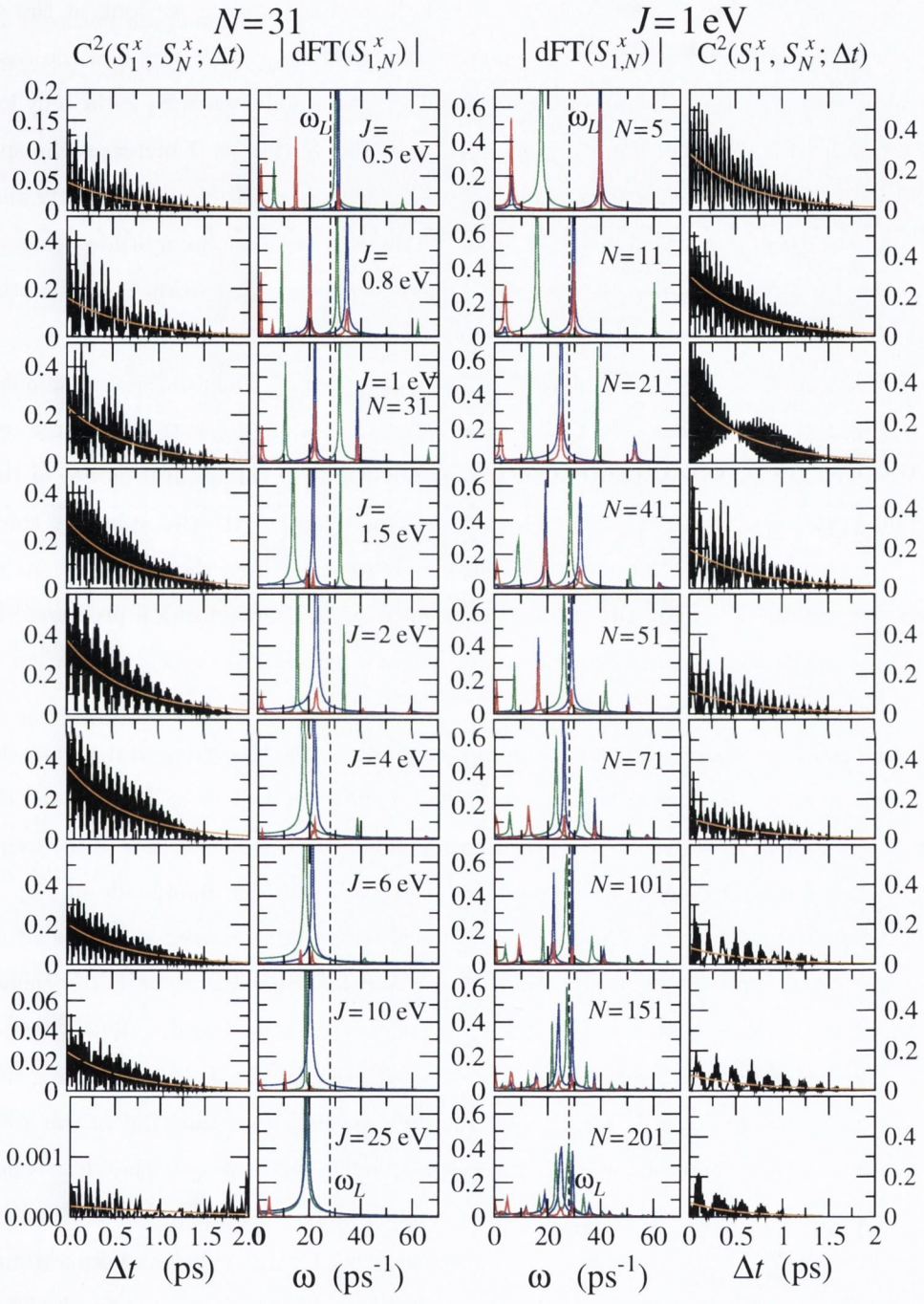

Figure 5.8: Investigation of the correlation between two classical spins (one driven and one free) at the ends of a metallic chain ($j_1 = 1$, $j_2 = N$) as a function of the *s-d* exchange strength J for a $N = 31$ atom chain (pairs of panels to the left) and as function of N for $J = 1\,\mathrm{eV}$ (pairs of panels to the right). Each case is represented by a pair of plots: one plot for the time-correlation function C^2 [see Eq. (5.3.15)] (black) fitted to an exponential trend $C_0 \mathrm{e}^{-\Delta t/\tau}$ (orange curve) and another plot for the spectra of $S_1^x(t)$ (blue), $S_N^x(t)$ (red curve) and again $S_1^x(t)$ but for the case when the free spin is absent from the chain (green curve).

In order to analyze the dynamical behaviour of the coupled system we look at the discrete Fourier transforms of the transverse x-components of the two spins. We compare the case when they are both present at the two ends of the chain with that obtained when $\mathbf{S}_1$ is the only localized spin in the chain (Fig. 5.8, left-hand side panels). We observe that as J increases the spectrum of S_1^x evolves from having one low-frequency peak and a higher-amplitude peak slightly above the Larmor frequency ($\omega_{\mathrm{L}} = 0.028\,\mathrm{fs}^{-1}$) for $J = 0.5$ eV, through two equal-amplitude peaks on each side of ω_L for $J < 1.5\,\mathrm{eV}$, and then saturates to a single peak somewhat below ω_L. The other spin S_N^x shares the same modes for $J < 10\,\mathrm{eV}$, although the amplitudes are different.

Qualitatively similar is also the evolution of the spectrum of S_1^x when the second spin is absent (green curves) and this becomes identical to that of the two spins for extremely large values of the s-d couplings J. In general there is always some red-shift of the natural modes of the field-driven spin-system as J is increased. Finally, for extremely large J the two spins are completely decoupled as the conducting minority-spin electrons are expelled from the spin-sites. As a result $\mathbf{S}_1$, "dressed" with its localized spin-up electrons (hence larger in magnitude), precesses at a rate lower than ω_L, while $\mathbf{S}_N$ is practically still (note that in our model dynamical simulation there is no Zeeman split in the electron gas).

Without aiming to analyse all the natural modes of the combined system of itinerant electrons and classical spins (an impractical task given the high number of degrees of freedom and the non-linearity of the dynamical response), we investigate numerically the dependence of the frequencies of the major modes on geometrical factors. For instance in the right-hand-side of Fig. 5.8 we illustrate the effect of the separation on the dynamical correlation between the spins situated at the two ends of the wire by varying its length ($L = Na$) for a fixed $J = 1\,\mathrm{eV}$. In general as N increases the precessional spectrum of S_1^x becomes richer. All natural modes show a tendency to red-shift as the chain becomes longer. This correlates with the increased electron ticking time (the time for an electron round trip). The modes also gain amplitude as they fall in the vicinity of ω_{L}. As a result the spectrum of the field-driven spin condenses about ω_{L}. The "free"-spin spectrum shows the same modes although they appear much more evenly populated. Evidently, the temporal correlations between the spins start off being rather high at very small separations, peak at around 40 atoms and decrease in amplitude as the chain length increases (see also Fig. 5.9). Above $N = 50$ we find a slower decrease of the correlation amplitude. We have approximated with a power law $\propto L^{\alpha}$ [linear on the log-log scale in Fig. 5.9 (b)] and obtained $\alpha \approx -0.38$. Despite the crudeness of the way α is extracted from the time-correlations, it suggests a rather long-range indirect exchange coupling between the spins in the wire. This observation comes in agreement to recent theoretical findings [31] of an enhanced range of the dynamical indirect exchange coupling

between adsorbed magnetic moments in metallic nanotubes, compared to the static version of it, suggesting that $|\alpha|$ could be smaller than 1.

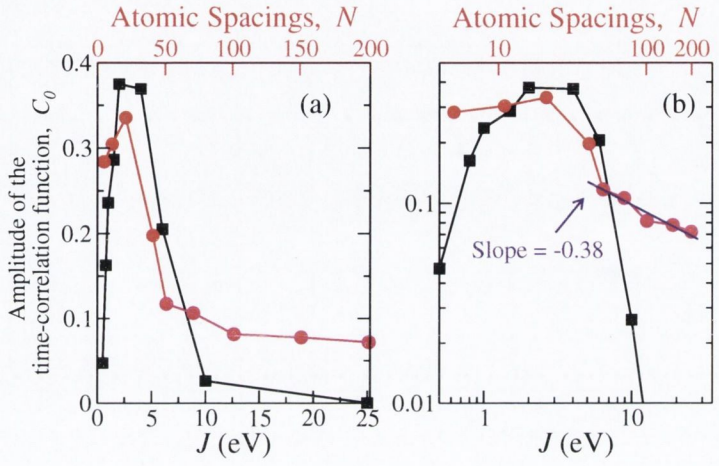

Figure 5.9: The amplitude of the computed time-correlation functions (see Fig. 5.8) as a function of J (bottom axis) or number of atoms N separating the two spins (upper axis, the distance is $L = Na$) in linear (a) and logarithmic scale (b). The tail of the dependence on distance is fitted to a power law decay $\sim L^{\alpha}$, where $\alpha = -0.38$.

Since the finite atomic chain acts as an electron-wave resonator, the correlations between the two spin impurities can be amplified or suppressed depending on the total length of the chain and the position of the site at which they are located. We have determined numerically that in an even-sited chain the field-driven spin can transfer spin excitation to the electron gas mainly locally, as illustrated in Fig. 5.10(a,b). In this case the standard deviation of the transverse spin distribution, which is a measure of the spin-density oscillation in the chain, peaks only at the site containing the spin impurity. The spectrum of $S_j^x(t)$ of the driven spin shows a single peak at the Larmor frequency for both even or odd j [Fig. 5.10(c)]. In order for the precessing spin to be able to transfer effectively spin excitation to the electron gas in the rest of the chain, this has to have an odd number of sites and the spin has to be at an odd-site location as illustrated in Fig. 5.10(e)]. The difference can be seen clearly from the spectrum [Fig. 5.10(f)], where two peaks, corresponding to combined modes of the coupled spin-system, replace the peak at ω_{L} .

Similar parity rules apply for the position of the second ("free") spin. In the case of odd chains (apparently more "susceptible" to localized spin-excitations) the temporal correlation and the mere amplitude of the excitation transferred between the two spins are substantially higher if the spins are both in odd positions (see Fig. 5.11). This can also be seen from the spectra of $S_{j_1}^x$ and $S_{j_2}^x$.

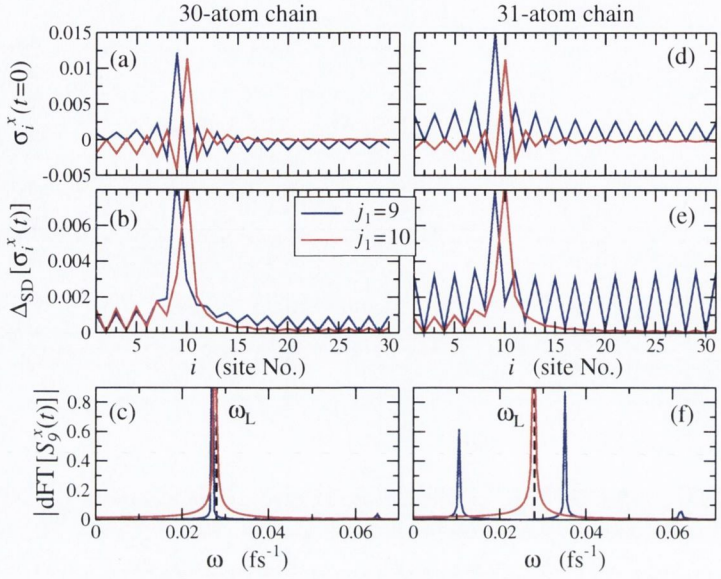

Figure 5.10: Simulations of a single magnetic-field driven spin $\mathbf{S}_{j_1}$ in 30 and 31-atom chains (left- and right-hand side panels, respectively). (a,d) The x-component of the onsite electron spin density at $t = 0$ and (b,e) its standard deviation for the time of the simulation vs. the site position. (c,f) The absolute value of the Fourier transform of $S^x_{j_1}$ for $j_1 = 9$ (blue) and $j_1 = 10$ (red curves). The position of ω_L is marked with a black dashed line.

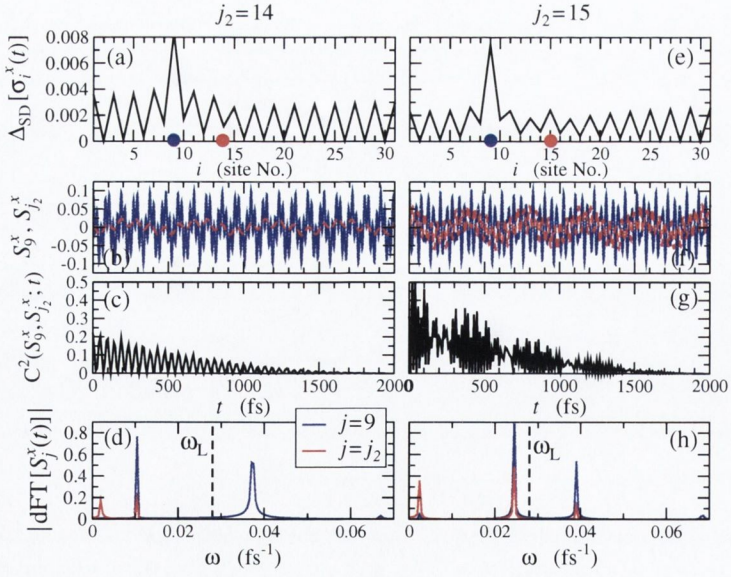

Figure 5.11: Simulations of two spins $\mathbf{S}_{(j_1=9)}$ ("driven"), $\mathbf{S}_{j_2=14,15}$ ("free") in a 31-atom chain. (a,e) Standard deviations $\Delta_{SD}\left[\langle\sigma^x\rangle_i(t)\right]$ vs position i, (b,f) x-components of the two local spins and (c,g) time-correlation functions [see Eq. (5.3.15)] between those vs time, (d,h) absolute value of the discrete Fourier transforms of the data in panels (b,f) with marked position of ω_L.

Further calculations (not presented here) have shown that typically the spin correlations do not depend as much on the positions of the two spins in the chain as they depend on the distance between them and the parity of the position j_1 of the driven spin. These seemingly peculiar odd-even effects originate from the fact that our electronic band structure is that of half-filling (1 e/atom) and the electronic temperature is low. We note that the electronic temperature actually enters our model with the Fermi distribution used for constructing the ground-state density matrix. In all calculations presented so far we have used some low electronic temperature $T = 50\,\mathrm{K}$. The spatial distribution of a spatially abrupt spin (or charge) excitation is rather corrugated at half band-filling because of the absence of modes with small enough wavelengths in the occupied spectrum. The Friedel-like fringes of spin density around the driven spin can be seen, for example, in Fig. 5.10(d).

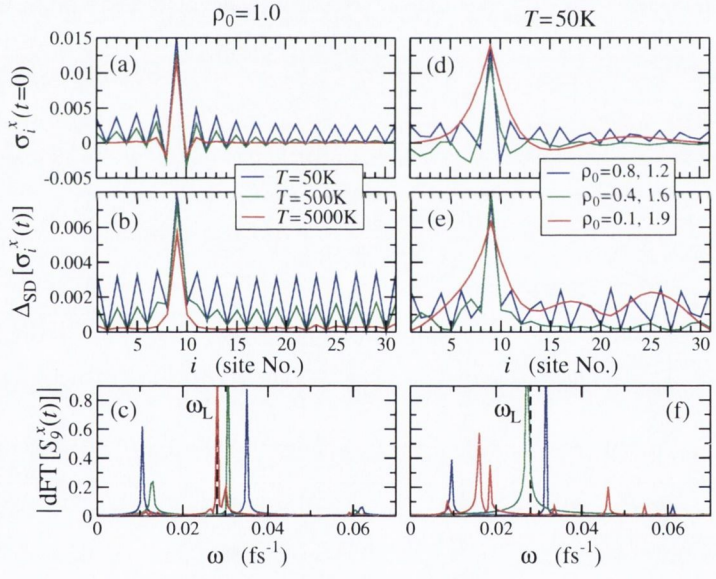

Figure 5.12: Effects on the spin dynamics of a single filed-driven spin placed at position $j_1 = 9$ in a 31-atom chain as a function of the band-filling, ρ_0, and the electron temperature (left- and right-hand side panels, respectively). The quantities plotted are the same as those represented in Fig. 5.10.

The rough spin-density texture is smeared as temperature is increased or a different from $\rho_0 = 1$ band-filling is considered. As an illustration of this effect, the case of a single driven spin in the 31-atom chain is repeated for different T and ρ_0, and the results are presented in Fig. 5.12. As the temperature is increased to introduce a Fermi level smearing $k_B T \approx 0.43\,\mathrm{eV}$ comparable to the bandwidth (4 eV), the interference pattern occurring in the spatial distribution of the transverse

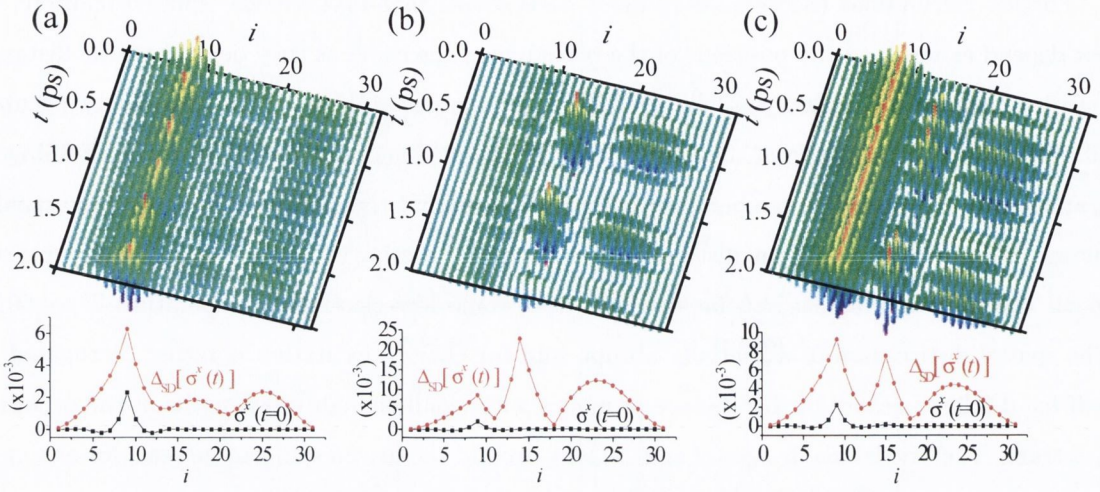

Figure 5.13: Trajectories of the expectation value of the transverse onsite spin-polarizations $\sigma_i^x(t)$ in a 31-atom chain with 1.9 e/atom and two spin-impurities $\mathbf{S}_{j_1}$ (magnetic field-driven) and $\mathbf{S}_{j_2}$ ("free"), for $j_1 = 9$ and (a) no second spin; (b) $j_2 = 14$; (c) $j_2 = 15$. The bottom plots represent the initial spatial distribution $\sigma_i^x(t = 0)$ (black lower curve) and its temporal standard deviation (grey curve).

electron spin is no longer present. As more modes are allowed to contribute at higher T, the electron localization is better defined spatially and the local spin spectra reduce to a single peak at $\omega_L = 0.028\,\mathrm{fs}^{-1}$.

The effect of changing the band-filling (e.g. by charging or discharging system) is in many ways similar to that of the temperature. Values of ρ_0 which are symmetric with respect to $1\,e$/atom produce the same spin-density pattern because of the electron-hole symmetry. We observe that intermediate band-fillings $1.3 < \rho_0 < 1.7$ quite resemble the high T case – electron spin excitation is localized and precession of the local spin is almost unaffected. For higher band-fillings, because of the big wavelengths at the Fermi level, a variety of resonant phenomena can occur. Figure 5.13 depicts some curious results of simulations of a driven and a free spin in electron gas with Fermi level close to the band edge ($\rho_0 = 1.9$). The real-space and time evolution of the transverse spin density reminds us to a "tsunami" effect. The long-wavelength (hole-like) spin-density excitations build up on the free spin, causing it to shake with an enormous (compared to the initial tilt of the driven spin) amplitude at some instances of time. As there is no dissipation in our system these are regularly recurring events.

5.3.3 Summary

In the foregoing chapter we have presented an approach for investigating the spin dynamics at the atomic scale. This is based on the adiabatic approximation for spin (the analogue of the Born-Oppenheimer approximation in lattice dynamics), according to which the spin degrees of freedom can be separated into slow and fast variables and the dynamics – described by equations of motion of the local spins and a standard single-particle spin-polarized equation for the itinerant spin-carriers [6]. Such separation is motivated by the significant mismatch of the relevant energy-scales for the inter-atomic exchange ($< 100\,\mathrm{meV}$) on one hand and the intra-atomic exchange and conduction band-widths, on the other. Hence in many magnetic systems the spin dynamics can be mapped onto an Ehrenfest dynamics. This, in the same spirit of the standard Molecular Dynamics simulations, can be used to explore various dynamical properties of complex spin systems.

As an illustration of the method's functionality, we have described an example in which magnon spectra can be computed and the indirect exchange interaction determined. As a second example we have presented a study on the dynamical correlations between spins in a metallic wire. We have demonstrated the microscopical mechanism of electron-mediated angular momentum transfer and investigated the scaling of the temporal correlations with the s-d exchange strength and the size of the system. We have demonstrated the importance of geometry, which determines the quantum interference patterns and the ability of the itinerant electrons to convey spin excitation. For the studied case of a finite monoatomic chain and half band-filling we have observed odd-even effects of the position of the oscillating spin, consisting of the lack of susceptibility of the electron gas to spin excitation at alternating sites. This effect is reduced by introducing a thermal smearing to the electronic structure or by charging/discharging the whole system.

Chapter 6

Dynamics of a spin domain wall coupled to itinerant electrons

6.1 Current-induced domain wall motion

The prospect of manipulating the magnetization texture of a device with a spin-polarized current is at the heart of a whole area in the field of spin electronics which takes the name of *spin transfer torque* (STT). This unifying notion originates from the work of Slonczewski [93], who made a pioneering theoretical prediction of current-induced magnetization dynamics in single-domain magnetic multilayers for the current perpendicular to the plane (CPP) geometry. Having a spin valve [1] in mind, the main idea is that the transversely spin-polarized electron flux generated by the first magnetic layer (polarizer) produces a torque upon the magnetization of the second layer (analyzer), effectively transferring spin between the two. A steady precession of the analyzer magnetization is predicted at a constant current, strong enough to dominate the Larmor precession about the Öersted field, and a repetitive magnetization switching is expected under a pulsed current. These phenomena can be detected through the magnetoresistance effect and both switching [54, 44] and precession [82, 62] have been observed experimentally in spin valve structures. More recently time-resolved ultrafast x-ray images [2] have been able to peek into the very process of magnetization reversal due to STT. The huge interest in the spin torque phenomena is constantly fuelled by industry as the miniaturization of magnetic storage devices progresses and new spin-torque based magnetic random access memory (MRAM) devices are about to become commercially available.

[1] The *spin valve* is a heterogeneous magnetic device consisting of two or more layers of conducting magnetic material. The essential functional part of it is the GMR trilayer, which consist of a magnetically hard material (pinned layer or polarizer) and a magnetically soft material (free layer or analyzer), separated by a conducting spacer layer.

6. DYNAMICS OF A SPIN DOMAIN WALL COUPLED TO ITINERANT ELECTRONS

Another founding contribution to the spin transfer torque theory was made even earlier. In the 70's Berger [14], by looking at the low-field magnetoresistance of some ferromagnets, noticed that "electrons crossing a (domain) wall apply a torque to it, which tends to cant the wall spins". This is again a spin-torque phenomenon similar to Slonczewski's one for the single-domain dynamics in spin valves. In fact, the spin torque occurs in any non-uniform magnetization pattern that is traversed by a spin-polarized current. In the case of the smoothly changing direction pattern of a magnetic domain wall (DW), the spin-transfer torque is converted to pressure, which pushes the wall in the direction of the electron flow (we shall explain this effect later in this Section) and this effect has been confirmed experimentally (for recent works see Refs. [43, 115, 57, 62]). The current-induced translation of the whole magnetic structure is particularly interesting from information storage point of view because the adjacent domains could represent binary bits. This is essentially the idea behind the widely-known proposal of magnetic racetrack memory device [77], where the sequences of magnetic domains are pushed along the device by pulsed spin-polarized currents.

Theoretical work is typically based on either semiclassical theory [114] or on the *s-d* model, where the local magnetization $\mathbf{M}(t,z)$ is continuously varied only along the direction (say, along z) of the current flow. The problem is usually addressed in a micromagnetic fashion by solving the Landau-Lifshitz-Gilbert (LLG) equation for the magnetization with additional *spin torque* terms describing the effect of the electron flux. For one-dimensional DWs Zhang and Li [135] have derived two current-induced spin-torque contributions, by starting from the *s-d* model and integrating out the electronic degrees of freedom in a linear response approximation. Their working assumption is that of a slowly varying magnetization direction. The length scale is set by their intrinsic spin-relaxation mechanism so that in the adiabatic limit, which they consider, the width of the wall is much bigger than the spin-flip length. The two current-induced torques, which Zhang and Li (ZL) derive are

$$\mathbf{T}_{\text{adiab}} = -\frac{b_J}{M^2}\mathbf{M}\times\left(\mathbf{M}\times\frac{\partial\mathbf{M}}{\partial z}\right), \tag{6.1.1}$$

$$\mathbf{T}_{\text{nonad}} = -\frac{c_J}{M}\mathbf{M}\times\frac{\partial M}{\partial z}. \tag{6.1.2}$$

The so-called *adiabatic* torque, $\mathbf{T}_{\text{adiab}}$, is analogous to the Slonczewski STT in spin valves. It is due to the fact that the electron spin tends to align to the local magnetic field as it passes adiabatically through regions of spatially varying magnetization and this torque is produced as a result of angular momentum conservation. For $|\mathbf{M}(z)| = const$ (only the direction of the magnetization varies) this can be rewritten [66] as $-b_J\frac{\partial\mathbf{M}}{\partial z}$, where by definition $b_J = Pj_e\mu_B/eM$, j_e being the electric current density, P the spin polarization and $M = |\mathbf{M}|$. The other torque $\mathbf{T}_{\text{nonad}}$ [Eq.

(6.1.2)] is perpendicular to $\mathbf{T}_{\text{adiab}}$ and is described as a *non-adiabatic* torque. In other theoretical works this torque is known as the β-torque and its microscopic origin is still controversial [103].

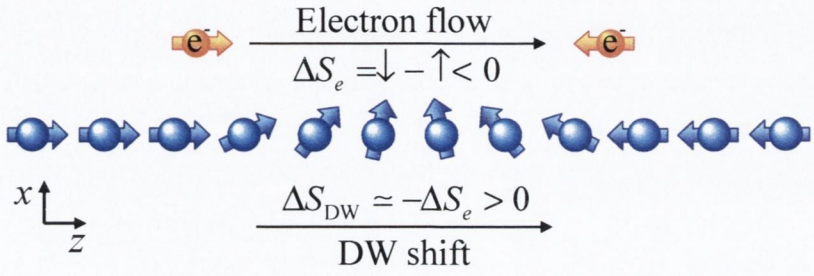

Figure 6.1: Illustration of the angular momentum transfer mechanism behind the adiabatic contribution to the current-induced DW motion. An incoming electron flips its spin direction by passing across a DW. Such a spin rotation is compensated by an equal an opposite change of the total local spin, which generates a DW motion.

A simple mechanism for understanding the origin of the adiabatic torque in a 1D Néel wall is illustrated in Fig. 6.1 (see for example Ref. [98]). An electron entering from the left-hand side with spin-up and following the wall magnetization adiabatically, eventually flips its spin on exit, i.e. $\Delta S_e = 2s = \hbar$. If all non-conservative spin relaxation mechanisms are neglected (for example electron scattering with impurities having a strong spin-orbit coupling) [120] then all of the angular momentum variation must be absorbed by the local magnetization. In the case envisaged in Fig. 6.1, the angular momentum gained by the DW for a single adiabatic electron crossing is $\Delta S_{\text{DW}} = -\Delta S_e > 0$ which corresponds to the DW shifting to the right (i.e. in the direction of the electron flow). Alternatively, one can think of the effective field that the adiabatic spin-rotation creates [120], which is transverse to the plane of the wall and produces a torque in that plane.

In contrast, the origin and the effect of the non-adiabatic torque in Eq. (6.1.2) [1] is not as easy to cartoon. It is introduced by Zhang and Li [135] as a result of the non-conservative spin-flip processes during the electron crossing of the DW. These are modelled by a phenomenological spin-relaxation term in the equation of motion of the electon spin density. Although for transition metal ferromagnets $c_J/b_J \approx 10^{-2}$ [135], the role of the nonadiabatic term is claimed to be crucial for sustaining the motion of the wall. According to Zhang and Li, the nonadiabatic term acts as a nonuniform time-dependent magnetic field with just the right distribution to sustain the

[1] This, also called β-term, is sometimes considered as adiabatic. For instance in Ref. [106]) T_{nonad} appears as part of the adiabatic torque as it also arises from the first order term in the gradient expansion of the STT. What they call non-adiabatic torques are the higher order terms in this expansion.

steady motion. More recently the Zhang and Li's picture was questioned by Stiles *et al.* [131] and calculations based on the Stoner model demonstrated that the prefactor c_J associated to the non-adiabatic torque is actually non-local and it is not necessarily associated with an intrinsic mechanism for spin-relaxation [17].

The other extreme approximation (contrary to the adiabatic one) that can still be addressed analytically is that of the very thin wall with a width w much smaller than the Fermi wavelength, i. e. $k_F w \ll 1$. In this case the STT effect vanishes, the wall can be described as a quasi-particle and the current-induced pressure is due to the linear momentum transfer of the backscattering conduction electrons [102, 35].

In order to investigate the spin transfer torques in the range of DW widths comparable with the Fermi wavelength (a few atomic spacings wide), we have developed an open-boundary spin dynamics simulation, which is described in the following section.

6.1.1 Computational method and static properties

Within our atomistic *s-d* model simulations of the spin dynamics we treat the electrons quantum-mechanically and integrate the set of Liouville equations for the discrete classical spins. This reads (as in Eq. 5.2.8 but without the external magnetic field)

$$\frac{\mathrm{d}\mathbf{S}_i}{\mathrm{d}t} = \frac{1}{\hbar}\left(\mathbf{S}_i \times \mathbf{B}_i\right) . \tag{6.1.3}$$

where

$$\mathbf{B}_i = J\left\langle \boldsymbol{\sigma} \right\rangle_i + J_S \sum_{j=i\pm 1} \mathbf{S}_j + 2J_z\left(\mathbf{S}_i \cdot \hat{\mathbf{z}}\right)\hat{\mathbf{z}} \tag{6.1.4}$$

is the effective local magnetic field at site i. Thus the classical spins are locally exchange-coupled to the instantaneous expectation value of the electronic spin $\left\langle \boldsymbol{\sigma} \right\rangle_i$ and this coupling produces all the contributions to the STT. In other words, there is no need for additional empirical current-induced torques in our LLG-like equation (6.1.3) as the effective field term accounts for all the adiabatic and nonadiabatic torques originating from the electron flow in our model.

In order to simulate the DW dynamics under bias at the atomic level, we have used the semi-empirical method of sustaining an electron flux in a finite system from Chapter 4. In this method, designed for Ehrenfest-type dynamical simulations [87], the atomistic system is partitioned into three subregions: two external regions, acting as a source (S) and a drain (D), coupled to a central region, where the atomistic device to be studied under bias is located (see Fig. 6.2). A modified Liouville equation is used to describe the electronic dynamics

$$\frac{\partial \hat{\rho}}{\partial t} = \frac{i}{\hbar}\left[\hat{\rho}, \hat{H}_V\right] - \Gamma\left(\hat{\rho} - \hat{\rho}_0\right) , \tag{6.1.5}$$

where Γ is a real parameter and $\hat{\rho}_0$ is a "tailor-made" density matrix such that

$$\{\hat{\rho}_0\}_{ij}(t) = \begin{cases} \rho_{ij}(t=0) & \text{for } i,j \in \mathrm{S},\mathrm{D} \\ \rho_{ij}(t) & \text{otherwise} \end{cases} . \tag{6.1.6}$$

By this definition the source/drain term proportional to Γ is applied only to the S and D regions. If the initial density matrix $\rho_{ij}(t=0)$ is set in such a way that the source and the drain carry an electron number imbalance, this will be maintained during the time evolution of the electron density with a relaxation time of $1/\Gamma$, and it will produce a steady current flow through the system. Such a source/drain polarized density matrix in our simulations is constructed from the eigenstates of the Hamiltonian with an applied external potential $2\Delta V$

$$\left\{\hat{H}_V\right\}_{ij}(\hat{\rho},t) = H_{ij}(\hat{\rho},t) + \begin{cases} -e\Delta V f_V(t)\delta_{ij} & \text{for } i,j \in \mathrm{S} \\ e\Delta V f_V(t)\delta_{ij} & \text{for } i,j \in \mathrm{D} \end{cases} . \tag{6.1.7}$$

where $H_{ij}(\hat{\rho},t)$ is the *s-d* exchange tight-binding Hamiltonian as in Eq. (5.2.2) and $f_V(t)$ is a smoothly decaying to 0 polynomial ramp. This is designed to vanish in a few tens of time-steps and it has been introduced for damping the charge oscillations that might originate from an abrupt removal of the initial bias. There is no external magnetic field and the hopping integral is $\chi = 1\,\mathrm{eV}$. In order to mimic a half-metallic electronic structure, we have chosen a band filling of 1.75, for which the Fermi level lies about 0.5 eV above the band edge of the fully-occupied spin-up band.

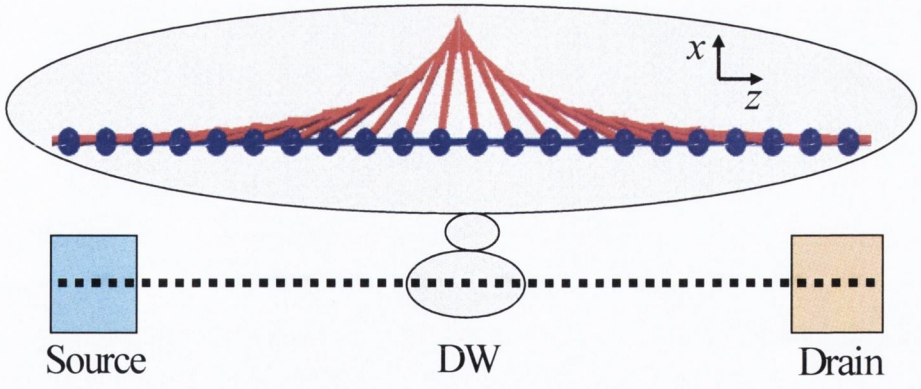

Figure 6.2: Scheme of the electron transport calculations through a mono-atomic wire containing a DW. The source and drain are introduced in the equation of motion as a phenomenological term that maintains charge imbalance at the edges of the wire [see Eq. (6.1.5)].

Ideally the source/drain term in Eq. (6.1.5) produces a constant carrier imbalance between the two ends of the wire therefore simulating an open system. Moreover, since ρ_0 is purely real it also provides for a phase-breaking mechanism in the source. This phenomenological method has been proven able to produce, under certain conditions described in Chapter 4, a current-carrying

state equivalent to the Landauer steady-state [70]. A major problem with the method remains the correct definition of the applied bias as the system is finite and there are no real electron reservoirs (as those thermodynamically defined in the Landauer picture). However, if one is not interested in the precise I-V characteristics of the system but only in the effect of the current, and if the current does not alter significantly the resistance of the device, then tuning the value of Γ could promote dynamically a steady-current state. Such is the case with the current-induced DW motion studied here where we are able to achieve a steady current for $\Gamma = 2\,\mathrm{fs}^{-1}$.

We have then carried out atomistic simulations of DW motion in such an open-boundary one-dimensional atomic wire under a bias. The wire is 200 atoms long and the DW is set in the middle. In the initial state (before the bias is applied) the DW and the electrons are relaxed self-consistently so that all torques in the system vanish within a certain tolerance (typically 10^{-7}eV/rad). For an infinite Heisenberg spin chain with a longitudinal anisotropy $J_z \neq 0$ (but $J = 0$, i.e. no coupling to the electron gas) the DW ground state is known. This is a planar (Nèel) DW with a longitudinal spin distribution $S_i^z = S\cos\theta_{z_i}$, where

$$\theta_{z_i} = 2\arctan\left[\exp\left(\frac{z_i - z_0}{z_\mathrm{w}}\right)\right]. \tag{6.1.8}$$

Here z_0 is the centre of the DW and z_w is the DW width at approximately 89% of its transverse-profile height [see Fig. 6.3(a)]. In the anisotropic Heisenberg model this is related to the direct exchange and the anisotropy parameters [11]

$$z_\mathrm{w} = a\sqrt{J_S/2J_z}\,. \tag{6.1.9}$$

We reproduce numerically this result for our finite spin-chain and investigate the effect of the exchange coupling to the itinerant electrons J. After initialising the DW in the x-z plane, we perform a damped dynamical spin relaxation [by adding a Landau-Lifshitz damping term $-\alpha\mathbf{S}_i \times (\mathbf{S}_i \times \mathbf{B}_\mathrm{i})$ to Eq. (6.1.3)] until all torques in the system are below the given threshold. The relaxed DW is still planar as can be seen in Fig. 6.3(a), where in the DW centre $S_0^x \approx 1$. By fitting the $S_i^x(i)$ profile to the angular distribution in Eq. (6.1.8) we calculate z_w for different values of J_z and $J \neq 0$. By comparing with Eq. (6.1.9) we extract an effective direct exchange parameter J_S^eff and find that, for our choice of parameters, the exchange with the electrons acts towards increasing J_S^eff [see Fig. 6.3(c)]. For $J = 1\,\mathrm{eV}$ this contribution is nearly as big as our model direct exchange $J_S = 20\,\mathrm{meV}$. Similar result was obtained also in Section 5.3.1 from the previous Chapter by studying the magnon spectra [see for example Fig. 5.6].

If one keeps the anisotropy constant J_z and number of electrons (band-filling $\rho_0 = 1.75\,e/\mathrm{atom}$) fixed, as J is increased the DW width z_w tends to saturate [see Fig. 6.3(b)]. The dip near the

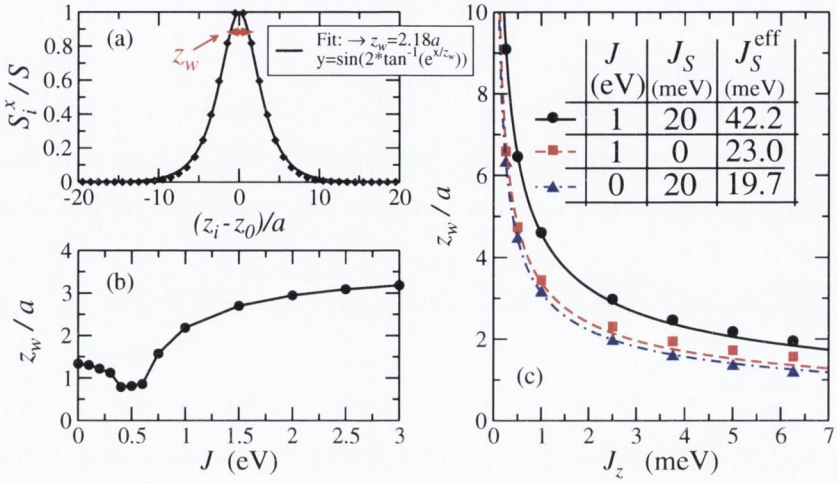

Figure 6.3: Characteristic dimensions of the DW in equilibrium as a function of J and J_z. (a) Typical transverse-spin profile of a relaxed DW and a fit to the exact expression for an infinite Heisenberg spin chain with longitudinal anisotropy [see Eq. (6.1.8)]. (b) Dependence of the DW width z_w on the s-d exchange J. (c) Dependences of z_w on the anisotropy constant J_z for $J = 0$ (Heisenberg chain, blue curve), $J_S = 0$ (red) and $J \neq 0$ & $J_S \neq 0$ (black), all fitted to the expression Eq. (6.1.9). Values of the effective direct exchange, J_S^{eff}, are listed in the table.

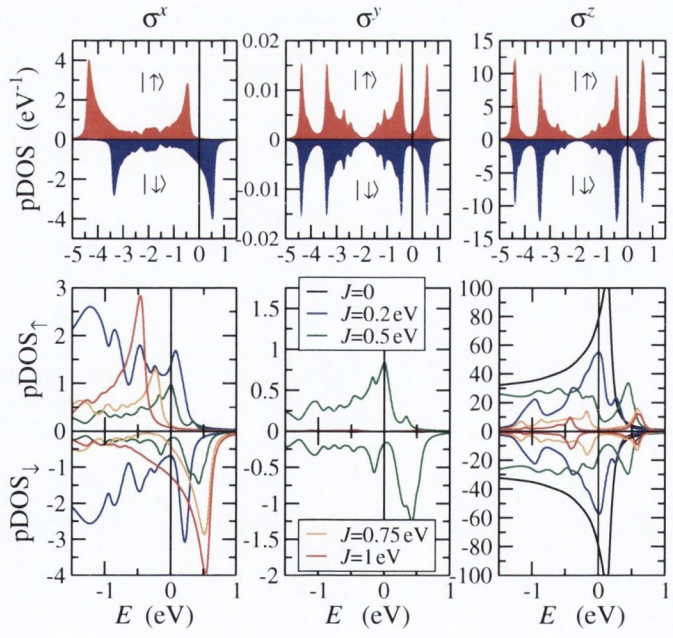

Figure 6.4: Spin-projected density of states (pDOS) for the conduction electrons in a 200-atom wire, containing a relaxed DW in $x - z$ plane with no bias applied. Top panels: the three spin projections of the DOS for $J = 1\,\text{eV}$. The Fermi level is at 0 eV. Bottom panels: a zoom around the Fermi level of the spin-projected DOS for J ranging from 0 to 1 eV.

beginning of the $z_{\mathrm{w}}(J)$ curve corresponds to a J-value for which the Fermi level is at the spin-up band edge. Above this value the system is a half-metal with only minority-spin electrons at the Fermi level. For our finite chain with a DW in the middle, the local spin along z is fully compensated and thus the σ^z-projected DOS (pDOS) are identical for the two spin-species (see Fig. 6.4). However, the transition to half-metalicity at $J = 0.5\,\mathrm{eV}$ can be seen in the σ^x-pDOS as the wall lies in the x-z plane. As the spin-split increases the transverse spin-up presence at the Fermi level goes through a peak and drops. For the critical value $J = 0.5\,\mathrm{eV}$ for which the Fermi level is closest to the edge of the spin-up band for a uniformly-polarized 1D spin-chain (not shown in this figure), we find that the planar DW is no longer possible and the relaxed DW develops a small twist out of the x-z plane, which manifests itself in the non-negligible and asymmetric σ^y-pDOS.

We summarise that for the half-metallic regime, which we are interested in, the DW thickness varies very little with J, for the range of values between 1 and 3 eV and for $J_z = 5\,\mathrm{meV}$. In this regime $z_{\mathrm{w}} \approx 2 \div 3a$ and the wall profile starts to deviate from the classical Heisenberg model result in Eq. (6.1.9) but is still not too far from it. These wall thicknesses are indeed comparable to the Fermi wavelength in our model. A rough estimation of the latter can be made from the σ^x-pDOS (see top panel of Fig. 6.4, $J = 1\,\mathrm{eV}$), where we clearly distinguish two 1D nearest-neighbour TB bands and the Fermi level splits the spin-down band as 7:1 from the bottom up. This determines that $k_F a = \arccos\left((E_c - E_F)/2\chi\right) \approx \arccos(-3/4) \approx 2.42$ which corresponds to $\lambda_F = 2\pi/k_F \approx 2.6a$. Thus our model parameters indeed provide for walls in the intermediate thickness range which is not directly accessible to analytical description.

6.1.2 Domain wall motion

When the DW is relaxed self-consistently in the presence of the itinerant electrons, a finite bias voltage is applied to two 10-atom-long segments at each end (S and D) of the wire by shifting their onsite energies according to Eq. (6.1.7). Then the quantum-classical system of equations of motion [Equations (6.1.3) and (6.1.5)] is integrated numerically. Typical real-space and real-time contour plots of the dynamical observables are illustrated in Fig. 6.5. Note that the DW is our simulations is moving opposite to the electron flux which does not contradict to the illustration in Fig. 6.1 since the carriers in our half-metallic wire are down-spin polarized, i.e. their spins point in the opposite direction to that of the local spin.

The current in our model is described in terms of the bond currents I_{nm} as discussed in Appendix C and in Ref.[109]. This is the electron current between two sites n and m, i.e.

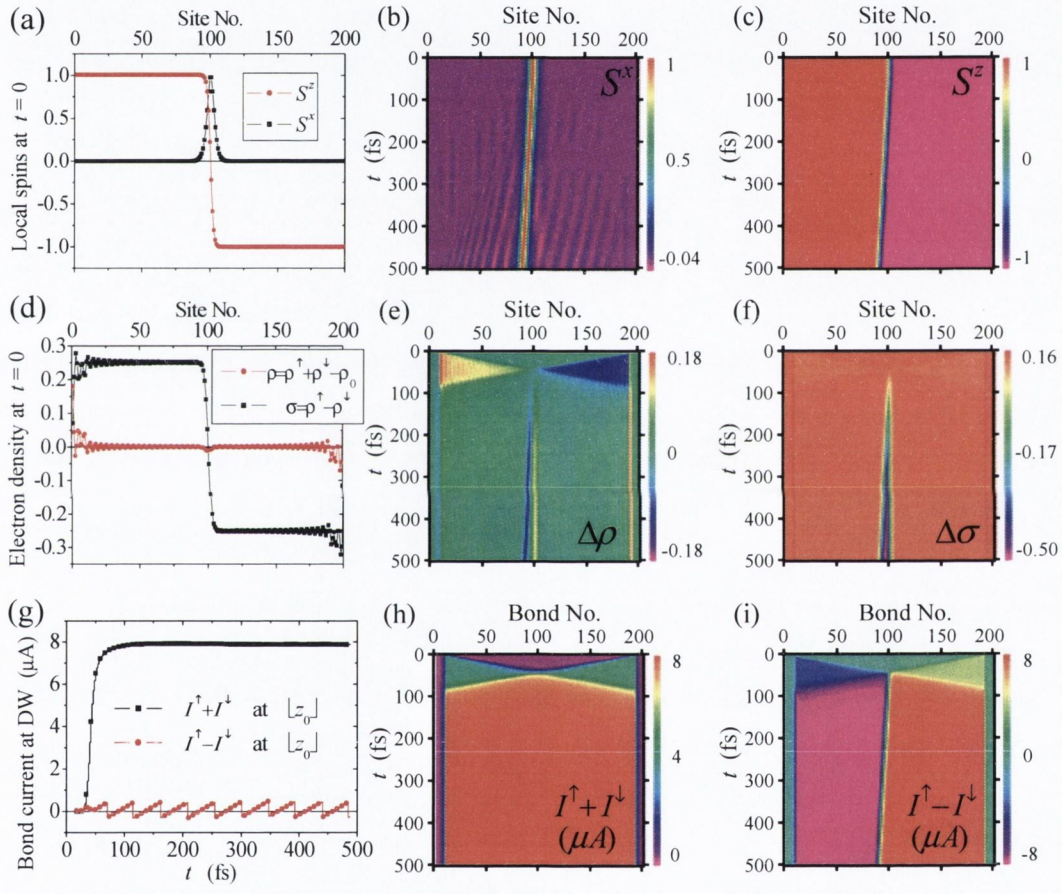

Figure 6.5: Self-consistently relaxed initial configuration of (a) local spin and (d) electron charge ($\rho^{\uparrow}+\rho^{\downarrow}-\rho_0$) and spin ($\rho^{\uparrow}-\rho^{\downarrow}$) density configuration of a 200-atom chain containing a DW. Space and time evolutions: (b,c) $S_{x,z}$ components of the local spins, (g,h) charge and spin bond currents [see Eq. (6.1.10,6.1.11)] and relative variation with respect to the initial state of (e) the onsite density ($\Delta\rho = \rho(t) - \rho(t=0)$), and (f) spin-density ($\Delta\sigma = \sigma(t) - \sigma(t=0)$).

$\sum_{m\neq n} I_{nm} = \{\dot{\rho}\}_{nn}$ with the right-hand side representing the rate of change of the on-site occupation. Following Todorov [109], we can define two partial bond currents for the two spin species with respect to the z axis

$$I^{\sigma}_{nm} = \frac{2e}{\hbar}\mathrm{Im}\left[\rho^{\sigma\sigma}_{nm}H^{\sigma\sigma}_{nm}\right], \tag{6.1.10}$$

where $\sigma = \uparrow, \downarrow$ and there is no summation over repeating indices. In our nearest-neighbour model these currents are non-zero only for $m = n \pm 1$. We denote the total particle current and the z-polarized spin current through the bond $(n, n+1)$ as

$$I_n = I^{\uparrow}_{n,n+1} + I^{\downarrow}_{n,n+1} \qquad \text{and} \qquad I^{\sigma_z}_n = I^{\uparrow}_{n,n+1} - I^{\downarrow}_{n,n+1}\,. \tag{6.1.11}$$

These two quantities as functions of time and the atomic position are shown in figure 6.5 (g,h), for an initially applied bias voltage of $\Delta V = 1\,\mathrm{V}$ and $J = 1\,\mathrm{eV}$. The contour plots illustrate how the steady-state is established when the charge-imbalances from the two ends propagate to the centre of the chain [see also the charge and spin density plots in panels (c,d) and their variations in panels (e,f)]. Since the steady-state current flow is not established instantaneously it takes a finite time before the DW starts to move. However, once the charge current is steady, it turns out not to be affected by the DW motion [the local spin components are depicted in panels (a,b)]. Because of the half-metallic electronic structure with a minority band at the Fermi level, $I^{\uparrow}_n = 0$ on the left-hand side of the DW, where the local spin is up, and $I^{\downarrow}_n = 0$ to the right-hand side. Thus the spin and the charge currents are the same on the right-hand side of the wall ($I_n = I^{\uparrow}_n = I^{\sigma_z}_n$) and have opposite signs on the other side ($I_n = I^{\downarrow}_n = -I^{\sigma_z}_n$).

We first investigate the evolution of the spin in our open-boundary system. The mere fact that the DW is moving means that our fictitious battery acts also as a spin sink in the system since a spin-dissipation mechanism can only be provided by the itinerant electrons through the open boundaries. As seen in the simulation of Fig. 6.6, the variation of the electron spin-density in the steady-state regime (with respect to the distribution at $t = 0$) is significant only inside the region swept by the moving wall [see 6.5 (f)]. In that region the on-site spin-polarization changes sign following the new local spin direction and if non-adiabatic torques are present a transverse spin could be dynamically accumulated. We calculate the total spin along the z direction as a function of time

$$S^z_{\mathrm{tot}} = \sum_{i=1}^{N}\langle\sigma^z\rangle_i + \sum_{i=1}^{N} S^z_i\,. \tag{6.1.12}$$

This consists of an electronic and a local spin contribution (Fig. 6.6). Initially only the electron spin decreases in time until the DW is reached by the electron flux (the classical spin is constant

while the wall is static). When the steady-state transport is established, the wall moves uniformly and $\sum_i S_i^z$ decreases linearly with nearly eight times (8.067) the slope of $\sum_i \langle \sigma^z \rangle_i (t)$. The ratio of the spin loss rates of electrons and local spins for adiabatic rotation is fixed by the band filling. Since $\rho_0 = 1.75$, there is an average on-site spin density of $0.25 S_i^z/2$ (in the uniform regions away from the wall). A local spin flip costs $2S_i^z$ and it is accompanied by an electron spin loss of $0.25 S_i^z$. Hence this produces the 8:1 ratio. The ratio that we find in this simulation is 8.067 which differs from the expected 8 by only 0.8%. This gives an estimation of the magnitude of electron transverse-spin accumulation due to non-adiabatic effects.

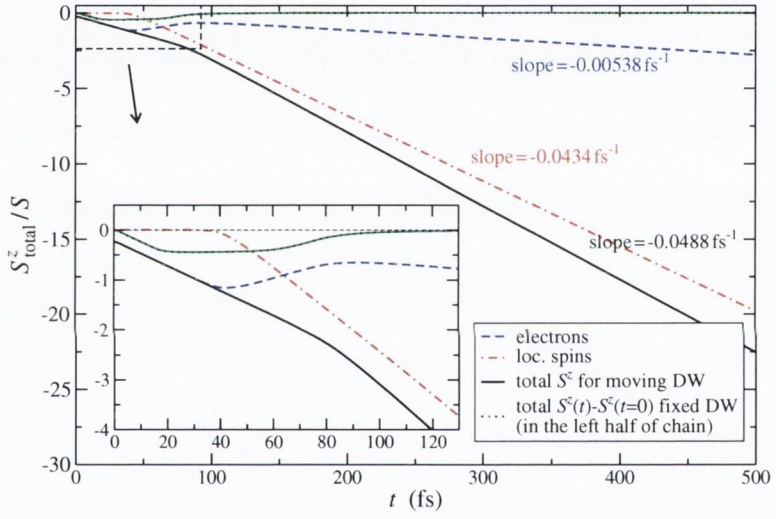

Figure 6.6: Time evolution of the total S^z_{tot} spin-component in a 200-atom chain, projected over the electronic (dashed curve) and the local spins (dot-dashed curve) contributions. The applied bias at $t = 0$ is 0.1 V and the DW is initially in the centre of the chain ($z_0 = 100.5a$). The dotted curve represents a test system, where an identical DW is initially prepared at $z_0 = 150.5a$ and is kept fixed for the whole simulation. This curve has actually been rigidly shifted by $S^z_{\text{tot}}(t = 0)$ to allow for a comparison.

If the DW is pinned (the local spins are affixed and not included in the dynamics), however, we find no net variation of the spin in the chain for the steady current flow (dotted curve in Fig. 6.6). This demonstrates that we have a spin-flipping battery and practically no spin accumulation – an electron entering the chain from the left-hand side as a spin-down flips at the wall and leaves the wire as a spin-up at the right-hand side boundary but then another electron with a spin-down enters the wire from the other side. Net spin accumulation is not found in the system if the wall is fixed.

We define the current at the wall I_{DW} as the spatially-averaged bond current in a region

of $\mathcal{Z}_{\rm DW} = \{z_0 \pm 20 z_{\rm w}\}$ around the centre of the wall (which contains all, say $N_{\rm DW}$, sites with substantial transverse spins) and then averaged over the steady-state time of the simulation and the corresponding DW velocity, $V_{\rm DW}$, for that period as

$$I_{\rm DW} = \frac{1}{N_{\rm DW}(N_T - N_0 + 1)} \sum_{n=1}^{N_{\rm DW}} \sum_{m=N_0}^{N_T} I_n(t_m), \qquad V_{\rm DW} = \frac{1}{N_T - N_0 + 1} \sum_{m=N_0}^{N_T} v_{\rm DW}(t_m) \quad (6.1.13)$$

where N_0 is some time step after the steady-state transport is established and $v_{\rm DW}(t)$ is the momentary DW velocity, obtained by a numerical differentiation of the wall position $z_0(t)$, which is defined through the equation $S^z(z_0) = 0$ and $S^z(z)$ is an interpolation of the set $\{[z_i, S_i^z]\}_{z_i \in \mathcal{Z}_{\rm DW}}$. We then examine how $I_{\rm DW}$ and $V_{\rm DW}$ depend on the choice of model parameters ΔV, J, J_z (see Fig. 6.7). Our reference set of parameters is

$$\Delta V = 0.1\,{\rm V}, \quad J = 1\,{\rm eV}, \quad J_z = 5\,{\rm meV}, \quad J_S = 20\,{\rm meV}\,. \quad (6.1.14)$$

As the only notion of distance in our model is the lattice spacing a, we define our current density at the DW as $j_{\rm DW} = I_{\rm DW}/a^2$. For the reference case above and a typical value $a = 2\,$Å our current density is about $8\,\mu A/4{\rm Å}^2 = 20 \times 10^9\,{\rm A/cm^2}$. This value is more than an order of magnitude bigger than the highest current densities used by [66] ($j = 1.5 \times 10^9\,{\rm A/cm^2}$). Our reference DW velocity is about 4.3 km/s, which is also nearly an order of magnitude higher than their maximal velocity (0.6 km/s). Thus the characteristics of the DW motion in our simulations agree (roughly) with those expected to originate from the adiabatic torque.

By varying the initialising bias voltage $0 < \Delta V < 0.15\,$V we find a perfectly linear correlation between $V_{\rm DW}$ and $I_{\rm DW}$ [Fig. 6.7(b)] with a slope of around $2.725\,a/({\rm ps}.\mu{\rm A})$, i.e. $2.725 \times 10^{18}\,a/{\rm C}$. We compare this result to the expected maximal (or if the one that corresponds to zero spin damping) DW velocity $V_{\rm ad} = -b_J = -Pj\mu_B/eM_s$ in the adiabatic limit [1] [66, 98]). In the expression for $V_{\rm ad}$, P is the spin polarization of the current, j is its density and M_s is the saturation

[1] The fact, pointed out by [66], that the factor b_J in the adiabatic torque in Eq. 6.1.1 represents the DW velocity $V_{\rm ad}$ can be understood from the following argument. Let us consider our 1D DW made of discrete classical spins from the moving (classical) reference frame of an electron from the flux. There the resting electron spin s is experiencing a passing-by at a constant velocity $\widetilde{V}_{\rm DW}$ planar spin-wall. If the spin is aligning instantaneously to the spin of the wall then it will be rotating with an angular velocity $\omega_s = \dot{\theta}_z = \widetilde{V}_{\rm DW}\nabla_z\theta_z(z_s + \widetilde{V}_{\rm DW}t)$, where z_s is the position of the spin, θ_z is the wall angular distribution with respect to $\hat{\mathbf{z}}$ (e.g. Eq. (6.1.8)). Such a rotation could effectively be produced by a torque $|T_e| = s\omega_s = s\widetilde{V}_{\rm DW}\nabla_z\theta_z(z_s + \widetilde{V}_{\rm DW}t)$ and by the second Newton law such a torque but in opposite direction must be acting on the wall. In the frame of the wall the torque on the wall at location z_i is similarly $T_{\rm DW}(z_i) = s\widetilde{V}_e\nabla_z\theta_z(z_i)$. We go back to the laboratory reference frame. As the spin conservation holds (see Fig. 6.1), if the spin s passes the DW of discrete spins $\{S_i\}$ for time Δt then $\Delta s = -2sV_e\Delta t/z_{\rm w} = -\Delta S = -2SV_{\rm DW}\Delta t/a$, where $z_{\rm w}$ is the whole length of spatial variation of spin in the wall [not the same quantity as in Eq. (6.1.8)], and therefore the velocities of the spin and the wall are related as $V_e/V_{\rm DW} = Sz_{\rm w}/sa$ so that in the adiabatic limit $z_{\rm w} \gg a$ and moreover if $S \gg s$ (classical local spins) then $V_e \gg V_{\rm DW}$ and $\widetilde{V}_e \approx V_e$. We obtain for the torque due to one electron $T_{\rm DW}(z_i) = V_{\rm DW}S(z_{\rm w}/a)\nabla_z\theta_z(z_i)$, which is indeed proportional to the wall velocity.

magnetization in the system. These quantities translate to our one-dimensional system as $j \to I_{\rm DW}/a^2$, $P = -1$ (half-metal) and $M_s \to 2\mu_B S_s/a^3$ where $S_s = 1 + (2 - \rho_0)/2 = 1.125$ (in units of $\hbar$ and $\rho_0 = 1.75$) is the total onsite spin (localized plus conduction band). Hence we obtain approximately $V_{\rm ad}/I_{\rm DW} \approx a/eS_s = 2.743 \times 10^{18}\, a/\mathrm{C}$. This value is different from our calculated slope [Fig. 6.7(b)] by less than 1%. This spectacular agreement suggests that the main diving torque for the DW motion we simulate is indeed adiabatic. Because of the different dimensionality of the systems we are comparing, we cannot say accurately what is the contribution of the non-adiabatic torques in our simulations but apparently they are small compared to the driving adiabatic torque which was also suggested by the level of spin accumulation.

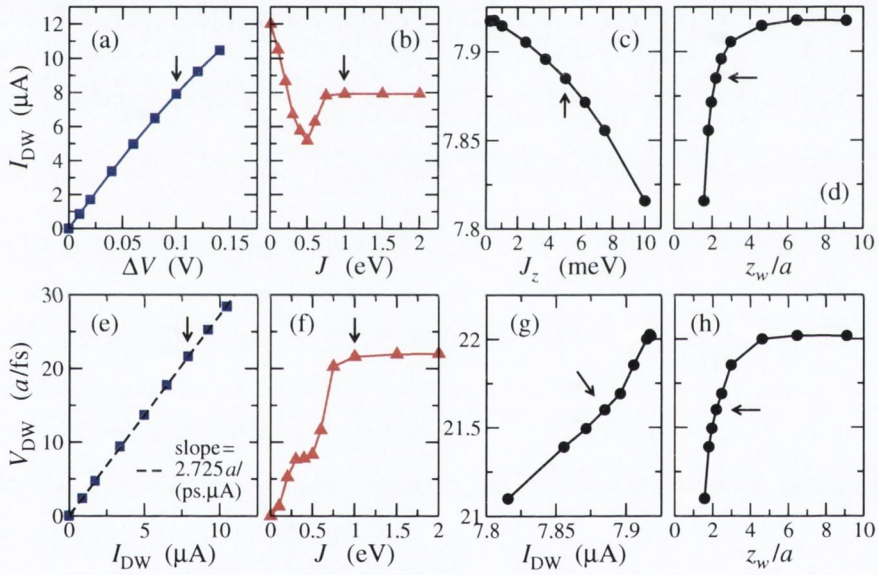

Figure 6.7: Dependences of the average steady-state current $I_{\rm DW}$ and the corresponding average DW velocity on bias ΔV ($J = 1\,\mathrm{eV}$, $J_z = 5\,\mathrm{meV}$) or on J, J_z and $z_{\rm w}$ for fixed $\Delta V = 0.1\,\mathrm{V}$. Same symbols correspond to same calculation. In particular, the variation of the arguments $z_{\rm w}$ (DW width) in panels (d,h) and $I_{\rm DW}$ in (g) are generated by changing the anisotropy J_z in (c). Arrows are pointing to calculations with the reference set of parameters (6.1.14).

Next we examine the dependence of the current and the DW velocity on the parameters in our model. We vary J (or J_z) with respect to the reference state (6.1.14). Dependences of both current and velocity on J [Fig. 6.7(b,f)] show some peculiarity around the critical J of the transition to halfmetalicity – a dip and a plateau, respectively. In the half-metallic regime, however, they both saturate. That is where our reference state is. The change of the anisotropy J_z with respect to the reference state affects the width of the wall $z_{\rm w}$ [see Fig. 6.3 (c)]. Both $I_{\rm DW}$ and $V_{\rm DW}$ appear rather insensitive to the variations of $z_{\rm w}$. We observe an overall change in $V_{\rm DW}$ of less than 5% and less

than 2% in I_{DW} for a nearly fivefold increase in the DW thickness [Fig. 6.7(d,h)]. The fact that $V_{\mathrm{DW}}(I_{\mathrm{DW}})$, obtained by the variation of the anisotropy, is almost linear [panel (g)] suggests that the main effect of the different J_z is on the conductance of the chain. We find that thinner walls are more resistive and because of the decreased current move slower. Though the overall variation in the conductance is small, the drop for thin walls is relatively steep and suggests non-adiabaticity, i.e. the inability of the conduction electron spins to follow the local spin direction while traversing the wall [119]. The adiabaticity is controlled by the *s-d* exchange parameter J. In our reference case ($J = 1\,\mathrm{eV}$) corresponds to a half-metallic state and we find that I_{DW} and V_{DW} are quite insensitive to a further increasing J (enhancing the adiabaticity) for a fixed anisotropy (i.e. DW width) [panel (b,f)], meaning that we our reference state is already close to the adiabatic. Again, what we see is a very little difference in the conductance for the range of wall widths we are working with (varying by a factor of 5). Both V_{DW} and I_{DW} show a tendency to saturation with the DW thickness and our reference state is on the verge of the saturation thickness, where the transport is adiabatic.

We now take a closer look at the details of the time evolution of walls with different thicknesses. In particular, we compare our reference case [Eq. (6.1.14), relaxed width is $z_{\mathrm{w}} = 2.2a$] to a more than 4 times thicker wall with $z_{\mathrm{w}} = 9.1a$ obtained for $J_z = 0.25\,\mathrm{meV}$. Here the overall length of the chain is increased (from 200 to 300 atoms) to allow for longer-lasting simulations and all remaining parameters (apart from anisotropy and voltage) are as in the reference case. The real space evolutions of the local spins in the two cases are presented in Fig. 6.8 where the initially applied bias is $\Delta V = 0.2\,\mathrm{V}$. The length of our simulations is still limited by the accumulation of numerical error during the time integration but we can safely reach times of about 2 ps (8×10^5 timesteps) during which the DWs appear to be moving rather uniformly. In both cases we see a very pronounced spin-wave pattern developing in time and the onset of deformations in the shape of the thicker wall in the initial stages of the dynamics (see Fig. 6.8). Interestingly, spin-waves develop at a much earlier stage in time for the thin wall than for the thick one. This indicates that the current-induced torques on the wall clearly depend on its width. There are qualitative differences even for the small range of widths investigated here. The thicker wall firstly deforms [see Fig. 6.8 (f)] by wriggling out of plane until some critical point which is the onset of the spin waves. This suggests that indeed non-adiabatic effects (like the spin waves) arise from the increased curvatures in the local spin texture [17].

Another non-adiabatic effect we find is that thin walls ($z_{\mathrm{w}} < 3a$) show a tendency to precess rigidly about the z-axis. This is illustrated in Fig. 6.9(e) where the time evolution of the S^x of the classical spins in the middle of the domain wall is fitted to $\cos(\omega t)$. We find that the precession rate

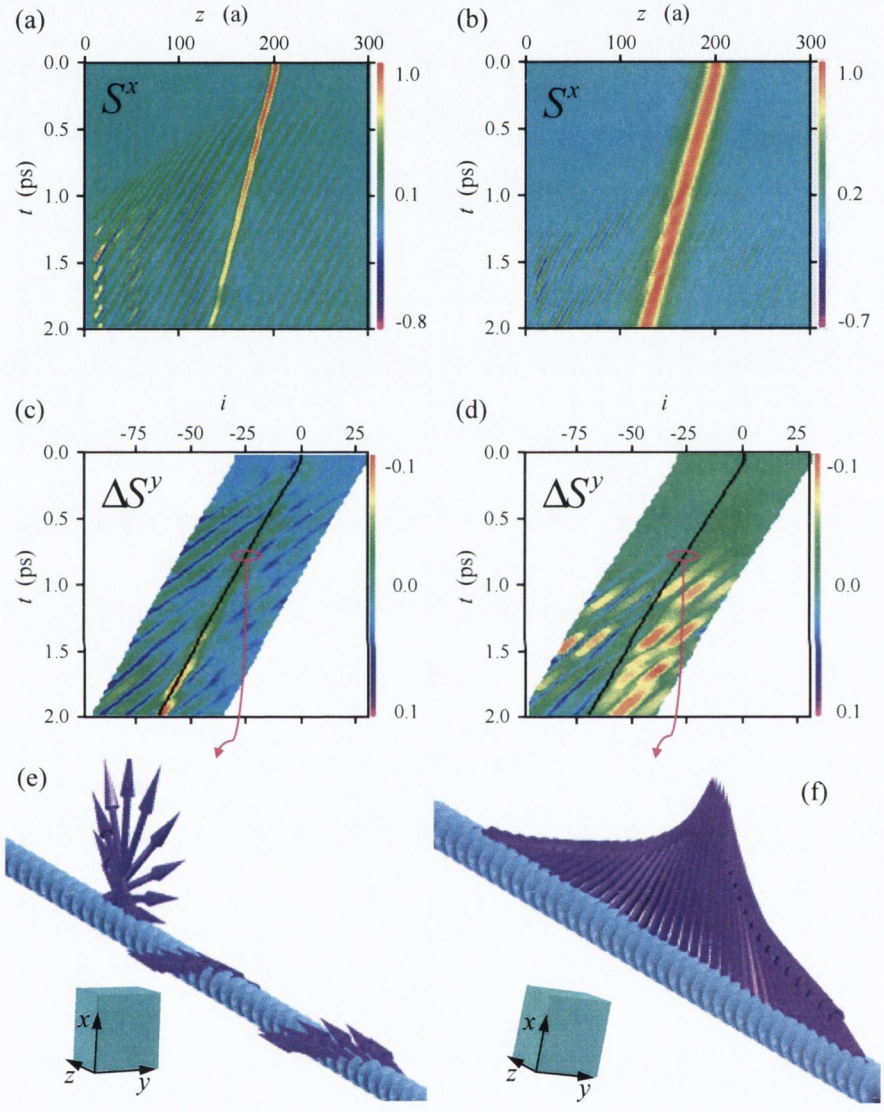

Figure 6.8: Real space and time evolution of two DWs of different width. The left-hand side pair of panels describe a thin DW ($z_\mathrm{w} = 2.2a$ obtained with $J_z = 5\,\mathrm{meV}$), while the right-hand side are for a thick one ($z_\mathrm{w} = 9.1a$ obtained with $J_z = 0.25\,\mathrm{meV}$). Panels (a,b) represent $S_i^x(t)$ and (c,d) represent the temporal variation of S_i^y in the vicinity of the wall (we define $\Delta S_i^y \equiv S^y_{z_0(t)+i} - S^y_{z_0(0)+i}$ for $i \in [-30, 30]$). The magnitude of these quantities is specified by individual grey-scale bars. The bottom panels (e,f) depict the DWs at 0.75 ps. The initially applied bias is $\Delta V = 0.2\,\mathrm{V}$ and the solid black lines in the panels (c) and (d) mark the exact DW centre $z_0(t)$.

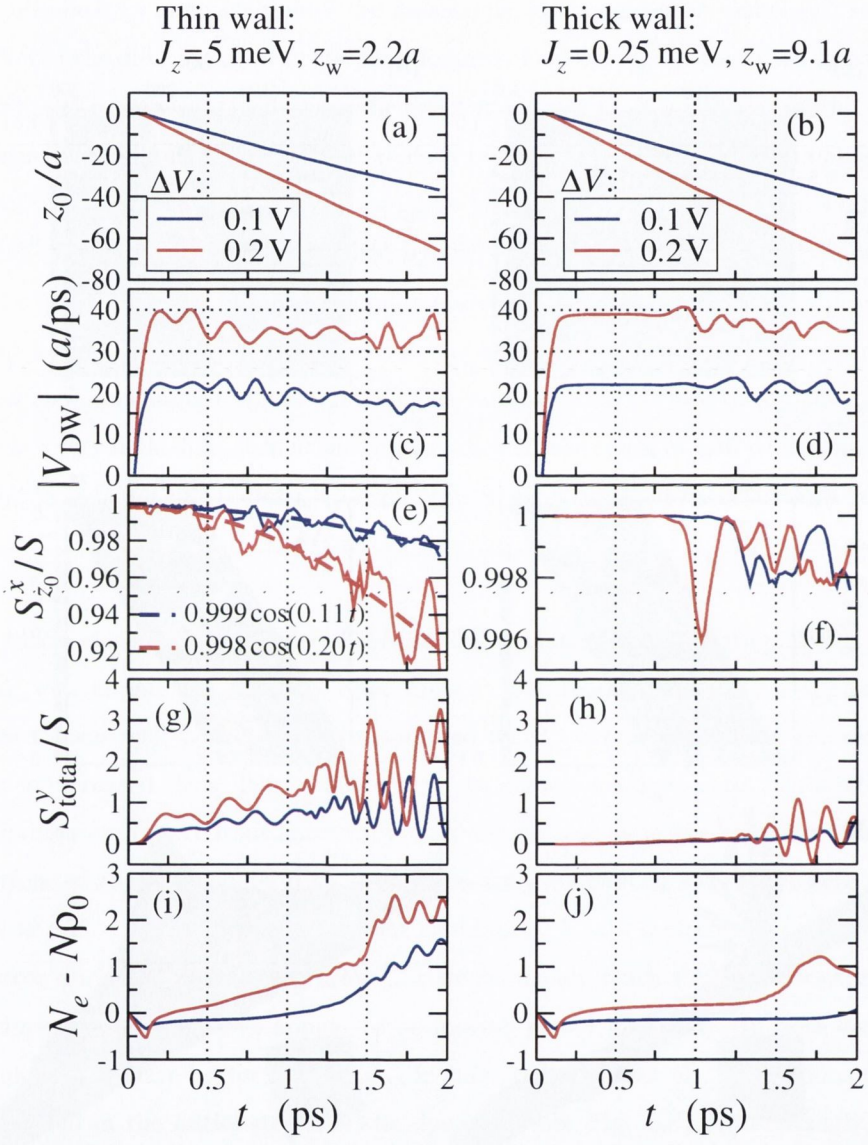

Figure 6.9: Time evolution of (a,b) the position of the DW's centre z_0 along the wire, (c,d) the average velocity V_{DW}, (e,f) the transverse local spin component S^x at z_0, (g,h) the total transverse spin in the system $S^y_{\mathrm{total}} = \sum_i(\langle\sigma^y\rangle_i + S^y_i)$ and (i,h) the variation of the number of itinerant electrons N_e with respect to the equilibrium. All the quantities are plotted for two different bias voltages, 0.1 V and 0.2 V. The left- and right-hand side panels represent thin and thick DW, respectively. Note that z_0 is defined such that $S^z_{z_0} = 0$, where $S^z(z)$ is an interpolation of $\{S^z_i\}$ with the classical DW-profile function (equation 6.1.8). $S^x_{z_0}$ is also the interpolation of $\{S^x_i\}$. The fluctuations in (c), (d), (e), (f), (g) and (h) correlate to the spin wave patterns in Fig. 6.8.

ω scales almost linearly with the applied bias voltage. In contrast thick walls develop slight out-of-plane deformation with the spins in the centre remaining in the x-z plane [Fig. 6.9(f)]. Apart from that, both types of walls move rather uniformly in time, with very similar velocities. One could speculate that the thin wall decelerates slightly although the timeframe of our simulations does not allow us to conclude whether or not the actual average DW velocity changes in time in the long time limit.

Evidently, both the DW velocity and the angular velocity of precession are characterized by large fluctuations. These are clearly correlated as the oscillation in the velocity match those of the transverse spin in the DW centre (see Fig. 6.9). They also both correlate with the spin-wave pattern illustrated in Fig. (6.8). Hence, we attribute variations in both the DW velocity and precession angular velocity to spin-wave emission. Importantly, in our computational scheme spin-waves are absorbed at the wire boundary. Therefore spin-wave emission provides a mechanism for spin relaxation. This will be further discussed in the next section.

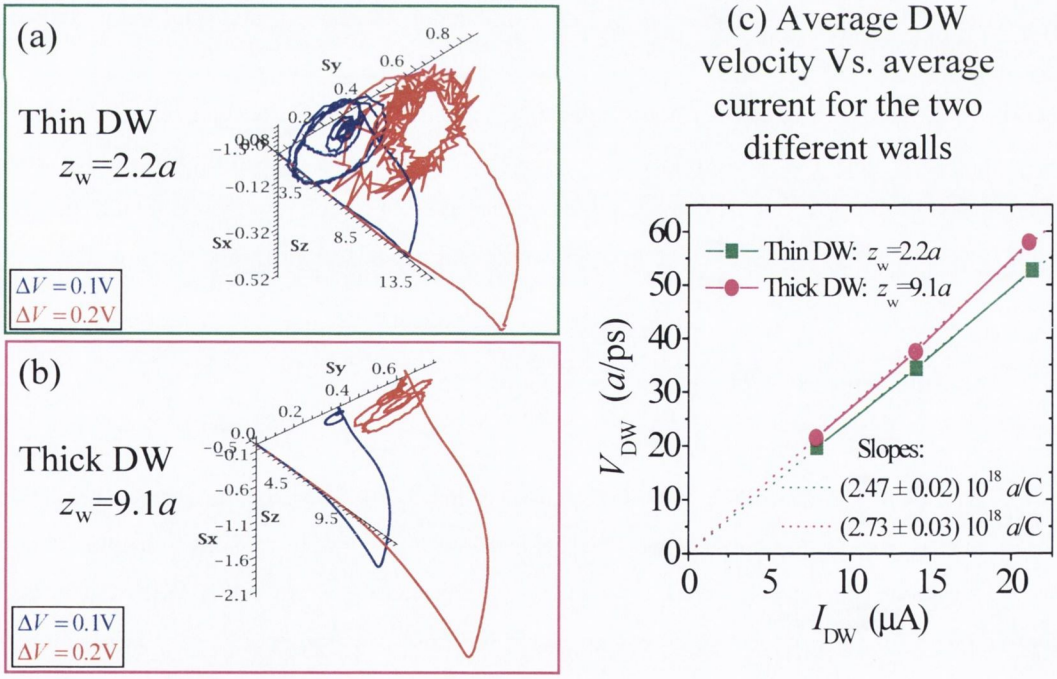

Figure 6.10: Trajectories in spin-space of the non-equilibrium itinerant spin accumulation defined as $\Delta\mathbf{S}_{\rm ne}(t) = \mathbf{S}_{\rm ne}(t) - \mathbf{S}_{\rm ne}(0)$ where $\mathbf{S}_{\rm ne}(t)$ [Eq. (6.1.15)] is the total non-equilibrium itinerant spin at time t for the thin (a) and for the thick wall (b) at two values of the initial bias voltage $\Delta V = 0.1\,\mathrm{V}$ and $0.2\,\mathrm{V}$. These are the same simulations as those in Fig. 6.9. The origin corresponds to the tip of the spin vector at $t = 0$. In panel (c) are the extracted plots of the averaged over the whole simulation DW velocity versus the averaged current at the wall.

We also find a small electron-number and transverse spin-density accumulation which scales with the bias and is more pronounced for the thinner wall [Fig. 6.9 (g,h,i,j)]. In order to isolate this effect we calculate the trajectory of the non-equilibrium spin in the system which is defined as

$$\mathbf{S}_{\mathrm{ne}} = \sum_i \mathbf{S}_i - 8 \sum_i \langle \boldsymbol{\sigma} \rangle_i \tag{6.1.15}$$

and plotted in Fig. 6.10 is actually the time variation of this quantity $\Delta\mathbf{S}_{\mathrm{ne}}(t) = \mathbf{S}_{\mathrm{ne}}(t) - \mathbf{S}_{\mathrm{ne}}(0)$. The factor of 8 before the total electronic spin in Eq. (6.1.15) is due to the equilibrium ratio of the onsite spin magnitudes – local spin $\hbar$ and itinerant spin-density $\hbar/8$ for a band-filling of $1.75e$/atom. Thus $\Delta\mathbf{S}_{\mathrm{ne}}(t)$ represents the accumulated non-equilibrium itinerant spin during the simulation. We find that after the initial, mainly longitudinal (along z), spin disruption until the steady state is established, $\Delta\mathbf{S}_{\mathrm{ne}}(t)$ falls into a precession very much confined to the x-y plane. Hence the accumulated spin during the current-induced DW motion is primarily transverse and it scales with the bias. With respect to this observation the two walls are very much alike. The difference is mainly in the amplitude of precession of $\Delta\mathbf{S}_{\mathrm{ne}}(t)$ about the y-axis which is perpendicular to the plane of the wall and we find higher amplitude oscillations for the thinner (and expectedly more non-adiabatic) wall.

In Fig. 6.10(c) are the plots of the averaged DW velocity V_{DW} against the average current I_{DW} at the wall during the whole simulation for each of the two walls. We again find a confirmation for the higher level of spin-transport non-adiabaticity for the thin wall as it is slower for nearly the same value of the current, which suggests a reduced efficiency of the STT mechanism. The relative difference in the slopes is about 8%.

6.1.3 Comparison with LLG equations

In this section we compare our combined quantum-classical simulations with the analytical predictions of Zhang and Li [135]. We recall that the Zhang and Li theory is derived from the *s-d* model by integrating out the electronic degrees of freedom, intrinsically coupled to a spin-relaxation bath, in the linear response limit. The resulting magnetization dynamics is then driven by two current-induced torques, one originating from the adiabatic dynamics and one originating from the non-adiabatic spin-relaxation effects. The Landau-Lifshitz-Gilbert (LLG) type of equation of motion derived by Zhang and Li [135] reads

$$\frac{\mathrm{d}\mathbf{S}_i}{\mathrm{d}t} = \frac{1}{\hbar}\left(J_S \sum_{j \in \mathrm{nn}[i]} \mathbf{S}_i \times \mathbf{S}_j + 2J_z \left(\mathbf{S}_i \cdot \hat{\mathbf{z}}\right)\left(\mathbf{S}_i \times \hat{\mathbf{z}}\right) \right) + b_J \frac{\partial \mathbf{S}_i}{\partial z} + c_J \mathbf{S}_i \times \frac{\partial \mathbf{S}_i}{\partial z} + \alpha \mathbf{S}_i \times \frac{\partial \mathbf{S}_i}{\partial t}, \tag{6.1.16}$$

where the last three torques are respectively the adiabatic term, the non-adiabatic one and the phenomenological Gilbert spin-damping term. We have then carried out numerical simulations of

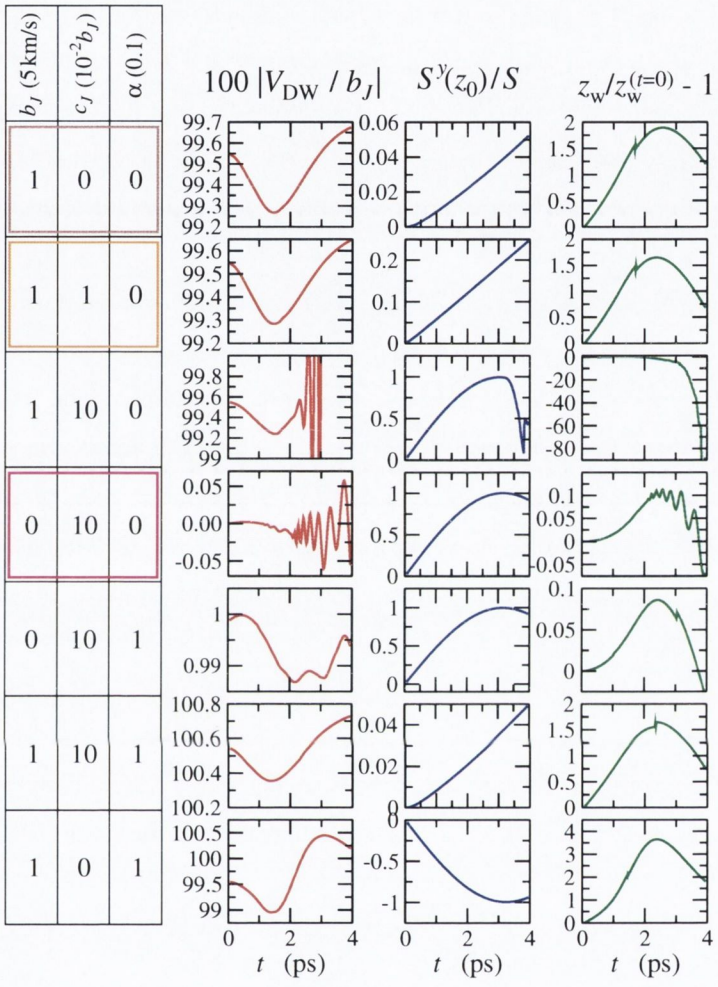

Figure 6.11: Results from simulations of a DW in a 400-atom spin chain modelled by Eq. (6.1.16) for different values of b_J, c_J and α, listed in the table. Plots from left to right represent the time evolution of the DW velocity (scaled by b_J), out-of-plane (y) local spin component at the DW centre and relative DW width.

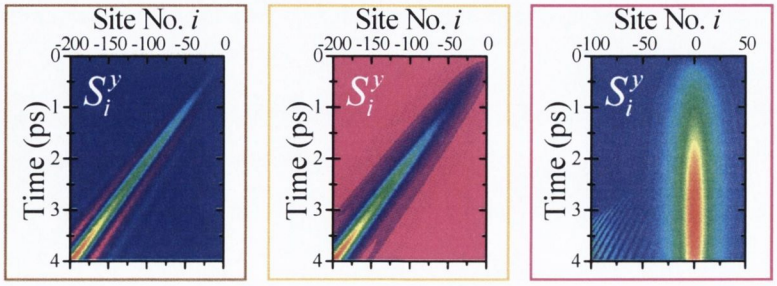

Figure 6.12: Local spins S_i^y evolutions in the colour-framed cases in Fig. 6.11 above. Magnitude is colour-coded (purple to red). The actual values at the DW can be deduced from Fig. 6.11.

the equation (6.1.16) investigating the torque-scaling constants b_J, c_J and α over a rather broad range. Our simulations are in some sense similar to those carried out by [89]. The results of those simulations are summarized in Fig. 6.11. As reference values for the various parameters we consider $b_J = 5\,\mathrm{km/s}$, $c_j = 10^{-2} b_j$ [66] and $\alpha = 0.1$. The value of b_J is actually chosen to reproduce similar velocities as the ones from our reference quantum-classical simulation [Eq. (6.1.14)] where $V_{\mathrm{DW}} \approx 20a/\mathrm{ps} \approx 5\,\mathrm{km/s}$ for $a = 2.5\text{Å}$.

Bearing in mind that our simulations effectively inspect only the short time-scale region (up to 4 ps) and that a thorough analysis is difficult, we can still conclude that the adiabatic torque is indeed the one driving the DW motion, at least at the beginning of its development. This is demonstrated by the fact that whenever $b_j = 0$ the DW does not move. Such a dynamics is in agreement with the quantum-classical simulations and with our previous observation that even for small DW thicknesses the electron spin-evolution is to a great extent adiabatic. The role of the non-adiabatic torque of Zhang and Li's form is instead more complicated. In general it drives the DW precession (see $S^y_{z_0}(t)$ in figure 6.11). Moreover for rather large values of c_J it generates DW deformation and spin waves emission [see the $(0, 10, 0)$ case in Fig. 6.12(c), where spin waves are excited in the second half of the simulation]. A similar effect is produced by the spin-damping term and indeed we observe situations where the damping and the non-adiabatic torque produce opposite dynamical evolution [see the $(1, 10, 1)$ case, where the DW precession is massively reduced, compared to the $(1, 10, 0)$ and $(1, 0, 1)$ cases where it evolves in different directions].

6.1.4 Summary on current-induced DW motion

We have investigated the current-induced DW motion within an time-dependent atomistic model, which in fewest words can be described as an open-boundary quantum-classical spin-dynamics. In this model the total spin is locally conserved throughout the system, apart from the boundaries, where phase-breaking and spin-relaxation takes place. As there is no explicit spin-relaxation mechanism in the interior, the only source of non-adiabaticity at the wall (or misalignment between the local and the itinerant spin) thus comes from the dynamically evolving spin-texture. As predicted by a few authors [17, 126, 131] non-adiabatic torques can arise from the mere "sharpness" (see Ref. [131]) of the wall, determined by non-negligible second gradients in the spin angular distribution. These effects decay with the width of the wall and the different models predict different powers in the inverse power law of this decay ranging from -1 to -5 [17] or even an exponential decay [131].

The advantage of our simulations is that they are based on fully quantum description of the itinerant electrons, there are no assumptions for the spin density distribution, no linear-response approximation and the starting texture of the wall is self-consistently relaxed. The disadvantage is

the computational cost and for this reason we restrict ourselves to systems of reduced dimensions with at most ~500 atoms and simulation times of a few picoseconds. For these times it is hard to extract information on the long-term behavior but we can semi-quantitatively analyze the processes that occur at the beginning of the current-induced dynamics. The spatial-scale we cover allows us to look at the medium-width walls which are too narrow to be treated in the adiabatic (diffusive) regime, but still not exactly point-like objects to be treated as such from a scattering viewpoint. We consider a range of DW widths between a few and a few tens of atomic spacings.

The results of comparing the current-induced dynamics of two walls that vary in size by a factor of four clearly demonstrate the presence of the non-adiabatic spin-transfer torques. Our aim has not been to make quantitative predictions but more to compare relative quantities for the two cases (our thinner wall is actually only a few atomic spacings wide, i.e. on the verge of being point-like object) and focus on the microscopic mechanism and the evolution of the non-adiabatic torque. Our main findings are that

- in both cases DW velocity scales linearly with current up to very high currents ($\sim 5 \times 10^{14}\mathrm{A/m^2}$ for typical interatomic distances of 2Å). The slopes are in fact very close to the one predicted if only the STT adiabatic torque was present [66] (though this is only an estimation which relies on the scalability of current-density to reduced dimension). However the slope of $V_{\mathrm{DW}}(I_{\mathrm{DW}})$ for the "thicker" wall is systematically higher by about 8%, indicating the better efficiency of the STT effect. This is, however, a very small variation, given the difference in the thicknesses of the walls.

- non-adiabatic torque generates spin waves, which is in agreement with the predicted oscillatory spatial dependence of that torque [131]. These occur much sooner for the "thinner" wall. There appears to be a critical point in the dynamics of the "thicker" wall after which the spin waves start to develop. During the pre-spin-waves dynamic the "thicker" wall is deformed by the STT.

- we can extract directly the non-equilibrium itinerant spin-density accumulation and map its trajectory. We have found that in both cases this is predominantly transverse. This quantity seems to precess about an axis nearly parallel to the chain with an increasing in time amplitude. In fact this amplitude scales with the magnitude of the current and is higher for the "thinner" wall.

Finally, we point out that further analysis is needed for the law of decay of the non-adiabatic torques with the increase of the thickness of the wall to be extracted or for a functional dependance

of $\mathbf{T}_{\text{nonad}}$ on the local spin texture to be deduced. It has been suggested [106] that higher-order torques in the gradient expansion of the local magnetization can be those responsible for the deformation of the wall and the Zhang and Li torque is just the first order in this expansion. Though we only observe the non-adiabatic effects related to the abruptness of the wall, we find that, at least in the short-timescale range (~4 ps), the non-adiabatic torques upon the wall on the verge of the atomic-scale abruptness have a minor effect on its average velocity. They, however, cause DW precession, deformation and spin-wave generation.

6.2 Spin motive force

6.2.1 Background and concepts

In the previous sections we have investigated how an electric current can affect the magnetization landscape of a magnetic nano-object. Here we explore the opposite effect, namely whether or not a driven magnetization dynamics can generate an electrical signal. Such an effect has been recently predicted by Barnes and Maekawa [12], who have proposed a generalization of Faraday's law to account for a non-conservative force of spin origin. This arises in systems with time-dependent order parameters as a result of Berry phase (BP) accumulation [18]. As an example they have considered a DW, formed in a finite ferromagnetic wire and precessing about a static co-axial external magnetic field, i.e. a magnetic system similar to those investigated in the previous sections. They demonstrated that in the adiabatic limit a constant potential shift $\Delta\phi$ is generated between the two ends of the wire. This is directly proportional to the angular frequency of precession of the wall ω,

$$\Delta\phi = \frac{\hbar}{e}\omega\,. \tag{6.2.1}$$

Moreover, if the ferromagnet is described by the Stoner mechanism $\Delta\phi$ exactly cancels the potential produced by the Zeeman interaction. Such a potential, described as a spin-motive force (SMF), has been recognized previously in the context of the Aharonov-Casher [86, 75] and Stern's [97] effects. These are all manifestations of BP related phenomena, where holonomies arise as a result of a parallel transport of some kind [4]. The latter does not need to be a quantum effect, another example being the classical Foucault pendulum [128].

In what follows we first demonstrate computationally the result of Eq. (6.2.1) through time-dependent quantum-classical simulations of an finite atomic wire incorporating a precessing DW. Then we also present an analytical classical argument for the driving mechanism of the SMF in this system. Our approach has the benefit of being "Berry-phase-free" in the sense that it does not need

to call for a Berry phase argument to explain the SMF and demonstrates the Newtonian nature of the conversion of the magnetic response of electronic spins into an electrostatic voltage drop. This is further illustrated with classical dynamical simulations for a system of classical magnetic dipoles in a rotating magnetic field mimicing the DW. In addition we show that if one abandons the Stoner model and accounts for a non-spin component of the magnetic moments forming the DW, the cancellation between the SMF and the Zeeman potential predicted by Barnes and Maekawa is incomplete. This leaves behind a non-zero net SMF, which can be experimentally measured.

Our simulations are also in this case based on the quantum-classical scheme and the *s-d* model both presented in section 5.2, and we use the Hamiltonian of equations (5.2.1) and (5.2.5). The parameters used for the simulations here are $\chi = -1$ eV, $\rho_0 = 1.75$, $U = 7$ eV, $J = 1$ eV, $J_z = 0.5$ meV, $g_S = 2$, $a \equiv R_{i,i+1} = 2.5$ Å. Note that here we consider interacting electrons and $U \neq 0$, which facilitates the definition of the intrinsic Coulombic potential in the system. $N = 400$ atoms so that the chain is much longer than the typical width of the relaxed DW (about 10 atomic spacings). The values of χ, J and $\rho_{(0)}$ are chosen such as to produce a halfmetallic system with a completely filled spin-up band, which lies about 0.5 V below the Fermi level.

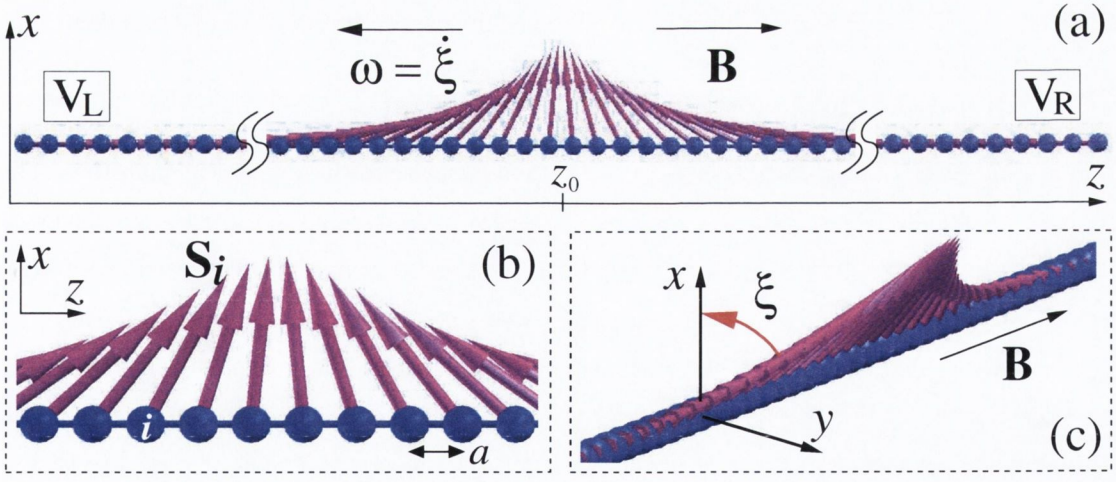

Figure 6.13: Different prospect views of the DW formed by the local spin $\{\mathbf{S}_i\}$ in the middle of a monoatomic chain. An external magnetic field, applied along the wire, induces a clockwise rotation of the DW about the z-axis.

The time-dependent simulations proceed as following. Initially the set of classical spins $\{\mathbf{S}_i\}^{(0)}$ is prepared in a DW arrangement (see Fig. 6.13) and relaxed self-consistently in the electronic environment. At time $t = 0$ the external magnetic field $\mathbf{B} = B\hat{\mathbf{z}}$ is switched on along the wire and a new initial electronic state is self-consistently determined for $\{\mathbf{S}_i\}^{(0)}$. The system is then

propagated according to Eqs. (5.2.8).

The electrostatic potentials $V_{\mathrm{L(R)}}$, developing away from the DW on the left(right)-hand-side of the chain, are computed as the spatial (over two identical sets $\mathbb{L}(\mathbb{R})$ of N_V atoms at each wire end) and temporal (over the evolution time T) averages of the onsite potential, i.e.

$$V_{\mathrm{L(R)}}(T) = 1/\left(TN_V\right) \sum_{i\in\mathbb{L}(\mathbb{R})} \int_0^T \mathrm{d}t \sum_{n=1}^{N} \frac{\kappa \Delta q_n(t)}{\sqrt{R_{in}^2 + (\kappa/U)^2}}\,, \tag{6.2.2}$$

where N is the total number of atoms and Δq_n is the excess electron charge on the n-th site. We investigate the stationary voltage drop $\Delta V_{\mathrm{calc}} = [V_{\mathrm{L}}(T) - V_{\mathrm{R}}(T)]$ that builds up across the system at the late stages T of the simulation. In the limit of local charge neutrality ($U \to \infty$) this potential build-up corresponds to the negative image of the energy landscape in the system. We anticipate two contributions to the overall potential drop

$$\Delta V = \Delta\phi - g_e \mu_{\mathrm{B}} B/e\,, \tag{6.2.3}$$

where the first term is due to the proposed non-conservative SMF from Eq. (6.2.1), while the second is due to the Zeeman split. In order to extract the effect of the SMF itself in the first set of simulations we have considered $g_e = 0$, so that only the first term in Eq. (6.2.3) remains.

6.2.2 Quantum-classical simulations

In Fig. 6.14 are the calculated time evolutions of some representative dynamical quantities. The DW in these simulations, driven by some large magnetic field, undergoes a steady-rate clockwise rotation (precession) with an angular frequency ω about the direction of the field [see Fig. 6.14(a)] and oscillates gently about a center z_0, slightly displaced to the left [see Fig. 6.14(b)]. Note that the wall does not propagate, since there is no net current or dissipation in the system. The steady rotation generates a SMF manifested in a potential drop with small oscillations that correlate with those of the DW centre (since the projection of the total spin in the system on the direction of the field is conserved) and which has an asymptotic time-averaged value ΔV_{calc} [see Fig. 6.14(c)]. The dependence $\Delta V_{\mathrm{calc}}(\omega)$, obtained by sweeping the external field between 20 T and 500 T, is linear [see Fig. 6.15(a)] with a slope $\hbar_{\mathrm{calc}} = 0.606\,\mathrm{eV\,fs} \approx 0.92\,\hbar$. Note that the extremely large magnetic fields employed in our simulation are only instrumental and facilitate a fast DW precession and therefore a higher SMF generation. This is necessary to guarantee that our time-dependent simulations do not run over long times, and therefore become numerically unstable. Importantly, our system remains adiabatic even at such large rotation frequencies (we elaborate on this later in this section).

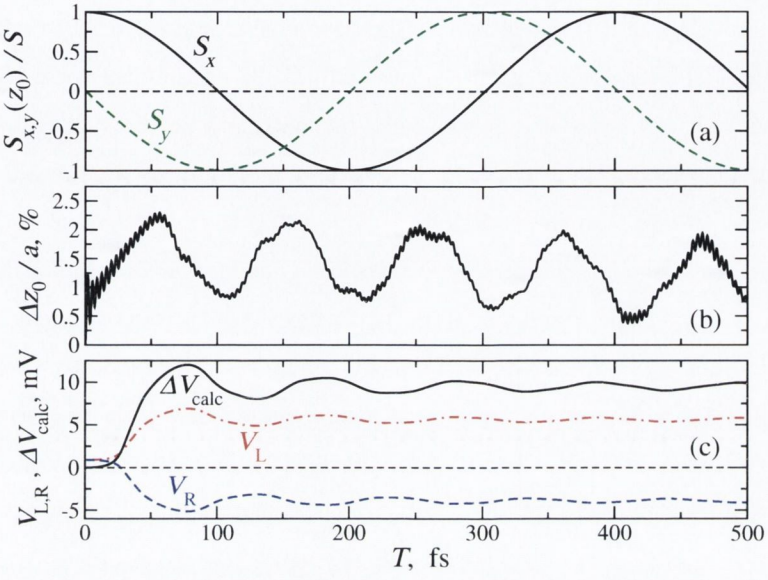

Figure 6.14: Time evolution of some dynamical variables at $B = 100\,\mathrm{T}$ and for $g_e = 0$: (a) $\mathbf{S}_x$ and $\mathbf{S}_y$ local spin components at the DW center z_0, showing the clockwise rotation of the DW about the z-axis. The angular frequency ω of the DW precession is extracted by fitting $S_x(T)$ to $\cos(\omega T)$; (b) longitudinal displacement of the DW center z_0; (c) averaged potentials V_L, V_R and ΔV_calc (see text).

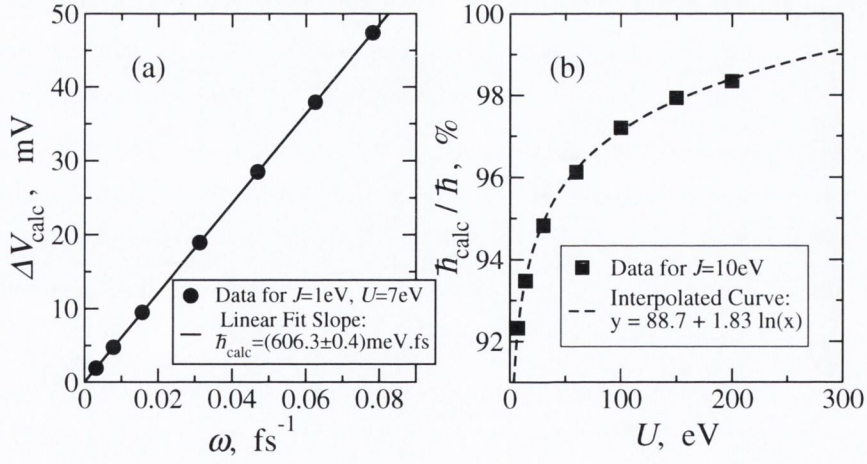

Figure 6.15: Calculated SMF as a function of the DW precession and dependence of the slope over the Coulomb parameter U for $g_e = 0$ and $g_\mathrm{S} = 2$. (a) The calculated stationary ΔV depends linearly on ω with a slope $\hbar_\mathrm{calc} \approx 0.92\hbar$ for realistic values of the parameters J and U; (b) $\hbar_\mathrm{calc}$ tends to saturate at the exact value of $\hbar$ with increasing U.

The deviation of $\hbar_{\mathrm{calc}}$ from the exact $\hbar$ [from Eq. (6.2.1)] is studied with respect to the two main assumptions which allow to identify the analytic result in Eq. (6.2.1) with our calculated potential drop $|\Delta V_{\mathrm{calc}}|$ from Eq. (6.2.2): (i) the adiabaticity and (ii) the local charge neutrality, which is exact only for $U \to \infty$. The first criterion is controlled by the value of J as in the limit $J \to \infty$ the system is perfectly adiabatic. In our previous analysis on the adiabaticity of the current-induced DW motion (previous section) we found that the typical value of the *s-d* exchange strength $J = 1\,\mathrm{eV}$ provides a predominantly adiabatic regime for walls of similar dimensions. Here we have tested that increasing J ten times results in less than 1% improvement in $\hbar_{\mathrm{calc}}/\hbar$. This ratio, however, is found to be sensitive to U and it asymptotically tends to 1 as U is increased [see Fig. 6.15(b)]. This result demonstrates the generation of SMF with magnitude given by Eq. (6.2.1), originating from the precession of the wall, in DWs at the atomic scale and is, in some sense, another confirmation of the adiabaticity of our model systems.

In reality, however, the effect of the applied magnetic field on the electrons cannot be switched off. We, therefore, return to Eq. (6.2.3) and rewrite it in the form

$$\Delta V = \frac{\hbar}{e}\omega - \frac{g_e}{g_{\mathrm{S}}}\frac{\hbar}{e}\omega_{\mathrm{S}} = \left(1 - \frac{g_e}{g_{\mathrm{S}}^*}\right)\frac{\hbar}{e}\omega. \tag{6.2.4}$$

Here $\omega_{\mathrm{S}} = g_{\mathrm{S}}\mu_B B/\hbar$ is the Larmor frequency of the local spins. The actual angular frequency of precession of the DW ω differs slightly from ω_{S} due to the exchange interaction with the conduction electrons. In order to account for this effect, we have introduced in Eq. (6.2.4) an effective g_{S}^* such that $\omega = g_{\mathrm{S}}^*\mu_B B/\hbar$. We have then verified Eq. (6.2.4) numerically by varying the value of g_{S} (see Fig. 6.16). The effective value g_{S}^* is determined by the calculated precession frequency of the wall (Fig. 6.16c). It is equivalent to $g_{\mathrm{S}} = g_{\mathrm{S}}^* = 2$ only when $g_e = g_{\mathrm{S}} = 2$. In any other case the conduction electrons act either as a friction ($g_e < g_{\mathrm{S}}$) or as a driving force ($g_e > g_{\mathrm{S}}$) to the DW rotation. First manifestation of such effect was observed in Section 5.3.1, where we have shown an increase of the spin-wave dispersion band-width as a function of the exchange parameter J (see Fig. 5.6). Finally we have again obtained a value of $\hbar_{\mathrm{calc}} \approx 0.92\,\hbar$, identical to the previous finding in the case $g_e = 0$ for the same choice of J and U.

Apparently, the voltage drop across the system fully disappears when $g_{\mathrm{S}} = g_{\mathrm{S}}^* = g_e$, as derived in Ref. [12] for the Stoner model. However, in *s-d* systems, where g_{S}^* might as well carry some orbital component, this is not the case and the SMF manifests itself as a measurable quantity. This could be used to determine the effective g-factor of the localized spins. In particular if the DW precession is blocked, the measured drop would be just equal to the Zeeman split, i.e. a measurement could determine if the wall is precessing or not. In the remaining part of the Chapter we discuss whether or not the mechanism for the SMF is expected also for a classical system.

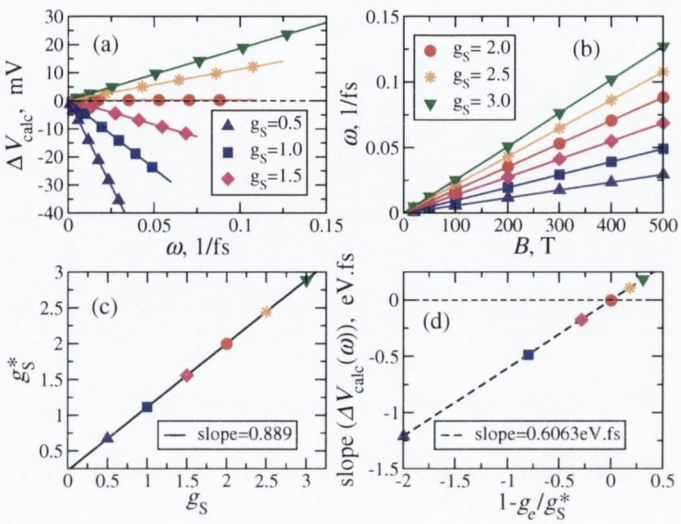

Figure 6.16: Computational demonstration of Eq. (6.2.4) for $g_e = 2$ and a set of values $g_S = 0.5 \div 3$. Panel (a) shows the linear dependence of the stationary potential drop $\Delta V_{\rm calc}$ on the angular precession frequency ω; (b) is used to determine the effective g-factors g_S^* and they are compared to the input values g_S in (c). Note that $g_S^* = g_S$ for $g_S = g_e = 2$. Panel (d) demonstrates the validity of Eq. (6.2.4).

6.2.3 Purely classical simulations

Instead of quantum electrons (as in the previous section) we now consider non-interacting classical particles with an intrinsic angular momentum $\mathbf{s}$ ($|\mathbf{s}| = s = \hbar/2$) and with the electron mass m_e. These are trapped in a one-dimensional box, immersed in a magnetic field of the form

$$\mathbf{b}(z,t) = b\,(\cos(ft)\sin(\theta_z),\, \sin(ft)\sin(\theta_z),\, \cos(\theta_z)) \tag{6.2.5}$$

Here $\theta_z = \theta(z)$ is chosen such as to mimic a continuous DW structure [1], [2], rotating rigidly with an angular frequency f. In this classical problem f is analogous to ω from the quantum simulation, though $f > 0$ corresponds to an anticlockwise rotation about the longitudinal axis. The classical Hamiltonian of the spin-particles (or classical magnetic dipoles) in the field $\mathbf{b}$ is analogous to that of the quantum electrons interacting with local spins $\{\mathbf{S}_i\}$,

$$\mathcal{H}_{\rm class} = \frac{p^2}{2m_e} - \gamma \mathbf{s}\cdot\mathbf{b}(z,t)\,, \tag{6.2.6}$$

[1] The energy-minimising angular distribution of a planar DW in one-dimensional anisotropic Heisenberg spin model is $\theta_z \equiv \theta(z) = 2\arctan\left(\exp((z-z_0)/z_{\rm w})\right)$, where z_0 is the position of the wall and $z_{\rm w}$ is its width.

[2] Note that such magnetic field is irrotational, i.e. it cannot be derived as a curl of a vector potential. This means that, strictly speaking, our predictions are not experimentally verifiable. In this case $\mathbf{b}$ is simply instrumental, used to map our quantum simulations onto classical ones.

where γ is the coupling strength (replacing J of the quantum case) and p is the canonical momentum of the particles. Then Hamilton's equations of motion [3] are

$$m_e \ddot{z} = \gamma \mathbf{s} \cdot \nabla_z \mathbf{b}(z,t), \quad \dot{\mathbf{s}} = \gamma \mathbf{s} \times \mathbf{b}(z,t)\,, \tag{6.2.7}$$

where $\nabla_z \equiv (\partial/\partial z)_{\mathbf{s},t}$.

We consider the limit of large γb, in which the dynamics of the spin-particle becomes adiabatic, in the sense that $\mathbf{s}$ remains closely aligned with $\mathbf{b}$ and its precession about $\mathbf{b}$ is by far the fastest motion in the system. However, in order for $\mathbf{s}$ to follow $\mathbf{b}(z,t)$, there must always be *some* residual misalignment [15] between the two. This is necessary in order to generate those torques, which, when averaged over the quick precession of $\mathbf{s}$, enable $\mathbf{s}$ to keep up with $\mathbf{b}(z,t)$. This small misalignment, marked by the angle φ in Fig. 6.17, is also the origin of the effective Newtonian force on the spin-particle that manifests itself as SMF.

The cartoon in Fig. 6.17 depicts $\mathbf{s}$ and $\mathbf{b}$ at some instance of the particle's migration and helps us to calculate the forces acting on the classical dipoles. This is achieved by differentiating the relation between the angles at the bottom vertex of the tetrahedron $\cos\alpha = \cos\varphi\cos\theta - \sin\varphi\sin\theta\cos\beta$ under the condition $s_{\varphi 1} = s\sin\varphi\sin\beta = \text{const}$ (which corresponds to keeping $\mathbf{s}$ and t fixed). In the adiabatic limit $\varphi \to 0$, we obtain

$$\nabla_z \varphi = -\cos(\beta)\,\nabla_z \theta\,. \tag{6.2.8}$$

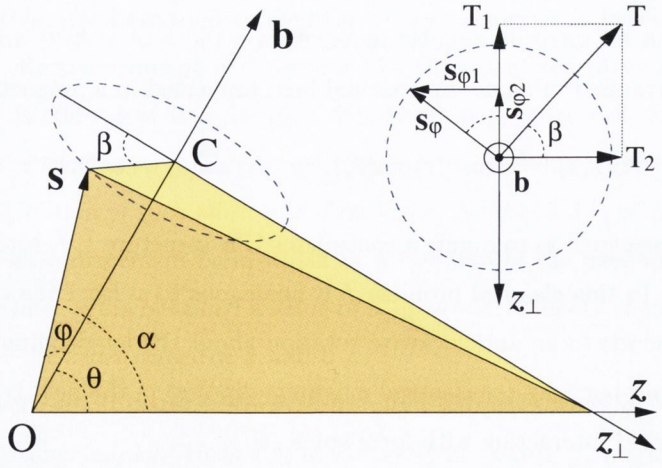

Figure 6.17: A snapshot of spin-particle's passage through the DW-like region of $\mathbf{b}(z,t)$.

From Eq. (6.2.7) the longitudinal force F_z and the torque $T = |\mathbf{T}| = \gamma s_\varphi b$ are related by

$$F_z = -\gamma|\mathbf{s}||\mathbf{b}|\sin(\varphi)\nabla_z\varphi = -T\nabla_z\varphi = T_2\nabla_z\theta\,, \tag{6.2.9}$$

where Eq. (6.2.8) has been applied and the full torque T decomposed into two orthogonal torques with magnitudes $T_1 = T\sin\beta$ and $T_2 = T\cos\beta$ (see the inset of Fig. 6.17).

In the adiabatic regime ($s_\varphi \ll s$), we average the two components of the torque over the fast precession of $\mathbf{s}$ about $\mathbf{b}$. These averaged torques $\overline{T_1}$ and $\overline{T_2}$ must be driving the two separate motions of the spin as the particle crosses the region of the rotating magnetic field. A rotation in the b-z plane enables $\mathbf{s}$ to keep up with the spatial variation of $\mathbf{b}$, and another rotation in a plane perpendicular to the z-axis which makes $\mathbf{s}$ follow the anticlockwise precession of $\mathbf{b}$, and thus

$$\overline{T_1} \approx s\dot{z}\nabla_z\theta, \qquad \overline{T_2} \approx -|\mathbf{s}\times\mathbf{f}| = -sf\sin\theta\,. \tag{6.2.10}$$

If one applies Eq. (6.2.9), the averaged linear force upon the spin-particle in the rotating magnetic field can be written as $\overline{F_z} = \overline{T_2}\nabla_z\theta = sf\sin(\theta)\nabla_z\theta$ and therefore the work done by the rotating DW-like field (or the SMF) on the spin-particle for one traversal (left to right) is

$$W_{\mathrm{L}\to\mathrm{R}} = \int_{z_\mathrm{L}}^{z_\mathrm{R}} \overline{F_z}\mathrm{d}z = -s\,f\int_0^\pi \sin(\theta)\mathrm{d}\theta = -2sf\,, \tag{6.2.11}$$

where $z_{\mathrm{L,R}}$ are the leftmost and the rightmost position of the spin-particle on the wire far from the region of spatial variation of the field. This result has been derived with the single assumption of adiabaticity. The adiabatic condition is $s_\varphi \ll s$ and for it to hold it is necessary that the two components of s_φ averaged over the rapid precession, simultaneously satisfy the latter, i.e.

$$\begin{aligned} \overline{s_{\varphi 1}} &= \overline{T_1}/\gamma b = sv\nabla_z\theta/\gamma b \ll s\,, \\ \overline{s_{\varphi 2}} &= \overline{T_2}/\gamma b = sf\cos(\theta)/\gamma b \ll s\,. \end{aligned} \tag{6.2.12}$$

Thus, considering the maximum attainable values of the right-hand sides and since $\max(\nabla_z\theta) = 1/z_\mathrm{w}$, the necessary conditions for adiabaticity are

$$1/t_\mathrm{w} \ll f_\mathrm{L}, \quad f \ll f_\mathrm{L} \tag{6.2.13}$$

where t_w is the time it takes for the spin-particle to cross the region, where the magnetic field $\mathbf{b}$ changes spatially over the width z_w and $f_\mathrm{L} = \gamma b$ is its Larmor precession frequency about $\mathbf{b}$.

In order to mimic the typical strength of the exchange interactions ($\sim 1\,\mathrm{eV}$) in our classical simulations, we have used $\gamma = 2\mu_B/\hbar$ and $b = 10^5$ T. We have simulated an ensemble of $N = 700$ noninteracting spin-particles, confined in a 400 Å-long atomic wire. The particles start at random positions within two regions near both wire ends and with velocities identical in magnitude ($v_0 = 8$ Å) but random in sign. The DW-like region has $z_\mathrm{w} = 5$ Åwhich is similar to the z_w, fitted to the relaxed DW profile in the quantum simulation (in units of atomic spacing) and the typical passage

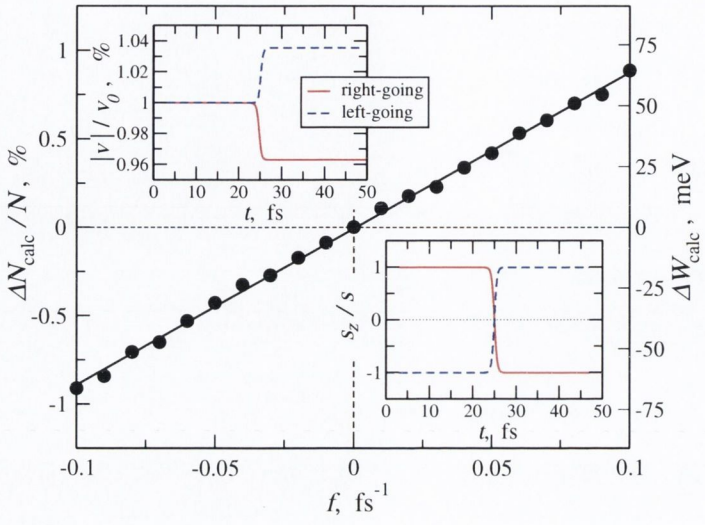

Figure 6.18: The spatial particle imbalance $\Delta N/N$ and the potential energy difference ΔW as a function of the angular frequency f of rotation of the DW-like field. The insets represent the change of the velocity and the longitudinal component of the spin of a particle for one left-to-right (solid) and one right-to-left (dashed line) traversal of the wire for $f = 0.2\,\mathrm{fs}^{-1}$.

time is $t_w \approx 1 \div 2\,\mathrm{fs}$. We have used frequencies $|f| \leq 0.2\,\mathrm{fs}^{-1}$. Since our $f_L = \gamma b = 17.6\,\mathrm{fs}^{-1}$, these parameters well satisfy the adiabatic conditions of Eq. (6.2.13).

We have integrated numerically Eqs. (6.2.7) and found a stationary difference in the number of particles to the left and to the right of the DW-like region, $\Delta N_{calc} = N_R - N_L$, developing in time and depending linearly on the frequency f of rotation of the field (see Fig. 6.18). By energy conservation, ΔN_{calc} converts to a potential energy shift

$$\Delta W_{calc} = 2m_e v_0^2 \Delta N_{calc}/N \tag{6.2.14}$$

and the latter is a manifestation of the SMF work $-W_{L\to R}$, derived in Eq. (6.2.11). Eq. (6.2.14), relating of particle imbalance to SMF, is only valid if the particles have enough initial kinetic energy to traverse the wall from both sides, which, from one of the sides, means climbing the SMF ramp. Thus the requirement

$$m_e v_0^2/2 > 2sf \tag{6.2.15}$$

sets a lower limit on the initial velocity of the spin-particles in our simulations, for a given f.

Within the adiabatic regime the dependence of ΔW_{calc} on f is found to be linear with a slope of $(0.643 \pm 0.012)\,\mathrm{eV.fs}$ (see the right-hand side scale of Fig. 6.18) and agrees with the analytical prediction of $2s = \hbar = 0.658\,\mathrm{eV.fs}$ in Eq. (6.2.11).

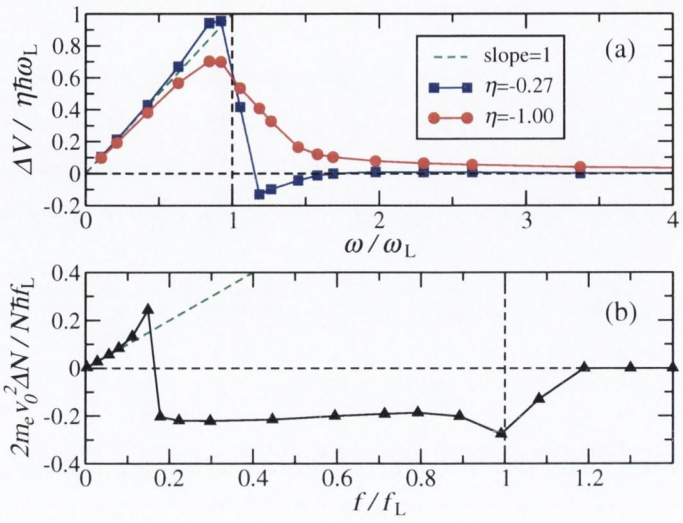

Figure 6.19: Plots of the SMF as a function of the DW rotation frequency in units of the Larmor precession frequency of the itinerant spins about the local field. We present the case of dynamics away from the adiabatic regime for both the quantum [panel (a)] and the classical [panel (b)] simulations. Dashed pale lines in both panels correspond to a slope of 1.

The directions of the SMF observed in the quantum and the classical simulations agree with the one set by Eq. (6.2.11), i.e. the SMF is opposite to the direction of the angular velocity of the DW rotation if the itinerant spins are aligned parallel to the local field. Note that with the choice of the band structure in our quantum simulations the effect is carried by the down-spin, so that for all other parameters being equal the sign of the SMF is opposite to that of the classical model. In general, the direction and magnitude of the voltage drop is found to scale with the Fermi level spin-polarization $\eta = (D_\uparrow - D_\downarrow)/(D_\uparrow + D_\downarrow)$, being $D_{\uparrow(\downarrow)}$ the spin-up(down) density of states at the Fermi level, and ω as $V_{\mathrm{L}\to\mathrm{R}} = -\eta\hbar\omega/\mathrm{e}$, where $\omega > 0$ corresponds to an anticlockwise rotation of the DW (spin) about the z-axis. For the half-metallic case studied here $\eta = -1$.

A further similarity between the quantum and the classical simulations, pointing to the classical origin of the "quantum" SMF, is that the quantum effect relies strongly on the adiabatic conditions set by Eq. (6.2.13). As illustrated by Fig. 6.19(a) the effect dies out completely above the Larmor precession frequency $\omega_{\mathrm{L}} = J/\hbar$ of the exchange coupled spins for any choice of band filling. The threshold in the classical case below f_{L} [see Fig. 6.19(b)] is an artefact of the classical model and occurs at $f = f_c = (m_e v_0^2/2)/\hbar$ as determined by Eq. (6.2.15). Once again, the classical result is the same in magnitude SMF $\Delta\phi = \hbar\omega/e$, where the $\hbar$ factor comes from the magnitude s of the intrinsic angular momenta, adopted to represent the electron spin, i.e. $2s = \hbar$.

6.2.4 Summary on the spin-motive force

In the forgoing Section we have demonstrated computationally the presence of a spin-motive force in a quantum-classical system with a spatially and temporally dependent order parameter and our calculated SMF has almost the same magnitude as the one described by Barnes and Maekawa [12]. In fact, the small deviations from the expected $\hbar\omega$ are a measure of the level of metallicity and spin-transport adiabaticity of the system. In addition, we have considered the more general case of an order parameter of mixed spin and orbital character in which case a measurable voltage drop across the system could indicate the presence of the SMF.

We have also presented a classical argument for the mechanism of the SMF in the adiabatic regime and specified the necessary conditions for the so-important adiabaticity. The latter analysis is supported by purely classical simulations of particles with intrinsic angular momentum in a magnetic field with the spatial and temporal properties of the order parameter in the quantum case. The result is the same in magnitude SMF $\Delta\phi = \hbar\omega/e$, where the $\hbar$ factor comes from the magnitude s of the intrinsic angular momenta, considered to represent the electron spin, i.e. $2s = \hbar$.

Chapter 7

Conclusion

The aim of this Thesis has been to develop a description of spin-dynamics at the atomic level and address spin-torque related phenomena in mesoscopic systems under current-carrying conditions. The phenomenology investigated here, stands at the borderline between the typical molecular spintronics problem of quantum transport in low-dimensional molecular junctions [83] and that of the current-induced spin-torque effect, for instance, in magnetization-switching spin-valves. Our spin-dynamics scheme in itself is based on the spin-analogy of the Born-Oppenheimer approximation [7, 6] and is very close in spirit to the electromigration problem in mesoscopic systems [95].

In Chapters 2 and 3 we focussed on the quasi-static approach to the spin-dynamics in a Landauer-type ballistic junction, where the two leads have opposite spin polarization and they are connected by a monoatomic spin-chain. We used a two-band collinear-spin TB model for the electronic structure and quasi-statically mapped out the activation barriers for thermally-activated DW migrations. We found a small, but non-linearly scaling with the bias, current-induced increase of the barrier heights. Typical barrier heights were of the order of 50 meV. We found a significant spin-filtering effect in the form of a strong dependence of the conductance on the microscopic spin arrangement inside the constriction and concluded that thermally activated spin-flips in the junction may lead to random telegraph noise in the conductance measurements. We also investigated the effect of band-hybridization and disorder and found that in both cases at any finite bias the activation barriers are asymmetric, promoting a pinning of the wall. The problem of the conservativeness of the current-induced torques was addressed numerically and the answer was negative, meaning that quasi-static spin-torques actually perform work for closed-loop spin-transitions on the expense of the battery. Finally, we introduced mechanical forces in the same framework and found that the magneto-mechanical interplay on the atomic scale is much stronger in one direction, being that structural rearrangements affect the spin-dynamics but not the converse. We attributed the relative insensitiveness of the atomic structure with respect to microscopical spin-rearrangements

to the fact that interatomic forces depend on the total charge density of the current-carrying electrons, not on their spin polarization.

In Chapter 4 we made a comparison between an empirical TD model of steady-state ballistic transport on an augmented finite system and the self-consistent NEGF description of the corresponding full-scale Landauer problem. We applied it to a model system, featuring multiple steady-states, degenerate in the static approach and found that the time-dependent method is able to self-select the energetically-preferable one. We also demonstrated that under certain assumptions about the binding of the device to the "open-boundary" capacitor and in the limit of "large" capacitor this empirical TD approach is identical to the Landauer steady-state.

In the last two Chapters (5 and 6) we presented and discussed the theoretical foundations of fully non-collinear time-dependent spin-dynamics simulations for both open and closed systems. This was also based on the adiabatic spin-approximation and constituted an Ehrenfest MD for spin. In particular we approached a range of phenomena including the calculation of spin-wave spectra, dynamical indirect exchange of localized spin in metallic medium and finally the current-induced domain wall (DW) motion and spin-motive force generation. We demonstrated how spin-dynamics can provide unique insights into the device behaviour, beyond what is possible with steady-state quasi-static approaches for the type of systems in focus. For instance, this can be used to investigate non-adiabatic (in terms of the local alignment of the itinerant spin to the localized spin) effects in the case of very narrow (a few lattice spacings) magnetic DWs. Other dynamical effect, accessible to the TD simulations, was the demonstrated generation of a spin-motive force by the precessing DW. This was further analyzed from a classical perspective and relevant parallels were demonstrated.

Although our calculations have been carried out in the framework of the self-consistent tight-binding method (including mean-field Hartree interactions), these are conceptually extendable to more general first-principles approaches such as the time-dependent density functional theory (TDDFT). A development in this direction would be the natural extension of the work presented in this Thesis and this is the objective of on-going consideration. We envision that these methods may soon become an invaluable tool for investigating spin-dynamics in nano- and atomic-scale devices.

Appendix A

Surface Green's function for a semi-infinite cubic lattice with a finite cross-section

All transport-relevant information about a perfectly periodic semi-infinite lead with a finite cross-section is in its *surface Green's function* $\hat{G}$ (a more formally-correct term for this object would be *surface Greenian operator*). The latter, when projected on a grid of atomic orbitals in a tight-binding (TB) fashion (see Appendix C for details on TB), is a matrix $\hat{G} \to \{G_{ij}\} \equiv \{G(\mathbf{R}_i, \mathbf{R}_j)\}$ of two-point stationery Green's functions (GFs), $\{G(\mathbf{R}_i, \mathbf{R}_j)\}$, as defined in Eq. (2.2.2) but for $\mathbf{R}_i$ and $\mathbf{R}_j$ representing atomic sites on the surface. Here we derive the analytic expression (3.2.16) for the surface Green's function matrix of a cubic-lattice semi-infinite lead within a single-orbital nearest-neighbour tight binding model. This derivation follows the derivation in Ref. [110, 107] and is based on the Dyson equation for the Greenian operator

$$\hat{G} = \hat{G}^0 + \hat{G}^0 \hat{V} \hat{G} \tag{A.0.1}$$

which describes the relation between the "unperturbed" Green's function $\hat{G}^0 = \left[E\hat{I} - \hat{H}^0\right]^{-1}$ and the "perturbed" one $\hat{G} = \left[E\hat{I} - \hat{H}^0 - \hat{V}\right]^{-1}$, where $\hat{H}^0$ is the unperturbed Hamiltonian, $\hat{V}$ is the perturbing potential [1] and we have omitted the E dependence for brevity.

[1] Note that V need not be small for the Dyson equation to hold. Equation (A.0.1) can be obtained easily by substituting the $\left[E\hat{I} - \hat{H}^0\right] = \left[\hat{G}^0\right]^{-1}$ into the expression for $\hat{G}$.

A. SURFACE GREEN'S FUNCTION FOR A SEMI-INFINITE CUBIC LATTICE WITH A FINITE CROSS-SECTION

We firstly look at the simplest example – the surface [1] Green's function of a semi-infinite linear chain. Let the sites in the chain be numbered starting from the end with number "1" as depicted in Fig. A.1(a). We can write the Dyson equation only for the cluster of the two end atoms "1" and "0" before and after they are connected [see Fig. A.1(b)] as if (only for this argument) "1" is not connected to the rest of the chain

$$\begin{pmatrix} G_{00} & G_{01} \\ G_{10} & G_{11} \end{pmatrix} = \begin{pmatrix} G^0_{00} & G^0_{01} \\ G^0_{10} & G^0_{11} \end{pmatrix} + \begin{pmatrix} G^0_{00} & G^0_{01} \\ G^0_{10} & G^0_{11} \end{pmatrix} \begin{pmatrix} 0 & \chi \\ \chi & 0 \end{pmatrix} \begin{pmatrix} G_{00} & G_{01} \\ G_{10} & G_{11} \end{pmatrix} , \qquad \text{(A.0.2)}$$

where $\chi < 0$ is the intersite hopping and the subscript 0 is for the Green's functions before the two atom cluster is coupled. It follows that

$$G_{00} = G^0_{00} + \chi G^0_{00} G_{10} , \qquad G_{10} = \chi G^0_{11} G_{00} . \qquad \text{(A.0.3)}$$

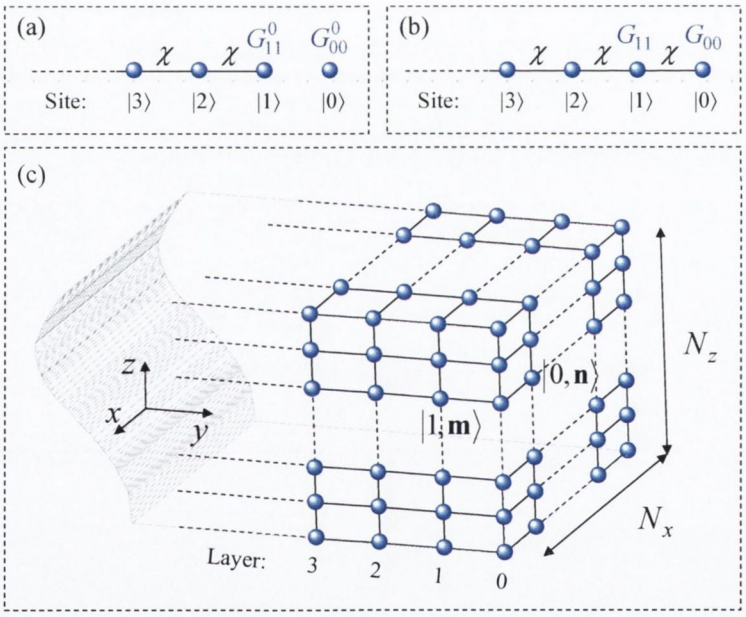

Figure A.1: fApp1 Schemes of semi-infinite cubic lattice structures: (a) and (b) represent an atomic chain before and after the end atom "0" is attached. In panel (c) is a 3D structure with finite cross-section and layers numbered similarly to the 1D chain.

If we bring back the rest of the chain into the discussion, as it extends to infinity, obviously attaching the atom "0" to it would not change its end Green's function and therefore $G_{00} = G^0_{11}$.

[1] Since it is a 1D case, it is probably more appropriate to talk about "end" Green's function instead of a surface one. Also we always consider the retarded (causal) Green's function.

Hence we obtain a quadratic equation for the surface Green's function of the chain in terms of the free atom's retarded Green's function G^0_{00} and the hopping χ

$$G_{00} = G^0_{00} + \chi^2 G^0_{00} \left(G_{00}\right)^2 , \quad \text{where} \quad G^0_{00} = \lim_{\eta \to 0+} 1/\left(E - \mathcal{E}_0 + i\eta\right) \tag{A.0.4}$$

as we consider a single level at some energy $\mathcal{E}_0$. The solution of Eq. (A.0.4) is

$$G_{00}(E, \mathcal{E}_0) = \frac{(E - \mathcal{E}_0) \pm \sqrt{(E - \mathcal{E}_0)^2 - 4\chi^2}}{2\chi^2} \tag{A.0.5}$$

with the following convention for the sign in front of the square root

$$\left\{ \begin{array}{l} -, \text{ for } |E - \mathcal{E}_0| < 2\,|\chi| \\ +, \text{ for } |E - \mathcal{E}_0| > 2\,|\chi| \text{ and } E - \mathcal{E}_0 < 0 \\ -, \text{ for } |E - \mathcal{E}_0| > 2\,|\chi| \text{ and } E - \mathcal{E}_0 > 0 \end{array} \right. \iff \left\{ \begin{array}{l} -, \text{ for } E > \mathcal{E}_0 - 2\,|\chi| \\ +, \text{ for } E < \mathcal{E}_0 - 2\,|\chi| \end{array} \right. , \tag{A.0.6}$$

which are based on the requirements [1] that $\mathrm{Im}\left[G_{00}\right] < 0$ and that $G_{00} \to G^0_{00}$ for $\chi \to 0$ [110, 107]

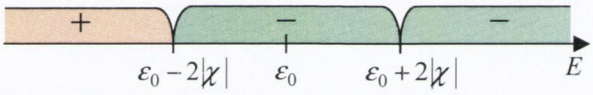

Figure A.2: A cartoon of the sign convention in Eq. (A.0.6).

We now use this result for the chain [Eq. (A.0.5)] to derive the surface Green's function of a three-dimensional (3D) cubic-lattice semi-infinite lead [see Fig. A.1(c)]. Since there is an analogy between the periodically repeating atomic sites of the chain and the transverse layers of the lead, we only need to unfold the 2D degrees of freedom within each layer of $N_x \times N_z$ atoms. Let us denote the single orbital on the site located at $\mathbf{n} = (n_x, n_z)$ on the l-th layer in isolation by $|l, \mathbf{n}\rangle$. Going into 2D momentum space, we have $N_x N_z$ eigenmodes with wavevectors $\mathbf{q} = (q_x, q_z)$, such that [107]

$$|l, \mathbf{q}\rangle = \sqrt{\frac{2}{N_x + 1}} \sqrt{\frac{2}{N_z + 1}} \sum_{n_x=1}^{N_x} \sum_{n_z=1}^{N_z} \sin\left(\frac{q_x n_x \pi}{N_x + 1}\right) \sin\left(\frac{q_z n_z \pi}{N_z + 1}\right) |l, \mathbf{n}\rangle , \tag{A.0.8}$$

[1] The physically relevant choice between these two solutions is described in Ref. [110]. If the expression under the square root is negative then the minus sign is taken as this provides for $\mathrm{Im}\left[G_{00}\right] < 0$ (electron number density is proportional to $-\mathrm{Im}(G_{00})$). If the expression under the root is positive the sign is determined by the condition $G_{00} \to G^0_{00} = 1/(E - \mathcal{E}_0)$ for $\chi \to 0$. To take the latter limit we rewrite Eq. (A.0.10) as

$$G_{00}(E, \mathbf{q}) = \frac{[E - \mathcal{E}_0]^2 - \left[(E - \mathcal{E}_0)^2 - 4\chi^2\right]}{2\chi^2 \left[E - \mathcal{E}_0) \mp \sqrt{(E - \mathcal{E}_0)^2 - 4\chi^2}\right]} = \frac{2}{E - \mathcal{E}_0 \mp \sqrt{(E - \mathcal{E}_q)^2 - 4\chi^2}} \to \frac{2}{E - \mathcal{E}_0 \mp |E - \mathcal{E}_0|} . \tag{A.0.7}$$

Now it is apparent that in the limit $\chi \to 0$ the relevant solution is the one with the minus for $E - \mathcal{E}_0 > 0$ [in Eq. (A.0.10)] and plus for $E - \mathcal{E}_0 < 0$. This convention for the sign is illustrated in Fig. A.2.

and eigenenergies

$$\mathcal{E}_q \equiv \mathcal{E}(\mathbf{q}) = -2\,|\chi| \cos\left(\frac{q_x \pi}{N_x + 1}\right) - 2\,|\chi| \cos\left(\frac{q_z \pi}{N_z + 1}\right). \tag{A.0.9}$$

Then, within a nearest-neighbour tight binding model (homogeneous in all directions) for a particular transverse mode $\mathbf{q}$ we define $G_{ll'}(E, \mathbf{q}) \equiv \left\langle l, \mathbf{q} \middle| \hat{G} \middle| l', \mathbf{q} \right\rangle$. Analogously to the chain's end GF [see Eq. (A.0.5)], the surface GF of the lead for a given transverse mode q is thus

$$G_{00}(E, \mathbf{q}) = G_{00}(E, \mathcal{E}_0 = \mathcal{E}_q) = \frac{E - \mathcal{E}_q \pm \sqrt{(E - \mathcal{E}_q)^2 - 4\chi^2}}{2\chi^2}, \tag{A.0.10}$$

and the relevant sign rule is as in Eq. (A.0.6) but with $\mathcal{E}_0$ swapped for $\mathcal{E}_q$.

Finally, we convert the surface Green's function back to real-space basis, using Eq. (A.0.8)

$$g_{mn}(E) \equiv G_{00}(E; \mathbf{m}, \mathbf{n}) = \textstyle\sum_{\mathbf{q}} \langle 0, \mathbf{m} | 0, \mathbf{q} \rangle\, G_{00}(E, \mathbf{q})\, \langle 0, \mathbf{q} | 0, \mathbf{n} \rangle = \tag{A.0.11}$$
$$= \sqrt{\tfrac{2}{N_x+1}} \sqrt{\tfrac{2}{N_z+1}} \textstyle\sum_{\mathbf{q}} \sin\left(\frac{q_x m_x \pi}{N_x+1}\right) \sin\left(\frac{q_z m_z \pi}{N_z+1}\right) \sin\left(\frac{q_x n_x \pi}{N_x+1}\right) \sin\left(\frac{q_z n_z \pi}{N_z+1}\right) G_{00}(E, \mathbf{q}),$$

where $\mathbf{m}$ and $\mathbf{n}$ represent two sites on the lead's surface and $G_{00}(E, \mathbf{q})$ is given by Eq. (A.0.10). In this form the surface GF matrix g_{mn} is used in constructing the self-energies of the cubic-latticed leads for the transport calculations in Chapter 3.

Appendix B

Mixing schemes in self-consistent calculations

All density functional theory (DFT) [48] based electronic structure calculations involve a self-consistent solution of some set of coupled non-linear integro-differential equations. The Kohn-Sham equations [60], solved in DFT, are formally a set of one-electron Schrödinger equations that depend non-linearly on the full electronic density ρ through the effective potential $V_{\text{eff}}[\rho]$. The sum of all Kohn-Sham wavefunctions squared is equal to ρ, which completes the system of equations. This leads, in general, to a recursive expression for ρ

$$\rho = F(\rho), \tag{B.0.1}$$

which can be rewritten as

$$\rho_{\text{in}} = \rho_{\text{out}}\left(\rho_{\text{in}}\right), \tag{B.0.2}$$

where ρ_{in} (ρ_{out}) is the input (output) density and Eq. (B.0.2) gives the convergence condition [1] for an iterative solution of Eq. (B.0.1). In any numerical implementation convergence can be defined as a gradual minimization of the distance between ρ_{in} and ρ_{out} in the ρ space, e.g. [53]

$$D\left[\rho_{\text{in}}, \rho_{\text{out}}\right] = ||\rho_{\text{out}} - \rho_{\text{in}}|| = \left(\rho_{\text{out}} - \rho_{\text{in}}, \rho_{\text{out}} - \rho_{\text{in}}\right)^{1/2}, \tag{B.0.3}$$

[1] In fact ρ and V_{eff} are equally good to be used as convergence criteria, since both the charge and the potential are equivalent when they are treated on the same footing, except that the total energy may not converge as quickly when V_{eff} is used as a criterion [53].

where $||\ ||$ designates the norm in the linear vector space $\rho \in \mathcal{D}$ [1] and $(\ ,\ )$ is the scalar product.

The problem of solving Eq. (B.0.2) is still essentially a problem of solving a system of non-linear equations as it can be taken in the form $\rho - F(\rho) = 0$. In electronic structure problems during the iterative numerical solutions, however, increasing in amplitude charge oscillations may arise and cause the divergence of the algorithm. Here we describe a few methods of damping those oscillations, purposely developed for self-consistent field (SCF) calculations. In fact such calculations do not only concern DFT. The Pulay method [80, 81], for example, has been developed for Hartee-Fock calculations. SCF calculations are encountered in this work whenever electron interactions (within mean-field approximation) are taken into account (both in the steady-state transport and in the time-dependent simulations).

B.1 Simple mixing

We start with the simplest approach to damping those charge oscillations in SCF iterative procedures. This is to take on the n-th iteration a linear combination of the input and the output densities, i.e.

$$\rho_{\text{in}}^{(n+1)} = (1-\alpha)\rho_{\text{in}}^{(n)} + \alpha\rho_{\text{out}}^{(n)}\,, \tag{B.1.1}$$

where typically the mixing parameter $\alpha \in [0,1]$. Convergence is usually achieved with a suitable choice of α. Smaller values of α are associated with better stability, though, for very small $\alpha \lesssim 0.04$, which are required for more complex systems (e.g. $3d$ impurities in noble metals [34]), the convergence may proceed extremely slow. Ranges of applicability for α in various situations are studied in Ref. [34]. More sophisticated mixing schemes, using optimized on-the-fly mixing parameters, can accelerate the convergence and reach solutions where the simple mixing fails.

In the following subsection we discuss the Anderson's mixing scheme. In this method the convergence acceleration is achieved on the expense of memory storage, as the dynamic optimization of the mixing is based on (some sort of) extrapolation over a set of old input and output densities. The dimension of that memory space, i.e. the number m of old iterations taken into consideration, may vary. Often in the literature the Anderson's scheme is called the two-step memory ($m = 2$) version of the scheme [53], though in Anderson's original work [5] the method is introduced for an arbitrary memory size. The Pulay's scheme is independently derived and identical in concept but introduced in a more implementation-friendly manner for $m > 2$. We shall follow the trends

[1] For example, if ρ is the density matrix in a single band tight binding model, $\mathcal{D}$ is the space of $N \times N$ matrices, where N is the number of atomic sites. Often one works with only the actual charge density (the diagonal elements of the density matrix) and then $\mathcal{D}$ is the space of vectors of size N.

and call the two-step version Anderson's, while the m-step version – Pulay's mixing scheme. The reason for considering them separately is that the two-step version nicely clarifies the concept of the method. Moreover we use that particular (Anderson's) mixing scheme in the initialization of the density matrix for our time-dependent simulations, while we use the more complex m-memory ($m = 4$) Pulay's version in our steady-state transport.

B.2 Anderson's mixing

In the Anderson scheme [5] linear combinations of input and output densities from two (or more) iterations are used in order to determine an optimized input $\widetilde{\rho}_{\text{in}}$ and output $\widetilde{\rho}_{\text{out}}$ densities for the next iteration

$$\widetilde{\rho}_{\text{in}}^{(n)} = \left(1 - \beta^{(n)}\right) \rho_{\text{in}}^{(n-1)} + \beta^{(n)} \rho_{\text{in}}^{(n)} \tag{B.2.1}$$

$$\widetilde{\rho}_{\text{out}}^{(n)} = \left(1 - \beta^{(n)}\right) \rho_{\text{out}}^{(n-1)} + \beta^{(n)} \rho_{\text{out}}^{(n)}, \tag{B.2.2}$$

where $\beta^{(n)}$ is an iteration-dependent mixing parameter.

Let us define $\delta\rho^{(n)} \equiv \rho_{\text{out}}^{(n)} - \rho_{\text{in}}^{(n)}$ and $\widetilde{\delta\rho}^{(n)} \equiv \widetilde{\rho}_{\text{out}}^{(n)} - \widetilde{\rho}_{\text{in}}^{(n)}$. The method is based on the minimization of the least-squares deviation $\left|\left|\widetilde{\delta\rho}^{(n)}\right|\right|^2$ with respect to $\beta^{(n)}$ to determine the optimal mixing coefficient. By definition

$$\left|\left|\widetilde{\delta\rho}^{(n)}\right|\right|^2 = \left(1 - \beta^{(n)}\right)^2 \left|\left|\delta\rho^{(n-1)}\right|\right|^2 + \left(\beta^{(n)}\right)^2 \left|\left|\delta\rho^{(n)}\right|\right|^2 + 2\left(1 - \beta^{(n)}\right) \beta^{(n)} \left(\delta\rho^{(n-1)}, \delta\rho^{(n)}\right). \tag{B.2.3}$$

From the minimization

$$\frac{\partial}{\partial\beta^{(n)}} \left|\left|\widetilde{\delta\rho}^{(n)}\right|\right|^2 = 0 \qquad \Longrightarrow \qquad \beta^{(n)} = -\frac{\left(\delta\rho^{(n-1)}, \delta\rho^{(n)} - \delta\rho^{(n-1)}\right)}{\left|\left|\delta\rho^{(n)} - \delta\rho^{(n-1)}\right|\right|^2}. \tag{B.2.4}$$

This optimal $\beta^{(n)}$ is used to construct $\widetilde{\rho}_{\text{in}}^{(n)}$ and $\widetilde{\rho}_{\text{out}}^{(n)}$ as in Eq. (B.2.1). The new guess for the next iteration is then made in a simple mixing step with an empirical mixing parameter $\alpha \in [0, 1]$

$$\rho_{\text{in}}^{(n+1)} = (1 - \alpha)\widetilde{\rho}_{\text{in}}^{(n)} + \alpha\widetilde{\rho}_{\text{out}}^{(n)}. \tag{B.2.5}$$

That last step is indeed necessary as it brings some output components into the new guess so that ρ_{in} does not remain trapped in the space of the old input densities.

B.3 Pulay's mixing

The Pulay method has been originally proposed for geometry optimization calculations [80, 81]. It is also called Residual Metric Minimization (RMM) method [21] and gives a straightforward prescription to the numerical implementation of the generalized to m-step memory Anderson's scheme. Here the *residual* $\delta\rho^{(n)}$ from the n-th iteration ($n > m$) is an m-dimensional vector. The optimized input and output densities are again a linear combination, this time, of the previous m inputs

$$\widetilde{\rho}_{\text{in}}^{(n)} = \sum_{i=1}^{m} c_i \rho_{\text{in}}^{(n-i+1)}, \qquad \widetilde{\rho}_{\text{out}}^{(n)} = \sum_{i=1}^{m} c_i \rho_{\text{out}}^{(n-i+1)}, \tag{B.3.1}$$

where $\sum_{i=1}^{m} c_i = 1$. The *residual* from the n-th iteration is again defined as $\delta\rho^{(n)} \equiv \rho_{\text{out}}^{(n)} - \rho_{\text{in}}^{(n)}$ and thus the residual associated with $\widetilde{\rho}_{\text{in}}^{(n)}$ is again a linear combination of residuals [1]

$$\widetilde{\delta\rho}^{(n)} = \sum_{i=1}^{m} c_i \delta\rho^{(n-i+1)}. \tag{B.3.2}$$

The requirement that $\widetilde{\delta\rho}^{(n)}$ approximates the zero vector in the mean-square sense leads to the following system of $m+1$ linear equations for the coefficients c_i

$$\begin{pmatrix} B_{11} & B_{12} & \dots & B_{1m} & -1 \\ B_{21} & B_{22} & \dots & B_{2m} & -1 \\ \vdots & \vdots & \dots & \vdots & \vdots \\ B_{m1} & B_{m2} & \dots & B_{mm} & -1 \\ -1 & -1 & \dots & -1 & 0 \end{pmatrix} \begin{pmatrix} c_1 \\ c_2 \\ \vdots \\ c_m \\ \lambda \end{pmatrix} = \begin{pmatrix} 0 \\ 0 \\ \vdots \\ 0 \\ -1 \end{pmatrix}, \tag{B.3.3}$$

where $B_{ij} = \left(\delta\rho^{(n-i+1)}, \delta\rho^{(n-j+1)}\right)$ and λ is a Lagrange multiplier, the value of which yields $\left|\left|\widetilde{\delta\rho}^{(n)}\right|\right|^2$. Solving Eq. (B.3.3) provides the optimized $\widetilde{\rho}_{\text{in}}^{(n)}$. As the final new guess cannot be made only of inputs, it is again a mixture of the optimal densities from Eq. (B.3.1)

$$\rho_{\text{in}}^{(n+1)} = (1-\alpha)\widetilde{\rho}_{\text{in}}^{(n)} + \alpha\widetilde{\rho}_{\text{out}}^{(n)}, \tag{B.3.4}$$

where α is an empirical constant in $[0, 1]$. Again the value of α can substantially affect the convergence rate and its choice depends on the physical system described.

For $n < m$ either simple mixing steps can be taken or for $n > 2$ Pulay steps (as described above) with increasing $m' = n$ until $m' = m$. Typically $m \sim 5$ is considered sufficient [21]. In our simulations $m = 4$.

[1] It is assumed that we are close enough to self consistency for variations of the densities and their associated residuals to be linearly related.

Appendix C

Tight-binding description of electrical current flow

In the discrete representation of the tight binding (TB) approximation the definition of an integral quantity like the electron current requires some extra attention. Here we justify the expressions for the *bond current* used in Chapter 4 and 6.

The TB method is based on the assumption that the atoms are relatively far away from each other, so that the overlap of the wave functions of the electrons in neighbouring atoms is small [10]. Hence the wave function of an electron with wavevector $\mathbf{k}$ moving in the crystal lattice can be approximated with a linear combination of localised orbitals (LCAO)

$$\psi_{\mathbf{k}\alpha}(\mathbf{r}) = \langle \mathbf{r}|\psi_{\mathbf{k}\alpha}\rangle = \sum_n e^{i\mathbf{k}\cdot\mathbf{R}_n}\phi_\alpha(\mathbf{r}-\mathbf{R}_n)\,, \tag{C.0.1}$$

where we introduce the notation $|\phi_{n\alpha}\rangle$ for the localised atomic-like orbital at site $\mathbf{R}_n$, such that $\phi_{n/\alpha}(\mathbf{r}-\mathbf{R}) \equiv \langle \mathbf{r}|\phi_{n\alpha}\rangle$. Everywhere α indicates the type of the atomic orbital (α is a collective quantum number $\alpha = \{n, l, m\}$). The foregoing TB state Eq. (C.0.1) satisfies the Bloch condition $\psi_{\mathbf{k}\alpha}(\mathbf{r}+\mathbf{R}) = e^{i\mathbf{k}\cdot\mathbf{R}}\psi_{\mathbf{k}\alpha}(\mathbf{r})$ (see for instance Ref. [8]). Here we follow Ref. [109] and consider a general electron state as a superposition of Bloch waves (C.0.1) or in fact localised orbitals $|\phi_{n\alpha}\rangle$

$$|\psi\rangle = \sum_{\mathbf{k}\alpha} \psi_{\mathbf{k}\alpha}\,|\psi_{\mathbf{k}\alpha}\rangle = \sum_{n\alpha} \psi_{n\alpha}\,|\phi_{n\alpha}\rangle\,, \tag{C.0.2}$$

where $\phi_{n\alpha}$ are the expansion coefficients. In doing so we may drift away from the initial assumption that $\{|\phi_{n\alpha}\rangle\}$ are the actual atomic orbitals. It is even advisable not to use the true atomic wave functions as in this case Bardeen and Van Vleck [10] have found a factor of three difference between

the two equivalent formulations of the current, e.g. the x-component of the current, carried by an electron in state $|\psi_{\mathbf{k}\alpha}\rangle$ (see for instance Ref. [73], pp. 92-93)

$$I_x^{(1)} = -ev_x = -\frac{eh}{4\pi\mu i}\int\left(\psi^*_{\mathbf{k}\alpha}\frac{\partial\psi_{\mathbf{k}\alpha}}{\partial x} - \psi_{\mathbf{k}\alpha}\frac{\partial\psi^*_{\mathbf{k}\alpha}}{\partial x}\right)\mathrm{d}^3r \tag{C.0.3}$$

$$I_x^{(2)} = -\frac{2\pi e}{h}\frac{\partial E_k}{\partial \mathbf{k}_x}\,, \tag{C.0.4}$$

where E_k is an exact eigenenergy of the Schrödinger equation (SE) with the periodic potential $V(\mathbf{r})$ of the lattice

$$-\frac{h^2}{8\pi^2\mu}\Delta\Psi_{\mathbf{k}\alpha} + V(\mathbf{r})\Psi_{\mathbf{k}\alpha} = E_k\Psi_{\mathbf{k}\alpha} \tag{C.0.5}$$

and $\Psi_{\mathbf{k}\alpha}$ is an exact eigenstate for which undoubtedly $I_x^{(1)} = I_x^{(2)}$ [10]. However, Eq. (C.0.1) is an approximation for which $\psi_{\mathbf{k}\alpha} \to \Psi_{\mathbf{k}\alpha}$ only in the limit of very distant atoms. In any case, the correctness of the TB approximation in Eq. (C.0.1) depends on the choice of the localised orbitals $\{|\phi_{n\alpha}\rangle\}$. If these are hydrogen-like atomic wavefunctions, i.e. $\phi_{n\alpha}(r) \sim e^{-r/r_0}$, Ref. [10] has shown that for these $I_x^{(1)} = \frac{1}{3}I_x^{(2)}$ and that ratio of 1:3 is found to persist even when both currents approach 0 in the limit of large interatomic distance. It has, however, been demonstrated that $I_x^{(1)} = I_x^{(2)}$ for local orbitals $\{\phi_{\mathbf{k}\alpha}\}$ corresponding to the screened (by the other valence electrons) atomic potential $U(r)$ which decays with distance much more rapidly than $1/r$ (exponentially) and imposes an asymptotic dependence of $\phi_{n\alpha}(r) \sim e^{-r/r_0}/r$ [10].

With this in mind, we go back to Eq. (C.0.2) and avoid associating $\{|\phi_{n\alpha}\rangle\}$ with real atomic orbitals. Instead we think of these as a discrete computational grid of localised basis functions. For convenience here we consider a grid $\{|\phi_{n\alpha}\rangle\}$ which coincides with the atomic lattice. The full Hamiltonian (as well as any one-electron TB operator) can be represented as

$$\hat{H} = \sum_{n,\alpha,m,\beta} |\phi_{n\alpha}\rangle\, H_{n\alpha m\beta}\, \langle\phi_{m\beta}|\,. \tag{C.0.6}$$

This matrix is Hermitian, i.e. $H_{n\alpha m\beta} = H^*_{m\beta n\alpha}$, and could depend in a self-consistent manner on the instantaneous electron density in the system as it does, for instance, in Eq. (4.3.4).

We assume that our basis is orthogonal

$$\langle\phi_{n\alpha}|\phi_{m\beta}\rangle = \delta_{nm}\delta_{\alpha\beta}\,. \tag{C.0.7}$$

We continue following Ref. [109]. A general time-dependent (TD) one-electron state can be expressed in the orthonormal positional basis as

$$|\psi(t)\rangle = \sum_{n,\alpha}\psi_{n\alpha}(t)\,|\phi_{n\alpha}\rangle\,. \tag{C.0.8}$$

This is a solution of the TD SE, which in a matrix form reads

$$\sum_{n\alpha} H_{n\alpha m\beta}\psi_{m\beta}(t) = i\hbar\dot{\psi}_{n\alpha}(t)\,. \tag{C.0.9}$$

We define a projection operator to each site n as

$$\hat{P}_n = \sum_{\alpha} |\phi_{n\alpha}\rangle \langle\phi_{n\alpha}|\,, \tag{C.0.10}$$

and $\left\{\hat{P}_n\right\}$ make a closed set $\sum_n \hat{P}_n = \hat{1}$ with $\hat{1}$ being the identity operator. A projection of the general TD electron state from Eq. (C.0.8) on site n is thus defined as

$$P_n(t) \equiv \langle\phi(t)|\,\hat{P}_n\,|\phi(t)\rangle = \sum_{\alpha} \psi^*_{n\alpha}(t)\psi_{n\alpha}(t) \tag{C.0.11}$$

and that represents the TD occupancy on that site. The rate of change of $P_n(t)$ is described by its equation of motion $\dot{P}_n(t) = \frac{1}{i\hbar}\langle\phi(t)|\left[\hat{P}_n, \hat{H}\right]|\phi(t)\rangle$. The current operator is hence identified with

$$\hat{\jmath}_n = \frac{1}{i\hbar}\left[\hat{P}_n, \hat{H}\right] = \frac{1}{i\hbar}\sum_{m\neq n}\left(\hat{P}_n\hat{H}\hat{P}_m - \hat{P}_m\hat{H}\hat{P}_n\right) = \sum_{m\neq n} \jmath_{mn}\,, \tag{C.0.12}$$

where we have used the closure relation for $\left\{\hat{P}_n\right\}$ and extracted the operators

$$\hat{\jmath}_{mn} \equiv \frac{1}{i\hbar}\left(\hat{P}_n\hat{H}\hat{P}_m - \hat{P}_m\hat{H}\hat{P}_n\right) = \frac{1}{i\hbar}\sum_{\alpha,\beta}\left(H_{n\alpha m\beta}\,|\phi_{n\alpha}\rangle\langle\phi_{m\beta}| - H_{m\beta n\alpha}\,|\phi_{m\beta}\rangle\langle\phi_{n\alpha}|\right)\,, \tag{C.0.13}$$

which naturally represent the flow of electrons from a site m to site n. This intersite operator $\hat{\jmath}_{mn}$ describes all the flux occurring between the two sites and is also called "bond current". The total current operator for a system of the Landauer type (see Chapter 2, e.g. Fig. 2.8) is then defined with respect to an open surface S which splits the system in two parts at the device region

$$\hat{\jmath}_S = \sum_{\substack{n\,\in\,L\\ m\,\in\,R}} \hat{\jmath}_{mn} = \frac{1}{i\hbar}\left(\hat{P}_R\hat{H}\hat{P}_L - \hat{P}_L\hat{H}\hat{P}_R\right) = \frac{1}{i\hbar}\left[\hat{P}_R, \hat{H}\right] = -\frac{1}{i\hbar}\left[\hat{P}_L, \hat{H}\right] \tag{C.0.14}$$

where L (R) designates the region to the left (right) of S, the new projection operators occurring are defined as $\hat{P}_{L(R)} = \sum_{n\in L(R)}\hat{P}_n$ and they obey the following relations [109]

$$\hat{P}_L\hat{P}_R = \hat{P}_R\hat{P}_L = 0\,, \qquad \hat{P}^2_{L(R)} = \hat{P}_{L(R)} \qquad \text{and} \qquad \hat{P}_L + \hat{P}_R = \hat{1}\,. \tag{C.0.15}$$

We note that the total current operator $\hat{\jmath}_S$ through surface S, contains bond-current contributions only from the bonds that are cut by S.

As an illustration of the bond and the total current concepts we consider a 1D chain in a single band ($\alpha = \beta$) nearest-neighbour TB model

$$H_{nm} \equiv H_{n\alpha m\alpha} = \begin{cases} \mathcal{E}_0\,, & \text{for } m = n \\ -\chi\,, & \text{for } m = n \pm 1 \end{cases}\,. \tag{C.0.16}$$

In this case, there are two bond currents associated with each site n, as described in Ref. [88]

$$\hat{\mathcal{J}}_{n\pm1,n} = \frac{1}{i\hbar}\left(H_{n,n\pm1}\left|\phi_{n\pm1}\right\rangle\left\langle\phi_n\right| - H_{n\pm1,n}\left|\phi_n\right\rangle\left\langle\phi_{n\pm1}\right|\right), \tag{C.0.17}$$

describing the inflow from the two neighbouring sites $n \pm 1$. The net current at n is thus given by $\hat{\mathcal{J}}_n = \mathcal{J}_{n-1,n} + \mathcal{J}_{n+1,n}$. For instance, if $|\psi(t)\rangle$ is a normalised Bloch state in N-atom long chain (with $N \to \infty$)

$$|\psi_k(t)\rangle = \frac{1}{\sqrt{N}} \mathrm{e}^{-iE_k t/\hbar} \sum_n \mathrm{e}^{ikna} \left|\phi_n\right\rangle, \tag{C.0.18}$$

where a is the interatomic distance and $E_k = \mathcal{E}_0 - 2\chi\cos(ka)$ then the bond currents are

$$\begin{aligned} I_{n\pm1,n} &= e\left\langle\psi_k(t)\right|\hat{\mathcal{J}}_{n\pm1,n}\left|\psi_k(t)\right\rangle = \frac{-e\chi}{Ni\hbar}\sum_{m,l}\left(\delta_{l,n\pm1}\delta_{mn} - \delta_{ln}\delta_{m,n\pm1}\right)\mathrm{e}^{ik(m-l)a} \\ &= \mp\frac{2e\chi}{\hbar N}\sin(ka) = \mp\frac{e}{Na}v_k \end{aligned} \tag{C.0.19}$$

where e is the electron charge, $v_k = \frac{1}{\hbar}\frac{\partial E_k}{\partial k} = 2\chi\sin(ka)$ is the group velocity of the Bloch state. Therefore, in this case of a pure Bloch state, the net current at n is exactly zero, i.e.

$$I_n = I_{n+1,n} + I_{n-1,n} = 0\,. \tag{C.0.20}$$

This is because of the exact balance of left- and right-going currents. For this reason the total current for the bond $(n, n+1)$ (as well as any other bond inside the chain) is also zero. In analogy to Eq. (C.0.14) we can associate a surface S cutting through that bond and the fact that $I_S = I_{n,n+1} + I_{n+1,n} = 0$ directly follows from Eq. (C.0.17). The individual bond currents $I_{n\pm1,n}$, however, are not zero as they are proportional to v_k. This illustrates the concept of conductance associated with a quantum channel, which we introduced in Chapter 2 and which is a finite quantity even if there is no net current.

Going back to the generalised formulation in Ref. [109] and Eqs. (C.0.13) and (C.0.14), we define the actual bond- and total currents as expectation values of the corresponding operators [1]

$$I_{nm} = e\mathrm{Tr}\left[\hat{\mathcal{J}}_{nm}\hat{\rho}\right] \qquad \text{and} \qquad I_S = e\mathrm{Tr}\left[\hat{\mathcal{J}}_S\hat{\rho}\right], \tag{C.0.21}$$

where [as in Eq. (2.2.35)]

$$\hat{\rho} = \int \hat{D}_L(E) f_L(E)\,\mathrm{d}E + \int \hat{D}_R(E) f_R(E)\,\mathrm{d}E \tag{C.0.22}$$

is the density matrix (in general, nonequilibrium) of the system and $D_{L(R)}$ are the partial densities of states associated with the left- (right-) travelling states [see for instance Eq. (4.2.8)]. The

[1] This is in fact what we did in the foregoing 1D example in Eq. (C.0.19).

analogue of Eq. (C.0.20) for the general Landauer problem is referred to as the zero-current theorem in Refs. [110, 109]

$$\mathrm{Tr}\left[\hat{\jmath}_{nm}\hat{D}(E)\right] = \frac{1}{i\hbar}\sum_{\alpha,\beta}\left(H_{m\beta n\alpha}D_{n\alpha m\beta} - H_{n\alpha m\beta}D_{m\beta n\alpha}\right) = 0 \tag{C.0.23}$$

as long as there exists an onsite unitary transformation of the TB basis in which the Hamiltonian $\hat{H}$ and the density of states operator $\hat{D} = \hat{D}(E) = \hat{D}_L(E) + \hat{D}_R(E)$ are symmetric matrices in the transformed basis, i.e. $\widetilde{H}_{n\alpha m\beta} = \widetilde{H}_{m\beta n\alpha}$ and $\widetilde{D}_{n\alpha m\beta} = \widetilde{D}_{m\beta n\alpha}$. This assumption is plausible in the absence of magnetic fields [109]. The result (C.0.23) applies also to $\hat{\jmath}_{nm}$. Based on that zero-current theorem, stating that the filled states outside the bias window do not contribute to the net current, both the bond I_{nm} and the fact that Eq. (C.0.22) can be rewritten as

$$\hat{\rho} = \int \hat{D}(E) f_R(E)\,\mathrm{d}E + \int \hat{D}_L(E)\left[f_L(E) - f_R(E)\right]\mathrm{d}E\,, \tag{C.0.24}$$

the total current through a surface I_S can be expressed as

$$I_{nm(S)} = e\int \left[f_L(E) - f_R(E)\right]\mathrm{Tr}\left[\hat{\jmath}_{nm(S)}D_L(E)\right]\,\mathrm{d}E\,. \tag{C.0.25}$$

This expression for I_S is shown to be equivalent to the NEGF expression in Eq. (2.3.10) for arbitrary open surface S in Ref. [109].

The expression for the local current which we used in Chapters 4 and 6 [see Eq. (4.3.7)] are derived directly from Eq. (C.0.21) for the case of a real symmetric Hamiltonian and a Hermitian density matrix

$$I_{nm} = e\mathrm{Tr}\left[\hat{\jmath}_{nm}\hat{\rho}\right] = \frac{e}{i\hbar}\sum_{\alpha\beta}H_{m\beta n\alpha}\left(\rho_{n\alpha m\beta} - \rho_{m\beta n\alpha}\right) = \frac{2e}{\hbar}H_{mn}\mathrm{Im}\left[\rho_{nm}\right]\,. \tag{C.0.26}$$

Appendix D

Time integrators

There exist plenty of numerical algorithms for integrating ordinary differential equations (ODE) (see for instance Ref. [105, 65]) and they all have one thing in common - they map the continuous differential equation onto one or more difference equations. For instance, in molecular dynamics (MD) the system of equations of motion of the particles needs to be integrated over time, given the initial conditions. The time-stepping algorithms, also called *time integrators*, used in MD, produce discretised (at equi-spaced points in time) approximations to the trajectories of the particles. How good this approximation is compared to the actual trajectory can be assessed by the following list of criteria [1] [13, 105]

- *accuracy*, i.e. to which power of the time step the numerical trajectory will deviate from the exact one after one integration step. Here, together with the inherent accuracy of the integrator scheme, a contribution to error accumulation has also the finite precision of the floating-point computation. The round-off errors, however, are typically assumed to be much smaller than the ones due to the algorithm [65].

- *stability*, which refers to the long-term asymptotic dynamics of the method, when applied to a linear ODE such as the harmonic oscillator. A numerical integrator is *asymptotically stable* if the growth of the solution for a linear model problem is asymptotically bounded [65].

- *energy conservation* (if the system is conservative), measured by two quantities: the *drift*, i.e. the steady deviation of the energy from its initial value along the trajectory and the *noise*, describing the fructuations on top of the drift. The drift is the more undesirable of the two, as it can drive an otherwise microcanonical MD simulation out of equilibrium.

[1] Not necessarily independent from each other.

- *time reversibility* has to be incorporated in the integrator if it is present in the equations of motion.

- *symplecticity* [1], which refers to whether or not the phase space geometry of the actual continuum dynamics is preserved by the integrator. This is, in a sense, the strongest of the symmetry-preserving criteria. Symplectic integrators preserve the phase space volume (a property inherent to continuum Hamiltonian systems by the Liouville theorem), but symplecticity is independent of time-reversibility (the latter also depends on the mere structure of the Hamiltonian, which could otherwise be symplectic). It is, though, related to stability and to energy (and other first integrals) conservation. It is known that symplectic integrators preserve exactly the discrete version of the total energy [105] at least for linear systems (for non-linear the drift is exponentially decaying with the decrease of the time step [65]).

Here we discuss the simplest integrator that has all the nice symmetry-preserving qualities and for this reason is widely used in MD simulations.

D.1 The Leapfrog Verlet integrator

The Verlet algorithm is a two-step method, belonging to the Runge-Kutta family, for integrating second order differential equations of the form

$$\ddot{x} = F\left[x(t), t\right] . \tag{D.1.1}$$

It can be derived [105] by adding the Taylor expansions for the coordinate x (working in 1D for simplicity) at $t = \pm\Delta t$ about $t = 0$

$$x(\Delta t) = x(0) + \Delta t\dot{x}(0) + \frac{\Delta t^2}{2}F\left[x(0), 0\right] + \frac{\Delta t^3}{6}\ddot{x}(0) + \mathcal{O}(\Delta t^4) \tag{D.1.2}$$

$$x(-\Delta t) = x(0) - \Delta t\dot{x}(0) + \frac{\Delta t^2}{2}F\left[x(0), 0\right] - \frac{\Delta t^3}{6}\ddot{x}(0) + \mathcal{O}(\Delta t^4) \tag{D.1.3}$$

[1] This comes from the term *symplectic map* which is a map in the phase space of the system which preserves the *structure matrix* $\mathbf{J}$ of a Hamiltonian system

$$\dot{\mathbf{z}} = \mathbf{J}\nabla_z H(\mathbf{z}), \tag{D.0.1}$$

where $\mathbf{z}$ is a $2d$-dimensional vector in the phase space. In the canonic phase-space, for instance, the structure matrix has the form

$$\mathbf{J} = \begin{pmatrix} 0 & +\mathbf{I}_d \\ -\mathbf{I}_d & 0 \end{pmatrix} , \tag{D.0.2}$$

where $\mathbf{I}_d$ is a $d \times d$ identity matrix. All flow maps [right-hand side of Eq. (D.0.1)] of canonical Hamiltonian systems are necessarily symplectic [65].

leading to

$$x(\Delta t) = 2x(0) - x(-\Delta t) + \Delta t^2 F\left[x(0), 0\right] + \mathcal{O}(\Delta t^4) \tag{D.1.4}$$

which we rewrite in terms of indexed time-step values $x_n \equiv x(n\Delta t)$ as

$$x_{n+1} = 2x_n - x_{n-1} + \Delta t^2 F\left[x_n, n\Delta t\right] + \mathcal{O}(\Delta t^4)\,. \tag{D.1.5}$$

Thus we need the last two values, x_n and x_{n-1}, to be able to produce the next one x_{n+1} (hence, two-step method). This is what is most often referred to as the *leapfrog method* as it only involves coordinates [65].The $\mathcal{O}(\Delta t^4)$ term means that the deviation of the exact solution from the numerical one in a single timestep is smaller than $\alpha_n \Delta t^4$, where α_n are finite and nonvanishing for $\Delta t \to 0$ numbers. However the error accumulates when integrated over a certain time interval $T \gg \Delta t$ and the global error for the method is actually $\mathcal{O}(\Delta t^2)$ [105]. Introducing the velocities at half-steps, the velocity-Verlet flavour of the method follows the equations

$$\begin{aligned} v_{n+\frac{1}{2}} &= v_n - \frac{\Delta t}{2} F\left[x_n, n\Delta t\right] \\ x_{n+1} &= x_n + \Delta t v_{n+\frac{1}{2}} \\ v_{n+1} &= v_{n+\frac{1}{2}} - \frac{\Delta t}{2} F\left[x_{n+1}, (n+1)\Delta t\right] \end{aligned} \tag{D.1.6}$$

Of course, this is just one formulation and other (equivalent) combinations of x and v at half-steps could be used depending on whether or not one is interested in velocities and coordinates at the same timesteps. One such formulation is the so called *3-level leapfrog method* [74]

$$\begin{aligned} x_{n+1} &= x_{n-1} + 2v_n \Delta t \\ v_{n+1} &= v_{n-1} + 2F\left[x_n, n\Delta t\right] \Delta t\,. \end{aligned} \tag{D.1.7}$$

Here one can very clearly see that the leapfrog method is time-reversible, i.e. invariant against the substitutions $\Delta t \leftrightarrow -\Delta t$ and $x_{n+1} \leftrightarrow x_{n-1}$. It is also symplectic [65] which, together with its simplicity, makes it a good choice for MD simulations. There is, however, one well-known situation when this algorithm becomes unstable. That is the case with velocity-dependent forces, which could arise, for instance, if the particle is moving in a magnetic field or if there is a dissipative force. Such a situation is inherently non-time-invertible and for this reason the time-invertible integrator is not behaving adequately. There is, however, a rather simple fix [74] and we discuss this in the following section.

D.2 Problem with non-conservative systems

Here we follow reference [74]. The reason for the instability lies in the fact that, as formulated in Eq. (D.1.7), the 3-level leapfrog method links directly the coordinates and velocities at only even timesteps or only odd timesteps. It also requires the initial conditions at two timesteps (x_0, v_0) and (x_1, v_1). Thus it appears that the numerical algorithm has twice as many degrees of freedom as the actual physical system. Eq. (D.1.7) can be summarised as

$$\mathbf{z}_{n+2} = \mathbf{z}_n + 2\mathbf{F}\left[\mathbf{z}_{n+1}, t_{n+1}\right]\Delta t\,, \tag{D.2.1}$$

where $\mathbf{z} = (x, v)$ is a vector in the phase space and $\mathbf{F} = (v, F)$ is a generalised force. It is easy to see that Eq. (D.2.1) can be separated into two subsystems – one even $\mathbf{a}$ and one odd $\mathbf{b}$, discretised at $2\Delta t$

$$\mathbf{a}_{2n+2} = \mathbf{a}_{2n} + 2\mathbf{F}\left[\mathbf{a}_{2n+1}, t_{2n+1}\right]\Delta t \tag{D.2.2}$$

$$\mathbf{b}_{2n+3} = \mathbf{b}_{2n+1} + 2\mathbf{F}\left[\mathbf{b}_{2n+2}, t_{2n+2}\right]\Delta t\,. \tag{D.2.3}$$

If $\mathbf{z} = (x, v)$ is a solution of Eq. (D.2.1), it is also a solution of the augmented difference system (D.2.2, D.2.3). This is, therefore, the physical solution of the problem for which $\mathbf{z} = \mathbf{a} = \mathbf{b}$. Other (unphysical) solutions for which $\mathbf{a} \neq \mathbf{b}$ can arise as valid solutions of the Eqs. (D.2.2) and (D.2.3) that cannot be distinguished from the physical ones. We can define a measure of the unphysical variation $\mathbf{w}$

$$\mathbf{a} = \mathbf{z} + \mathbf{w}\,, \qquad \mathbf{b} = \mathbf{z} - \mathbf{w}\,. \tag{D.2.4}$$

Hence, a parasitic solution $\widetilde{\mathbf{z}}$ in finite difference form would be

$$\widetilde{\mathbf{z}}_n = \mathbf{z}_n + (-1)^n \mathbf{w}_n\,, \tag{D.2.5}$$

i.e. it would contain both physical $\mathbf{z}_n$ and unphysical $\mathbf{w}_n$ modes. These by themselves are solutions of

$$2\dot{\mathbf{z}} = \mathbf{F}\left[\mathbf{z} - \mathbf{w}, t\right] + F\left[\mathbf{z} + \mathbf{w}, t\right] = \mathbf{F}\left[\mathbf{z}, t\right] + \mathcal{O}(\mathbf{w}^2) \tag{D.2.6}$$

$$2\dot{\mathbf{w}} = \mathbf{F}\left[\mathbf{z} - \mathbf{w}, t\right] - F\left[\mathbf{z} + \mathbf{w}, t\right] = \mathbf{DF}\left[\mathbf{z}, t\right] \cdot \mathbf{w} + \mathcal{O}(\mathbf{w}^3)\,, \tag{D.2.7}$$

where we have expanded the system in powers of $\mathbf{w}$ and $\mathbf{DF}$ is the matrix of partial derivatives $\partial F_i / \partial z_j$. It is now becoming apparent how velocity-dependent forces (for which $\mathbf{DF} \neq 0$) could give rise to an amplification of the parasitic modes $\mathbf{w}$. Such amplifications are exponential and inevitably lead to numerical catastrophies. If a constraint $\mathbf{w} = 0$ is adjoint to Eq. (D.2.6) it

is, in principle, maintained by Eq. (D.2.7), but in numerical implementations imperfect initial conditions and round-off errors inevitably introduce nonzero $\mathbf{w}$, leading to a divergency.

The only way to cure this instability is to keep reimposing $\mathbf{w} = 0$ during the integration. Various methods exist, which suppress the unphysical split to odd and even degrees of freedom [74]. What we have used in Chapters 4 and 6 is the cure suggested in Ref. [22].

D.3 Integrating the damped Liouville equation

As a reminder, in Chapters 4 and 6 we integrate a modified Liouville equation, which includes a dissipative Γ-term

$$\dot{\hat{\rho}} = \frac{1}{i\hbar}[\hat{H}[\hat{\rho}], \hat{\rho}] - \Gamma(\hat{\rho} - \hat{\rho}^0)\,, \tag{D.3.1}$$

where $\hat{\rho}^0$ is a specially designed electrically polarised density matrix [see Eq. (4.3.3)]. This is a first order differential equation hence we employ the first-order version of the leapfrog method above. Analogously to Eq. (D.2.1) the algorithm is contained in

$$z_{n+2} = z_n + 2F\left[z_{n+1}, t_{n+1}\right]\Delta t\,, \tag{D.3.2}$$

where in our simulations $z \equiv \rho_{ij}$ and $F \equiv (1/i\hbar)[\hat{H}, \hat{\rho}]_{ij}$.

Apparently, all the above discussion can be repeated for this case of doubly reduced phase-space and the odd-even problems would, just in the same way, show up at the end. In order to decorrelate the odd-even bifurcation we perform a simple Euler step once every ~500 timesteps (typically $\Delta t = 0.005\,\mathrm{fs}$)

$$z_{n+2} = z_{n+1} + F\left[z_{n+1}, t_{n+1}\right]\Delta t\,. \tag{D.3.3}$$

The effect of this "Euler-fix" is demonstrated on Fig. (D.1). This is a simulation of a current-induced DW motion in a 200-atom chain. While the onsite charge without the fix diverges at only 47 fs, the one with the fix is perfectly stable for as long as the simulation goes (some 500 fs). We have tested the "fixed" integrator against conservation of the total spin in the system (for a pinned DW, see Fig. 6.6) and found its performance satisfactory with a relative variation below 10^{-4} for the 500 fs-simulation.

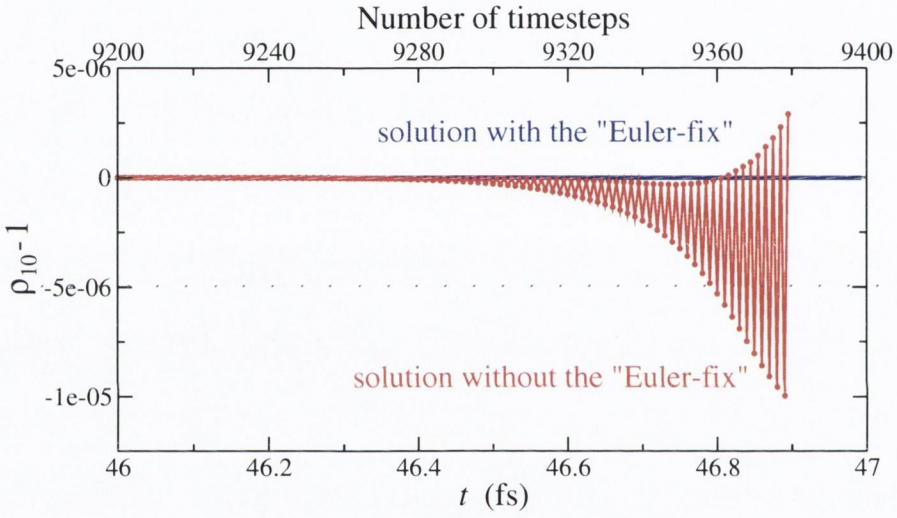

Figure D.1: Time evolution of one onsite electron density (spin-up polarised component) in a 200-atom current-carrying wire with a DW (one of the calculations described in Fig. 6.5; for all these spin-up band is fully filled with 1 e/atom and $\Gamma = 3\,\mathrm{eV}$), with and without the "Euler fix". If the uninterrupted leapfrog is used an odd-even timestep instability develops and the calculation diverges. Instead, with one simple Euler step at every 500 it is very stable and may run to the picosecond range ($> 10^5$ timesteps).

Appendix *

List of Publications

1. *Current-driven magnetic rearrangements in spin-polarized point contacts*
   Phys. Rev. B, **72**, 134407, (2005)
   M. Stamenova, S. Sanvito and T. N. Todorov

2. *Magneto-mechanical interplay in spin-polarized point contacts*
   Phys. Rev. B, **73**, 094439, (2006)
   M. Stamenova, S. Sahoo, C. G. Sánchez T. N. Todorov and S. Sanvito

3. *Molecular conduction: Do time-dependent simulations tell you more than the Landauer approach?*
   J. Chem. Phys., **124**, 214708, (2006)
   C. G. Sánchez, M. Stamenova, S. Sanvito, D. R. Bowler, A. P. Horsfield and T. N. Todorov

4. *Structure-related effects on the domain wall migration in atomic point contacts*
   Journ. Magn. Magn. Mat., **316**, e934-e936, (2007)
   M. Stamenova, S. Sahoo, T. N. Todorov and S. Sanvito

5. *Newtonian origin of the spin motive force in ferromagnetic atomic wires*
   Phys. Rev. B, **77**, 054439, (2008)
   M. Stamenova, T. N. Todorov and S. Sanvito

6. *Atomistic Spin Dynamics*

   Oxford Handbook of Nanoscience and Technology: Frontiers and Advances,

   Vol. 1: *Physics and Chemistry of Nanomaterials*,

   to be published by Oxford University Press

   M. Stamenova and S. Sanvito

References

[1] *Maple^{TM}10, Waterloo Maple Inc.* 90

[2] Y. Acremann, J. P. Strachan, V. Chembrolu, S. D. Andrews, T. Tyliszczak, J. A. Katine, M. J. Carey, B. M. Clemens, H. C. Siegmann, and J. Stöhr. Time-resolved imaging of spin transfer switching: Beyond the macrospin concept. *Phys. Rev. Lett.*, **96**:217202, 2006. 109

[3] Y. Aharonov and A. Stern. Origin of the geometric forces accompanying berrys geometric potentials. *Phys. Rev. Lett.*, **69**:3593, 1992. 136

[4] J. Anandan. The geometric phase. *Nature*, **360**:307, 1992. 130

[5] D. G. Anderson. Iterative procedures for nonlinear integral equations. *Journal of the ACM*, **12**:547, 1965. 148, 149

[6] V.P. Antropov, M.I. Katsnelson, B.N. Harmon, M. van Schilfgaarde, and D. Kuznezov. Spin dynamics in magnets: Equation of motion and finite temperature effects. *Phys. Rev. B*, **54**:1019, 1996. 3, 31, 47, 107, 141

[7] V.P. Antropov, M.I. Katsnelson, M. van Schilfgaarde, and B.N. Harmon. Ab initio spin dynamics in magnets. *Phys. Rev. Lett.*, **75**:729, 1995. 3, 31, 47, 141

[8] N. W. Ashcroft and N. D. Mermin. *Solid State Physics*. Brooks/Cole, 1976. 7, 15, 41, 47, 89, 151

[9] M. N. Baibich, J. M. Broto, A. Fert, F. Nguen Van Dau, F. Petroff, G. Creuzet, A. Friederich, and J. Chazelas. Giant magnetoresistance of (001)fe/(001)cr magnetic superlattices. *Phys. Rev. Lett.*, **61**:2472, 1988. 1

[10] J. Bardeen and J. H. Van Vleck. Expressions for the current in the bloch approximation of "tight binding" for metallic electrons. *Proc. Natl. Acad. Sci. USA*, **25**:82–86, 1939. 151, 152

[11] S. E. Barnes and S. Maekawa. Current-spin coupling for ferromagnetic domain walls in fine wires. *Phys. Rev. Lett.*, **95**:107204, 2005. 114

[12] S.E. Barnes and S. Maekawa. Generalization of faraday's law to include nonconservative spin forces. *Phys. Rev. Lett.*, **98**:246601, 2007. 130, 134, 140

[13] H. J. C. Berendsen and W. F. van Gunsteren. *Practical algorithms for molecular dynamics simulation, pp.43-65*, **vol. 97** of *Molecular Dynamics Simulation of Statistical Mechanical Systems, Proceedings ot he International School of Physics "Enrico Fermi", Varenna 1985*. Amsterdam, North-Holland, 1986. 157

[14] L. Berger. Low-field magnetoresistance and domain drag in ferromagnets. *J. Appl. Phys.*, **49**:2156, 1978. 110

[15] L. Berger. Possible existence of a josephson effect in ferromagnets. *Phys. Rev. B*, **33**:1572, 1986. 6, 136

[16] L. Berger. Emission of spin waves by a magnetic multilayer traversed by a current. *Phys. Rev. B*, **54**:9353, 1996. 2

[17] L. Berger. Relation between damping, current-induced torques, and wall resistance for domain walls in magnetic nanowires. *Phys. Rev. B*, **75**:174401, 2007. 112, 122, 128

[18] M. V. Berry. Quantal phase factors accompanying adiabatic changes. *Proc. R. Soc. Lond.*, **45**:392, 1984. 130

[19] G. Binasch, P. Grünberg, F. Saurenbach, and W. Zinn. Enhanced magnetoresistance in layered magnetic structures with antiferromagnetic interlayer exchange. *Phys. Rev. B*, **39**:4828, 1989. 1

[20] L. Bogani and W. Wernsdorfer. Molecular spintronics using single-molecule magnets. *Nature Matt.*, **7**:179, 2008. 1, 2

[21] D. R. Bowler and M. J. Gillan. An efficient and robust technique for acheiving self consistency in electronic structure calculations. *Chem. Phys. Lett.*, **325**:473, 2000. 150

[22] D. R. Bowler, A. P. Horsfield, C. G. Snchez, and T. N. Todorov. Correlated electronion dynamics with open boundaries: formalism. *J. Phys.:Cond. Matt.*, **17**:3985, 2005. 6, 77, 161

[23] M. Brandbyge, J. L. Mozos, P. Ordejón, J. Taylor, and K. Stokbro. Density-functional method for nonequilibrium electron transport. *Phys. Rev. B*, **65**:165401, 2002. 23, 24

[24] A. Brataas, G. E. W. Bauer, and P. J. Kelly. Non-collinear magnetoelectronics. *Phys. Rep.*, **427**:157, 2006. 2, 39, 85

[25] A. Brataas, Yu. V. Nazarov, and G. E. W. Bauer. Finite-element theory of transport in ferromagnet-normal metal systems. *Phys. Rev. Lett.*, **84**:2481, 1999. 39

[26] P. Bruno. Geometrically constrained magnetic wall. *Phys. Rev. Lett.*, **83**:2425, 1999. 28

[27] K. Capelle, G. Vignale, and B. L. Gyrffy. Spin currents and spin dynamics in time-dependent density-functional theory. *Phys. Rev. Lett.*, **87**:206403, 2001. 3

[28] R. Car and M. Parrinello. Structural, dynamical, and electronic properties of amorphous silicon: An ab initio molecular-dynamics study. *Phys. Rev. Lett.*, **60**:204, 1988. 88

[29] T. Y. Chen, Y. Ji, C. L. Chien, and M. D. Stiles. Current-driven switching in a single exchange-biased ferromagnetic layer. *Phys. Rev. Lett.*, **93**:026601, 2004. 27

[30] H. D. Chopra, M. R. Sullivan, J. N. Armstrong, and S. Z. Hua. The quantum spin-valve in cobalt atomic point contacts. *Nature Materials*, **11**:832, 2005. 27

[31] A. T. Costa, R. B.Muniz, and M.S. Ferreira. Dynamic interaction between localized magnetic moments in carbon nanotubes. *New J. Phys.*, **10**:063008, 2008. 102

[32] S. Datta. *Electronic Transport in Mesoscopic Systems.* Cambridge University Press, 1995. 8, 9, 10, 11, 16

[33] S. Datta. *Quantum Transport: Atom to Transistor.* Cambridge University Press, 2006. 4, 12, 13, 14, 17, 18, 19

[34] P. H. Dederichs and R. Zeller. Self-consistency iterations in electronic-structure calculations. *Phys. Rev. B*, **28**:5462, 1983. 148

[35] V. K. Dugaev, V. R. Vieira, P. D. Sacramento, J. Barna, M. A. N. Arajo, and J. Berakdar. Current-induced motion of a domain wall in a magnetic nanowire. *Phys. Rev. B*, **74**:054403, 2006. 112

[36] B. N. Engel, N. D. Rizzo, J. Janesky, J. M. Slaughter, R. Dave, M. DeHerrera, M. Durlam, and S. Tehrani. The science and technology of magnetoresistive tunneling memory. *IEEE Trans. Nanotech.*, **1**:32, 2002. 2

[37] H.-L. Engquist and P. W. Anderson. Definition and measurement of the elecrical and thermal resistances. *Phys. Rev. B*, **24**:1151, 1981. 8

[38] A. Fert. The origin, dvelopment and future of spintronics. *Nobel Lecture*, 2007. 1

[39] R. P. Feynman. Forces in molecules. *Phys. Rev.*, **56**:340, 1939. 28

[40] P. Gambardella. Magnetism in monatomic metal wires. *J. Phys.: Cond. Matt.*, **15**:S2533, 2003. 2, 85

[41] Th. Gerrits, H. A. M. van den Berg, J. Hohlfeld, L. Bär, and Th. Rasing. Ultrafast precessional magnetization reversal by picosecond magnetic field pulse shaping. *Nature*, **418**:509, 2002. 3

[42] T. L. Gilbert. A phenomenological theory of damping in ferromagnetic materials. *IEEE Trans. Mag.*, **40**:3443, 2004. 2, 85

[43] J. Grollier, P. Boulenc, V. Cros, A. Hamzi, A. Vaurs, A. Fert, and G. Faini. Switching a spin valve back and forth by current-induced domain wall motion. *Appl. Phys. Lett.*, **83**:509, 2003. 110

[44] J. Grollier, V. Cros, A. Hamzic, J. M. George, H. Jaffrs, A. Fert, G. Faini, J. Ben Youssef, and H. Legall. Spin-polarized current induced switching in co/cu/co pillars. *Appl. Phys. Lett.*, **78**:3663, 2001. 109

[45] P. M. Haney, D. Waldron, R. A. Duine, A. S. Nez, H. Guo, and A. H. MacDonald. Current-induced order parameter dynamics: Microscopic theory applied to co/cu/co spin valves. *Phys. Rev. B*, **76**:024404, 2007. 3

[46] B. Heinrich, Y. Tserkovnyak, G. Woltersdorf, A. Brataas, R. Urban, and G. E. W. Bauer. Dynamic exchange coupling in magnetic bilayers. *Phys. Rev. Lett.*, **90**:187601, 2003. 97

[47] J. E. Hirsch. Metallic ferromagnetism in a band model: Intra-atomic versus interatomic exchange. *Phys. Rev. B*, **56**:11022, 1997. 37

[48] P. C. Hohenberg and W. Kohn. Inhomogeneous electron gas. *Phys. Rev.*, **136**:B864, 1964. 147

[49] A. P. Horsfield, D. R. Bowler, A. J. Fisher, T. N. Todorov, and M. J. Montgomery. Power dissipation in nanoscale conductors: classical, semi-classical and quantum dynamics. *J. Phys.: Cond. Matter*, **16**:3609, 2004. 96

[50] A. Hubert and R. Schäfer. *Magnetic Domains*. Springer, Berlin, 1998. 39

[51] L. E. Hueso, J. M. Pruneda, V. Ferrari, G. Burnell, J. P. Valdes-Herrera, B. D. Simons, P. B. Littlewood, E. Artacho, A. Fert, and N. D. Mathur. Transformation of spin information into large electrical signals using carbon nanotubes. *Nature*, **445**:410, 2007. 2, 98

[52] Y. Imry and R. Landauer. Conductance viewed as transmission. *Rev. Mod. Phys.*, **71**:S306, 1999. 7

[53] D. D. Johnson. Modified broyden's method for accelerating convergence in self-consistent calculations. *Phys. Rev. B*, **38**:12807, 1988. 147, 148

[54] J. A. Katine, F. J. Albert, R. A. Buhrman, E. B. Myers, and D. C. Ralph. Current-driven magnetisation reversal and spin-wave excitations in co/cu/co pillars. *Phys. Rev. Lett.*, **84**:3149, 2000. 109

[55] E. Kim and Y. H. Lee. Structural, electronic, and vibrational properties of liquid and amorphous silicon: Tight-binding molecular-dynamics approach. *Phys. Rev. B*, **49**:1743, 1994. 88

[56] D. F. Kirwan, C. G. Rocha, A. T. Costa, and M. S. Ferreira. Sudden decay of indirect exchange coupling between magnetic atoms on carbon nanotubes. *Phys. Rev. B*, **77**:085432, 2008. 98

[57] M. Klui, C. A. F. Vaz, J. A. C. Bland, W. Wernsdorfer, G. Faini, E. Cambril, and L. J. Heyderman. Domain wall motion induced by spin polarized currents in ferromagnetic ring structures. *Appl. Phys. Lett.*, **83**:105, 2003. 110

[58] J. Knoch, W. Riess, and J. Appenzeller. Outperforming the conventional scaling rules in the quantum capacitance limit. *IEEE El. Dev. Lett.*, **29**:372, 2008. 75

[59] M. Koentopp, C. Chang, K. Burke, and R. Car. Density functional calculations of nanoscale conductance. *J. Phys.: Cond. Matt.*, **20**:083203, 2008. 84

[60] W. Kohn and L. J. Sham. Self-consistent equations including exchange and correlation effects. *Phys. Rev.*, **140**:A1133, 1965. 147

[61] T. S. Komatsu, N. Nakagawa, S. Sasa, and H. Tasaki. Steady-state thermodynamics for heat conduction: Microscopic derivation. *Phys. Rev. Lett.*, **100**:230602, 2008. 68

[62] I. N. Krivorotov, N. C. Emley, J. C. Sankey, S. I. Kiselev, D. C. Ralph, and R. A. Buhrman. Time-domain measurements of nanomagnet dynamics driven by spin-transfer torques. *Science*, **307**:228, 2005. 109, 110

[63] R. Landauer. Spatial variation of currents and fields due to localized scatterers in metallic conduction. *IBM J. Res. Dev.*, **1**:223, 1957. 4, 7

[64] R. Landauer. Electrical resistance of disordered one-dimensional lattices. *Phil. Mag.*, **21**:863, 1970. 4, 7

[65] B. Leimkuhler and S. Reich. *Simulating Hamiltonian Dynamics*. Cambridge University Press, 2004. 157, 158, 159

[66] Z. Li and S. Zhang. Domain-wall dynamics and spin-wave excitations with spin-transfer torques. *Phys. Rev. Lett.*, **92**:207203, 2004. 5, 110, 120, 128, 129

[67] V. I. Litvinov and V. K. Dugaev. Rkky interaction in one- and two-dimensional electron gases. *Phys. Rev. B*, **58**:3584, 1998. 44, 96

[68] K. L. Liu and S. H. Vosko. A time-dependent spin density functional theory for the dynamical spin susceptibility. *Can. J. Phys.*, **67**:1015, 1989. 3

[69] I. I. Mazin. How to define and calculate the degree of spin polarization in ferromagnets. *Phys. Rev. Lett.*, **83**:1427, 1999. 31

[70] E. J. McEniry, D. R. Bowler, D. Dundas, A. P. Horsfield, C. G. Sanchez, and T. N. Todorov. Dynamical simulation of inelastic quantum transport. *J. Phys.: Cond. Matt.*, **19**:196201, 2007. 67, 114

[71] G. E. Moore. Cramming more components onto integrated circuits. *Electronics*, **38**:8, 1965. 1

[72] R. Mota and M. D. Coutinho-Filho. Two-band model for the magnetism of iron. *Phys. Rev. B*, **33**:7724, 1985. 37

[73] N. F. Mott and H. Jones. *The Theory of the Properties of Metals and Alloys*. Courier Dover Publications, 1958. 152

[74] K. C. B. New, K. Watt, C. W. Misner, and J. M. Centrella. Stable 3-level leapfrog integration in numerical relativity. *Phys. Rev. D*, **58**:064022, 1998. 159, 160, 161

[75] S. Oh, C. M. Ryu, and S. H. Suck Salk. Equivalence between aharonov-bohm and aharonov-casher effects, and motive forces. *Phys. Rev. A*, **50**:5320, 1994. 130

[76] M. Onoda and N. Nagaosa. Dynamics of localized spins coupled to the conduction electrons with charge and spin currents. *Phys. Rev. Lett.*, **96**:066603, 2006. 98

[77] S. S. P. Parkin, M. Hayashi, and L. Thomas. Magnetic domain-wall racetrack memory. *Science*, **320**:190, 2008. 110

[78] M. Pratzer, H. J. Elmers, M. Bode, O. Pietzsch, A. Kubetzka, and R. Wiesendanger. Atomic-scale magnetic domain walls in quasi-one-dimensional fe nanostripes. *Phys. Rev. Lett.*, **87**:127201, 2001. 2, 37, 45, 85

[79] P. Pulay. *Ab initio* calculation of force constants and equilibrium geometries in polyatomic molecules. i. theory. *Mol. Phys.*, **17**:197, 1969. 29

[80] P. Pulay. Convergence acceleration of iterative sequences. the case of scf iteration. *Chem. Phys. Lett.*, **73**:393, 1980. 148, 150

[81] P. Pulay. Improved scf convergence acceleration. *J. Comp. Chem.*, **3**:556, 1982. 148, 150

[82] W. H. Rippard, M. R. Pufall, S. Kaka, S. E. Russek, and T. J. Silva. Direct-current induced dynamics in co90fe10/ni80fe20 point contacts. *Phys. Rev. Lett.*, **92**:027201, 2004. 27, 109

[83] A. R. Rocha, V. M. Garcia Suarez, S. W. Bailey, C. J. Lambert, J. Ferrer, and S. Sanvito. Towards molecular spintronics. *Nature Materials*, **4**:335, 2005. 2, 141

[84] E. Runge and E. K. U. Gross. Density-functional theory for time-dependent systems. *Phys. Rev. Lett.*, **52**:997, 1984. 74, 75

[85] G. S. Rushbrooke and P. J. Wood. On the curie points and high temperature susceptibilities of heisenberg model ferromagnets. *J. Mol. Phys.*, **1**:257, 1958. 37

[86] C.M. Ryu. Spin motive force and faraday law for electrons in mesoscopic rings. *Phys. Rev. Lett.*, **76**:968, 1996. 130

[87] C. G. Sanchez, M. Stamenova, S. Sanvito, D. R. Bowler, A. P. Horsfield, and T. N. Todorov. Molecular conduction: Do time-dependent simulations tell you more than the landauer approach? *J. Chem. Phys.*, **124**:214708, 2006. 5, 75, 112

[88] S. Sanvito. *Ab-initio methods for spin-transport at the nanoscale level in "Handbook of Computational Nanotechnology"*. American Scientific Publishers (Stevenson Ranch, California), 2005. also cond-mat/0503445. 154

[89] C. Schieback, M. Klui, U. Nowak, U. Rdiger, and P. Nielaba. Numerical investigation of spin-torque using the heisenberg model. *Eur. Phys. J. B*, **59**:429, 2007. 128

[90] L. Schiff. *Quantum Mechanics*. McGarw-Hill, Inc., 1968. 12

[91] U. Schröter, E. Scheer, R. Arnold, C. Bacca, T. Böhler, J. Grebing, P. Konrad, V. Kunej, N. Kang, H.-F. Pernau, and C. Schrim. Current transport at the atomic scale. *Adv. Eng. Mat.*, **7**:795, 2005. 27, 28

[92] P. Seneor, A. Bernard-Mantel, and F. Petroff. Nanospintronics: when spintronics meets single electron physics. *J. Phys.: Condens. Matt.*, **19**:165222, 2007. 1

[93] J. Slonczewski. Current-driven excitation of magnetic multilayers. *J. Magn. Magn. Mater.*, **159**:L1, 1996. 2, 27, 109

[94] A. K. Solanki, R. F. Sabiryanov, E. Y. Tsymbal, and S. S. Jaswal. Conductance of ni nanocontacts within first-principle approach. *J. Magn. Magn. Mater.*, **272-276**:1730, 2004. 62

[95] R. Sorbello. Electromigration and the local transport field in mesoscopic systems. *Phys. Rev. B*, **39**:4984, 1989. 27, 141

[96] M. Stamenova, S. Sanvito, and T. N. Todorov. Current-driven magnetic rearrangements in spin-polarized point contacts. *Phys. Rev. B*, **72**:134407, 2005. 20

[97] A. Stern. Berrys phase, motive forces, and mesoscopic conductivity. *Phys. Rev. Lett.*, **68**:1022, 1992. 130

[98] M. D. Stiles, W. M. Saslow, M. J. Donahue, and A. Zangwill. Adiabatic domain wall motion and landau-lifshitz damping. *Phys. Rev. B*, **75**:214423, 2007. 111, 120

[99] A. D. Stone and A. Szafer. What is measured when you measure a resistance? - the landauer formula revisited. *IBM J. Res. Dev.*, **32**:384, 1988. 8

[100] A. P. Sutton and T. N. Todorov. A maxwell relation for current-induced forces. *Mol. Phys.*, **102**:919, 2004. 30, 48, 49

[101] A. P. Sutton, T. N. Todorov, M. J. Cawkwell, and J. Hoekstra. A simple model of atomic interactions in noble metals based explicitly on electronic structure. *Phil. Mag. A*, **81**:1833, 2001. 52, 57, 63

[102] G. Tatara and H. Kohno. Microscopic theory of current-driven domain wall motion. *J. Electr. Micr.*, **54**:i69, 2005. 112

[103] G. Tatara, H. Kohno, and J. Shibata. Theory of domain wall dynamics under current. *J. Phys. Soc. Jap.*, **77**:031003, 2008. 111

[104] J. Theilhaber. Ab initio simulations of sodium using time-dependent density-functional theory. *Phys. Rev. B*, **46**:12990, 1992. 96

[105] J. Thijssen. *Computational Physics.* Cambridge University Press, 2007. 157, 158, 159

[106] M. Thorwart and R. Egger. Current-induced nonadiabatic spin torques and domain-wall motion with spin relaxation in a ferromagnetic metallic wire. *Phys. Rev. B*, **76**:214418, 2007. 111, 130

[107] T. N. Todorov. Calculation of the residual resistivity of three-dimensional quantum wires. *Phys. Rev. B*, **54**:5801, 1996. 35, 143, 145

[108] T. N. Todorov. Time-dependent tight binding. *J. Phys.: Condens. Matter*, **13**:10125, 2001. 30, 32, 56, 57

[109] T. N. Todorov. Tight-binding simulations of current-carrying nanostructures. *J. Phys.: Condens. Matter*, **14**:3049, 2002. 77, 116, 118, 151, 152, 153, 154, 155

[110] T. N. Todorov, G. A. D. Griggs, and A. P. Sutton. Elastic quantum transport through small structures. *J. Phys.: Condens. Matter*, **5**:2389, 1993. 77, 143, 145, 155

[111] T. N. Todorov, J. Hoekstra, and A. P. Sutton. Current-induced forces in atomic-scale conductors. *Phil. Mag. B*, **80**:421, 2000. 4, 30, 48, 55, 56

[112] T. N. Todorov, J. Hoekstra, and A. P. Sutton. Current-induced embrittlement of atomic wires. *Phys. Rev. Lett.*, **86**:3606, 2001. 31, 50, 52, 58

[113] C. Toher, A. Filippetti, S. Sanvito, and K. Burke. Self-interaction errors in density-functional calculations of electronic transport. *Phys. Rev. Lett.*, **95**:146402, 2005. 84

[114] Y. Tserkovnyak, A. Brataas, G. E. W. Bauer, and B. I. Halperin. Nonlocal magnetization dynamics in ferromagnetic heterostructures. *Rev. Mod. Phys.*, **77**:1375, 2005. 97, 110

[115] M. Tsoi, R. E. Fontana, and S. S. P. Parkin. Magnetic domain wall motion triggered by an electric current. *Appl. Phys. Lett.*, **83**:2617, 2003. 110

[116] K. Tsukagoshi, B. W. Alphenaar, and H. Ago. Coherent transport of electron spin in a ferromagnetically contacted carbon nanotube. *Nature*, **401**:572, 1999. 2

[117] C. Untiedt, D. M. T. Dekker, D. Djukic, and J. M. van Ruitenbeek. Absence of mechanically induced fractional quantization in atomic contacts. *Phys. Rev. B*, **69**:081401(R), 2004. 28, 66

[118] S. Urazhdin, N. O. Birge, W.P. Pratt, , and J. Bass. Current-driven magnetic excitations in permalloy-based multilayer nanopillars. *Phys. Rev. Lett.*, **91**:146803, 2003. 27, 46

[119] J. B. A. N. van Hoof, K. M. Schep, and A. Brataas. Ballistic electron transport through magnetic domain walls. *Phys. Rev. B*, **59**:138, 1999. 122

[120] A. Vanhaverbeke and M. Viret. Simple model of current-induced spin torque in domain walls. *Phys. Rev. B*, **75**:024411, 2007. 111

[121] M. Di Ventra. *Electrical Transport in Nanoscale Systems.* Cambridge University Press, 2008. 30

[122] M. Di Ventra, Y.-C. Chen, and T. N. Todorov. Are current-induced forces conservative? *Phys. Rev. Lett.*, **92**:176803, 2004. 48

[123] M. Di Ventra and S. T. Pantelides. Hellmann-feynman theorem and the definition of forces in quantum time-dependent and transport problems. *Phys. Rev. B*, **61**:16207, 2000. 29, 30, 32

[124] M. Di Ventra and T. N. Todorov. Transport in nanoscale systems: the microcanonical versus grand-canonical picture. *J. Phys.: Cond. Matt.*, **16**:8025, 2004. 5, 68, 74, 84

[125] M. Viret, W. H. Rippard, S. Berger, M. Gabureac, F. Oh, D. Olligs, I. Petej, J. F. Gregg, C. Fermon, G. Francinet, and G. LeGoff. Magnetoresistance through a single nickel atom. *Phys. Rev. B*, **66**:220401(R), 2002. 2, 27, 46, 85

[126] X. Waintal and M. Viret. Current-induced distortion of a magnetic domain wall. *Europhys. Lett.*, **65**:427, 2004. 128

[127] C. Z. Wang, C. T. Chan, and K. M. Ho. Tight-binding molecular-dynamics study of phonon anharmonic effects in silicon and diamond. *Phys. Rev. B*, **42**:11276, 1990. 88

[128] F. Wilczek and A. Shapere, editors. *Geometrical Phases in Physics.* World Scientific, Singapore, 1996. 130

[129] S. A. Wolf, D. D. Awschalom, R. A. Buhrman, J. M. Daughton, S. von Molnr, M. L. Roukes, A. Y. Chtchelkanova, and D. M. Treger. Spintronics: A spin-based electronics vision for the future. *Science*, **294**:1488, 2001. 1, 2

[130] J. C. Xavier, R. G. Pereira, E. Miranda, and I. Affleck. Dimerization induced by the rkky interaction. *Phys. Rev. Lett.*, **90**:247204, 2003. 96

[131] J. Xiao, A. Zangwill, and M.D. Stiles. Spin-transfer torque for continuously variable magnetisation. *Phys. Rev. B*, **73**:054428, 2006. 112, 128, 129

[132] K. H. Yang and J. O. Hirschfelder. Generalizations of classical poisson brackets to include spin. *Phys. Rev. A*, **22**:1814, 1980. 87

[133] K. Yosida. *Theory of Magnetism.* Spinger-Verlag, 1996. 35, 86

[134] A. Zangwill and P. Soven. Resonant photoemission in barium and cerium. *Phys. Rev. Lett.*, **45**:204, 1980. 76

[135] S. Zhang and Z. Li. Roles of nonequilibrium conduction electron on the magnetisation dynamics of ferromagnets. *Phys. Rev. Lett.*, **93**:127204, 2004. 5, 110, 111, 126